Tectonics in Nevada and Southern California: Subsidence of the Ediacaran Johnnie Formation, Cumulative Offset Along the Lavic Lake Fault, and Geomorphic Surface Development Along the Southern San Andreas Fault

Thesis by

Rebecca Amber Witkosky

In Partial Fulfillment of the Requirements for

the degree of

Doctor of Philosophy

CALIFORNIA INSTITUTE OF TECHNOLOGY

Pasadena, California

2019

(Defended 12 October 2018)

ACKNOWLEDGEMENTS

The material that I present in this thesis is based upon work supported by the National Science Foundation Graduate Research Fellowship Program (under grant 1144469). Mako thermal hyperspectral airborne imagery was acquired under the auspices of the Aerospace Corporation's Independent Research and Development program. I thank my colleagues at The Aerospace Corporation: Dave Tratt, Kerry Buckland, Dave Lynch, Tamara Volquarts, Paul Adams, and Pat Johnson, for providing me with a cornucopia of data, as well as fruitful collaboration and discussion throughout my years as a graduate student. I thank the interns who have helped me during my time at Caltech: Gillian Ferguson, Maggie Andersen, and Jack Nguyen. I thank the Marine Corps Air Ground Combat Center in Twentynine Palms, California, for allowing us access to the military base for geological research; that was really fun and interesting. I thank Ginny Short, Manager of the Thousand Palms Oasis Preserve, for granting access to field sites in the Coachella Valley. Additional acknowledgements are formally included at the end of each chapter, specific to help provided for the individual projects. Thank you to everyone who supported me and helped me with field work, performing the research, preparing the manuscripts, and anything else that I might have not explicitly remembered in this moment.

In my experience, the Acknowledgements section of a graduate student's thesis can often be the most enjoyable, and inspiring part to read. It is like crafting an acceptance speech for an absolutely fabulous award! So, I wanted to make mine special (i.e., way too long and drawn out), and to do that, I wanted to have fun writing this, and hopefully also make it fun for you, the reader. Thank you, Reader, for honoring me by taking the time to acknowledge and review my effort.

There are many people who I would like to thank on a more personal level. My PhD thesis advisors: Joann Stock, thank you so much for helping me earn my PhD; Brian Wernicke, thank you for helping me improve my writing; Jean-Philippe Avouac, thank you for charmingly advising my oral exam project on the Franz Josef Glacier in New Zealand; Bethany Ehlmann, George Rossman, and John Grotiznger, thank you all for working on my thesis advisory committee, and especially for the thoughtful reviews of my work that you provided. All of the Caltech professors and teaching assistants who taught the graduate courses that I completed and learned a lot from. My mentors who helped me arrive and thrive at Caltech: Doug Yule (CSUN/Caltech), Jamshid Hassanzadeh (Caltech/CSUN), Dick Heermance (CSUN), and Kate Scharer (USGS). My fellow Caltech Arms pitsters: Sean Mullin (good community and eats), and Florian Hofmann (good pranks). My friends that I made as a graduate student in the Division of Geological and Planetary Sciences: Elle Chimiak (Hey Girl!), Leah Sabbeth (the Scandinavian swimmer), Heather Steele, Frank Sousa (many pumpkin spices), Jason Price (a true Alpine geologist), Lisa Christiansen, Julie Lee, Janet Harvey, and Ted Present (deep and abundant laughter). All of the many Caltech administrative personnel who handled and assisted in various matters throughout my time here. My friends at the Caltech Center for Diversity: Erin-Kate Escobar, Taso Dimitriadis, and Monique Thomas, thank you for supporting me and helping me discover others and myself. I probably learned some of the most important lessons in my life, and got to see some of the most interesting speakers and presentations during my time at Caltech through events made possible by the Diversity Center. I highly encourage everyone to attend these events, because they celebrate, uplift and raise voices of those who have been systematically oppressed throughout history. You will learn something special about others and yourself, to

be sure! I learned how to recognize the marginalization of people of color, and how to acknowledge the privilege I experience as a white, able-bodied person. I also learned about the great Leslie Feinberg, and how ze once said "…the most powerful way for peoples who face different oppressions to understand each other is by fighting back shoulder to shoulder." That is how I plan to live my life from now on, in solidarity with others who have struggled to be accepted by society. Thank you all for making my experience at Caltech so memorable and providing me with support through times of struggle. I am sorry if I forgot anyone, please don't be offended!

Academic research has helped me find discipline and balance in my life. In earning the PhD, I have also earned self-respect, self-esteem, and patience through the thousands of labor hours that go into writing a thesis. Although this is certainly not a requirement for everyone, I feel like for myself personally, the culmination of this experience has given me the ability to not only pass my oral exam and thesis defense as a student, but more importantly, to pass in life as an empathetic and real human being. I have also realized that a typical grad student's experience can perhaps be summarized quite briefly, in the following manner. I am about to spill the tea on how it often plays out, and you could say, here, that *the category is* PhD annual progression realness: The First year fear (of not passing your oral exam, or the dreaded "quals"); the Second year slump (classes mean little, but you still have to take a bunch!); the Third year throes (struggling to find meaning, discipline, and direction); the Fourth year freedom (no more social obligations, can finally devote 100% of your time to research!); and finally, the Fifth year finale (time to wrap it up and quick, because by now you know how fast a year goes by). From reading other students' theses, I discovered that students always seem to thank their favorite vices, so for me it is

decaffeinated coffee, sugar-free soda, and non-alcoholic beer(; For others who read this and might be struggling, I like to offer this piece of advice that I heard recently: some people like to say that things will get better, but since that is not always the case, perhaps a better outlook is to believe that things will get different.

My final thanks go to my closest loved ones. My blood family: my mom (Anita), dad (Mitchell), stepdad (Sammy), Scarlett, Samantha, Megan, Cyrus, Sasha, and Kai. I love you all so much, and I miss you all the time! My chosen family: Chris, Joy, Brianna, Cassie, and Sasha the dog. I know that the past few years I have been such a doubting Thomassina, but now that I have finally unlocked this epic achievement (woot!), we will all get to spend more time together, just like Nostradama predicted. Thank you Mom, for always encouraging me to return to school and pursue higher education. I would also like to thank Goddexx, whoever, whatever, and wherever she might be ☿

ABSTRACT

While we know the ages and tectonic histories of many critical geologic events in the history of the Earth, there are still questions regarding the timing of key events and structures that have and continue to influence life on this planet. This thesis includes three separate studies in Nevada and southern California: two potential new methods for measuring/organizing geologic time, and also an analysis of the long-term displacement along an active fault in the eastern California shear zone. In Chapter II, we used tectonic subsidence modeling to find that the Shuram carbon isotopic excursion in the Ediacaran Johnnie Formation likely occurred from 585-579 Ma, and that incision of the Rainstorm Member shelf occurred during the 579 Ma Gaskiers glaciation. The pre-Shuram-excursion chemostratigraphic carbon isotope profiles from the Khufai Formation in Oman and the type locality of the Johnnie Formation in Nevada are both generally positive and therefore possibly correlative. In Chapter III, we determined the cumulative tectonic offset along the Lavic Lake fault, an active structure that ruptured with >5 m of coseismic slip in the 1999 Mw 7.1 Hector Mine earthquake. We calculated a net slip of 960 +70/-40 m, based on the slip vector formed by a vertically separated lithologic contact and a horizontally separated older cross fault. The net slip we calculated is significantly less than a previous estimate that was based on an offset magnetic gradient, a disparity that may be explained by considering off-fault deformation, as well as the unknown depth and nature of the source of the magnetic contrast. In Chapter IV, we explored using a new method for the relative dating of Quaternary geomorphic surfaces, which is based on the positive correlation between increased spectral contrast in thermal hyperspectral airborne imagery and surface age. With field data, we found that desert varnish scores, desert pavement scores, and vegetation spacing estimates also

correlate positively with surface age, implying that these factors could contribute to the increased spectral contrast in airborne remote sensing spectra. Additionally, the general increase in the band depth of airborne spectra at 9.16 μm could be due to increasing clay mineral abundance in progressively heavier desert varnish coatings on older surfaces. The positive correlation observed in this study between surface age and spectral contrast in airborne spectra can perhaps be used to develop a method for relative dating of varnished geomorphic surfaces elsewhere. All of the chapters in this thesis are broadly related by the concepts of geologic time and tectonic activity, which are two aspects of modern geology that are intrinsic to the science as a whole.

PUBLISHED CONTENT AND CONTRIBUTIONS

Witkosky, R., and Wernicke, B.P., 2018, Subsidence history of the Ediacaran Johnnie Formation and related strata of southwest Laurentia: Implications for the age and duration of the shuram isotopic excursion and animal evolution: Geosphere, v. 14, n. 5, https://doi.org/10.1130/GES01678.1.

R.A.W. participated in the field work and conception of the project, completed the laboratory work and data modeling, and led the writing of the manuscript.

TABLE OF CONTENTS

LIST OF TABLES AND FIGURES

Chapter 1

INTRODUCTION

One of the most fundamental goals of geological science is the identification and temporal organization of natural events that define the history of the Earth. While radioactive dating is a reliable method for determining ages of some terrestrial material, the required minerals and/or rock types are not always conveniently present. This has motivated the discovery of other methods, such as those based on tectonic subsidence of the crust of the Earth, for measuring geologic time. Another fundamental goal in geoscience is reconstruction of crustal movement. Many independent methods have allowed us to determine the motion of tectonic plates, which is nearly imperceptible on timescales relative to the human experience. Of great interest to Earth scientists are measurements of fault motion that has accumulated over geologic timescales, as well as other processes that have shaped the landscape.

The geographic locations of the study areas in this thesis are all located in Nevada and southern California, but the research covers a variety of geologic settings. During the Ediacaran period, siliciclastic and carbonate sediments accumulated on a thermally subsiding passive margin on the equatorial coast of Laurentia; these sediments are now the lithified and tilted strata of the Johnnie Formation in Nevada. Sometime during the early Pliocene to Micoene, regional tectonic deformation triggered the inception of many distinct right-lateral faults, including the active Lavic Lake fault, in what is now the eastern California shear zone. Finally, geomorphic surfaces continue to develop due to San Andreas fault motion, coupled

with the warm and arid environment of the Coachella Valley in southern California. A diversity of time periods and tectonic activity were considered in this compilation of projects.

In Chapter II of this thesis, we used tectonic subsidence modeling to investigate the specific timing and duration of a globally-recognized chemostratigraphic anomaly: the Shuram carbon isotope excursion. The Shuram excursion is an extreme deviation in the ratio of ^{13}C to ^{12}C found in carbonate rocks. Metabolic pathways involve mass-dependent fraction of carbon isotopes, so it is possible that the excursion signals an event that influenced the evolution of animals. While not well dated, the excursion is present in the Ediacaran Johnnie Formation, a section of siliciclastic and carbonate rocks located in southern Nevada and California. At the Johnnie Formation type locality near Pahrump, Nevada, we performed detailed field mapping and stratigraphic measurements. On carbonate rocks that we sampled, we performed carbon and oxygen isotope fraction measurements, which allowed us to correlate the chemostratigraphy of the Johnnie Formation with sub-Shuram-excursion chemostratigraphic profiles from the Khufai Formation in Oman. While the correlation in itself did not yield an age for the Shuram excursion, the correlation helped us bracket the age of the Shuram excursion within Johnnie Formation to somewhere between 600-550 Ma. We then combined the stratigraphic thickness we measured for the Johnnie Formation with the thicknesses of overlying formations (some of which have been dated) that span through end Devonian time. With the complete stratigraphic thickness, and some known ages at specific stratigraphic positions in overlying formations, we constructed a tectonic subsidence model for this ancient passive margin environment. We used this model to extrapolate ages for stratigraphic positions within the Johnnie Formation, and other key Ediacaran horizons of unknown age in the section. We found that the Shuram excursion within the Johnnie

Formation occurred from 585-579 Ma, and that incision of the Rainstorm Member shelf occurred during the 579 Ma Gaskiers glaciation.

In Chapter III, we combined fieldwork with thermal hyperspectral airborne remote sensing imagery to investigate the long term cumulative slip of the Lavic Lake fault in eastern California. The Lavic Lake fault ruptured in the 1999 Mw 7.1 Hector Mine earthquake with >5 m of coseismic right-lateral slip, but the long-term bedrock offset is not well-defined. While the Lavic Lake fault is located on military-restricted government land, we gained access in 2012 and 2014 to collect new field data. The field lithologic samples we collected, in addition to field photographs, served as ground truth for geologic maps we produced using supervised and unsupervised classifications of airborne remote sensing imagery. We also incorporated data from older geologic maps of the same area into our analysis. In comparing our classification maps with older geologic maps, we discovered a boundary between units in our supervised classification map that correlated with a lithologic contact from the older map. This lithologic contact is cut and displaced by the Lavic Lake fault, and there is also an older cross fault that is cut and displaced by the Lavic Lake fault: we used these two displaced features to measure the vertical and horizontal components of the slip vector. The net fault slip of the Lavic Lake fault is 960 +70/-40 m, which is significantly less than a previous estimate of cumulative offset that was based on an offset magnetic gradient. The disparity between our measurement and the displaced magnetic gradient can be at least partially explained by off-fault deformation along proximal smaller structures, as well as the unknown depth and nature of the source of the magnetic contrast. Our cumulative displacement can be combined with bedrock ages to calculate the Lavic Lake fault's geologic slip rate, and it can also be included in a tectonic reconstruction of the eastern California shear zone.

Chapter IV of this thesis is about a potential new method for the relative dating of Quaternary geomorphic surfaces. The development of features that increase with time, such as desert varnish coatings and smoothed topography known as desert pavement, are characteristic to many geomorphic surfaces. We used thermal hyperspectral airborne remote sensing imagery of geomorphic surfaces to investigate a spectral feature at 9.16 μm with band depth that generally increases with surface age. The 9.16 μm feature is indicative of clay minerals, which can be found in abundance in desert varnish. Supplemental field data show that desert varnish and desert pavement scores (where a higher score is given to more advanced development), as well as vegetation spacing estimates, all correlate positively with surface age. In ground-based lithologic spectra that we collected, an absorption feature at 9.2-9.4 μm is also indicative of clay minerals, albeit at a slightly different position than that for the airborne data. All of the spectra indicate a mineral mixture that includes clay, quartz, and feldspars. Furthermore, ground-based vegetation spectra are generally flat and featureless: this could be why sparse vegetation correlates with increased spectral contrast in the airborne data. Taking everything into consideration, the positive correlation between surface age and spectral contrast in airborne spectra can perhaps be used for relative dating of varnished Quaternary geomorphic surfaces with desert varnish and desert pavement.

While the individual chapters of this thesis cover disparate topics, the driving motivation in each is related to quantifying geologic time and/or tectonic displacement. Moreover, each chapter is a complete study, offering a unique contribution to the breadth of knowledge that we use to tell the story of the Earth.

Chapter 2

SUBSIDENCE HISTORY OF THE EDIACARAN JOHNNIE FORMATION AND RELATED STRATA OF SOUTHWEST LAURENTIA: IMPLICATIONS FOR THE AGE AND DURATION OF THE SHURAM ISOTOPIC EXCURSION AND ANIMAL EVOLUTION

Witkosky, R., and Wernicke, B.P., 2018, Subsidence history of the Ediacaran Johnnie Formation and related strata of southwest Laurentia: Implications for the age and duration of the Shuram isotopic excursion and animal evolution: Geosphere, v. 14, n. 5, https://doi.org/10.1130/GES01678.1.

ABSTRACT

The Johnnie Formation and associated Ediacaran strata in southwest Laurentia are ~3000 m thick, with a Marinoan cap carbonate sequence at the bottom, and a transition from Ediacaran to Cambrian fauna at the top. About halfway through the sequence, the Shuram negative carbon isotopic excursion occurs within the Rainstorm Member near the top of the Johnnie Formation, followed by a remarkable valley incision event. At its type locality in the northwest Spring Mountains, Nevada, the Johnnie lithostratigraphy consists of three distinctive sand-rich intervals alternating with four siltstone/carbonate-rich intervals, which appear correlative with other regional Johnnie Formation outcrops. Carbon isotope ratios in the sub-Rainstorm Member part of the Johnnie Formation are uniformly positive for at least 400 m below the Shuram excursion and compare well with sub-Shuram excursion profiles

from the Khufai Formation in Oman. There is historical consensus that the Johnnie and overlying formations were deposited on a thermally subsiding passive margin. Following previous authors, we used Paleozoic horizons of known biostratigraphic age to define a time-dependent exponential subsidence model, and extrapolated the model back in time to estimate the ages of the Shuram excursion and other prominent Ediacaran horizons. The model suggests that the Shuram excursion occurred from 585 to 579 Ma, and that incision of the Rainstorm Member shelf occurred during the 579 Ma Gaskiers glaciation. It further suggests that the base of the Johnnie is ca. 630 Ma, consistent with the underlying Noonday Formation representing a Marinoan cap carbonate sequence. Our results contrast with suggestions by previous workers that the Shuram excursion followed the Gaskiers event by some 20 - 30 m.y. We suggest instead that the Shuram and Gaskiers events were contemporaneous with the biostratigraphic transition from acanthomorphic to leiospherid acritarchs, and with the first appearance of widespread macroscopic animal life, 38 m.y. prior to the Ediacaran-Cambrian boundary.

INTRODUCTION

Ediacaran strata record a critical period in Earth history (635-541 Ma), during which metazoan life first appeared (Knoll et al., 2004, 2006; Narbonne et al., 2012). They also record a significant rise in atmospheric and oceanic oxygen (Fike et al., 2006; Canfield et al., 2007; McFadden et al., 2008; Sahoo et al., 2012), which was a prerequisite to metabolic function in animals (Knoll and Carroll, 1999; Och and Shields-Zhou, 2012). Neoproterozoic oxygenation resulted in atmospheric levels generally interpreted as similar to those of the

present day (Holland, 2006; Kump, 2008). Today, atmospheric oxygen levels are maintained by photosynthesis from land plants and marine organisms in roughly equal proportions (e.g., Field et al., 1998). It has therefore long been enigmatic that land plants are not preserved in rocks older than ca. 400 Ma, or ~150 m.y. later than the first appearance of animals. For that reason, it is widely presumed that the rise of animal life required sufficient oxygen production, from either marine photosynthesis, or perhaps some sort of "bootstrap" mechanism from animals themselves, to survive (e.g., Butterfield, 2009; Lenton et al., 2014). In any event, progress toward understanding the fundamental question, "what is the origin of animals?," hinges in part on understanding how and when oxygen became sufficiently available to make animal metabolism possible (e.g., Nursall, 1959).

Among the most fruitful avenues of research along these lines to date has been exploration of proxies for the chemistry of seawater in which animal life first appeared, primarily the stable isotope geochemistry of shallow-marine carbonate strata. The best-preserved Ediacaran strata around the globe that contain carbonate all feature a singularly large (by about a factor of two) negative anomaly in the isotopic composition of carbon, which has been attributed primarily to the isotopic composition of ancient seawater itself (Fike et al., 2006; McFadden et al., 2008; but for an alternative view, see Swart and Kennedy, 2012). The anomaly is best preserved and documented in the Ediacaran Shuram Formation in Oman (Burns and Matter, 1993; Le Guerroué et al., 2006a, 2006b; Osburn et al., 2015), and is generally referred to as the "Shuram excursion," taking its name from the discovery formation. A similar excursion has been documented in Neoproterozoic sections on five of Earth's seven modern continents, and it occurs only once in each section: Africa (Kaufman et al., 1991; Halverson et al., 2005), Asia (Burns and Matter, 1993; Condon et al., 2005;

Melezhik et al., 2005; Fike et al., 2006; McFadden et al., 2008; Macdonald et al., 2009; Osburn et al., 2015), Australia (Calver, 2000; Husson et al., 2015), Europe (Melezhik et al., 2005; Prave et al., 2009), and North America (Myrow and Kaufman, 1999; Corsetti et al., 2000; Corsetti and Kaufman, 2003; Kaufman et al., 2007; Bergmann et al., 2011; Petterson et al., 2011; Verdel et al., 2011; Macdonald et al., 2013). The Shuram excursion is the largest known Neoproterozoic or younger carbon isotope anomaly (Grotzinger et al., 2011), and its magnitude is among the largest recorded in Earth history (see, for example, the Paleoproterozoic Lomagundi-Jatuli excursion; Bekker and Holland, 2012).

Global chemostratigraphic expression of the Shuram excursion is a remarkable discovery from at least three perspectives. First, it represents a presumably isochronous fingerprint of a specific interval of time from sections with notoriously sparse age constraints. Second, it implies that a geologically extreme event of uncertain origin occurred at the same time as the rise of animals. Last, the singular magnitude of the excursion contributes to the goal of creating a global composite time series of secular variations in marine carbon isotope ratios. In regard to the third point, the duration of the anomaly raises the potential for using the shapes of the curves, rather than simply the magnitudes of the excursions, as a correlation tool from section to section; this of course presumes a relatively constant sedimentation rate at the hundred-meter scale (Halverson et al., 2005; Saltzman and Thomas, 2012). For the Shuram excursion, $\delta^{13}C$ values rapidly descend with stratigraphic position to < -11‰ followed by a recovery that is at first gradual and then moderate in slope, with the change occurring near -4 ‰ (Figure 2 in Condon et al., 2005; Figure 3 in Prave et al., 2009; Figure 16 in Verdel et al., 2011; Figure 3 in Grotzinger et al., 2011; Figure 13 in Macdonald et al., 2013; Figure 1A in Husson et al., 2015).

At present, the most significant impediment to understanding Ediacaran biostratigraphy is the lack of internal age control in most sections around the globe. The ages of the boundaries of the Ediacaran Period are well defined radiometrically in multiple sections. The base is defined by the lithologically distinctive post-Marinoan cap carbonate sequence, which is associated with a -6 ‰ $\delta^{13}C$ excursion in carbonate and is precisely dated at 635 Ma in Namibia and China (Hoffmann et al., 2004; Condon et al., 2005). The top is defined by the first appearance of the trace fossil *Treptichnus pedum* (541 Ma), which is also associated with a -6 ‰ $\delta^{13}C$ excursion in carbonate. Other than the first appearance of large Ediacaran body fossils, which usually occurs rather high in most sections relative to the Ediacaran-Cambrian boundary, the Shuram excursion has emerged as the single most distinctive stratigraphic datum that is globally recognized. However, its precise age is poorly constrained, precluding any attempt to meaningfully subdivide some 94 m.y. of Ediacaran time, and creating first-order uncertainties in the relative timing of major environmental and biostratigraphic events (Xiao et al., 2016). A second major stratigraphic feature, largely restricted to sections in the North Atlantic region, is the Gaskiers glaciation (Myrow and Kaufman, 1999), which, in contrast to the Shuram event, is precisely dated at 579 Ma (Bowring et al., 2003a, 2003b; Pu et al., 2016). The mismatch between sections with glaciogenic rocks and precise radiometric ages on one hand, and the Shuram excursion in carbonate strata on the other, has left it uncertain whether or not these two events are correlative (Xiao et al., 2016). A 580 Ma age for the Shuram excursion provides an obvious correlation between the two most conspicuous events in the Ediacaran record (e.g., Xiao et al., 2004; Fike et al., 2006; Zhou et al., 2007; Halverson et al., 2005, 2010; Loyd et al., 2012; Schiffbauer et al., 2016). Alternatively, the stratigraphic proximity of the Shuram excursion

to the Precambrian-Cambrian boundary, and a 551 Ma ash bed near the apparent upper zero crossing of the excursion in the Doushantuo Formation of China, suggests that it may be as much as 20-30 m.y. younger than the Gaskiers glaciation (Condon et al., 2005; Bowring et al., 2007; Cohen et al., 2009; Sawaki et al., 2010; Narbonne et al., 2012; Macdonald et al., 2013; Tahata et al., 2013; Xiao et al., 2016).

One chronological tool that has heretofore only been sparingly applied to Ediacaran strata is thermal subsidence analysis (e.g., Le Guerroué et al., 2006b). It is well known that thermal subsidence associated with seafloor spreading is a useful chronometer that can predict the age of the ocean floor based on the exponential decay of its elevation with respect to the abyssal plains for lithosphere older than 20 m.y. (e.g., Equation 22 in Parsons and Sclater, 1977). The same principle also applies to models of the subsidence history of passive-margin basins, which include an initial thickness of newly stretched continental crust and substantial sediment loading (McKenzie, 1978). The decay is predicted by laws of diffusive heat transport of physical rigor that are on par with laws of closed-system radioactive decay used to date the timing of crystallization of minerals. The principal limitations in using thermal conduction as a chronometer are (1) the requirement that subsidence records thermal relaxation without significant mechanical modification of the lithosphere, such as extension, flexural loading, instability of a thermal boundary layer, or unmodeled sources of dynamic topography; and (2) correction of the observed stratigraphic subsidence for the compaction and lithification of sediment after deposition, and for water depth and changes in sea level (e.g., Steckler and Watts, 1978; Allen and Allen, 2005).

In comparison with Phanerozoic sedimentary basins, published subsidence analyses of Ediacaran strata have been limited, with most of the effort thus far concentrated on the

western Laurentian continental margin (Stewart and Suczek, 1977; Bond et al., 1983; Armin and Mayer, 1983; Levy and Christie-Blick, 1991; Yonkee et al., 2014). The focus on this region as a testing ground for thermal subsidence modeling was due to the fact that it is perhaps the best-preserved example of an ancient passive margin, analogous to present-day Atlantic-type margins, but with virtually complete surface exposure of apparent synrift and postrift sedimentary archives spanning several hundred million years (Stewart, 1972; Gabrielse, 1972; Burchfiel and Davis, 1972, 1975; Stewart and Poole, 1974; Dickinson, 1977; Monger and Price, 1979). Because these sequences span the Ediacaran-Cambrian boundary, such that roughly half their thickness is Proterozoic in age, temporal control on subsidence has been restricted mainly to the Phanerozoic portion of subsidence curves. The lack of age control on the lower part of the section precludes precise definition of the transition from mechanical extension to pure thermal subsidence. Fortunately, the accurate definition of an exponentially decaying system, in particular, extrapolating stratigraphic age backward in time from a curve with known ages, is independent of the timing of onset and total amount of purely thermal subsidence.

Here, we address the problem of the correlation and age of the Shuram isotopic excursion through lithostratigraphic and chemostratigraphic study of the type locality of the Ediacaran Johnnie Formation in the Spring Mountains of southern Nevada. The Johnnie Formation is at least 1800 m thick at the type locality, and it makes up more than half of the maximum known thickness of ~3000 m of total Ediacaran strata exposed in this region. The underlying Noonday Formation provided the first isotopic match between the Marinoan cap carbonate sequence in Namibia (Hoffman et al., 1998) and a section from another continent (Petterson et al., 2011). The overlying Stirling and Wood Canyon Formations contain

Ediacaran and Lower Cambrian fossil assemblages that define the Cambrian-Precambrian boundary within the lower part of the Wood Canyon Formation (Corsetti and Hagadorn, 2000; Hagadorn and Waggoner, 2000), 1200 m above the top of the Johnnie Formation in the Spring Mountains. The uppermost 300 m of section of the Johnnie Formation contains the best expression of the Shuram excursion in Laurentia (Corsetti and Kaufman, 2003; Kaufman et al., 2007; Bergmann et al., 2011; Verdel et al., 2011). Therefore, to the extent that the section was deposited at or very near sea level on a thermally subsiding continental shelf, subsidence analysis may be used to estimate the age of the Shuram excursion and perhaps even broadly constrain the overall age of the Johnnie Formation.

GEOLOGIC SETTING

Neoproterozoic-Cambrian strata in western Laurentia are divisible into two principal components, including a lower diamictite and volcanic sequence, and an upper terrigenous detrital sequence (Stewart and Suczek, 1977; Poole et al., 1992). The Johnnie Formation is the lowest siliciclastic formation in the upper terrigenous detrital sequence, forming the basal deposits of a westward-thickening continental margin terrace wedge, widely regarded to have developed in the wake of late Neoproterozoic rifting of the Rodinian supercontinent (Li et al., 2008, 2013). The formation is a few hundred meters thick near its eastern pinchout beneath Lower Cambrian cratonic strata, systematically increasing to at least 1500 m thick in its westernmost exposures, where the base is not definitively exposed (Stewart, 1970; this report). Lithologically, it is primarily variegated siltstone and very fine-grained sandstone that contains varying amounts (10-40%) of carbonate and orthoquartzite, distinguishing it

from the carbonate-dominated Noonday Formation below and coarse siliciclastic rocks of the Stirling Formation above (Figure 1).

The Johnnie Formation was first defined and described in the northwest Spring Mountains in the Johnnie Wash area (Figure 2; Nolan, 1924, 1929), where its contact with the underlying Noonday Formation is apparently not exposed, and hence its thickness is a minimum for this location. Nolan's (1924) thickness and description were included in the regional stratigraphic synthesis of Stewart (1970). The type locality was subsequently mapped and briefly described by Burchfiel (1964, 1965), and relatively complete lithostratigraphic sections were measured by Hamill (1966) and Benmore (1978). The type locality has since received little attention in comparison to the much thinner sections in the Nopah Range and environs 70 km to the south, or equivalents 100 km to the west in the Panamint Range, where its basal contact with the Noonday Formation is extensively exposed (e.g., Hazzard, 1937; Wright and Troxel, 1966; Labotka et al., 1980; Albee et al., 1981; Benmore, 1978; Summa, 1993; Fedo and Cooper, 2001; Corsetti and Kaufman, 2003; Kaufman et al., 2007; Verdel et al., 2011). With the exceptions of detailed studies of parts of the formation (Summa, 1993; Abolins, 1999; Bergmann et al., 2011), no systematic attempt has yet been made to describe and interpret the entire formation at its type locality in terms of key bed forms, depositional environments, sequence architecture, or chemostratigraphy, at the level of more southerly or westerly sections.

The uppermost part of the Johnnie Formation, the Rainstorm Member, is a lithostratigraphically distinctive unit that can be correlated with confidence over a broad region of southwestern North America, including eastern California and southern Nevada (Stewart, 1970), and it probably occurs as far south as northern Sonora, Mexico, where it

forms a part of the Clemente Formation (Stewart et al., 1984). The basal strata of the Rainstorm Member are its most distinctive part. They include a thin (~2 m), siltstone-enveloped, regionally extensive oolitic marker bed known as the "Johnnie oolite" (e.g., Bergmann et al., 2011). The oolite is underlain by greenish gray siltstone, and it is overlain by distinctive pale-red, fine-grained sandstone with or without associated sandy or silty micrites ("liver-colored limestones"). The overlying units characteristically contain groove marks, flute casts, intraformational conglomerate, and other indicators of shallow water, high-energy currents. These carbonates record the onset and most negative part of the Shuram excursion in eastern California and southern Nevada (Corsetti and Kaufman, 2003; Kaufman et al., 2007; Verdel et al., 2011), as well as in the Sonora sections (Loyd et al., 2012). Similar to formation-scale thickness variations in the terrigenous detrital sequence as a whole, the Rainstorm Member generally thickens westward from as little as 20 m in the thinnest measured section to more than 300 m in the thickest sections (Stewart, 1970; Verdel et al., 2011).

Lower and middle Johnnie Formation strata are sufficiently variable in their lithostratigraphy, that recognition of regionally mappable members is not as straightforward as in the case of the Rainstorm Member. As noted by Summa (1993), sub-Rainstorm Member depositional settings of the Johnnie Formation are interpreted as inner-shelf to tidally influenced nearshore environments that were highly susceptible to sea level fluctuation (Benmore, 1978; Fedo and Cooper, 2001; Schoenborn et al., 2012). As we describe herein, depositional environments tend to be more landward to the south and east in these units, as suggested by the abundance versus absence of dessication features, fluvial versus marine deposition, and medium- to coarse-grained sandstones versus fine- to medium-grained

sandstones. Although this variability complicates simple lithostratigraphic correlation, if interpreted correctly, it can be used as an effective indicator of sea-level rise and fall.

Reported age constraints from the Johnnie and correlative Clemente Formations include (1) a 640 Ma U-Pb age from a single detrital zircon grain in sub-Rainstorm Member siltstones in the Panamint Range of eastern California (Verdel et al., 2011), and (2) potential Ediacaran body and trace fossils (e.g., *Cyclomedusa plana* and *Palaeophycus tubularis*, respectively) ~75 m below the oolite in the Clemente Formation (McMenamin, 1996). The U-Pb age, because it is based on a single grain, is subject to the uncertainty of contamination during mineral processing and needs to be confirmed with duplicate analyses. The putative fossils have been questioned after examination by other paleontologists (e.g., J.W. Hagadorn, 2017, personal communication), and they have generally not been accepted in subsequent stratigraphic studies of the region (e.g. Loyd et al., 2012, 2015). Latest Ediacaran fossils have been recovered from the uppermost Stirling Formation and the Lower Member of the Wood Canyon Formation in the Spring Mountains and neighboring Montgomery Mountains to the south (e.g. *Cloudina* and *Swartpuntia*; Hagadorn and Waggoner, 2000; Smith et al., 2017), from sections in stratigraphic continuity with the type Johnnie Formation. These are succeeded immediately upward by Lower Cambrian trace fossils (*Treptichnus pedum*), which places the Ediacaran-Cambrian boundary in the Lower Member of the Wood Canyon Formation (Figure 1; Corsetti and Hagadorn, 2000).

The underlying Noonday Formation has been interpreted as the cap carbonate sequence of the Marinoan “snowball Earth” glaciation (Petterson et al., 2011), which by definition would place its base at the beginning of the Ediacaran period (635 Ma; Knoll et al., 2004, 2006; Narbonne et al., 2012). The Johnnie Formation’s basal contact with the

Noonday Formation is lithostratigraphically gradational, transitioning from sandy dolostones of the upper Noonday Formation (Mahogany Flats Member of Petterson et al., 2011), to interstratified dolomitic sandstone and orthoquartzite in the lower Johnnie Formation (Transitional Member of Stewart, 1970). Although traditionally regarded as a conformable contact on the basis of this gradation (Hazzard, 1937; Stewart, 1970; Wright and Troxel, 1984), the identification of local karstic surfaces along the contact raises the possibility that it is a disconformity with a substantial depositional hiatus (Summa, 1993).

In terms of chemostratigraphic constraints on age, the conspicuous excursions to -6 ‰ at the base and top of the Ediacaran section are well expressed in the south Laurentian sections (e.g., Petterson et al., 2011; Smith et al., 2016). The presence of the Shuram excursion in the Rainstorm Member, despite its value as a correlation tool, does little to constrain the depositional age, because unlike the tightly constrained boundary excursions, hard chronological constraints are lacking, as noted already.

For almost a century, the terrigenous detrital sequence has been studied extensively on many different levels. Much of the early work focused on stratigraphic group-level packages that record the transition from Precambrian to Cambrian time (Nolan, 1929; Burchfiel, 1964; Stewart, 1970). More recent work on the Johnnie Formation has focused largely on outcrops in eastern California (Summa, 1993; Fedo and Cooper, 2001; Verdel et al., 2011; Schoenborn and Fedo, 2011; Schoenborn et al., 2012), or on specific features related to the Rainstorm Member, such as an incision-related conglomeratic member (Summa, 1993; Abolins, 1999; Abolins et al., 2000; Clapham and Corsetti, 2005; Verdel et al., 2011), giant ooids (Trower and Grotzinger, 2010), or detailed chemostratigraphy of the Johnnie oolite (Bergmann et al., 2011). The lower and middle portions of the Johnnie

Formation have not been given as much detailed attention, except in areas close to the craton miogeoclinal hinge where the Johnnie Formation is only a few hundred meters thick. The 1600 m stratigraphic thickness of sub-Shuram excursion Johnnie Formation at the type locality exceeds the thickness of any globally correlative Ediacaran strata of which we are aware. Furthermore, total Ediacaran stratigraphic thickness in southwest Laurentia measures over 3000 m, greater than the approximate thicknesses of sections in Australia (2500 m), Oman (1500 m), and China (300 m). Strata of the lower and middle Johnnie Formation at its type locality therefore represent one of the best opportunities among sections globally to provide a relatively complete record of Ediacaran time prior to the Shuram excursion. An important gap in our understanding of Ediacaran chemostratigraphy is the paucity of carbonate strata below the Shuram anomaly in most sections. Of the major global sections that contain it, only the Oman example contains abundant carbonate in immediately underlying strata, the Khufai Formation. Discovery of correlative carbonate-bearing strata in one or more sections around the globe would thus represent a significant step in expanding the global inventory of chemostratigraphic time series for a critical interval in Neoproterozoic time.

METHODS

Lithostratigraphy

To identify a structurally intact section of the Johnnie Formation, we performed geologic mapping at 1:10,000 scale in the northwest Spring Mountains, Nevada, both of the type

locality at Johnnie Wash, and in an area ~4 km to the southwest near Nevada Highway 160, 3 km west-southwest of Mount Schader (Figure 2). We used the Mount Schader, Nevada 1:24,000 quadrangle map (U.S. Geological Survey, 1968) as a topographic base. Our field mapping spanned 9 days total between 21 April 2015 and 2 May 2015. The geologic maps were used to identify optimum transects for measuring stratigraphic section. The Mount Schader section was measured and sampled in detail using a Jacobs staff mounted with a Brunton® compass set to the dip of bedding. For each stratigraphic subunit, we recorded (1) fresh and weathered color of lithology using a Munsell color chart, (2) grain size, and (3) bedding thickness (supplemental text). Section was measured to the resolution of ~0.5 m (or finer in some instances, if warranted). The Johnnie Wash section was measured using geologic cross sections, and the general lithologic characteristics were recorded in the field during geologic mapping (see Appendix for unit names and descriptions).

Chemostratigraphy

For carbon and oxygen isotope chemostratigraphy, we collected samples at 0.3-1 m resolution in carbonate units. Samples from the upper ~400 m of sub-Rainstorm Member lithostratigraphic units were collected from the Mount Schader section during stratigraphic logging. Samples from two prominent carbonate horizons that occur below the deepest exposed strata of the Mount Schader section were collected in the Johnnie Wash locality of the Spring Mountains, and at a location ~3 km north of Johnnie Wash (Locality A in Figure 2A). In total, 107 centimeter-scale sample chips were collected for carbon and oxygen isotopic analysis, including 36 from the Johnnie Wash section and Locality A and 71 from

the Mount Schader section. In the laboratory, sample chips were sliced open using a diamond-bladed wet saw to expose fresh, unweathered surfaces. From the fresh surfaces, a high-speed rotary tool with a diamond-tipped drill bit was used to powder the sample. We carefully extracted ~0.1 mg of analyte from each sample chip, taking care to avoid any visible alteration or veining. Sample powder was loaded into vials and the air was purged and replaced with helium gas, and then the powder was digested in phosphoric acid at 72° C for at least one hour to evolve sufficient CO_2 gas for analysis. Carbon and oxygen isotope ratios were measured at Caltech using a Delta V Plus Isotope Ratio mass spectrometer ("gas bench"). Our values for $\delta^{13}C$ and $\delta^{18}O$ are reported relative to the Vienna Pee Dee Belemnite (VPDB) standard in per mil notation. We used Caltech's laboratory working standards, which were calibrated to NBS 18 and NBS 19 and have uncertainties of +/-0.1 ‰. Standards were measured once for every nine samples to assess systematic error.

Subsidence Analysis

Our tectonic subsidence analysis is based on stratigraphic thicknesses compiled from multiple sources for the northwest Spring Mountains, Nevada. The inner shelf to fluvial-deltaic facies of virtually all units within the terrigenous detrital sequence in this region suggest shallow water deposition, removing the need for paleobathymetric correction (Levy and Christie-Blick, 1991). We used thicknesses from this study combined with thicknesses for overlying formations principally based on Stewart (1970) and Burchfiel et al. (1974). Our analysis encompasses known time points ranging from the Ediacaran-Cambrian boundary in the Lower Member of the Wood Canyon Formation (Corsetti and Hagadorn, 2000; Hagadorn

and Waggoner, 2000; Smith et al., 2016, 2017) at 541 Ma, up through the Devonian-Mississippian boundary at the top of the Devils Gate Formation (Burchfiel et al., 1974) at 359 Ma (Ogg et al., 2016). The only previous attempt at a geohistory analysis of the Spring Mountains (Levy and Christie-Blick, 1991) was temporally constrained mainly by the Lower-Middle and Middle-Upper Cambrian boundaries, which were then deemed to be ~30 m.y. older than their currently accepted ages. We followed methods described in Allen and Allen (2005) to delithify and progressively unload (backstrip) the stratigraphic column in order to obtain the tectonic component of subsidence. Delithification parameters for siliciclastic rocks were taken from Table 9.1 in Allen and Allen (2005), and parameters for carbonate rocks were taken from Equation 3 in Halley and Schmoker (1983). Tectonic subsidence curves were calculated using *Backstrip*, an open-source software for decompaction and tectonic subsidence calculations (Cardozo, 2009). Results for our earliest model runs were verified by hand using a spreadsheet program (e.g., Larrieu, 1995).

RESULTS

Lithostratigraphy

The most salient feature of the Johnnie Formation in the Johnnie Wash type locality (Figure 3) is that, although very fine-grained sandstone and siltstone is present in all mappable units (distinguishing it from the overlying Stirling and underlying Noonday formations), three intervals are characterized by an abundance of fine- to medium-grained sandstone (identified with Roman numerals I, II, and III on Figure 4). The sand-rich intervals

range from 160-430 m thick, form distinct, resistant ridges within the otherwise recessive Johnnie Formation, and establish a basis for subdividing it into mappable units. Each sand-rich interval exhibits characteristics that readily distinguish it from the other two, in terms of either bedforms (intervals I and II) or parasequence architecture (interval III). Further subdivision of the formation is afforded by a conspicuous, 30 to 40 m-thick cherty carbonate unit near the middle of the section, and by lithological variation within sand-rich interval III. Our subdivision into map units includes the Rainstorm Member at the top, underlain by twelve informal units designated A through L (Figures 4 and S1). Sand-rich intervals I and II define units B and D, and their enveloping sand-poor strata define units A, C, and E. The cherty carbonate marker and overlying sand-poor strata define units F and G. The upper sand-rich interval exhibits rhythmic variations of sandstone, siltstone, and carbonate that are divided into five units, H through L, each of which is defined at the base of a 30 to 100 m-thick sand-rich subinterval (Figures 3, 4, and S1).

At the Johnnie Wash type section, bedding strikes approximately north-south and dips moderately to steeply eastward (Figure 3). The total thickness of sub-Rainstorm strata is 1595 m. The lowest stratigraphic unit (unit A) encountered is a recessive, slope-forming phyllitic siltstone which contains a continuous cleavage at high angle to bedding. The base of unit B is defined by the lowest occurrence of meter-scale orthoquartzite beds, which are abundant in the unit. Unit B is readily distinguished from higher sand-rich intervals by pervasive penecontemporaneous deformation. Nearly every sandstone horizon is affected, principally by ball-and-pillow structure, so much so that individual orthoquartzite beds are difficult to trace along strike for more than a few tens of meters. Individual ball-and-pillow structures are up to meter-scale in size (roughly equal to orthoquartzite bed thickness) and

occur where fine-grained sandstone and siltstone underlie coarser sandstone. The ball-and-pillow structure is in places manifested as simple load casts with folded lamination (Figure 5A), and in others as completely detached sand bodies that have slumped downward into the underlying siltstone, surrounded by flame structure developed within the siltstone (Figure 5B). At the type locality, the occurrence of ball-and-pillow structure in the Johnnie Formation is restricted to unit B, but was also observed along one horizon at the top of the Rainstorm Member in the Mt. Schader section (Figures 6 and 7).

Unit C marks a return to generally inconspicuous, slope-forming siltstone with a prominent orthoquartzite marker horizon near the middle of the unit. The uppermost beds include a brown, resistant, 2-m-thick dolostone bed, which marks the lowest occurrence of carbonate in the type section.

Unit D includes orthoquartzite and less abundant siltstone. The sedimentary characteristic that distinguishes unit D from the other two sand-rich intervals is abundant high-angle cross-stratification, preserved in medium- to thick-bedded orthoquartzite (Figure 8A). Millimeter- to centimeter-scale laminae or thin beds are preserved in foresets within decimeter- to meter-scale beds that can be followed for tens of meters along strike. Foreset lamination is consistently truncated at high angles, ranging from 20-30°, by overlying beds (Figure 8B). In stratigraphic coordinates (corrected by tilting to horizontal about the line of strike), poles to foreset lamination are strongly unimodal, dispersed in trend by more than 90° around a mean vector of ~N30°E 65° (Figure 8B). We measured grain-size variation with stratigraphic height across a sequence of about ten foreset layers (Figure 8C and 8D), to test for the presence of reverse grading, which is characteristic of dry grain flows on the lee side of dunes (e.g., Hunter, 1977; Boggs, 2012). The result indicated that the mean grain

size of ~200 microns varies little through the sample, if anything fining slightly upward. In general, the lamination is not defined by concentrations of detrital heavy minerals. Opaque phases in these quartzites are largely diagenetic and relatively uniformly distributed throughout the rock.

The boundary between Units D and E is among the most readily mappable in the area and is also associated with a color change on remote imagery from dark brown to light brown, which is the most conspicuous color contrast in the section (Figure 2A). Unit E is about 280 m thick, and is dominated by very fine-grained sandstone and siltstone, generally lacking the mature, fine- to medium-grained quartzitic sandstone characteristic of unit D. Near the top, unit E contains an interval of about 30 medium-bedded cycles that alternate between massive, immature fine-grained sandstone and laminated siltstone. Unit F is a conspicuous, 30 to 40 m-thick, gray cherty dolostone (Figure 5C) that can be followed for at least 5 km along strike, albeit with some minor faulting. Unit G, 135 m thick, returns to siltstone and very fine-grained sandstone similar to unit E, with a few inconspicuous orthoquartzite beds.

The overall lithostratigraphic character changes beginning at the base of unit H, from relatively thick, homogeneous sandstone-, siltstone-, or carbonate-dominated units below, to the far more compositionally heterogeneous units above. From the base of unit H up to the base of the Rainstorm Member, the section contains abundant orthoquartzite, defining the uppermost of the three sand-rich intervals in the Johnnie Formation (Figure 4). For mapping purposes, the most straight forward subdivision of sand-rich interval III in the Johnnie Wash area is defined by five quartzite-dominated subunits ranging from 10 to 100 m thick, which define the lower parts of units H, I, J, K, and L (Figures 4 and S1). Each of these subunits is overlain by variable thicknesses of recessive, variegated siltstone (Figure 5E). The

occurrence of carbonate is sporadic. In the section in Johnnie Wash units I, J, and K are each capped by a resistant, 1 to 3 m-thick subunit of brown-weathering, laminated dolostone (Figure 5D), and units H and L do not contain carbonate (Figure 4). The Mt. Schader section contains a lesser proportion of quartzitic sandstone and a greater proportion of carbonate and siltstone (Figures 6 and 7), which is the basis for selecting it, instead of the type locality, for detailed measurement and chemostratigraphic sampling. Even within the Johnnie Wash area, the distribution of quartzite, siltstone, and carbonate changes along strike, on a scale of a few kilometers (Abolins, 1999). Although orthoquartzite beds in units H through L locally exhibit some high-angle cross-stratification in the Johnnie Wash section, they contrast with unit D (sand-rich interval II) in mainly being parallel-bedded or, in the case of the Mt. Schader section, hummocky cross-stratified. Orthoquartzite in units H-L is generally fine- to medium-grained, and appears to contrast with lower sand-rich intervals in containing a greater proportion of medium-grained and locally coarse-grained sand.

Our informal unit nomenclature ends at the base of the formally defined Rainstorm Member which, as noted earlier, is readily identified throughout the region on the basis of lithologic characteristics. In the northern Spring Mountains, the Rainstorm Member contrasts with the underlying units H through L in lacking fine- to medium-grained orthoquartzite beds. At the base of the Rainstorm Member, a fissile, phyllitic siltstone is overlain by the ochre-colored, 2 m-thick Johnnie oolite. The ooids are up to about 2 mm in diameter (Figure 5F) and exhibit local cross-stratification. The oolite horizon has erosional basal and upper contacts, locally including intraformational breccia and conglomerate, containing cobbles and small boulders of the oolite. Above the Johnnie oolite, pale-red limestones locally contain dispersed, coarse quartz grains interstratified with carbonate-cemented, fine-grained

sandstone. These carbonate-rich rocks are overlain by argillaceous mudstone with interbedded limestones, with scattered horizons of intraformational conglomerate. The uppermost part of the Rainstorm Member in the Mt. Schader section contains a 4 m-thick triad of quartzite, siltstone, and dolostone, in which the quartzite is disrupted by locally intense ball-and-pillow structure (Figure 5G and 5H). The base of the overlying A Member of the Stirling Formation is marked by highly resistant, massively textured to cross-stratified, medium- to thick-bedded, medium- to coarse-grained orthoquartzite. The principal contrast between the Stirling Formation's A Member and any of the orthoquartzites in the Johnnie Formation is the coarse grain size, including the common occurrence of granules and small pebbles of vein quartz and jasper in the Stirling Formation A Member. Neither the Johnnie Wash nor the Mt. Schader sections appear to preserve incised valley fill characteristic of the conglomeratic member of the Johnnie Formation (Abolins, 1999; Verdel et al., 2011).

Chemostratigraphy

Carbon isotope ratios range from a low of -4.4 ‰ (VPDB) to a high of 4.9 ‰ (Table S1). The data are mainly concentrated in carbonate beds in units H through L, which constitute the uppermost 400 m of pre-Rainstorm Member strata (Figure 7). Within the underlying c. 1100 m of exposed Johnnie Formation strata, carbonate intervals are present only in units C and F, approximately 1440 m and 860 m below the base of the Rainstorm Member, respectively (Figures 4 and 9). The lowest and highest values of $\delta^{13}C$ occur in the stratigraphically highest samples, and define a strong negative trend, beginning near the top of unit K and ending at the top of the Johnnie oolite bed. Below this marked trend in the data,

there is otherwise no general trend. More than 90% of the values recorded from the bottom of unit K to the unit C carbonate are positive, averaging 1.5 ‰ with a standard deviation of 1.2 ‰. The scatter in values within individual carbonate intervals is approximately the same as variations in the average values between carbonate intervals (Figure 7). However, variation in $\delta^{13}C$ values with stratigraphic position within each relatively thin carbonate interval does not appear to be entirely random (Figure 10). For example, carbonates from units C and the lower part of unit K show decreasing $\delta^{13}C$ values stratigraphically upward (R^2 = 0.74, 0.88 respectively), whereas values from the lower two carbonates in unit H and the upper carbonate interval in unit J suggest increasing $\delta^{13}C$ values stratigraphically upward (R^2 = 0.26 - 0.83).

Oxygen isotope ratios range from a low of -16.0 ‰ (VPDB) to a high of -5.0 ‰, with an average value of -9.4 ‰ (Table S1). There is no general trend in the mean values for each individual carbonate interval with stratigraphic position (Figure 7C). The range of values within the carbonate intervals is as great as 6 ‰, i.e., greater than the variation of mean values for each interval. Correlation of $\delta^{18}O$ and $\delta^{13}C$ is poor for the dataset as a whole (Figure 11). Plots of $\delta^{18}O$ versus stratigraphic position with side-by-side comparison with $\delta^{13}C$ values are presented in the Supplemental Items (Figure S2). Correlation of $\delta^{18}O$ values with stratigraphic position within each interval is also generally poor. Of twelve beds with > 3 samples, $R^2 > 0.5$ only for beds Zjj1, Zji2, and Zjc (see Table 1 for nomenclature). In regard to correlation of $\delta^{18}O$ with $\delta^{13}C$, only the carbonate in unit C shows good positive correlation (R^2 = 0.9), but this interval only has four data points. Intervals with 10 or more data points all show poor ($R^2 < 0.1$) intrabed correlation of $\delta^{18}O$ with $\delta^{13}C$ (Figure S2).

Subsidence Analysis

Our analyses focused on modeling the tectonic component of subsidence for strata in the Spring Mountains section: Johnnie unit A through the Devonian Devils Gate Formation (Table 1). The model results define the relationship between the stratigraphic thickness *S*, and the tectonic component of subsidence *Y* (Table 2), which yields a resulting curve for the function *Y*(*S*) (Figure 12). This curve depends on parameters that describe lithification and isostatic adjustment due to sediment loading (Tables 2 and 3), and is independent of time (Eqs. 1 and 2 in Steckler and Watts, 1978). We will model the time dependence of subsidence in the Discussion section below.

Our determinations of *Y*(*S*) include the effects of some 3000 m of Mississippian through Triassic overburden that lay above the Johnnie-Devils Gate interval during Jurassic and Early Cretaceous time (Giallorenzo et al., 2017). They also include two major sources of uncertainty. The first is the possible effect of a significant sedimentary substrate, pre-dating Johnnie unit A, on the calculated tectonic subsidence. The substrate may either have been (1) limited to the Noonday Formation or its equivalents, which are at most a few hundred meters thick and may be represented by the lowest units of the Johnnie Wash section (values Y_{ns} indicate "no substrate"); or (2) a thick succession of Proterozoic Pahrump Group strata (Crystal Spring through Kingston Peak formations), which could be present at depth beneath the northwest Spring Mountains (values Y_{ws} indicate "with substrate"; note that in Figure 12, Y_{ws} values were plotted using the base of the Spring Mountains section as a datum for zero, for a direct comparison to Y_{ns}). The oldest Pahrump Group strata, the Crystal Spring Formation, were c. 500 m.y. old in Ediacaran time, and therefore these models may

somewhat overestimate its effect on late Cryogenian-Ediacaran subsidence. The second major source of uncertainty lies in the resulting density of the delithified sediment column (Bond and Kominz, 1984; Bond et al, 1988). We simulated this error by varying sediment grain density by ±5%, and note that the effect of sediment unloading is such that the lowest assumed density results in the highest tectonic component of subsidence and vice-versa. This density range yields variations in values of Y for a given S (Y_{low} or Y_{high}; Table 4) that are similar to those obtained by Bond and Kominz (1984) and Levy and Christie-Blick (1991).

The resulting plots for $Y(S)$ (Figure 12) show a decreasing ratio of tectonic subsidence per meter of sediment thickness, with slopes ($\Delta Y/\Delta S$) ranging from values near 1.0 at the base of the section for the "no substrate" curves, to as little as 0.1 near the middle of the section for the "with substrate" curve. More typically, slopes range from 0.3 to 0.6. There is an abrupt change in slope at $S \approx 3500$ m, where the section transitions from predominantly siliciclastic to predominantly carbonate sedimentation. On the no-substrate curve, the slopes defined by the five values closest to $S = 3500$ m are 0.5 ($S < 3500$ m) and 0.2 ($S > 3500$ m), with each of the two arrays appearing quite linear. Corresponding values on the "with substrate" curve are 0.4 and 0.1. Thus, although there is a degree of gradual curvature above and below $S = 3500$ m, most of the flattening of $Y(S)$ is associated with the lithologic transition.

The effect of including a thick substrate of Pahrump Group strata is to greatly reduce our estimate of Y for any given S. In other words, by not accounting for the substrate, we overestimate the tectonic component of subsidence by 50% or more, particularly in the early phases of subsidence. Physically, the reason for this is that the no-substrate model inadvertently places incompressible basement rocks where a compacting substrate exists; in

the event that there is substrate, the model incorrectly assigns the compaction of the substrate to tectonic subsidence, resulting in an overestimate.

The uncertainties in *Y* due to sediment grain density are generally in the ± 10 to 15% range. And, to the extent that a thick sedimentary substrate is present below the lowest exposures of the Johnnie Formation in Johnnie Wash, tectonic subsidence may be overestimated by several tens of percent. Despite the sensitivity of both the density and substrate effects on the absolute value of *Y*, as we will discuss in the next section, their effects on estimating the age of tectonic subsidence are not large, because these estimates depend mainly on relative, not absolute values of *Y*. Specifically, (1) errors arising from density and substrate are correlated, such that $Y(S)$ retains its shape even though *Y* may vary significantly, and (2) the exponential equation describing time dependence of *Y* is defined by ratios between values of *Y*, rather than their absolute magnitudes.

DISCUSSION

Perhaps the most basic question in regard to the origin of the Johnnie Formation is whether the sub-oolite interval contains recognizable sub-units that can be correlated across its region of exposures, and the extent to which the section contains major unconformities. These issues are best addressed through lithostratigraphic characteristics and comparisons between the Spring Mountains section and the two other major sections in the region, the Desert Range to the north and the Nopah Range to the south. A second important question is whether or not the sub-oolite (sub-Shuram excursion) interval is a chemostratigraphic correlative with the sub-Shuram excursion Khufai Formation in Oman. A third significant

issue is whether continuous Johnnie Formation (and subsequent) deposition occurred through most or all of Ediacaran time, because this aspect is critical to dating the Johnnie using thermal subsidence modeling. A time-dependent exponential thermal subsidence model, applied to our decompacted and backstripped subsidence model, *Y*(*S*) (Figure 12), implies continuous sedimentation along the southwest Laurentian passive margin through the whole of Ediacaran time (i.e., from basal Noonday to early Wood Canyon time, or 635 - 541 Ma). If such a model is correct, it provides an independent estimate of the age and duration of the Shuram excursion, and whether or not it occurred near the time of the Gaskiers glaciation.

Lithostratigraphy

Although lithostratigraphic correlation of sub-Rainstorm Member Johnnie Formation units is not as straightforward as for the overlying intervals, neither is it particularly complex. The two thickest sections, which both lie in Nevada, the northern part of the Johnnie outcrop belt, include the northern Spring Mountains and Desert Range sections. Both sections are readily divisible into alternating sand-rich and siltstone/carbonate-rich intervals, each of order one hundred to a few hundred meters thick (I, II, III in Figure 13 on the northern Spring Mountains section). The three sand-rich intervals of the Johnnie Formation are succeeded by four additional sand-rich intervals that have long been recognized as regionally correlative units (IV-VII in Figure 13 on the northern Spring Mountains section), of which the top three have paleontological age constraints. The two sections each contain three sand-rich intervals below the Rainstorm Member that are of proportionate relative thickness. Further, the

siltstone/carbonate-rich interval between sand-rich intervals II and III contains a c. 40 m-thick cherty dolostone unit in both sections, strengthening correlation, as noted by Stewart (1970) and Benmore (1978). We correlate sand-rich interval I of the Spring Mountains (unit B) with the Carbonate member in the Desert Range section, on the basis of stratigraphic position. We note, however, that the pervasive soft sediment deformation in unit B has not been reported from orthoquartzites in the Carbonate member, and that unit B does not contain carbonate. Unit A, which is predominantly siltstone, would therefore correlate with siltstones and oolitic limestones underneath the Carbonate member. The oolitic limestone unit at the base of the Desert Range section has been considered to be correlative with the Noonday Formation (Longwell et al., 1965; Gillett and Van Alstine, 1982), implying that unit A in the Spring Mountains may also be a Noonday correlative (Figure 13).

The southern Nopah Range section is approximately half the thickness of the northern Spring Mountains and Desert Range sections, and contains a number of subaerial erosion surfaces that thus far have not been observed in the thicker Nevada sections (Summa, 1993). Like the Nevada sections, however, it does contain three sub-Rainstorm sand-rich intervals, suggesting lithostratigraphic correlation (Figure 13). Specifically, the lower part of the Transitional, Quartzite, and Upper carbonate-bearing members of Stewart (1970) would correspond to sand-rich intervals I, II, and III, respectively, in the Spring Mountains. The correlation is strengthened by: 1) the alternating orthoquartzite/carbonate cycles evident in sand-rich interval III in both the northern Spring Mountains and southern Nopah Range sections; 2) the lack of carbonate and abundance of high-angle cross stratification in interval II in all three sections (Quartzite member = upper part of Lower quartzite and siltstone member = unit D, Figure 13); 3) the consistency of unimodal, south-southwest directed

paleoflow directions in pre-Rainstorm orthoquartzites in the Spring Mountains and Desert Range sections (Figure 14); and 4) the lithological similarity between the lowest sand-rich intervals in the southern Nopah Range and Desert Range sections, both of which contain a mixed carbonate-siliciclastic assemblage. Militating against these lithostratigraphic correlations are the observations that: (1) the interval III correlative in the Desert Range lacks carbonate; (2) interval I in the Spring Mountains (unit B) also lacks carbonate; and (3) the proposed Noonday substrate of interval I is lithostratigraphically dissimilar in the three sections, ranging from pale-gray quartz-rich dolomite boundstone in the Nopah Range, to phyllitic siltstone in the Spring Mountains to medium-gray oolitic limestone in the Desert Range. Regardless of the details of these correlations, the most important facets of the two sections in Nevada are (1) the sub-Rainstorm sections are at least twice as thick as the Nopah Range section, and (2) evidence for subaerial erosion, such as grikes, paleosols, channel scour, and dessication cracks, which is conspicuous in the Nopah Range section, appears to be lacking. Although significant depositional hiatuses within the Nevada sections cannot be ruled out, the overall lithostratigraphic uniformity or "monotony" of these sections (siltstone and fine- to medium-grained sandstone and orthoquartzite, with sporadic thin carbonate beds) is consistent with conformable sedimentation on a stably subsiding continental shelf (Stewart, 1970; Fedo and Cooper, 2001; Schoenborn et al., 2012).

The pervasive ball-and-pillow and other paleoliquefaction structures in sand-rich interval I (unit B) are most simply interpreted as reflecting a period of high sediment flux in early Johnnie Formation deposition. These structures may have significance for the timing of transition from mechanical stretching of the lithosphere to purely thermal subsidence, because 1) rapid subsidence is characteristic of both the rift phase and early thermal

subsidence phase of passive margin formation (e.g. Sawyer et al., 1982), and 2) such structures could be evidence for seismic shaking (e.g. Sims, 2012). The observation that essentially the entire 160 m thickness of unit B is affected implies that, whatever its cause, it was persistent over a sustained period of time. The other significant observation is that with only one exception, paleoliquefaction structures do not appear anywhere else higher in the section, despite the ubiquity of meter-scale interbeds of fine- to medium-grained sandstone overlying fine-grained sandstone or siltstone throughout the section. Thus, the cause, or causes, of soft-sediment deformation appears to be temporally restricted to, at most, sand-rich interval I and enveloping siltstone units A and C, and presumably ended by the time of deposition of sand-rich interval II (unit D). If it is assumed that the cause is earthquakes, then sand-rich intervals I and II record a transition from frequent seismic shaking to apparent seismic quiescence. Such an interpretation is consistent with previous suggestions that the end of mechanical stretching may have occurred near the base of the Johnnie Formation (Summa, 1993; Fedo and Cooper, 2001; Schoenborn et al., 2012). A ready alternative to a seismic trigger, however, is the effect of pressure contrasts from storm waves, which have also been shown to induce liquefaction and soft sediment deformation, including ball-and-pillow structure (Alfaro et al., 2002).

Chemostratigraphy

A composite plot of $\delta^{13}C$ values of carbonate from the Johnnie Formation in southwest Laurentia (Verdel et al., 2011; this study) yields an overall pattern that is similar to profiles in Oman that contain the Shuram excursion, including a period of positive values

as high as 4 - 6 ‰, rapid descent to values as low as -11 to -12 ‰, and a more gradual rise back to positive values (Figure 15). The uniformly positive $\delta^{13}C$ values below the excursion in southwest Laurentia, generally of 1 - 3 ‰, invite detailed comparison with chemostratigraphic profiles in the carbonate-rich Khufai Formation in Oman, which lies immediately below the type Shuram excursion. The stratigraphic thickness of units between the zero crossings of the Shuram excursion in Oman and southwest Laurentia are similar, approximately 500 - 700 m (Verdel et al., 2011). We therefore compared our profile to those from Oman without any modification to the vertical scaling (stratigraphic height), fixing the zero crossings at the base of the Shuram excursion at the same height. The Khufai sections in general are positive in $\delta^{13}C$ and show considerable variation, depending on the degree of diagenetic alteration. In least altered sections (Mukhaibah Dome area), maximum values range up to 6 ‰, averaging 4 - 5 ‰ (Figure 16A), considerably more positive than the Johnnie profile. In more-altered sections (Buah Dome area, Figure 16B), the profiles are quite similar to that of the Johnnie Formation. Given the close correspondence between the Johnnie profile and most of the Oman profiles (Figure S3), we conclude that the data are consistent with, but do not absolutely demonstrate, temporal correlation of the upper part of the sub-Rainstorm Johnnie Formation (units H through L in the Spring Mountains) and the Khufai Formation.

The least altered Khufai sections are generally considered to be representative of sea water carbon isotopic composition, defining a prolonged interval of $\delta^{13}C$ values in sea water near 6 ‰. Therefore, it seems clear that subsequent diagenesis is primarily responsible for reducing $\delta^{13}C$ values, in both Oman and the sub-Rainstorm Mt. Schader section by as much as 4 - 5 ‰. In the Pleistocene environment, such reduction has been shown to result from

carbon isotopic exchange between carbonate beds and meteoric water, often resulting in $\delta^{13}C$ values decreasing stratigraphically upward at the scale of a few meters in beds exposed to erosion (Allan and Matthews, 1977; 1982; Quinn, 1991; Melim et al., 1995; Melim et al., 2001). The strong intrabed variations in $\delta^{13}C$ values in 1 - 2 m-thick carbonate intervals in the Johnnie Formation (Figure 10) could potentially be explained by this mechanism, although $\delta^{13}C$ values of meteoric water at that time are poorly constrained and may not have been as strongly negative as modern values. Further, the intrabed trends in $\delta^{13}C$ values both increase and decrease downward, and there is no evidence of subaerial exposure on the tops of any of the beds. As with most Neoproterozoic carbonates, determining the mechanisms of depletion of $\delta^{13}C$ values and their relationship to diagenetic textures and the biosphere is a difficult and controversial issue (Knauth and Kennedy, 2009; Derry, 2010a; 2010b; Grotzinger et al., 2011), beyond the scope of this paper to resolve. One thing we can say, however, about the Mt. Schader data set is that it displays no clear correlations between $\delta^{18}O$ and $\delta^{13}C$ (Figure 11), as predicted by various isotopic exchange models (Figure 4 in Osburn et al., 2015). Despite this controversy, the good match between the type Johnnie sub-Rainstorm Member section and the Khufai Formation supports the hypothesis that regardless of the origin of the anomalies, they nonetheless appear to be a useful correlation tool (Grotzinger et al., 2011). Tectonic reconstructions of the Neoproterozoic continent Rodinia put both the Shuram and Johnnie formations roughly at the equator in Ediacaran time, but the two formations were located anywhere from 10,000 - 15,000 km away from each other (Li et al., 2008; Li et al., 2013), making the isotopic correlation of the Shuram and sub-Shuram intervals all the more impressive.

One of the hallmarks of Neoproterozoic glacial cap carbonates is their frequent

occurrence as thin, isolated intervals amid large thicknesses of enveloping strata that are entirely siliciclastic. Below unit H, there are two such isolated carbonate intervals, one in unit C and the other composing the entirety of unit F. Given their stratigraphic position between the Marinoan cap carbonate sequence (Noonday Formation, Figure 1) and the base of the Cambrian, it is possible that either one of these units represents post-glacial carbonate "rainout," for example, as might be expected in the more southerly latitudes in the wake of the Gaskiers glaciation at 579 Ma (e.g. Pu et al., 2016). The generally positive $\delta^{13}C$ values in the unit C and unit F carbonates, averaging between 1 - 2 ‰, argue strongly against either of these intervals representing a Gaskiers cap carbonate, which in Newfoundland yielded $\delta^{13}C$ values of -8 to -2 ‰ (Myrow and Kaufman, 1999). Further, textural features widely described from cap carbonates (e.g. sheet cracks, tubes, teepee structures, etc.) are not observed in either of these intervals.

Subsidence Analysis

The substantial thickness of the Johnnie Formation, lack of evidence for unconformities in the Nevada sections, and the strengthened isotopic tie to the type Shuram excursion, motivate the hypothesis that the Noonday through Lower Wood Canyon interval records continuous deposition through most or all of Ediacaran time. In the last section, backstripping and decompaction defined tectonic subsidence *Y* as a function of stratigraphic position *S*, independent of time. In this section, we model the element of time as exponential subsidence, assuming that Johnnie and subsequent deposition of the passive-margin wedge occurred as a result of conductive cooling of rifted lithosphere. Subsidence analysis with

well-defined ages at the Cambrian-Precambrian boundary (541 Ma) and at the base of Cambrian Age 5 (509 Ma) creates a considerably improved basis over previous studies for estimating stratigraphic age in Ediacaran strata by extrapolating the subsidence history back in time.

Regardless of the absolute elevation following mechanical extension of the lithosphere, once thermal subsidence begins, the elevation *e* of the surface, above its equilibrium value at $t = \infty$, is closely approximated by:

$$e(t) \cong E_0 r \mathrm{e}^{-\frac{t}{\tau}}, (1)$$

where $E_0 r$ is the elevation of stretched lithosphere above its equilibrium depth at infinite time (or in the case of infinite stretching, the height of the ocean floor above the abyssal plains), *t* is time, τ is the characteristic time (time at which $\frac{e}{E_0 r} = \frac{1}{\mathrm{e}}$), and:

$$r = \frac{\beta}{\pi} \sin \frac{\pi}{\beta}, (2)$$

where β is the stretching factor (Figure 17; eqns. 10 and 11 in McKenzie, 1978). E_0 and *r* are not parameters of interest when using subsidence as a chronometer, because we are attempting to use the late history of post-rift subsidence, which is well dated, to constrain the earlier history of post-rift subsidence, which is not. The simple exponential formula for elevation versus time $e(t)$ of Equation 1 is converted to subsidence depth *Y* versus time by substituting ($E_0 r$ - *Y*) for *e*, yielding:

$$Y(t) \cong E_0 r \left(1 - \mathrm{e}^{-\frac{t}{\tau}}\right). (3)$$

In the case of mid-ocean ridges, where $\beta = \infty$ and $r = 1$, $E_0 r$ is empirically shown to be within a few percent of 3.2 km (Parsons and Sclater, 1977). We note that this value does not correspond to the actual ridge elevation above the abyssal plain, which is much higher for oceanic crust less than 20 m.y. old. The characteristic time τ, which depends on the thermal diffusivity and thickness of equilibrium lithosphere, shows somewhat greater variation depending on the ridge (±10% for the best-constrained ridges; Table 1 in Parsons and Sclater, 1977), but a generally accepted value in subsidence analyses of passive margins is 50 - 65 m.y. (McKenzie, 1978; Allen and Allen, 2005). This corresponds to a "half-life" of thermal subsidence of 35 - 45 m.y.. Even though this key parameter may vary significantly, we can estimate τ directly from our subsidence model, as an independent test of the hypothesis that the margin is in a state of exponential thermal subsidence, comparable to well-studied Mesozoic and Cenozoic examples. If our estimate of τ lies significantly outside the range of 50 - 65 m.y., it would falsify the thermal subsidence hypothesis.

Even though we do not know $E_0 r$, estimation of τ and extrapolation of the curve back in time requires as few as two known elevation-time pairs, (e_1, t_1) and (e_2, t_2) (Figure 17). Substituting these pairs into Equation 1, differencing the equations and solving for τ yields:

$$\tau = \frac{(t_2 - t_1)}{\ln(\frac{e_1}{e_2})}. (4)$$

The differencing of the two equations eliminates $E_0 r$, and hence the most important parameters in estimating both τ and the thermal subsidence curve itself are the elevation of two points relatively well separated in time from each other, and an estimate of zero elevation, i.e., where $e(\infty) = 0$ or the slope of $Y(t)$ is negligible. The thermal subsidence curve is then presumably applicable back in time to whatever point in the section we are still confident that the margin is in a state of pure thermal subsidence. As noted above, this level is probably no higher in the section than the lower part of the Johnnie Formation, and it may be much deeper, perhaps within the upper part of the underlying Pahrump Group.

Temporal constraints on the younger part of the subsidence curve are fairly similar to those used by Levy and Christie-Blick (1991) with the exception of their two oldest points, the base of the Cambrian Age 5 (~Middle Cambrian, 509 Ma, Walker et al., 2013) and the base of the Paibian (~Upper Cambrian, 497 Ma, Walker et al., 2013), which at the time were estimated to be 540 Ma and 523 Ma, respectively. Critically for this study, both the position and age of the Ediacaran/Cambrian boundary are well defined, lying within the Lower Member of the Wood Canyon Formation with an age of 541 Ma (Corsetti and Hagadorn, 2000). The 541 and 509 Ma constraints thus function as points (e_1, t_1) and (e_2, t_2) respectively in our initial analysis, defining an exponential subsidence curve. As the oldest reliable temporally constrained points on the curve, they are the strongest constraints on extrapolating the curve back in time.

Points younger than 509 Ma are also well-dated. These points clearly postdate the Sauk marine transgression, which marks a transition from predominantly siliciclastic to carbonate sedimentation due to flooding of the craton through middle and late Cambrian time. Associated with the transgression, the average deposition rate (the time derivative of

$S(t)$, dS/dt) increases markedly from c. 20 m/m.y. from 541 to 509 Ma to c. 80 m/m.y. from 509 to 497 Ma (Table 4). Clearly, a four-fold increase in accumulation rate appears incompatible with any form of exponential subsidence. As explained below, the remarkable increase in subsidence rate owes its origin to the combination of sea level rise and carbonate sedimentation, not renewed tectonism. The important point here is to note that the 541 and 509 Ma data points occur within the Lower Wood Canyon and Lower Carrara formations, respectively, both of which are shallow water, mixed carbonate-siliciclastic facies associations that were probably deposited at similar points in global sea level. Both were deposited during highstand intervals relative to their transgressive substrates (the Stirling E Member and Zabriskie Formation respectively). In the case of the Lower Wood Canyon Formation, the system evolved into a glacial drawdown of sea level (Smith et al., 2016). In the case of the Lower Carrara Formation, sea level kept rising to a level that generally exceeded those of Ediacaran-early Cambrian time (Palmer, 1981).

The late subsidence history is characterized by very slow accumulation in Silurian and Early Devonian time (<3 m/m.y., Table 4), and hence the difference between Silurian and Devonian values of Y to those at 541 and 509 Ma provides firm estimates of e_1 and e_2. We note that with these constraints, the precise values of time and elevation for Paibian through Upper Ordovician strata provide little additional constraint on the form of the exponential subsidence curve.

Temporal Model

We present a temporal model of both observed subsidence $S(t)$ (i.e., stratigraphic

thickness) and tectonic subsidence $Y(t)$ using a novel mode of presentation that orthogonally projects $Y(t)$ and $t(S)$ onto a graph of the numerically determined function $Y(S)$ (Figure 18). In this approach, $Y(S)$ is plotted in the upper left corner, $Y(t)$ in the upper right corner, $t(S)$ in the lower left corner, and $S(t)$ in the lower right corner. The plot shows a simultaneous projection of Y and S onto their respective temporal models, graphically showing the influence of the slope of $Y(S)$ on the observed subsidence rates. The graph shows that, between 509 and 485 Ma, the increase in compressibility of the carbonate sediment (lower slope on $Y(S)$), combined with the accelerated schedule of subsidence caused by the flooding of the craton (higher slope on $Y(t)$), resulted in a dramatic increase in sediment accumulation rate (lower slope on $t(S)$ and higher slope on $S(t)$), even though exponential subsidence was slowly decreasing. This result is critical because it obviates the primary reason that most previous workers have cited in favor of Cambrian rifting along western Laurentia (e.g., Bond and Kominz, 1984; Levy and Christie-Blick, 1991; Yonkee et al., 2014).

Parameter Estimates and Sensitivities

Estimates of the exponential time constant τ vary according to two main uncertainties, firstly the sediment grain density assumed in our delithification model, and secondly whether or not a thick substrate of Pahrump Group strata is present at depth beneath the exposed Spring Mountains section. We calculated values of τ for values of tectonic subsidence Y in a series of models that encompass these parameter variations (Table 5). In addition, we defined Y according to two different assumptions for the point at which mechanical stretching ends and purely thermal subsidence begins, where $Y = 0$ (i.e. $e = E_0 r$). One is at the lowest exposed

stratum (base of unit A), and the other is within unit C, above the youngest ball-and-pillow structure at the top of unit B, assuming seismic shaking ended near this point. In Table 5, models with no Pahrump Group substrate are designated Y_{ns}, and those that include the substrate are designated Y_{ws}; intermediate density models contain no additional subscript, and low and high density models are also subscripted "low" and "high" respectively. Models with superscript "4" define $Y = 0$ within unit C, and models with no superscript assume $Y = 0$ at the base of unit A. We defined the value of Y for which $e = 0$ to be the average of Y(393 Ma) and Y(383 Ma), designated Y(c. 388) in Table 5. The results are insensitive to this choice because there is so little variation in Y between 444 and 383 Ma. We cannot choose the next younger point in the subsidence profile (359 Ma) because it clearly reflects the onset of subsidence associated with Antler foredeep sedimentation.

The contrast in τ between models Y_{ns} and Y_{ws} is only 3 m.y., with $\tau = 55$ and 52 m.y. respectively. As expected from Equation 4, the definition point of $Y = 0$ has no effect, because we define e_1 and e_2 on the basis of differences in Y values late in the subsidence history. For models with no substrate, varying the density between $Y_{ns,\,low}$ and $Y_{ns,\,high}$ (corresponding to the assumption of high and low sediment grain density respectively), has a substantial effect on τ, which ranges from 42 to 65 m.y., respectively. For models $Y_{ws,\,low}$ to $Y_{ws,\,high}$, the sensitivity is even greater, with τ varying from 36 to 63 m.y., respectively. Clearly, the upper part of these ranges accords with subsidence patterns in Mesozoic and Cenozoic basins. Despite the nearly 30 m.y. variation in τ among these models, we note that there is relatively little variation in the modeled age and duration of the Shuram excursion (Table 5). Among this suite of models, the onset varies by 12 m.y. (from 569 to 581 Ma), the termination by 9 m.y. (from 566 to 575 Ma) and the duration varies by 3 m.y. (from 3 to 6 m.y.).

A further consideration in estimating τ is the fact that because the Sauk transgression was well underway by 509 Ma, relative sea level may have been slightly higher than at 541 Ma. To the extent that it was, a significant systematic error is introduced in our estimate of τ. For example, for the model with no substrate and intermediate density, a correction in $Y(509)$ of just -50 m to account for the change in sea level (+50 m in e_2) changes the estimate of τ from 55 to 69 m.y. (Equation 1 in Steckler and Watts, 1978; Equation 4 herein). Thus, although the suite of models used for our sensitivity analysis may suggest an estimate of 50 ± ~15 m.y. for τ, the systematic error introduced by the Sauk transgression, and the range of values indicated by models of Mesozoic and Cenozoic basins, both suggest a value toward the upper end of this range. We further note that the earliest empirical fits to long-term seafloor subsidence data suggested a value of 62.8 m.y. (Equation 22 in Parsons and Sclater, 1977; Table 1 in McKenzie, 1978).

Based on these considerations, we develop a second suite of models for estimating pre-541 Ma ages of various horizons within the Johnnie Formation. For this suite, we chose a "midrange" model using what are perhaps the simplest set of assumptions: 1) intermediate sediment grain density values; 2) negligible Pahrump Group substrate; and 3) a time constant of τ = 65 m.y. Using these assumptions, we tie the subsidence curve to the oldest dated time point at 541 Ma, minimizing both the amount of extrapolation back in time, and the degree to which the data reflect sea level rise due to the Sauk and subsequent cratonic flooding events. The resulting subsidence model for the Spring Mountains section is shown in Figure 18, and in Table 6 in the second column from the right hand side. The remaining columns in Table 6 and Table S2 demonstrate the sensitivity of our resulting age estimates for the Shuram excursion and other horizons in the Johnnie and Stirling formations to variations in

density, τ, and the presence or absence of a substrate. Varying only sediment grain density, limits on the Shuram excursion (tops of units Zjr1 to Zjr2) are 581 - 575 Ma (low density case), 585 - 579 Ma (intermediate density), and 592 - 585 Ma (high density) (Figure S4). Thus, we see that the end of the excursion varies from 575 - 585 Ma, a range which is centered on the timing of the Gaskiers glaciation. We also note that the duration of the excursion is 6 - 7 m.y., and it is therefore insensitive to variations in sediment grain density. With regard to sensitivity to the time constant, the end of the Shuram excursion for intermediate density values is 579, 576, and 573 Ma for τ = 65, 60, and 55 m.y. respectively (Figure S5). In terms of the error introduced by the presence of a Pahrump Group substrate (Figure S6 and Table S2), for τ = 65 m.y. and intermediate values of density, the Shuram excursion occurs from 584 - 578 Ma, which is only 1 m.y. later than, and of the same duration as, the case of no substrate. The duration of the Shuram excursion, across all models in this suite ranges from 4 - 7 m.y. If we exclude with-substrate models (Table S2), the variation decreases to 5 - 7 m.y., and if we further restrict the time constant to 65 m.y., it decreases to 6 - 7 m.y. These estimates are consistent with recent estimates of 8 - 9 m.y. for the Johnnie, South Australia (Wonoka), and central China (Doushantuo) sections, based on rock magnetic chronostratigraphy (Minguez et al., 2015; Minguez and Kodama, 2017; Gong et al., 2017). These estimates are all considerably shorter than the subsidence-based estimate of 50 m.y. for the Shuram excursion in Oman (Le Guerroué et al., 2006b), which has been called into question on the basis that the Khufai/Shuram interval was probably not deposited on a thermally subsiding continental shelf (Bowring et al., 2007).

In sum, because the timing of the Shuram excursion is within c. 0.5τ of 541 Ma, varying parameters in the exponential subsidence model yields variations in our estimate of

age and duration of the Shuram excursion of just a few million years. The fact that a fairly broad range of parameters leads to estimates of the end of the Shuram excursion centered on 579 Ma, suggests that the valleys incised into the Rainstorm Member are indeed a manifestation of the Gaskiers glaciation at equatorial latitudes. To conclude otherwise strains credulity, because Johnnie/Stirling sequence architecture is relatively uneventful for 400 - 500 m both above and below the Rainstorm Member (Stirling Member A/B and Johnnie units H through L, respectively). If incision was unrelated to the Gaskiers glaciation, it requires (1) that the most dramatic stratigraphic event in the Johnnie/Stirling interval was close in time, but unrelated to, glaciation, and (2) that the Gaskiers glaciation itself had virtually no impact on the section. In essence, the subsidence analysis provides a relatively coarse estimate of age that "registers" the section with possible correlatives elsewhere. The detailed stratigraphy then fine tunes the age estimate based on a specific correlation with well-dated events elsewhere: in this case, shelf-incision and the Gaskiers glaciation.

The overall consistency of exponential subsidence models with the hypothesis that incision of the Rainstorm Member shelf is an expression of the Gaskiers glaciation suggests that modeled ages of other horizons in the Johnnie/Stirling interval may also be accurate to within a few million years. The overall accuracy of this model can be further tested by assessing how well it estimates the age of the lowermost Johnnie and Noonday interval. As noted above in our discussion of the possible correlation of unit A with the Noonday Formation, we would expect the age of this unit to be close to the age of the base of the Noonday Formation, or 635 Ma (Petterson et al., 2011). The range of modeled ages for the base of unit A are 639 - 608 Ma (Table 6), with the "mid-range" model shown in Figure 18B predicting an age of 628 Ma. As shown in Figure 18D, linear extrapolation below the deepest

exposed strata of unit A, assuming a linear deposition rate, would require only an additional 288 m of "sub-unit A" strata to bring the section to the base of the Noonday Formation and the Ediacaran Period. This thickness, plus the 125 m thickness of unit A yields a total thickness of 413 m, which is consistent with maximum known thicknesses of the Noonday Formation (Petterson et al., 2011). The apparent success of exponential subsidence models in predicting the age of both the Gaskiers event and the base of the Ediacaran Period at their most likely stratigraphic levels, supports the hypothesis that Ediacaran deposition on the southwest Laurentian margin was largely continuous, and that the Noonday through Wood Canyon interval in its thickest, most basinal exposures does not contain unconformities with significant depositional hiatuses.

CONCLUSIONS

Lithostratigraphic and chemostratigraphic details of the Johnnie Formation at its type locality in the northwest Spring Mountains of southern Nevada provide a basis for regional lithostratigraphic correlation, global chemostratigraphic correlation, and subsidence analysis of the southwest Laurentian continental margin. The regional lithostratigraphy of Ediacaran through Cambrian Age 4 strata defines seven sand-rich intervals separated by siltstone- and carbonate-rich intervals, the upper two of which are the Sauk I and Sauk II sequences of Cambrian age (Palmer, 1981). The great overall thickness of the Johnnie Formation at its type locality (c. 1800 m), and the apparent absence of subaerial exposure surfaces or other evidence of erosion that are well expressed in more cratonic sections such as the Nopah Range section, support the hypothesis of continuous deposition. Nonetheless, the

lithostratigraphy is strongly cyclic at kilometer scale, suggesting that significant hiatuses, or at least greatly reduced rates of sediment flux, may be associated with the base of each of the seven sand-rich intervals, even in the more basinal sections. We therefore caution that the true slope of the observed sediment accumulation curve $S(t)$ is almost certainly more variable than shown in Figure 18D, especially for the segment between 635 Ma and 541 Ma. This concern is tempered by the fact that sediment flux was sufficient in Ediacaran and Paleozoic time to fill the accommodation space to within a few meters to a few tens of meters of sea level, implying that the tectonic component of subsidence is fully recorded.

Carbon isotopic data from sub-Rainstorm Member (sub-Shuram excursion) units in the Mt. Schader section are generally positive, and support correlation of Johnnie units H through L with the Khufai Formation in Oman, but they do not require it. If correlative, the Mt. Schader section would provide the first confirmation of an extended period (represented by 300 – 400 m of section) of positive $\delta^{13}C$ values prior to the Shuram excursion in both Oman and Nevada.

The Gaskiers glaciation marks the beginning of widespread preservation of macroscopic Ediacaran animals (Xiao et al., 2016), and the Shuram excursion is the largest known carbon isotopic excursion in the geological record. A central issue in animal evolution is thus whether or not the Shuram excursion was approximately synchronous with the Gaskiers event, because it suggests that the Shuram excursion, whatever its cause, was genetically related to creating a surface environment that could support the metabolic requirements of macroscopic animals. A second consequence of Shuram-Gaskiers correlation is that it places the transition from diverse, ornamented acritarchs to a lower diversity, unornamented assemblage in synchronism with the appearance of macroscopic

animals, rather than at some later time. The issue is addressable in southwest Laurentia, to the extent that deposition of Johnnie and related strata occurred more-or-less continuously on a thermally subsiding passive margin.

Based on this assumption, subsidence analysis strongly suggests that the end of Johnnie Formation deposition, at the time of valley incision and subsequent fill with the conglomeratic member, was correlative with the Gaskiers glaciation at 579 Ma. The analysis also suggests that the onset of the Shuram excursion near the base of the Rainstorm Member occurred at ~585 Ma. The implied 6 m.y. duration of the Shuram excursion is consistent with paleomagnetic and other proxies from sections in Laurentia and Australia. The subsidence analysis further indicates that if the assignment of the Gaskiers event to uppermost Johnnie time is correct, then the base of the Johnnie Formation is approximately 630 Ma. If so, then the Johnnie through lower Wood Canyon interval in the Spring Mountains represents a relatively complete, 3000 m-thick section that records most or all of Ediacaran time.

ACKNOWLEDGEMENTS

We are grateful to Gillian Ferguson, Leah Sabbeth, Fenfang Wu, and the late Lindsey Hedges for assistance in the field and laboratory, and to Associate Editor Christopher J. Spencer and reviewer Tony Prave for insightful and constructive reviews. This material is based upon work supported by the National Science Foundation Graduate Research Fellowship Program under grant 1144469 awarded to R. Witkosky, and grant EAR 14-51055 awarded to B. Wernicke.

APPENDIX. DESCRIPTION OF MAP UNITS

Descriptions apply to geologic maps and stratigraphic columns shown in Figures 3, 4, 6, and 7.

Qa: Alluvium and colluvium in active/ephemeral channels and piedmont-forming slopes.

QTl: In Johnnie Wash, a topographically prominent ridge of coarse, poorly-sorted debris, here interpreted as a landslide deposit.

Zsa: **Stirling Formation**. A Member (labeled "Zs" in map). Very pale orange, grayish-black weathering, medium-grained orthoquartzite, laminated to massive, medium- to thick-bedded, with trough cross-stratification. Contains some interbedded carbonate-cemented sandstone. In places, bedding is destroyed by secondary brecciation and recementation, forming irregular dark weathering masses. Unit forms resistant ridges relative to underlying Johnnie Formation.

Zjr: **Johnnie Formation**. Rainstorm Member. Includes four distinct subunits, from bottom to top: (1) green phyllitic siltstone, (2) highly-resistant, ochre-colored oolitic dolostone ("Johnnie oolite," indicated by red open-dotted line, c. 2 meters thick), (3) pale red, carbonate-cemented fine-grained sandstone and sandy limestone, and (4) a heterogeneous upper unit that includes siltstone, carbonate-rich sandstone, flaser-bedded sandy carbonate, and intraformational limestone breccia. In the Mt. Schader section, a c. 4 m-thick triad of orthoquartzite, siltstone, and dolostone immediately underlies the Stirling Formation. Orthoquartzite is affected by m-scale ball-and-pillow structure.

Zjl: Orthoquartzite and variegated siltstone. Generally a recessive/slope-forming unit. Red

dotted line in Mt. Schader map indicates a resistant, laminated, brown dolomitic marker bed, c. 2 meters thick.

Zjk: Orthoquartzite, variegated siltstone, and dolostone. Orthoquartzite is parallel bedded and forms erosionally resistant base; siltstone locally contains ripple laminations; resistant, brown, dolomitic marker bed, indicated by red dotted line in Mt. Schader map area, is hummocky cross-stratified, and contains chert in its lower portion.

Zjj: Orthoquartzite, variegated siltstone, and minor dolomitic sandstone. Orthoquartzite and siltstone occur in ~5 meter cycles. Orthoquartzite is white, resistant, locally granular and contains high-angle (c. 20°) cross-stratification; dolomitic sandstones are thick, brown, resistant, fine- to medium-grained beds. Red dotted line on both maps indicates a hummocky cross-stratified, brown dolomite marker bed.

Zji: Orthoquartzite, variegated siltstone, and dolomitic sandstone. Parallel bedded in the Johnnie Wash section, hummocky cross-stratified in the Mt. Schader section. Orthoquartzite is fine-grained and occurs as conspicuous thick bedded intervals in 5-10 meter cycles with siltstones. Red dotted line on Mt. Schader map indicates a hummocky cross-stratified, brown dolomitic sandstone marker bed.

Zjh: Orthoquartzite and variegated siltstone. Red dotted lines on Mt. Schader map indicate brown, hummocky cross-stratified dolomite marker beds that contain stromatolitic mounds.

Zjg: Variegated fine-grained sandstone and siltstone, weakly cemented. Also occasional interstratified orthoquartzite, fine to medium-grained, medium- to thick-bedded.

Zjf: Dolostone with centimeter- to decimeter-thick, centimeter- to meter-long chert nodules and lenses. The dolostone forms a conspicuous pale-weathering ridge. Finely laminated to massive texture. Microcrystalline varieties weather gray, coarser grained, secondary

dolomite weathers dark gray to brown.

Zje: Massive, fine-grained sandstone and laminated siltstone. Upper part contains several dozen rhythmic cycles, c. 2 m-thick, of sandstone and siltstone. Each cycle has a sharp, load-casted bottom and grades upward from sandstone to siltstone. Generally an olive hued, recessive/slope-forming unit, with occasional beds of cross-stratified sandstone, similar to unit D.

Zjd: Well-cemented, fine-grained orthoquartzite in meter-scale beds featuring cross-stratification with steep truncation angles (up to ~30°), interstratified with medium-grained, weakly hematite-cemented ferruginous sandstone and variegated siltstone. Unit forms resistant ridge that is conspicuously darker weathering than unit E.

Zjc: Siltstone (as Zja) with a calcareous, medium-grained orthoquartzite marker bed, similar to unit D, indicated on Figure 3 by green dotted line. The lowest carbonate in the Johnnie Wash section appears near the top of this unit as a brown, medium-grained, fabric-retentive dolostone.

Zjb: Interstratified fine-grained orthoquartzite and phyllitic siltstone. Orthoquartzite occurs in meter-scale beds with parallel lamination, pervasively disrupted by soft sediment deformation, primarily ball-and-pillow structure, such that individual beds are difficult to trace along strike.

Zja: Phyllitic siltstone, with a distinct crenulation cleavage at high angle to bedding. Generally a recessive unit.

REFERENCES CITED

Abolins, M.J., 1999, I. Stratigraphic constraints on the number of discrete Neoproterozoic glaciations and the relationship between glaciation and Ediacaran evolution; II. The Kwichup Spring thrust in the northwest Spring Mountains, Nevada: Implications for large-magnitude extension and the structure of the Cordilleran thrust belt [Ph.D. thesis]: Pasadena, California Institute of Technology, 341 p.

Abolins, M., Oskin, R., Prave, T., Summa, C., and Corsetti, F., 2000, Neoproterozoic glacial record in the Death Valley region, California and Nevada, *in* Lageson, D.R., Peters, S.G., and Lahren, M.M., eds., Great Basin and Sierra Nevada: Boulder, Colorado, Geological Society of America Field Guide 2, p. 319–336.

Albee, A.L., Labotka, T.C., Lanphere, M.A., and McDowell, S.D., 1981, Geologic map of the Telescope Peak Quadrangle, California: U.S. Geological Survey Geological Quadrangle Map GQ-1532, scale 1:62500, 1 sheet.

Alfaro, P., Delgado, J., Estévez, A., Molina, J.M., Moretti, M., and Soria, J.M., 2002, Liquefaction and fluidization structures in Messinian storm deposits (Bajo Segura Basin, Beltic Cordillera, southern Spain): International Journal of Earth Sciences, v. 91, p. 505- 513, doi: 10.1007/s00531-001-0241-z.

Allan, J.R., and Matthews, R.K., 1977, Carbon and oxygen isotopes as diagenetic and stratigraphic tools: Surface and subsurface data, Barbados, West Indies: Geology, v. 5, p. 16-20.

Allan, J.R., and Matthews, R.K., 1982, Isotope signatures associated with early meteoric diagenesis: Sedimentology, v. 29, p. 797-817.

Allen, P.A., and Allen, J.R., 2005, Basin analysis: principles and applications, second edition: Blackwell Publishing, Malden Massachusetts, 549 p.

Allmendinger, R.W., Cardozo, N., and Fisher, D., 2012, Structural geology algorithms: Vectors and tensors in structural geology: Cambridge University Press, 302 p.

Armin, R.A., and Mayer, L., 1983, Subsidence analysis of the Cordilleran miogeocline: Implications for timing of late Proterozoic rifting and amount of extension: Geology, v. 11, p. 702-705.

Bekker, A., and Holland, H.D., 2012, Oxygen overshoot and recovery during the early Paleoproterozoic: Earth and Planetary Science Letters, v. 317-318, p. 295-304, doi: 10.1016/j.epsl.2011.12.012.

Benmore, W.C., 1978, Stratigraphy, sedimentology, and paleoecology of the late Paleophytic or earliest Phanerozoic Johnnie Formation, eastern California and southwestern Nevada [Ph.D. thesis]: Santa Barbara, University of California, 243 p.

Bergmann, K.D., Zentmyer, R.A., and Fischer, W.W., 2011, The stratigraphic expression of

a large negative carbon isotope excursion from the Ediacaran Johnnie Formation, Death Valley: Precambrian Research, v. 188, p. 45-56, doi: 10.1016/j.precamres.2011.03.014.

Boggs, S. Jr., 2012, Principles of sedimentology and stratigraphy, 5th edition: New Jersey, Pearson Prentice Hall, 585 p.

Bond, G.C., Kominz, M.A., and Devlin, W.J., 1983, Thermal subsidence and eustacy in the Lower Palaezoic miogeocline of western North America: Nature, v. 306, n. 5945, p. 775-779, doi:10.1038/306775a0.

Bond, G.C., and Kominz, M.A., 1984, Construction of tectonic subsidence curves for the early Paleozoic miogeocline, southern Canadian Rocky Mountains: Implications for subsidence mechanisms, age of breakup, and crustal thinning: Geological Society of America Bulletin, v. 95, n. 2, p. 155-173.

Bond, G.C., Kominz, M.A., and Grotzinger, J.P., 1988, Cambro-Ordovician eustasy: Evidence from geophysical modelling of subsidence in Cordilleran and Appalachian passive margins, *in* Kleinspehn, K.L., and Paola, C., eds., New Perspectives in Basin Analysis: Springer, New York, p. 129-160.

Bowring, S., Myrow, P., Landing, E., Ramezani, J., Condon, D. and Hoffmann, K.H., 2003a: Geochronological constraints on Neoproterozoic glaciations and the rise of metazoans: Geological Society of America Abstracts with Programs, v. 35, n. 6, p. 516.

Bowring, S.A., Myrow, P.M., Landing, E., and Ramezani, J., 2003b, Geochronological constraints on terminal Neoproterozoic events and the rise of metazoans: Geophysical Research Abstracts, v. 5, 13219, p. 219.

Bowring, S.A., Grotzinger, J.P., Condon, D.J., Ramezani, J., Newall, M.J., and Allen, P.A., 2007, Geochronologic constraints on the chronostratigraphic framework of the Neoproterozoic Huqf Supergroup, Sultanate of Oman: American Journal of Science, v. 307, p. 1097-1145, doi: 10.2475/10.2007.01.

Burchfiel, B.C., 1964, Precambrian and Paleozoic stratigraphy of Specter Range quadrangle, Nye County, Nevada: American Association of Petroleum Geologists Bulletin, v. 48, n. 1, p. 40-56.

Burchfiel, B.C., 1965, Structural geology of the Specter Range quadrangle, Nevada, and its regional significance: Geological Society of America Bulletin, v. 76, n. 2, p. 175-192.

Burchfiel, B.C., and Davis, G.A., 1972, Structural framework and evolution of the southern part of the Cordilleran orogeny, western United States: American Journal of Science, v. 272, n. 2, p. 97-118.

Burchfiel, B.C., and Davis, G.A., 1975, Nature and controls of Cordilleran orogenesis, western United States: Extensions of an earlier synthesis: American Journal of Science, v.

275-A, p. 363-396.

Burchfiel, B.C., Fleck, R.J., Secor, D.T., Vincelette, R.R., and Davis, G.A., 1974, Geology of the Spring Mountains, Nevada: Geological Society of America Bulletin, v. 85, p. 1013-1022.

Burchfiel, B.C., Hamill, G.S. IV, and Wilhelms, D.E., 1983, Structural geology of the Montgomery Mountains and the northern half of the Nopah and Resting Spring Ranges, Nevada and California: Geological Society of America Bulletin, v. 94, p. 1359-1376.

Burns, S.J., and Matter, A., 1993, Carbon isotopic record of the latest Proterozoic from Oman: Eclogae Geologicae Helvetiae, v. 86, no. 2, p. 595-607.

Butterfield, N.J., 2009, Oxygen, animals, and oceanic ventilation: an alternative view: Geobiology, v. 7, p. 1-7, doi: 10.1111/j.1472-4669.2009.00188.x.

Calver, C.R., 2000, Isotope stratigraphy of the Ediacaran (Neoproterozoic III) of the Adelaide Rift Complex, Australia, and the overprint of water column stratification: Precambrian Research, v. 100, p. 121-150.

Canfield, D.E., Poulton, S.W., and Narbonne, G.M., 2007, Late-Neoproterozoic deep- ocean oxygenation and the rise of animal life: Science, v. 315 (5808), p. 92-95, doi: 10.1126/science.1135013.

Cardozo, N., 2009, Backstrip: http://www.ux.uis.no/~nestor/work/programs.html (accessed August 2017).

Cardozo, N., and Allmendinger, R.W., 2013, Spherical projections with OSXStereonet: Computers & Geosciences, v. 51, p. 193-205, doi: 10.1016/j.cageo.2012.07.021.

Clapham, M.E., and Corsetti, F.A., 2005, Deep valley incision in the terminal Neoproterozoic (Ediacaran) Johnnie Formation, eastern California, USA: Tectonically or glacially driven?: Precambrian Research, v. 141, p. 154-164, doi: 10.1016/j.precamres.2005.09.002.

Cohen, P.A., Bradley, A., Knoll, A.H., Grotzinger, J.P., Jensen, S., Abelson, J., Hand, K., Love, G., Metz, J., McLoughlin, N., Meister, P., Shepard, R., Tice, M., and Wilson, J.P., 2009, Tubular compression fossils from the Ediacaran Nama Group, Namibia: Journal of Paleontology, v. 83, p. 110-122.

Condon, D., Zhu, M., Bowring, S., Wang, W., Yang, A., and Jin, Y., 2005, U-Pb ages from the Neoproterozoic Doushantuo Formation, China: Science, v. 308, p. 95- 98, doi: 10.1126/science.1107765.

Corsetti, F.A., Awramik, S.M., Pierce, D., and Kaufman, A.J., 2000, Using chemostratigraphy to correlate and calibrate unconformities in Neoproterozoic strata from

the southern Great Basin of the United States: International Geology Review, v. 42, p. 516-533, doi: 10.1080/00206810009465096.

Corsetti, F.A., and Hagadorn, J.W., 2000, Precambrian-Cambrian transition: Death Valley, United States: Geology, v. 28, no. 4, p. 299-302.

Corsetti, F.A., and Kaufman, A.J., 2003, Stratigraphic investigations of carbon isotope anomalies and Neoproterozoic ice ages in Death Valley, California: Geological Society of America Bulletin, v. 115, no. 8, p. 916-932, doi: 10.1130/B25066.1.

Deer, W.A., Howie, R.A., and Zussman, J., 1992, An introduction to the rock-forming minerals, second edition: England, Pearson Education Limited, 696 p.

Derry, L.A., 2010a, A burial diagenesis origin for the Ediacaran Shuram-Wonoka carbon isotope anomaly: Earth and Planetary Science Letters, v. 294, no. 1-2, p. 152- 162, doi: 10.1016/j.epsl.2010.03.022.

Derry, L.A., 2010b, On the significance of $\delta^{13}C$ correlations in ancient sediments: Earth and Planetary Science Letters, v. 296, p. 497-501, doi:10.1016/j.epsl.2010.05.035.

Dickinson, W.R., 1977, Paleozoic plate tectonics and the evolution of the Cordilleran continental margin, *in* Stewart, J. H., Stevens, C. H., and Fritsche, A. E., eds., Paleozoic paleogeography of the western United States: Society of Economic Paleontologists and

Mineralogists, Pacific Section, Pacific Coast Paleogeography Symposium 1, p. 137-156.

Fedo, C.M., and Cooper, J.D., 2001, Sedimentology and sequence stratigraphy of Neoproterozoic and Cambrian units across a craton-margin hinge zone, southeastern California, and implications for the early evolution of the Cordilleran margin: Sedimentary Geology, v. 141-142, p. 501-522.

Field, C.B., Behrenfeld, M.J., Randerson, J.T., and Falkowski, P., 1998, Primary production of the biosphere: Integrating terrestrial and oceanic components: Science, v. 281, p. 237-240, doi: 10.1126/science.281.5374.237.

Fike, D.A., Grotzinger, J.P., Pratt, L.M., and Summons, R.E., 2006, Oxidation of the Ediacaran ocean: Nature, v. 444, p. 744-747, doi: 10.1038/nature05345.

Gabrielse, H., 1972, Younger Precambrian of the Canadian Cordillera: American Journal of Science, v. 272, n. 6, p. 521-536.

Giallorenzo, M.A., Wells, M.L, Yonkee, W.A., Stockli, D.F., and Wernicke, B.P., 2017, Timing of exhumation, Wheeler Pass thrust sheet, southern Nevada and California: Late Jurassic to middle Cretaceous evolution of the southern Sevier fold-and-thrust belt: Geological Society of America Bulletin, doi: https://doi.org/10.1130/B31777.1.

Gillett, S.L., and Van Alstine, D.R., 1982, Remagnetization and tectonic rotation of Upper

Precambrian and Lower Paleozoic strata from the Desert Range, southern Nevada: Journal of Geophysical Research, v. 87, n. B13, p. 10929-10953.

Gong, Z., Kodama, K.P., and Li, Y.-X., 2017, Rock magnetic cyclostratigraphy of the Doushantuo Formation, South China and its implications for the duration of the Shuram carbon isotope excursion: Precambrian Research, v. 289, p. 62-74, doi: 10.1016/j.precamres.2016.12.002.

Grotzinger, J.P., Fike, D.A., and Fischer, W.W., 2011, Enigmatic origin of the largest-known carbon isotope excursion in Earth's history: Nature Geoscience, v. 4, no. 5, p. 285-292, doi: 10.1038/ngeo1138.

Hagadorn, J.W., and Waggoner, B., 2000, Ediacaran fossils from the southwestern Great Basin, United States: Journal of Paleontology, v. 74, no. 2, p. 349-359.

Halley, R.B., and Schmoker, J.W., 1983, High-porosity Cenozoic carbonate rocks of south Florida: Progressive loss of porosity with depth: American Association of Petroleum Geologists Bulletin, v. 67, n. 2, p. 191-200.

Halverson, G.P., Hoffman, P.F., Schrag, D.P., Maloof, A.C., and Rice, A.H.N., 2005, Toward a Neoproterozoic composite carbon-isotope record: Geological Society of America Bulletin, v. 117, p. 1181-1207, no. 9/10, doi: 10.1130/B25630.1.

Halverson, G.P., Wade, B.P., Hurtgen, M.T., and Barovich, K.M., 2010, Neoproterozoic chemostratigraphy: Precambrian Research, v. 182, p. 337–350.

Hamill, G.S. IV, 1966, Structure and stratigraphy of the Mt. Shader quadrangle, Nye County, Nevada - Inyo County, California [Ph.D. thesis]: Houston, Texas, Rice University, 83 p.

Hazzard, J.C., 1937, Paleozoic section in the Nopah and Resting Springs Mountains, lnyo County, California: California Journal of Mines and Geology, v. 33, no. 4, p. 273-339.

Heaman, L.M., and Grotzinger, J.P., 1992, 1.08 Ga diabase sills in the Pahrump Group, California: Implications for development of the Cordilleran miogeocline: Geology, v. 20, p. 637-640.

Hoffman, P.F., Kaufman, A.J., Halverson, G.P., and Schrag, D.P., 1998, A Neoproterozoic Snowball Earth: Science, v. 281, p. 1342-1346, doi: 10.1126/science.281.5381.1342.

Hoffmann, K.-H., Condon, D.J., Bowring, S.A., and Crowley, J.L., 2004, U-Pb zircon date from the Neoproterozoic Ghaub Formation, Namibia: Constraints on Marinoan glaciation: Geology, v. 32, p. 817-820, doi: 10.1130/G20519.1.

Holland, H.D., 2006, The oxygenation of the atmosphere and oceans: Philosophical Transactions of the Royal Society B, v. 361, p. 903-915, doi: 10.1098/rstb.2006.1838.

Hollingsworth, J.S., 2005, The earliest occurrence of trilobites and brachiopods in the Cambrian of Laurentia: Palaeogeography, Palaeoclimatology, Palaeoecology, v. 220, p. 153-165, doi: 10.1016/j.palaeo.2004.08.008.

Hunt, D.L., 1990, Trilobite faunas and biostratigraphy of the Lower Cambrian Wood Canyon Formation, Death Valley region, California [Master's thesis]: Davis, University of California, 140 p.

Hunter, R.E., 1977, Basic types of stratification in small eolian dunes: Sedimentology, v. 24, n. 3, p. 361-387.

Husson, J.M., Maloof, A.C., Schoene, B., Chen, C.Y., and Higgins, J.A., 2015, Stratigraphic expression of Earth's deepest $\delta^{13}C$ excursion in the Wonoka Formation of South Australia: American Journal of Science, v. 315, p. 1-45, doi: 10.2475/01.2015.01.

Kamb, W.B., 1959, Ice petrofabric observations from Blue Glacier, Washington, in relation to theory and experiment: Journal of Geophysical Research, v. 64, no. 11, p. 1891-1909.

Kaufman, A.J., Hayes, J.M., Knoll, A.H., and Germs, G.J.B., 1991, Isotopic compositions of carbonates and organic carbon from upper Proterozoic succesions in Namibia: stratigraphic variation and the effects of diagenesis and metamorphism: Precambrian Research, v. 49, p. 301-327.

Kaufman, A.J., Corsetti, F.A., and Varni, M.A., 2007, The effect of rising atmospheric oxygen on carbon and sulfur isotope anomalies in the Neoproterozoic Johnnie Formation, Death Valley, USA: Chemical Geology, v. 237, p. 47-63, doi: 10.1016/j.chemgeo.2006.06.023.

Knauth, L.P., and Kennedy, M.J., 2009, The late Precambrian greening of the Earth: Nature, v. 460, no. 7256, p. 728-732, doi: 10.1038/nature08213.

Knoll, A.H., and Carroll, S.B., 1999, Early animal evolution: emerging views from comparative biology and geology: Science, v. 284 (5423), p. 2129-2137, doi: 10.1126/science.284.5423.2129.

Knoll, A.H., Walter, M.R., Narbonne, G.M, and Christie-Blick, N., 2004, A new period for the geologic time scale: Science, v. 305, p. 621-622.

Knoll, A.H., Walter, M.R., Narbonne, G.M., and Christie-Blick, N., 2006, The Ediacaran Period: a new addition to the geologic time scale: Lethaia, v. 39, p. 13-30, doi: 10.1080/00241160500409223.

Kump, L.R., 2008, The rise of atmospheric oxygen: Nature, v. 45, p. 277-278, doi: 10.1038/nature06587.

Labotka, T.C., Albee, A.L., Lanphere, M.A., and McDowell, S.D., 1980, Stratigraphy,

structure, and metamorphism in the central Panamint Mountains (Telescope Peak quadrangle), Death Valley area, California: Summary: Geological Society of America Bulletin, v. 91, p. 125-129.

Larrieu, T.L., 1995, Basin analysis with a spreadsheet: Journal of Geological Education, v. 43, p. 107-113.

Le Guerroué, E., Allen, P.A., Cozzi, 2006a, Chemostratigraphic and sedimentological framework of the largest negative carbon isotope excursion in Earth history: The Neoproterozoic Shuram Formation (Nafun Group, Oman): Precambrian Research, v. 146, p. 68-92, doi: 10.1016/j.precamres.2006.01.007.

Le Guerroué, E., Allen, P.A., Cozzi, A., Etienne, J.L., and Fanning, M., 2006b, 50 Myr recovery from the largest negative $\delta^{13}C$ excursion in the Ediacaran ocean: Terra Nova, v. 18, p. 147-153, doi: 10.1111/j.1365-3121.2006.00674.x.

Lenton, T.M, Boyle, R.A., Poulton, S.W., Shields-Zhou, G.A., and Butterfield, N.J., 2014, Co- evolution of eukaryotes and ocean oxygenation in the Neoproterozoic era: Nature Geoscience, v. 7, p. 257-265, doi: 10.1038/NGEO2108.

Levy, M., and Christie-Blick, N., 1991, Tectonic subsidence of the early Paleozoic passive continental margin in eastern California and southern Nevada: Geological Society of America Bulletin, v. 103, p. 1590-1606.

Li, Z.X., et al., 2008, Assembly, configuration, and break-up of Rodinia: A synthesis: Precambrian Research, v. 160, p. 179-2010, doi: 10.1016/j.precamres.2007.04.021.

Li, Z.X., Evans, D.A.D., and Halverson, G.P., 2013, Neoproterozoic glaciations in a revised global palaeogeography from the breakup of Rodinia to the assembly of Gondwanaland: Sedimentary Geology, v. 294, p. 219-232, doi: 10.1016/j.sedgeo.2013.05.016.

Longwell, C.R., Pampeyan, E.H., Bowyer, B., and Roberts, R.J., 1965, Geology and mineral deposits of Clark County, Nevada: Nevada Bureau of Mines, Bulletin 62, 218 p.

Loyd, S.J., Marenco, P.J., Hagadorn, J.W., Lyons, T.W., Kaufman, A.J., Sour-Tovar, F., and Corsetti, F.A., 2012, Sustained low marine sulfate concentrations from the Neoproterozoic to the Cambrian: Insights from carbonates of northwestern Mexico and eastern California: Earth and Planetary Science Letters, v. 339-340, p. 79-94, doi: 10.1016/j.epsl.2012.05.032.

Loyd, S.J., Corsetti, F.A., Eagle, R.A., Hagadorn, J.W., Shen, Y., Zhang, X., Bonifacie, M., and Tripati, A.K., 2015, Evolution of Neoproterozoic Wonoka-Shuram Anomaly-aged carbonates: Evidence from clumped isotope paleothermometry: Precambrian Research, v. 264, p. 179-191, doi: 10.1016/j.precamres.2015.04.010.

Macdonald, F.A., Jones, D.S., and Schrag, D.P., 2009, Stratigraphic and tectonic implications of a newly discovered glacial diamictite-cap carbonate couplet in southwestern

Mongolia: Geology, v. 37, no. 2, p. 123-126, doi: 10.1130/G24797A.1.

Macdonald, F.A., Strauss, J.V., Sperling, E.A., Halverson, G.P., Narbonne, G.M., Johnston, D.T., Kunzmann, M., Schrag, D.P., and Higgins, J.A., 2013, The stratigraphic relationship between the Shuram carbon isotope excursion, the oxygenation of Neoproterozoic oceans, and the first appearance of the Ediacaran biota and bilaterian trace fossils in northwestern Canada: Chemical Geology, v. 362, p. 250-272.

Mahon, R.C., Dehler, C.M., Link, P.K., Karlstrom, K.E., and Gehrels, G.E., 2014, Geochronologic and stratigraphic constraints on the Mesoproterozoic and Neoproterozoic Pahrump Group, Death Valley, California: A record of the assembly, stability, and breakup of Rodinia: Geological Society of America Bulletin, v. 126, n. 5/6, p. 652-664, doi: 10.1130/B30956.1.

McFadden, K.A., Huang, J., Chu, X., Jiang, G., Kaufman, A.J., Zhou, C., Yuan, X., and Xiao, S., 2008, Pulsed oxidation and biological evolution in the Ediacaran Doushantuo Formation: Proceedings of the National Academy of Sciences, v. 105, no. 9, p. 3197-3202.

McKenzie, D., 1978, Some remarks on the development of sedimentary basins: Earth and Planetary Science Letters, v. 40, p. 25-32.

McMenamin, M.A.S., 1996, Ediacaran biota from Sonora, Mexico: Proceedings of the National Academy of Sciences, v. 93, p. 4990-4993.

Melezhik, V.A., Fallick, A.E., and Pokrovsky, B.G., 2005, Enigmatic nature of thick sedimentary carbonates depleted in ^{13}C beyond the canonical mantle value: The challenges to our understanding of the terrestrial carbon cycle: Precambrian Research, v. 137, p. 131-165, doi: 10.1016/j.precamres.2005.03.010.

Melim, L.A., Swart, P.K., and Maliva, R.G., 1995, Meteoric-like fabrics forming in marine waters: Implications for the use of petrography to identify diagenetic environments: Geology, v. 23, no. 8, p. 755-758.

Melim, L.A., Swart, P.K., and Maliva, R.G., 2001, Meteoric and marine-burial diagenesis in the subsurface of the Great Bahama Bank, *in* Ginsburg, R.N., ed., Subsurface geology of a prograding carbonate platform margin, Great Bahama Bank: Results of the Bahamas Drilling Project: Society of Economic Paleontologists and Mineralogists (Society for Sedimentary Geology) Special Publication no. 70, p. 137-161.

Minguez, D., Kodama, K.P., and Hillhouse, J.W., 2015, Paleomagnetic and cyclostratigraphic constraints on the synchroneity and duration of the Shuram carbon isotope excursion, Johnnie Formation, Death Valley Region, CA: Precambrian Research, v. 266, p. 395-408, doi: 10.1016/j.precamres.2015.05.033.

Minguez, D., and Kodama, K.P., 2017, Rock magnetic chronostratigraphy of the Shuram carbon isotope excursion: Wonoka Formation, Australia: Geology, v. 45, n. 6, p. 567-570,

doi: 10.1130/G38572.1.

Monger, J.W.H., and Price, R.A., 1979, Geodynamic evolution of the Canadian cordillera—progress and problems: Canadian Journal of Earth Sciences, v. 16, n. 3, p. 770-791, doi: 10.1139/e79-069.

Myrow, P.M., and Kaufman, A.J., 1999, A newly discovered cap carbonate above Varanger-age glacial deposits in Newfoundland, Canada: Journal of Sedimentary Research, v. 69, no. 3, p. 784-793.

Narbonne, G.M., Xiao, S., Shields, G.A., and Gehling, J.G., 2012, The Ediacaran Period, *in* Gradstein, F.M., Ogg, J.G., Schmitz, M., and Ogg, G.M., eds., The Geologic Timescale 2012, Volume 1: Elsevier, p. 413-435, doi: 10.1016/B978-0-444-59425-9.00018-4.

Nolan, T. B., 1924, Geology of the northwest portion of the Spring Mountains, Nevada [Ph.D. thesis]: New Haven, Connecticut, Yale University, 125 p.

Nolan, 1929, Notes on the stratigraphy and structure of the northwest portion of Spring Mountain, Nevada: American Journal of Science, Series 5, v. 17, n. 101, p. 461-472.

Nursall, J.R., 1959, Oxygen as a prerequisite to the origin of the metazoa: Nature, v. 183, no. 4669, p. 1170-1172.

Och, L.M., and Shields-Zhou, G.A., 2012, The Neoproterozoic oxygenation event: Environmental perturbations and biogeochemical cycling: Earth-Science Reviews, v. 110, p. 26-57, doi: 10.1016/j.earscirev.2011.09.004.

Ogg, J.G., Ogg, G., and Gradstein, F.M., 2016, A concise geologic timescale: 2016: Amsterdam, Netherlands, Elsevier, 240 p.

Osburn, M.R., Owens, J., Bergmann, K.D., Lyons, T.W., and Grotzinger, J.P., 2015, Dynamic changes in sulfate sulfur isotopes preceding the Ediacaran Shuram Excursion: Geochimica et Cosmochimica Acta, v. 170, p. 204-224.

Palmer, A.R., 1981, Subdivision of the Sauk sequence, *in* Taylor, M.E., ed., Short papers for the Second International Symposium on the Cambrian System, U.S. Geological Survey Open File report 81-743, p. 160-163.

Palmer, A.R., and Halley, R.B., 1979, Physical stratigraphy and trilobite biostratigraphy of the Carrara Formation (Lower and Middle Cambrian) in the Southern Great Basin: U.S. Geological Survey Professional Paper 1407, 131 p.

Parsons, B. and Sclater, J.G., 1977, An analysis of the variation of ocean floor bathymetry and heat flow with age: Journal of Geophysical Research, v. 82, no. 5, p. 803-827.

Petterson, R., Prave, A.R., Wernicke, B.P., and Fallick, A.E., 2011, The Neoproterozoic

Noonday Formation, Death Valley region, California: Geological Society of America Bulletin, v. 123, no. 7/8, p. 1539-1559, doi: 10.1130/B30281.1.

Poole, F.G., Stewart, J.H., Palmer, A.R., Sandberg, C.A., Madrid, R.J., Ross, Jr., R.J., Hintze, L.F., Miller, M.M., and Wrucke, C.T., 1992, Latest Precambrian to latest Devonian time; Development of a continental margin, *in* Burchfiel, B.C., Lipman, P.W., and Zoback, M.L., eds., The Cordilleran Orogen: Conterminous U.S.: Boulder, Colorado, Geological Society of America, The Geology of North America, v. G-3.

Prave, A.R., Fallick, A.E., Thomas, C.W., and Graham, C.M., 2009, A composite C-isotope profile for the Neoproterozoic Dalradian Supergroup of Scotland and Ireland: Journal of the Geological Society, London, v. 166, p. 845-857, doi: 10.1144/0016-76492008-131.

Pu, J.P., Bowring, S.A., Ramezani, J., Myrow, P., Raub, T.D., Landing, E., Mills, A., Hodgin, E., and Macdonald, F.A., 2016, Dodging snowballs: Geochronology of the Gaskiers glaciation and the first appearance of Ediacaran biota: Geology, v. 44, n. 11, p. 955-958, doi:10.1130/G38284.1.

Quinn, T., 1991, Meteoric diagenesis of Plio-Pleistocene limestones at Enewetak Atoll: Journal of Sedimentary Petrology, v. 61, no. 5, p. 681-703.

Sahoo, S.K., Planavsky, N.J., Kendall, B., Wang, X., Shi, X., Scott, C., Anbar, A.D., Lyons, T.W., and Jiang, G., 2012, Ocean oxygenation in the wake of the Marinoan glaciation:

Nature, v. 489, p. 546-549, doi: 10.1038/nature11445.

Saltzman, M.R., and Thomas, E., 2012, Carbon isotope stratigraphy, *in* Gradstein, F.M., Ogg, J.G., Schmitz, M., and Ogg, G.M., eds., The Geologic Timescale 2012, Volume 1: Elsevier, p. 207-232, doi: 10.1016/B978-0-444-59425-9.00011-1.

Sawaki, Y., Ohno, T., Tahata, M., Komiya, T., Hirata, T., Maruyama, S., Windley, B.F., Han, J., Shu, D., and Li, Y., 2010, The Ediacaran radiogenic Sr isotope excursion in the Doushantuo Formation in the Three Gorges area, South China: Precambrian Research, v. 176, p. 46-64.

Sawyer, D.S., Swift, B.A., Sclater, J.G., and Toksöz, M.N., 1982, Extensional model for the subsidence of the northern United States Atlantic continental margin: Geology, v. 10, p. 134-140.

Schiffbauer, J.D., Huntley, J.W., O'Neil, G.R., Darroch, S.A.F., Laflamme, M., and Cai, Y., 2016, The latest Ediacaran wormworld fauna: Setting the ecological stage for the Cambrian explosion: GSA Today, v. 26, n. 11, doi: 10.1130/GSATG265A.1.

Schoenborn, W.A., and Fedo, C.M., 2011, Provenance and paleoweathering reconstruction of the Neoproterozoic Johnnie Formation, southeastern California: Chemical Geology, v. 285, p. 231-255, doi: 10.1016/j.chemgeo.2011.04.014.

Schoenborn, W.A., Fedo, C.M., and Farmer, G.L., 2012, Provenance of the Neoproterozoic Johnnie Formation and Stirling Quartzite, southeastern California, determined by detrital zircon geochronology and Nd isotope geochemistry: Precambrian Research, v. 206-207, p. 182-199, doi:10.1016/j.precamres.2012.02.017.

Sims, J.D., 2012, Earthquake-induced load casts, pseudonodules, ball-and-pillow structures, and convolute lamination: Additional deformation structures for paleoseismic studies, *in* Cox, R.T., Tuttle, M.P., Boyd, O.S., and Locat, J., eds., Recent Advances in North American Paleoseismology and Neotectonics East of the Rockies: Geological Society of America Special Paper 493, p. 191-201, doi:10.1130/2012.2493(09).

Smith, E.F., Nelson, L.L., Strange, M.A., Eyster, A.E., Rowland, S.M., Schrag, D.P., and Macdonald, F.A., 2016, The end of the Ediacaran: Two new exceptionally preserved body fossil assemblages from Mount Dunfee, Nevada, USA: Geology, v. 44, n. 11, p. 911-914, doi:10.1130/G38157.1.

Smith, E.F., Nelson, L.L., Tweedt, S.M., Zeng, H., and Workman, J.B., 2017, A cosmopolitan late Ediacaran biotic assemblage: new fossils from Nevada and Namibia support a global biostratigraphic link: Proceedings of the Royal Society of London B, v. 284, n. 1858, doi: 10.1098/rspb.2017.0934.

Steckler, M.S., and Watts, A.B., 1978, Subsidence of the Atlantic-type continental margin off New York: Earth and Planetary Science Letters, v. 41, p. 1-13.

Stewart, J.H., 1970, Upper Precambrian and lower Cambrian strata in the southern Great Basin, California and Nevada: U.S. Geological Survey Professional Paper 620, 206 p.

Stewart, J.H., 1972, Initial deposits in the Cordilleran geosyncline: Evidence of a Late Precambrian (<850 m.y.) continental separation: Geological Society of America Bulletin, v. 83, p. 1345-1360.

Stewart, J.H., and Poole, F.G., 1974, Lower Paleozoic and uppermost Precambrian Cordilleran miogeocline, Great Basin, western United States, *in* Dickinson, W.R., ed., Tectonics and Sedimentation: Society of Economic Paleontologists and Mineralogists Special Publication 22, p. 28-57.

Stewart, J.H., and Suczek, C.A., 1977, Cambrian and latest Precambrian paleogeography and tectonics in the western United States, *in* Stewart, J.H., Stevens, C.H., and Fritsche, A.E., eds., Paleozoic paleogeography of the western United States: Pacific Section Society of Economic Paleontologists and Mineralogists, p. 1-17.

Stewart, J.H., McMenamin, M.A.S., and Morales-Ramirez, J.M., 1984, Upper Proterozoic and Cambrian rocks in the Caborca region, Sonora, Mexico-Physical stratigraphy, biostratigraphy, paleocurrent studies, and regional relations: U.S. Geological Survey Professional Paper 1309, 36 p.

Summa, C.L., 1993, Sedimentologic, stratigraphic, and tectonic controls of a mixed carbonate-siliciclastic succession: Neoproterozoic Johnnie formation, southeast California [Ph.D. thesis]: Cambridge, Massachusetts, Massachusetts Institute of Technology, 331 p.

Swart, P.K., and Kennedy, M.J., 2012, Does the global stratigraphic reproducibility of $\delta^{13}C$ in Neoproterozoic carbonates require a marine origin? A Pliocene-Pleistocene comparison: Geology, v. 40, n. 1, p. 87-90, doi: 10.1130/G32538.1.

Tahata, M., Ueno, Y., Ishikawa, T., Sawaki, Y., Murakami, K., Han, J., Shu, D., Li, Y., Guo, J., Yoshida, N., and Komiya, T., 2013, Carbon and oxygen isotope chemostratigraphies of the Yangtze platform, South China: Decoding temperature and environmental changes through the Ediacaran: Gondwana Research, v. 23, p. 333-353.

Trower, E.J., and Grotzinger, J.P., 2010, Sedimentology, diagenesis, and stratigraphic occurrence of giant ooids in the Ediacaran Rainstorm Member, Johnnie Formation, Death Valley region, California: Precambrian Research, v. 180, p. 113-124, doi: 10.1016/j.precamres.2010.03.007.

U.S. Geological Survey, 1968, Mt. Schader quadrangle, Nevada - Nye County: 7.5 minute series (topographic), scale 1:24,000.

Verdel, C., Wernicke, B.P., and Bowring, S.A., 2011, The Shuram and subsequent Ediacaran carbon isotope excursions from southwest Laurentia, and implications for

environmental stability during the metazoan radiation: Geological Society of America Bulletin, v. 123, no. 7/8, p. 1539-1559, doi: 10.1130/B30369.1.

Walker, J.D., Geissman, J.W., Bowring, S.A., and Babcock, L.E., 2013, The Geological Society of America Geologic Time Scale: Geological Society of America Bulletin, v. 125, n. 3/4, p. 259-272, doi: 10.1130/B30712.1.

Wright, L.A., and Troxel, B.W., 1966, Strata of late Precambrian-Cambrian age, Death Valley region, California-Nevada: American Association of Petroleum Geologists Bulletin, v. 50, n. 5, p. 846-857.

Wright, L.A., and Troxel, B.W., 1984, Geology of the north 1/2 Confidence Hills 15' quadrangle, Inyo County, California: California Division of Mines and Geology Map Sheet 34, scale 1:24000, 1 sheet, 31 p. text.

Xiao, S., Bao, H., Wang, H., Kaufman, A.J., Zhou, C., Li, G., Yuan, X., and Ling, H., 2004, The Neoproterozoic Quruqtagh Group in eastern Chinese Tianshan: Evidence for a post-Marinoan glaciation: Precambrian Research, v. 130, p. 1-26.

Xiao, S., Narbonne, G.M., Zhou, C., Laflamme, M., Grazhdankin, D.V., Moczydlowska-Vidal, M., and Cui, H., 2016, Towards an Ediacaran time scale: Problems, protocols, and prospects: Episodes, v. 39, n. 4, p. 540-555, doi: 10.18814/epiiugs/2016/v39i4/103886.

Yonkee, W.A., Dehler, C.D., Link, P.K., Balgord, E.A., Keeley, J.A., Hayes, D.S., Wells, M.L., Fanning, C.M., and Johnston, S.M., 2014, Tectono-stratigraphic framework of Neoproterozoic to Cambrian strata, west-central U.S.: Protracted rifting, glaciation, and evolution of the North American Cordilleran margin: Earth-Science Reviews, v. 136, p. 59-95, doi: 10.1016/j.earscirev.2014.05.004.

Zhou, C., Xie, G., McFadden, K., Xiao, S., and Yuan, X., 2007, The diversification and extinction of Doushantuo-Pertatataka acritarchs in South China: Causes and biostratigraphic significance: Geological Journal, v. 42, p. 229-262.

FIGURE CAPTIONS

Figure 1 (p. 90): Generalized stratigraphic column of Precambrian-Cambrian strata; thicknesses represent sections in the northwest Spring Mountains, Nevada (from Stewart, 1970). Cryogenian-Ediacaran boundary (635 Ma) is based on the interpretation that the Noonday Dolomite is the Marinoan cap carbonate sequence (Petterson et al., 2011) and the definition for the base of the Ediacaran period (Knoll et al., 2004; Knoll et al., 2006; Narbonne et al., 2012). Precambrian-Cambrian boundary (541 Ma) is based on paleontology (Hagadorn and Waggoner, 2000; Corsetti and Hagadorn, 2000). The Noonday Formation and Stirling Formation are generally resistant, cliff-forming units, in contrast to the recessive, slope-forming Johnnie and lower Wood Canyon Formations. The letter C indicates the conglomeratic member of the Johnnie Formation, which fills local valleys incised into the Rainstorm Member.

Figure 2 (p. 91): (A) Google Earth image and (B) corresponding geologic map of Precambrian-Cambrian strata in the northwest Spring Mountains, Nevada, in the vicinity of the type locality of the Johnnie Formation in Johnnie Wash. GF- Grapevine fault; JW- Johnnie Wash; MA- Montgomery anticline; NV-160- Nevada State Highway 160; PF- Paddy's fault. Dotted line labeled d/e indicates the conspicuous surface trace of the contact between informal members D and E of the Johnnie Formation. Data were compiled from Abolins (1999), Burchfiel et al. (1974, 1983), and this study.

Figure 3 (p. 92): Geologic map and cross sections of Johnnie Wash and environs. Definitions of unit labels and the description of map units are given in the Appendix.

Figure 4 (p. 93): Generalized lithostratigraphic column of the Johnnie Formation at its type locality in Johnnie Wash, with thicknesses based on cross sections A - A' and B - B' in Figure 3 for units A through L, and Stewart (1970) for the Rainstorm Member. Roman numerals on left side of column indicate the three sand-rich intervals discussed in text.

Figure 5 (p. 94): Photographs of selected lithostratigraphic elements of the Johnnie Formation. (A) Load cast with folded laminae in sandstone bed, unit B, Johnnie Wash area. Hammer is 28 cm long. (B) Ball-and-pillow structure in unit B, with light-colored siltstone (just above pocket knife) protruding upward between bulbous masses of fine-grained sandstone. Pocket knife is 9 cm long. (C) Gray cherty dolostone, unit F, Johnnie Wash. Pencil is 15 cm long (D) Brown-weathering, laminated dolostone, typical of carbonate beds in units

H through L. Hammer is 28 cm long. (E) Variegated siltstone typical of all units in the Johnnie Formation. Pocket knife is 9 cm long. (F) Johnnie oolite, Johnnie Wash, ooids are 1 - 2 mm in diameter. (G) Large, bulbous mass of orthoquartzite (left of hammer), surrounded by smaller masses lying in a matrix of siltstone, uppermost bed of the Rainstorm Member, Mt. Schader section. Hammer is 33 cm long. (H) Base of orthoquartzite bed in (G), showing load cast structures with underlying siltstone. Hammer is 33 cm long.

Figure 6 (p. 95): Geologic map of the Mt. Schader section, showing measured and sampled transects. Definition of unit labels and description of map units are given in the Appendix.

Figure 7 (p. 96): (A) Detailed lithostratigraphic column of the Mt. Schader section, from unit G of the Johnnie Formation through the lowermost part the A Member of the Stirling Formation, showing thicknesses based on Jacobs staff measurements (transects shown in Figure 6). Detailed description of subunits 1 - 48 are given in the Supplemental Text. (B) and (C), carbon and oxygen isotope ratios, respectively, in carbonate, as a function of stratigraphic position. Numerical values are found in Table S1. VPDB- Vienna Peedee Belemnite

Figure 8 (p. 97): (A) Photograph of tabular planar cross-stratification in unit D, Johnnie Wash. Notebook is 13 cm wide. (B) Equal area stereogram of poles to foreset laminations measured at Locality A (Figure 2A), with bedding tilt removed. Dots are data (n = 65), larger square in circle is the mean vector. Plotted using *Stereonet* software (Allmendinger et al., 2012; Cardozo and Allmendinger, 2013), with Kamb contours at 2σ intervals (Kamb, 1959).

(C) Photograph of steep foreset laminations (bedding parallel to base of photograph), showing 9 cm scale bar at location of petrographic measurements of mean grain size in (D). (D) Mean grain size as a function of stratigraphic height in sample of foreset laminations, showing relatively constant value of 200 μm.

Figure 9 (p. 98): (A) and (B), carbon and oxygen isotope ratios, respectively, in carbonate as a function of stratigraphic position, for units C and F in the Johnnie Wash area. Numerical values are found in Table S1. VPDB-Vienna Peedee Belemnite.

Figure 10 (p. 99): Carbon isotope ratios as function of stratigraphic position, expanding the vertical scale within each carbonate bed, to reveal any intrabed trends. Beds are numbered from bottom to top within a given unit, e.g. Zjj1 is the lowest carbonate bed in unit J. VPDB-Vienna Peedee Belemnite.

Figure 11 (p. 100): Cross plot of $\delta^{18}O$ versus $\delta^{13}C$, color coded by stratigraphic unit, showing linear regression lines. VPDB- Vienna Peedee Belemnite.

Figure 12 (p. 101): Plot showing calculated tectonic subsidence *Y* as a function of observed stratigraphic thickness *S*. Lower curve shows results assuming unit A of the Johnnie Formation at the type locality is immediately underlain by crystalline basement. Error bars show range of estimates of *Y* produced by a ±5 % variation in sediment grain density. Upper curve shows results assuming unit A is underlain by c. 2000 m of hypothetical Pahrump Group strata.

Figure 13 (p. 102): Lithostratigraphic columns of the Johnnie Formation and enveloping Ediacaran-Cambrian formations at three key localities in Nevada and California, indicating the stratigraphic distribution of sand-rich intervals versus siltstone/carbonate-rich intervals. Informal member and unit designations in the southern Nopah and Desert Range sections are after Stewart (1970); note that the informal "Carbonate member" in the Desert Range section is predominantly sand-rich carbonate and fine- to medium-grained orthoquartzite with no siltstone. Bold numbers to the left of the scale bar are ages in Ma as follows: 509, base of Middle Cambrian (Palmer and Halley, 1979); 514 and 520, base of *Bonnia-Olenellus* and *Fallotaspis* trilobite zones respectively (Hunt, 1990; Hollingsworth, 2005); 541 and 550, base of Cambrian and first-appearance datum of cloudinids (Corsetti and Hagadorn, 2000; Smith et al., 2016; Narbonne et al., 2012); 579, 585, and 624, model age estimates from this study; 635, base of Ediacaran (Petterson et al., 2011). Roman numerals indicate sand-rich intervals beginning with unit B of the type Johnnie Formation.

Figure 14 (p. 103): Paleoflow rosettes showing foreset lamination dip directions, corrected for bedding dip. Upper two rosettes compare data from sand-rich interval II (Figure 8B) with data from all sub-unit H strata (p. 224 in Benmore, 1978). Bottom rosette shows data from all pre-Rainstorm orthoquartzites in the Desert Range (p. 221 in Benmore, 1978).

Figure 15 (p. 104): Composite chemostratigraphy of the upper Johnnie Formation, showing carbon isotopic ratios in carbonate from unit H up to the oolite marker horizon in the lowermost Rainstorm Member (Mt. Schader section, this study) and values from just below

the base of the Rainstorm Member to the top of the member (southern Panamint Range, Verdel et al., 2011). VPDB- Vienna Peedee Belemnite.

Figure 16 (p. 105): Chemostratigraphic profiles comparing carbon isotopic data from the Johnnie Formation from unit H through the lowermost Rainstorm Member (ending at the top of the oolite marker bed, Figure 7), with profiles from (A) the Mukhaibah Dome (MD5); and (B) the Buah Dome (BD5) areas of Oman (Osburn et al., 2015). Vertical axis shows measured stratigraphic height in all profiles. Six additional profile comparisons are presented in Figure S3. VPDB- Vienna Peedee Belemnite.

Figure 17 (p. 106): Plot showing an exponential subsidence model $Y(t)$, based on conductive cooling of extended lithosphere (McKenzie, 1978). Plotted on curve are the onset of thermal subsidence at $t = 0$, and two arbitrary points in the history of subsidence. Note that so long as the stratigraphic position of $e(\infty) = 0$ is well defined, the form of the subsidence curve, including the exponential decay constant τ, is uniquely determined, and does not depend on $e(0) = E_0 r$.

Figure 18 (p. 107): Plots showing subsidence data and model for northwest Spring Mountains section of southwest Laurentia: (A) observed subsidence (stratigraphic thickness) S versus tectonic subsidence Y; (B) temporal control on tectonic subsidence Y versus time applied to Cambrian and younger points (solid circles), temporal model shown with plus symbols; (C) same as (B), except showing S versus t; and (D) same as (C) with axes inverted. Dotted red line and number in (B) show projected age of the base of Johnnie unit A; Dotted red line and

circle in (D) show the amount of additional, hypothetical strata that would be needed below unit A in the Spring Mountains in order for sedimentation to extend linearly back in time to 635 Ma.

TABLES

Table 1: Nomenclature of stratigraphic units used in subsidence analysis tables	
Stratigraphic unit: can be partitioned/combined formations (Fm) and/or members (Mbr)	Abbreviation
Spring Mountains section	
Carbonate overburden	MzPzco
Devils Gate Fm	Ddg
Nevada Fm	Dn
Laketown Fm (upper 50%)	Dl
Laketown Fm (lower 50%)	Sl
Ely Springs Fm	Oes
Eureka Fm	Oe
Pogonip Group (upper third)	Op2
Pogonip Group (lower two thirds)	Op1
Nopah Fm (upper third)	OЄn2
Nopah Fm (lower two thirds)	OЄn1
Dunderberg Fm	Єd
Bonanza King Fm (Banded Mountain Mbr, upper 36%)	Єbk2
Bonanza King Fm (Mbrs: Papoose Lake & Banded Mountain, lower 64%)	Єbk1
Carrara Fm (upper two thirds)	Єc2
Carrara Fm (lower third)	Єc1
Zabriskie Fm	Єz
Wood Canyon Fm (Ediacaran/Cambrian boundary to top)	ЄZwc2
Wood Canyon Fm (to Ediacaran/Cambrian boundary)	ЄZwc1
Stirling Fm (members A through E)	Zsa - Zse
Johnnie Fm (Rainstorm Mbr, oolite bed's base to top of Mbr)	Zjr2
Johnnie Fm (Rainstorm Mbr, base to oolite bed's base)	Zjr1
Johnnie Fm (members A through L)	Zja - Zjl
Pahrump Group substrate (hypothetical)	
Johnnie Fm (Presumed equivalent to the Transitional Mbr of Stewart, 1970)	Zjt
Kingston Peak Fm (Mbr: South Park, sub-Mbr: Wildrose)	Zkpw
Kingston Peak Fm (Mbr: South Park, sub-Mbr: Thorndike)	Zkpth
Kingston Peak Fm (Mbr: South Park, sub-Mbr: Mountain Girl)	Zkpmg
Kingston Peak Fm (Mbr: South Park, sub-Mbrs: Sourdough & Middle Park)	Zkpsmp
Kingston Peak Fm (Limekiln-Surprise Mbr)	Zkpls
Beck Springs Fm/Kingston Peak Fm (lower)	Zbs
Horse Thief Springs Fm	Zhs
Crystal Springs Fm (upper)	Ycs2
Crystal Springs Fm (lower)	Ycs1

Table 2: Nomenclature of parameters used in delithification and backstripping analysis[1]	
ϕ_0	Surface porosity (%)
c	Porosity depth coefficient (km^{-1})
ρ_{sg}	Sediment grain density ($kg\ m^{-3}$)
h	Stratigraphic thickness (m)
S	Cumulative stratigraphic thickness (m)
*S**	Delithified/decompacted thickness (m)
Y	Tectonic subsidence (m)

[1]Subscripts for *S*, *S**, and *Y*:
ns, no Pahrump Group substrate;
ws, with Pahrump Group substrate;
low, low subsidence from using +5% ρ_{sg};
high, high subsidence from using -5% ρ_{sg}.

Table 3: Parameters used in delithification and backstripping analysis of the Spring Mountains section[1]								
Unit	Age[2] (Ma)	Lithology	ϕ_0 (%)	c (km^{-1})	ρ_{sg} (kg m^{-3})	h (m)	S_{ns} (m)	S_{ws} (m)
MzPzco[3]	Ca. 243	l/d	43	0.58	2785	3000	9720	11745
Ddg	359	d	43	0.58	2710	286	6720	8745
Dn	383	d	43	0.58	2860	286	6434	8459
Dl	393	d	43	0.58	2860	71.5	6148	8173
Sl	419	d	43	0.58	2860	71.5	6076.5	8101.5
Oes	444	d	43	0.58	2860	95	6005	8030
Oe	458	s	49	0.27	2650	71	5910	7935
Op2	-	l	43	0.58	2710	230	5839	7864
Op1[4]	470	l	43	0.58	2710	460	5609	7634
OЄn2	-	d	43	0.58	2860	95	5149	7174
OЄn1	485	d	43	0.58	2860	191	5054	7079
Єd	-	sh	63	0.51	2720	48	4863	6888
Єbk2	-	d	43	0.58	2860	197	4815	6840
Єbk1	497	d	43	0.58	2860	637	4618	6643
Єc2	-	sh	63	0.51	2720	286	3981	6006
Єc1	509	sh	63	0.51	2720	143	3695	5720
Єz	-	s	49	0.27	2650	24	3552	5577
ЄZwc2	-	s/slt	49	0.27	2650	523	3528	5553
ЄZwc1	541	s/slt	49	0.27	2650	144	3005	5030
Zse	-	s	49	0.27	2650	340	2861	4886
Zsd[5]	-	d	46	0.43	2755	10	2521	4546
Zsc	-	slt/s	49	0.27	2650	190	2511	4536
Zsb	-	s/slt	49	0.27	2650	90	2321	4346
Zsa	-	s	49	0.27	2650	369	2231	4256
Zjr2[6]	-	slt/s/l/d	47	0.37	2695	250	1862	3887
Zjr1[7]	-	slt	49	0.27	2650	17	1612	3637
Zjl	-	s/slt	49	0.27	2650	60	1595	3620
Zjk	-	s/slt	49	0.27	2650	95	1535	3560
Zjj	-	s/slt	49	0.27	2650	190	1440	3465
Zji	-	s/slt	49	0.27	2650	55	1250	3275
Zjh	-	s/slt	49	0.27	2650	60	1195	3220
Zjg	-	slt	49	0.27	2650	135	1135	3160
Zjf[8]	-	d	43	0.58	2860	40	1000	3025
Zje	-	s/slt	49	0.27	2650	280	960	2985
Zjd[9]	-	s	49	0.27	2650	300	680	2705
Zjc2	-	slt	49	0.27	2650	45	380	2405
Zjc1[10]	-	slt	49	0.27	2650	50	335	2360
Zjb[11]	-	s	49	0.27	2650	160	285	2310
Zja	-	slt	49	0.27	2650	125	125	2150
Zjt[12]	-	d/s	46	0.43	2755	125	-	2025
Zkpw[13]	635	ss	49	0.27	2650	100	-	1900
Zkpth	-	d	43	0.58	2860	100	-	1800
Zkpmg	-	s	49	0.27	2650	100	-	1700
Zkpsmp	-	slt	49	0.27	2650	200	-	1600
Zkpls	-	s/cgl	49	0.27	2650	400	-	1400
Zbs	-	d	43	0.58	2860	200	-	1000
Zhs[14]	<787	s	49	0.27	2650	200	-	800
Ycs2	>1087	d	43	0.58	2860	200	-	600
Ycs1[15]	-	s	49	0.27	2650	400	-	400

[1]Values from table 9.1 *in* Allen and Allen (2005), Equation 3 *in* Halley and Schmoker (1983), Deer et al. (1992), or weighted averages for lithologic mixtures. Abbreviations for lithology are: s, sandstone; slt, siltstone; l, limestone; d, dolostone; sh, shale; cgl, conglomerate. See Table 2 for parameter definitions.

[2]Ages are at top of unit.

[3]Lithologic ratio used is 50/50; average for ρ_{sg}.

[4]Carbonate is mostly limestone (fig. 2 *in* Burchfiel et al., 1974).

[5]Dolostone is sandy (stratigraphic column for Spring Mountains, plate 2 *in* Stewart, 1970).

[6]Shuram excursion ends. Lithologic ratio is slt+s/l/d = 67/16.5/16.5 (table 3 *in* Stewart, 1970).

[7]Shuram excursion begins.
[8]Cherty dolostone.
[9]High-angle cross-bedding.
[10]Onset of thermal subsidence (based on interpretation of ball-and-pillow structure, see text).
[11]Ball-and-pillow structure.
[12]Lithologic ratio is d/s = 50/50.
[13]Age from Petterson et al. (2011).
[14]Maximum age from Mahon et al. (2014).
[15]Minimum age from Heaman and Grotzinger (1992).

Table 4: Results from delithification and backstripping analysis of the Spring Mountains section[1]

Unit	Age[2] (Ma)	S_{ns}	S^*_{ns}	$Y_{ns,\ low}$	Y_{ns}	$Y_{ns,\ high}$	S_{ws}	S^*_{ws}	$Y_{ws,\ low}$	Y_{ws}	$Y_{ws,\ high}$
MzPzco	Ca. 243	9720	9714	2670	3193	3715	11745	11736	3128	3768	4406
Ddg	359	6720	7489	2412	2791	3169	8745	9548	2905	3401	3895
Dn	383	6434	7246	2380	2743	3105	8459	9310	2878	3358	3836
Dl	393	6148	7002	2367	2713	3058	8173	9071	2871	3334	3795
Sl	419	6076.5	6940	2364	2706	3046	8101.5	9011	2869	3328	3785
Oes	444	6005	6881	2361	2699	3035	8030	8953	2868	3322	3776
Oe	458	5910	6799	2357	2689	3020	7935	8874	2866	3315	3763
Op2	-	5839	-	-	-	-	7864	-	-	-	-
Op1	470	5609	6541	2320	2636	2950	7634	8622	2836	3269	3700
OЄn2	-	5149	-	-	-	-	7174	-	-	-	-
OЄn1	485	5054	6070	2280	2564	2846	7079	8167	2811	3212	3611
Єd	-	4863	-	-	-	-	6888	-	-	-	-
Єbk2	-	4815	-	-	-	-	6840	-	-	-	-
Єbk1	497	4618	5694	2264	2522	2778	6643	7804	2809	3183	3556
Єc2	-	3981	-	-	-	-	6006	-	-	-	-
Єc1	509	3695	4798	2125	2327	2528	5720	6949	2710	3029	3347
Єz	-	3552	-	-	-	-	5577	-	-	-	-
ЄZwc2	-	3528	-	-	-	-	5553	-	-	-	-
ЄZwc1	541	3005	4024	1844	2009	2173	5030	6220	2475	2757	3037
Zse	-	2861	3865	1786	1943	2100	4886	6072	2428	2702	2975
Zsd	-	2521	3481	1642	1781	1919	4546	5718	2313	2570	2824
Zsc	-	2511	3469	1638	1777	1914	4536	5708	2311	2566	2821
Zsb	-	2321	3250	1553	1682	1809	4346	5507	2245	2490	2735
Zsa	-	2231	3144	1512	1635	1758	4256	5411	2213	2454	2693
Zjr2	-	1862	2706	1337	1441	1544	3887	5018	2083	2304	2523
Zjr1	-	1612	2400	1221	1311	1399	3637	4748	2004	2210	2415
Zjl	-	1595	2379	1212	1301	1388	3620	4730	1997	2203	2407
Zjk	-	1535	2303	1179	1264	1349	3560	4663	1973	2176	2377
Zjj	-	1440	2179	1125	1204	1284	3465	4556	1936	2133	2329
Zji	-	1250	1930	1012	1082	1150	3275	4343	1859	2046	2231
Zjh	-	1195	1856	978	1045	1110	3220	4280	1836	2020	2203
Zjg	-	1135	1775	941	1004	1066	3160	4212	1812	1992	2171
Zjf	-	1000	1589	853	909	964	3025	4058	1756	1929	2101
Zje	-	960	1537	835	889	941	2985	4015	1747	1918	2087
Zjd	-	680	1132	633	671	709	2705	3689	1624	1779	1933
Zjc2	-	380	664	385	406	427	2405	3331	1486	1624	1762
Zjc1	-	335	591	344	363	382	2360	3278	1465	1601	1736
Zjb	-	285	507	297	313	329	2310	3217	1441	1574	1707
Zja	-	125	230	138	145	152	2150	3024	1365	1489	1612
Zjt	-	-	-	-	-	-	2025	2871	1304	1422	1538
Zkpw	635	-	-	-	-	-	1900	2722	1255	1365	1475
Zkpth	-	-	-	-	-	-	1800	2597	1204	1308	1412
Zkpmg	-	-	-	-	-	-	1700	2480	1173	1271	1368
Zkpsmp	-	-	-	-	-	-	1600	2349	1116	1209	1300
Zkpls	-	-	-	-	-	-	1400	2086	1000	1081	1162
Zbs	-	-	-	-	-	-	1000	1546	756	815	873
Zhs	<787	-	-	-	-	-	800	1288	669	716	762
Ycs2	>1087	-	-	-	-	-	600	993	523	558	593
Ycs1	-	-	-	-	-	-	400	707	408	431	453

[1]See Table 2 for parameter definitions. For subscript “ns,” *S* was measured relative to the base of Zja, and for “ws,” relative to the base of Ycs1.
[2]Ages are at top of unit.

Table 5: Estimates for the time constant τ[1]								
Model	*Y*(541)	*Y*(509)	*Y*(393)	*Y*(383)	*Y*(c. 388)[2]	τ (m.y.)	SE[3] begin (Ma)	SE[3] end (Ma)
Y_{ns}	2009	2327	2713	2743	2728	55	578	573
Y_{ns}[4]	1646	1964	2350	2380	2365	55	578	573
Y_{ws}	2757	3029	3334	3358	3346	52	575	570
$Y_{ns, low}$	1844	2125	2367	2380	2374	42	574	569
Y_{ns}	2009	2327	2713	2743	2728	55	578	573
$Y_{ns, high}$	2173	2528	3058	3105	3082	65	581	575
$Y_{ns, low}$[4]	1500	1781	2023	2036	2030	42	574	569
Y_{ns}[4]	1646	1964	2350	2380	2365	55	578	573
$Y_{ns, high}$[4]	1791	2146	2676	2723	2700	65	581	575
$Y_{ws, low}$	2475	2710	2871	2878	2875	36	569	566
Y_{ws}	2757	3029	3334	3358	3346	52	575	570
$Y_{ws, high}$	3037	3347	3795	3836	3816	63	578	573

[1]Units for τ are millions of years (my). Units for all *Y* values are in meters (m).
[2]Mean value of *Y*(393 Ma) and *Y*(383 Ma).
[3]SE = Shuram excursion.
[4]*Y* values were adjusted by assuming a zero datum that represents a specific point in the stratigraphic column inferred to represent cessation of mechanical stretching and inception of passive-margin thermal subsidence.

Table 6: All ages modeled using no substrate										
		Model ages (Ma)								
		τ = 55 m.y.			τ = 60 m.y.			τ = 65 m.y.		
Unit	Age[1] (Ma)	Min	Int	Max	Min	Int	Max	Min	Int	Max
MzPzco	Ca. 243	-	-	-	-	-	-	-	-	-
Ddg	359	-	-	-	-	-	-	-	-	-
Dn	383	-	-	-	-	-	-	-	-	-
Dl	393	341	328	303	323	309	281	305	289	260
Sl	419	363	349	323	347	332	303	331	314	283
Oes	444	378	364	337	363	348	319	348	332	300
Oe	458	393	381	352	380	366	335	366	352	317
Op1	470	435	428	415	425	418	404	416	407	393
OЄn1	485	467	460	446	460	452	437	453	445	429
Єbk1	497	481	472	455	475	466	447	470	460	439
Єc1	509	514	509	499	511	506	496	509	503	492
ЄZwc1	541	541	541	541	541	541	541	541	541	541
Zse	-	545	546	547	546	546	547	546	547	548
Zsd	-	555	556	559	556	558	560	557	559	562
Zsc	-	555	556	559	556	558	561	557	559	562
Zsb	-	560	562	565	561	563	567	563	565	569
Zsa	-	562	564	568	564	566	570	565	568	573
Zjr2	-	570	573	578	573	576	581	575	579	585
Zjr1	-	575	578	584	578	582	588	581	585	592
Zjl	-	575	579	584	578	582	588	581	586	592
Zjk	-	576	580	586	580	584	590	583	587	594
Zjj	-	579	582	588	582	586	592	585	590	597
Zji	-	582	587	593	586	591	598	590	595	602
Zjh	-	584	588	594	587	592	599	591	596	604
Zjg	-	585	589	596	589	593	601	593	598	606
Zjf	-	588	592	599	592	597	604	596	601	610
Zje	-	588	593	600	592	597	605	597	602	610
Zjd	-	594	599	606	599	604	612	603	609	618
Zjc2	-	600	605	614	605	611	620	611	617	627
Zjc1	-	601	606	615	606	612	622	612	618	628
Zjb	-	602	608	616	607	614	623	613	620	630
Zja	-	605	611	620	611	618	627	617	624	635
(base)	-	608	614	623	614	621	631	620	628	639

[1]Ages are at top of unit.

FIGURES

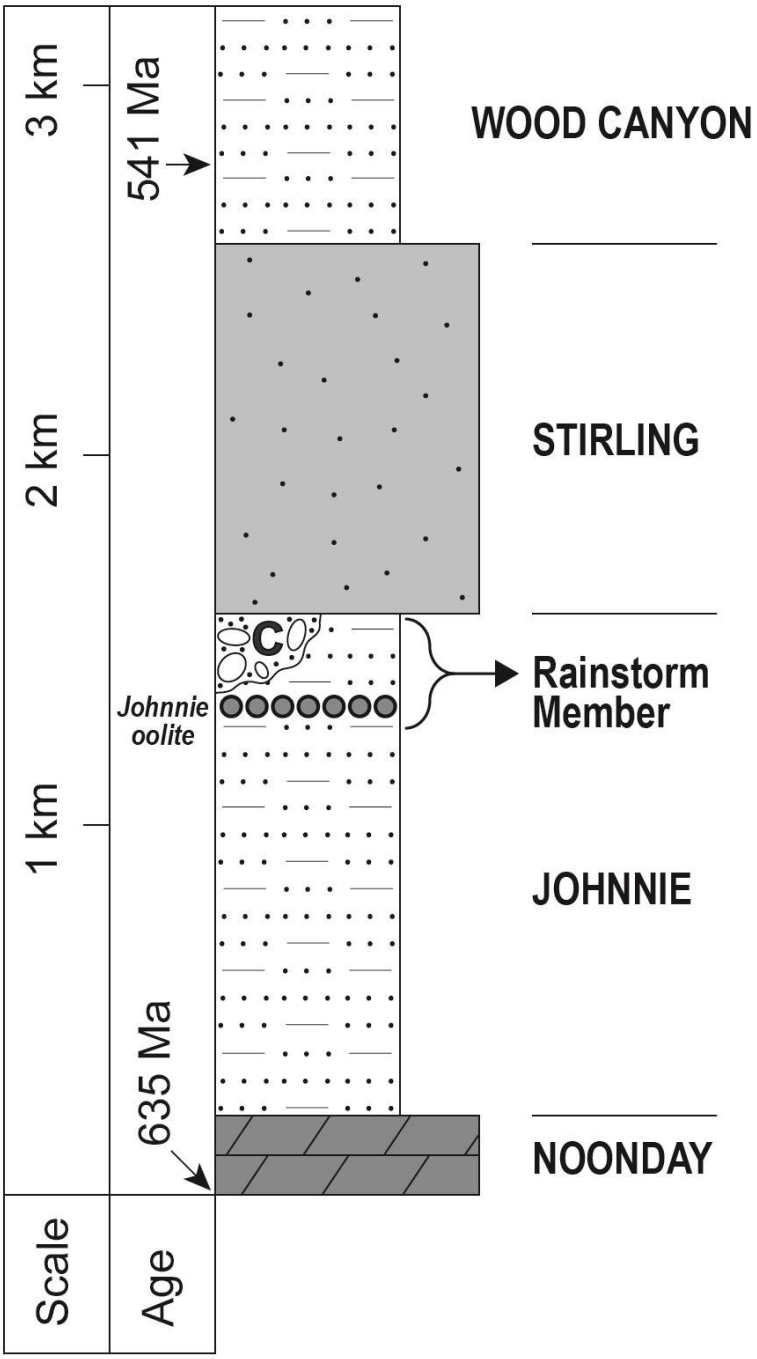

Figure 1

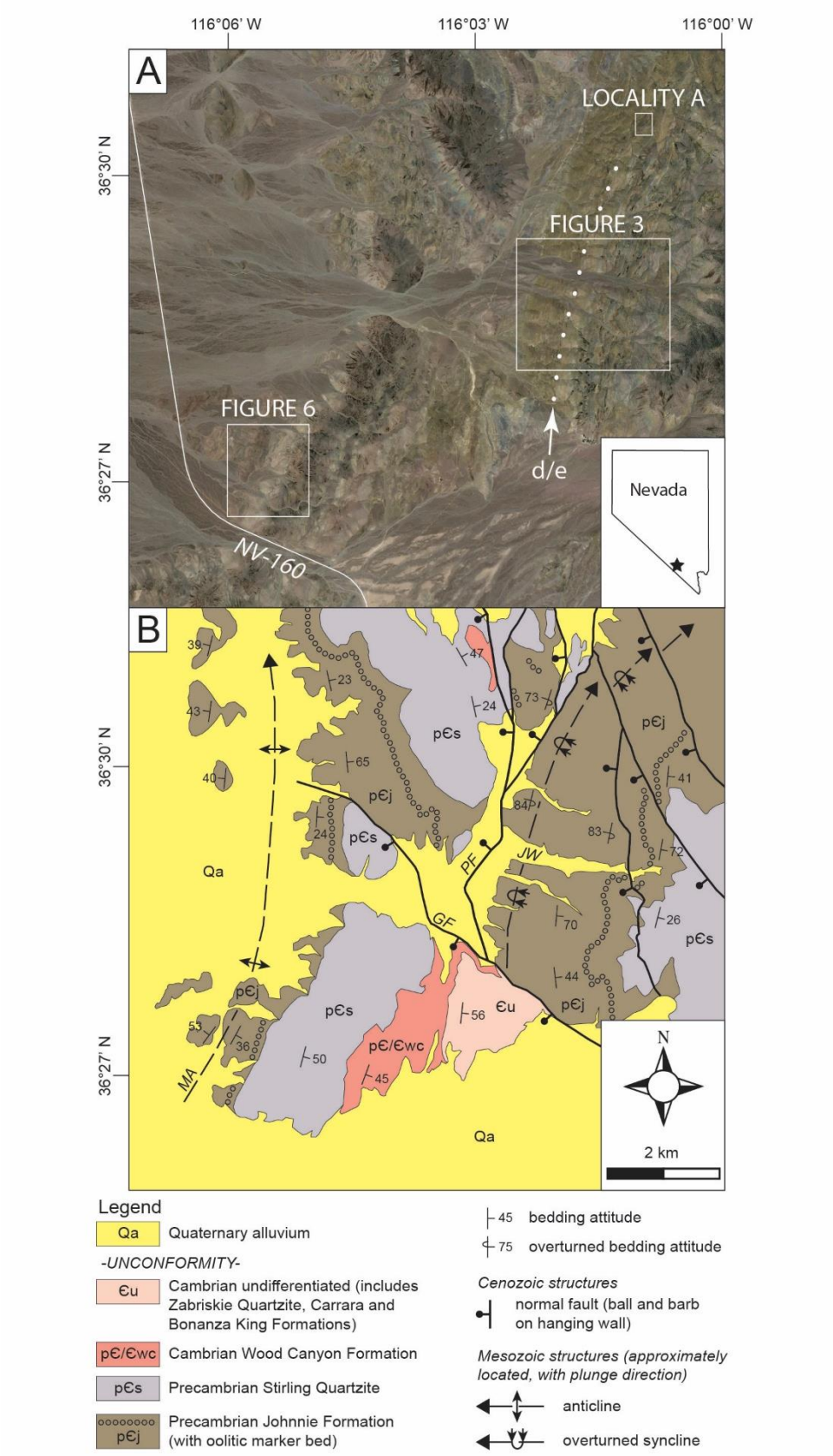
116°06' W
116°03' W
116°00' W
36°30' N
36°27' N
A
LOCALITY A
FIGURE 3
FIGURE 6
d/e
Nevada
NV-160
B
pЄs
pЄj
Qa
PF
JW
GF
MA
pЄ/Єwc
Єu
N
2 km
Legend
Qa Quaternary alluvium
-UNCONFORMITY-
Єu Cambrian undifferentiated (includes Zabriskie Quartzite, Carrara and Bonanza King Formations)
pЄ/Єwc Cambrian Wood Canyon Formation
pЄs Precambrian Stirling Quartzite
pЄj Precambrian Johnnie Formation (with oolitic marker bed)
45 bedding attitude
75 overturned bedding attitude
Cenozoic structures
normal fault (ball and barb on hanging wall)
Mesozoic structures (approximately located, with plunge direction)
anticline
overturned syncline

Figure 2

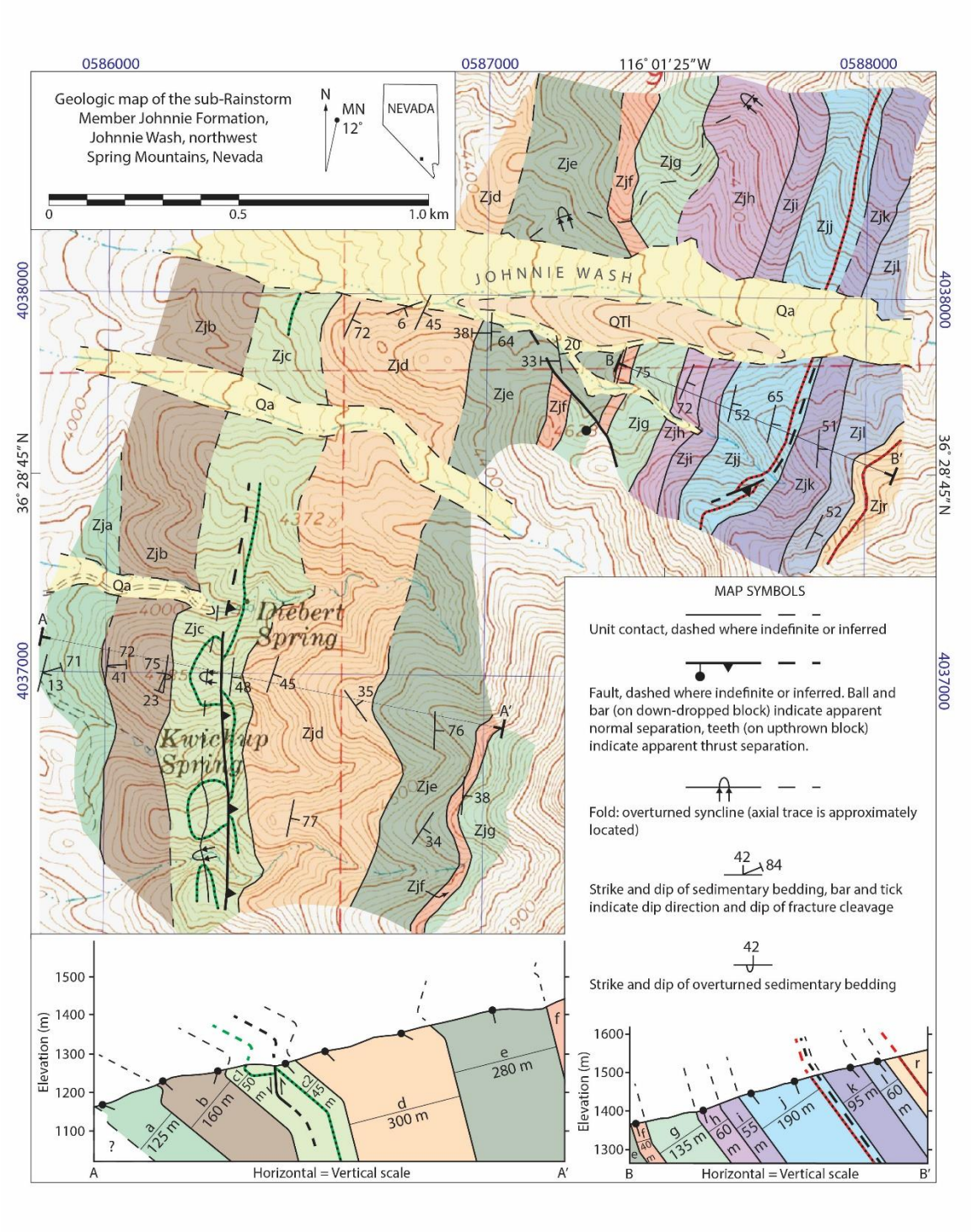
Geologic map of the sub-Rainstorm Member Johnnie Formation, Johnnie Wash, northwest Spring Mountains, Nevada
N
MN 12°
NEVADA
0
0.5
1.0 km
0586000
0587000
116° 01' 25"W
0588000
4038000
4037000
36° 28' 45"N
JOHNNIE WASH
Qa
QTl
Zja
Zjb
Zjc
Zjd
Zje
Zjf
Zjg
Zjh
Zji
Zjj
Zjk
Zjl
Zjr
Diebert Spring
Kwichup Spring
A
A'
B
B'
MAP SYMBOLS
Unit contact, dashed where indefinite or inferred
Fault, dashed where indefinite or inferred. Ball and bar (on down-dropped block) indicate apparent normal separation, teeth (on upthrown block) indicate apparent thrust separation.
Fold: overturned syncline (axial trace is approximately located)
Strike and dip of sedimentary bedding, bar and tick indicate dip direction and dip of fracture cleavage
Strike and dip of overturned sedimentary bedding
Elevation (m)
1500
1400
1300
1200
1100
a 125 m
b 160 m
c 50 m
d 300 m
e 280 m
f
Horizontal = Vertical scale
1600
1500
1400
1300
g 135 m
h 60 m
i 55 m
j 190 m
k 95 m
l 60 m
r
Horizontal = Vertical scale

Figure 3

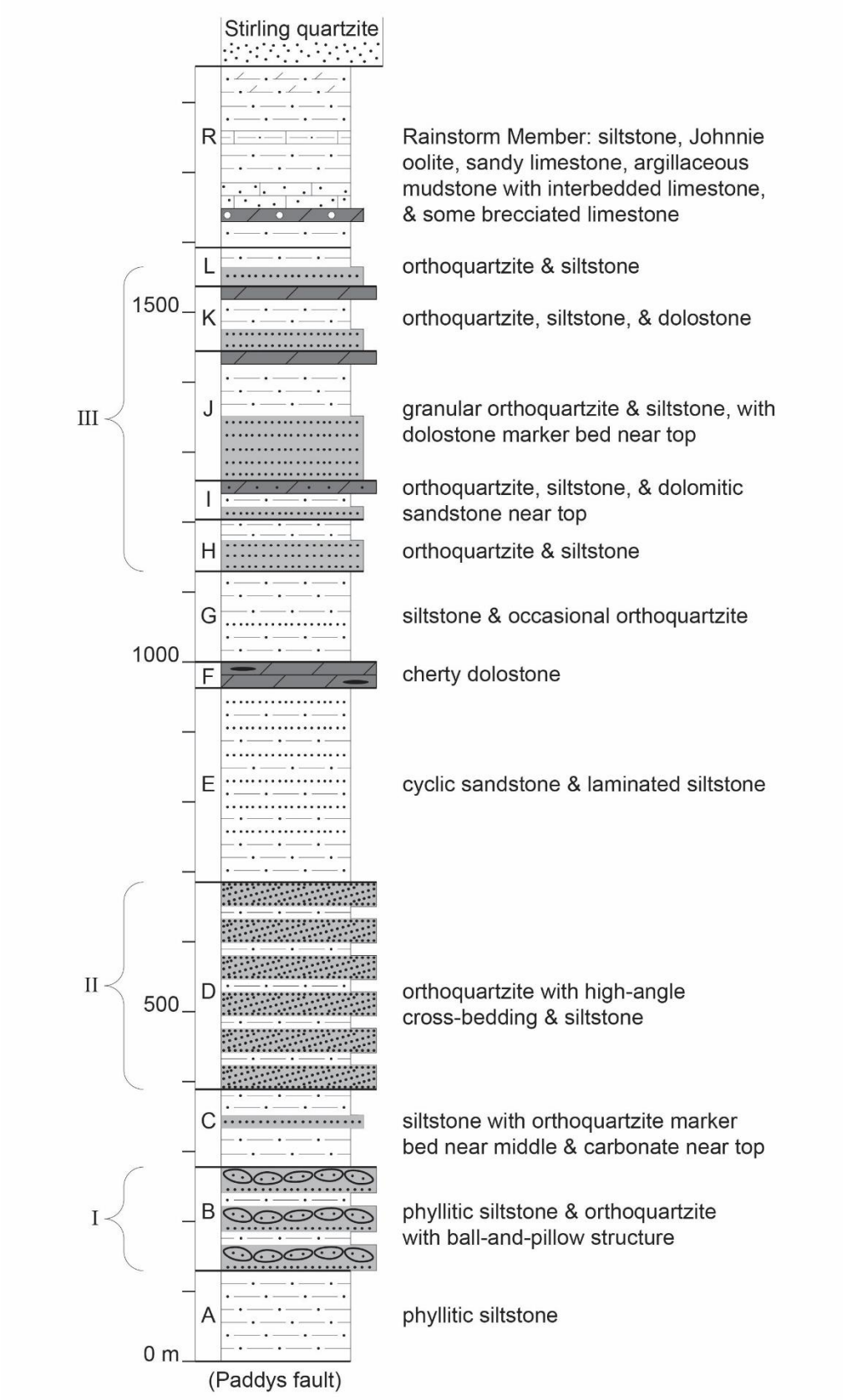
Stirling quartzite
R
Rainstorm Member: siltstone, Johnnie oolite, sandy limestone, argillaceous mudstone with interbedded limestone, & some brecciated limestone
L
orthoquartzite & siltstone
1500
K
orthoquartzite, siltstone, & dolostone
III
J
granular orthoquartzite & siltstone, with dolostone marker bed near top
I
orthoquartzite, siltstone, & dolomitic sandstone near top
H
orthoquartzite & siltstone
G
siltstone & occasional orthoquartzite
1000
F
cherty dolostone
E
cyclic sandstone & laminated siltstone
II
500
D
orthoquartzite with high-angle cross-bedding & siltstone
C
siltstone with orthoquartzite marker bed near middle & carbonate near top
I
B
phyllitic siltstone & orthoquartzite with ball-and-pillow structure
A
phyllitic siltstone
0 m
(Paddys fault)

Figure 4

Figure 5

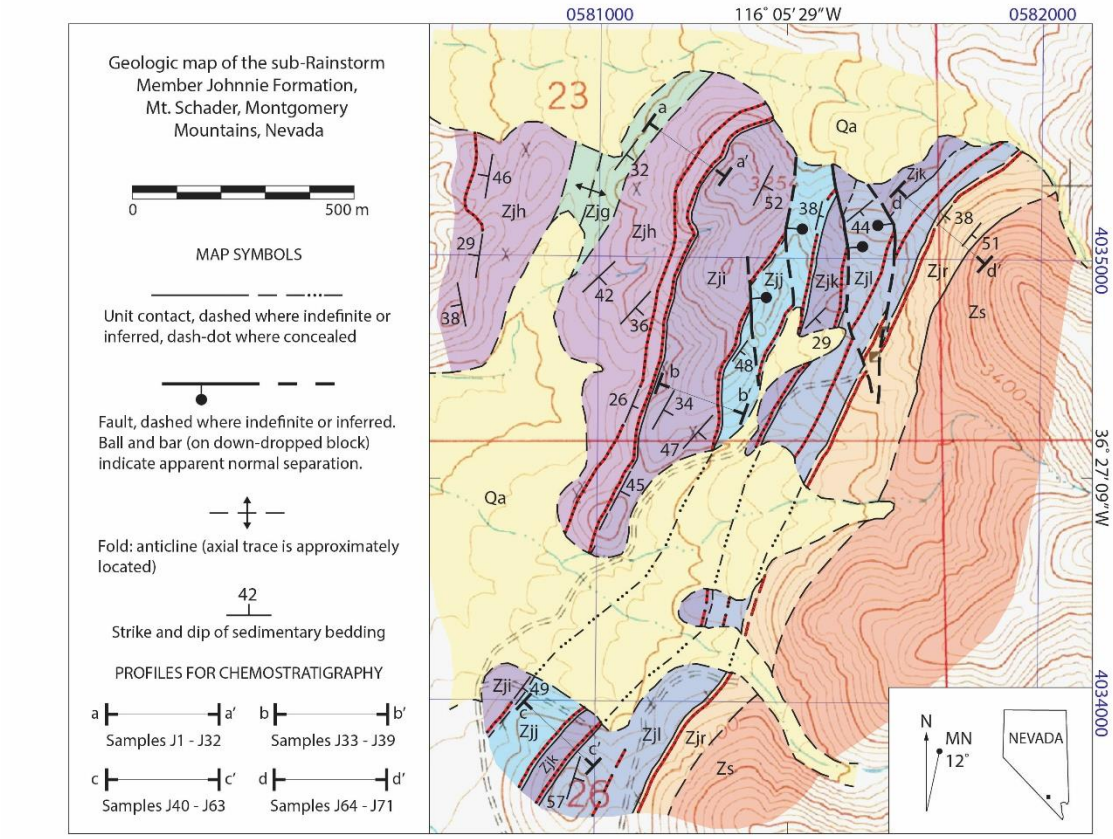
Geologic map of the sub-Rainstorm Member Johnnie Formation, Mt. Schader, Montgomery Mountains, Nevada
0
500 m
MAP SYMBOLS
Unit contact, dashed where indefinite or inferred, dash-dot where concealed
Fault, dashed where indefinite or inferred. Ball and bar (on down-dropped block) indicate apparent normal separation.
Fold: anticline (axial trace is approximately located)
42
Strike and dip of sedimentary bedding
PROFILES FOR CHEMOSTRATIGRAPHY
a a' Samples J1 - J32
b b' Samples J33 - J39
c c' Samples J40 - J63
d d' Samples J64 - J71
0581000
116° 05' 29"W
0582000
4035000
36° 27' 09"W
4034000
Qa
Zjh
Zjg
Zji
Zjj
Zjk
Zjl
Zjr
Zs
23
28
N
MN
12°
NEVADA

Figure 6

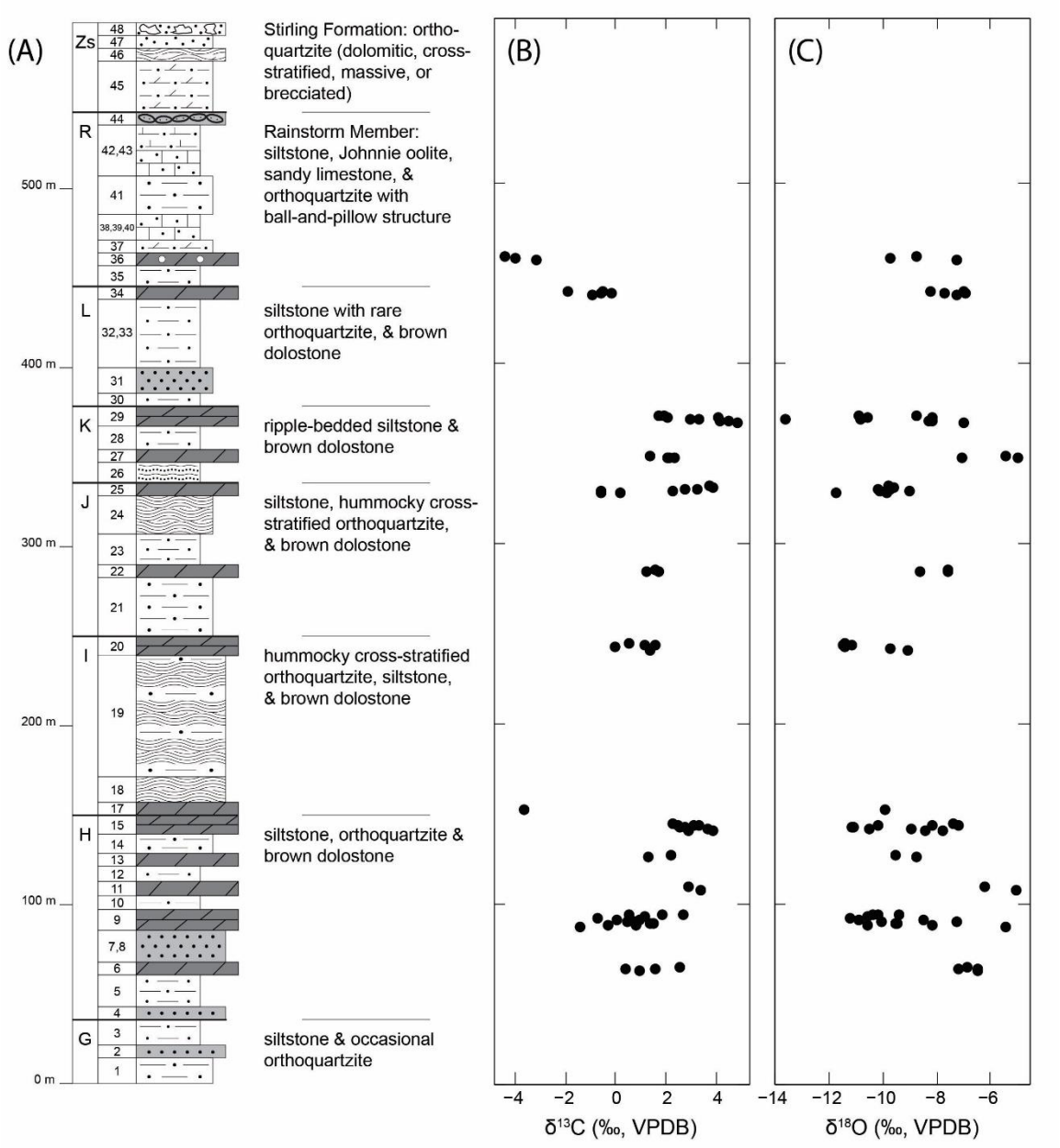
(A)
(B)
(C)
Zs
R
L
K
J
I
H
G
48
47
46
45
44
42,43
41
38,39,40
37
36
35
34
32,33
31
30
29
28
27
26
25
24
23
22
21
20
19
18
17
15
14
13
12
11
10
9
7,8
6
5
4
3
2
1
500 m
400 m
300 m
200 m
100 m
0 m
Stirling Formation: ortho-quartzite (dolomitic, cross-stratified, massive, or brecciated)
Rainstorm Member: siltstone, Johnnie oolite, sandy limestone, & orthoquartzite with ball-and-pillow structure
siltstone with rare orthoquartzite, & brown dolostone
ripple-bedded siltstone & brown dolostone
siltstone, hummocky cross-stratified orthoquartzite, & brown dolostone
hummocky cross-stratified orthoquartzite, siltstone, & brown dolostone
siltstone, orthoquartzite & brown dolostone
siltstone & occasional orthoquartzite
−4
−2
0
2
4
δ13C (‰, VPDB)
−14
−12
−10
−8
−6
δ18O (‰, VPDB)

Figure 7

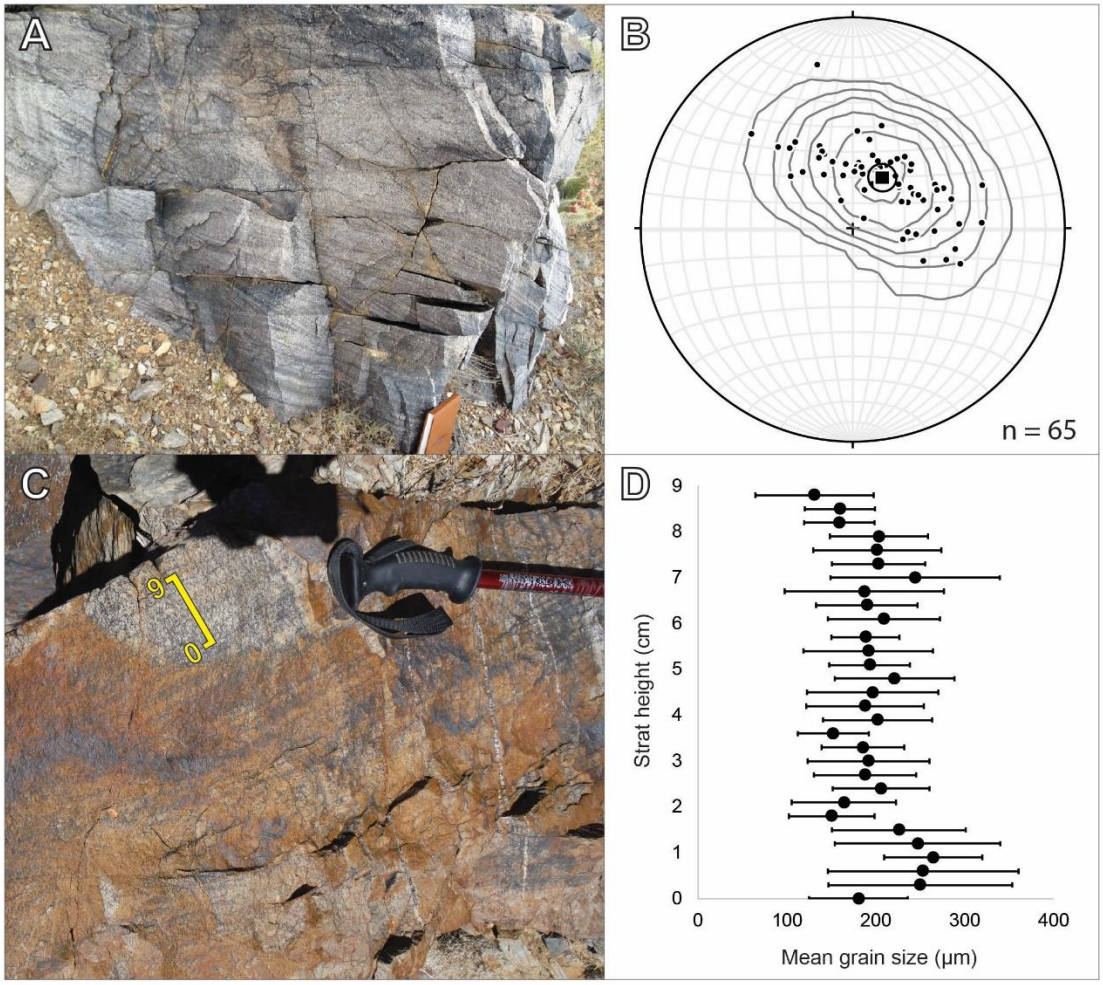
A
B
n = 65
C
9
0
D
Strat height (cm)
0
1
2
3
4
5
6
7
8
9
0
100
200
300
400
Mean grain size (μm)

Figure 8

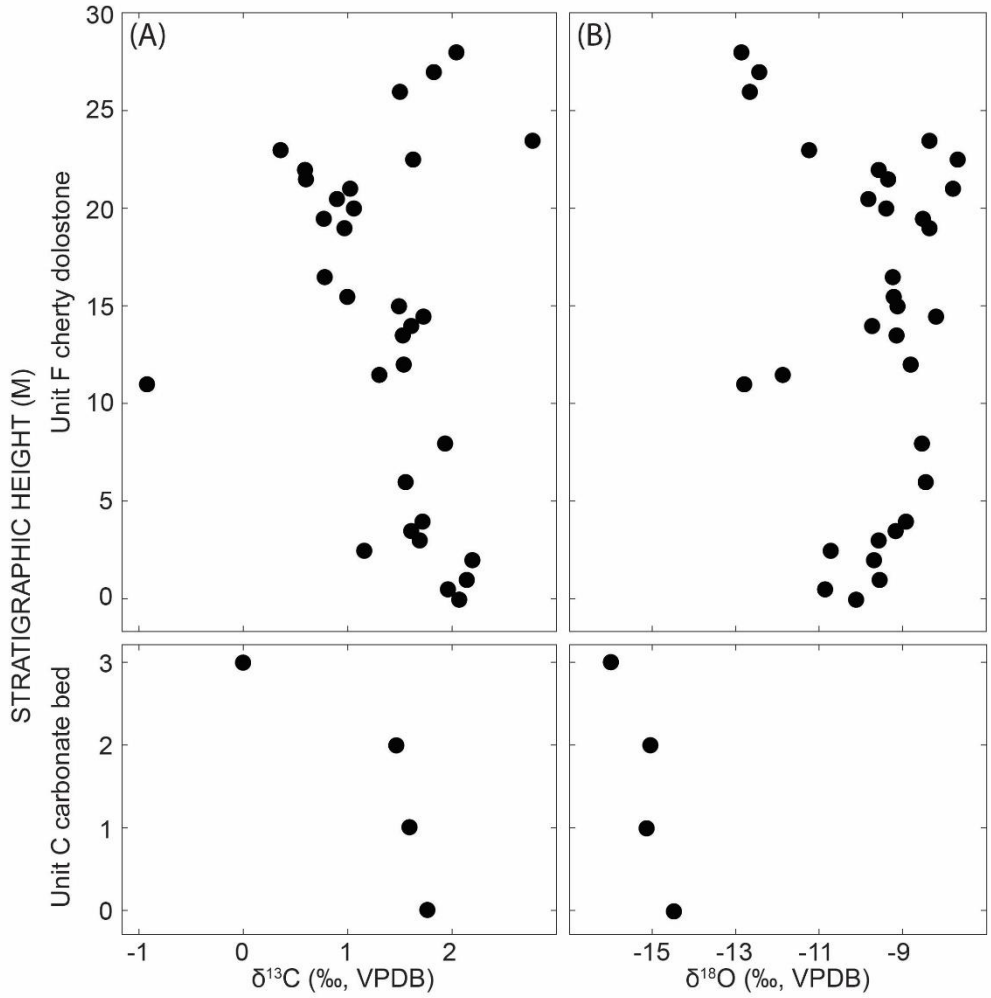
(A)
(B)
STRATIGRAPHIC HEIGHT (M)
Unit F cherty dolostone
Unit C carbonate bed
30
25
20
15
10
5
0
3
2
1
0
-1
0
1
2
-15
-13
-11
-9
δ13C (‰, VPDB)
δ18O (‰, VPDB)

Figure 9

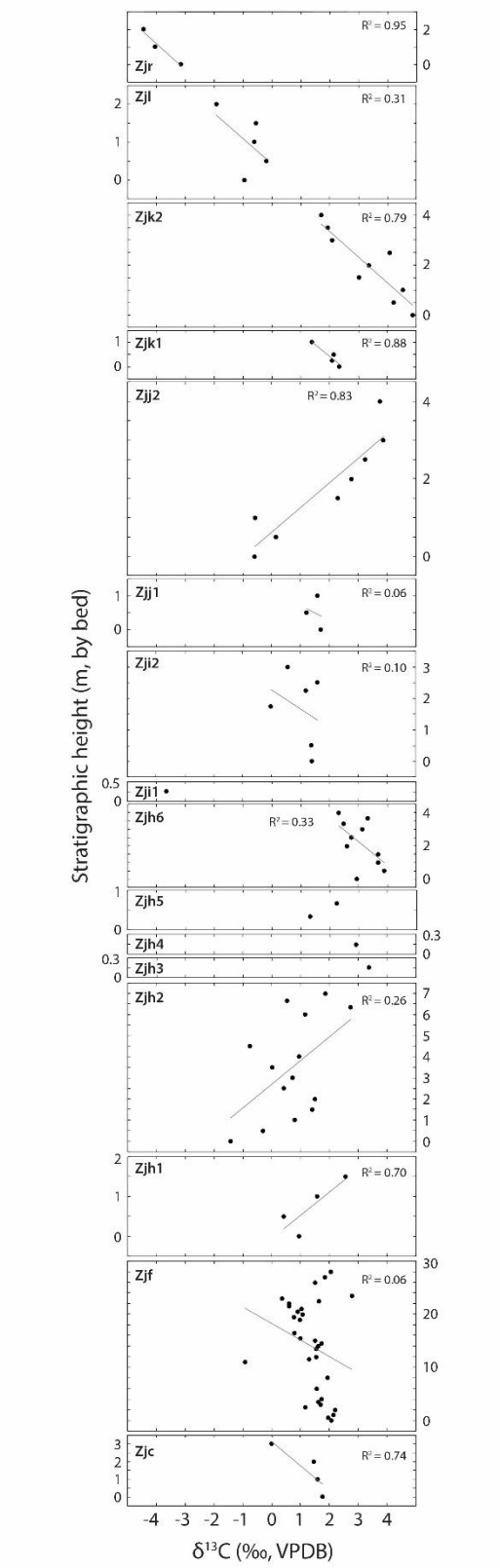
Zjr
R² = 0.95
Zjl
R² = 0.31
Zjk2
R² = 0.79
Zjk1
R² = 0.88
Zjj2
R² = 0.83
Zjj1
R² = 0.06
Zji2
R² = 0.10
Zji1
Zjh6
R² = 0.33
Zjh5
Zjh4
Zjh3
Zjh2
R² = 0.26
Zjh1
R² = 0.70
Zjf
R² = 0.06
Zjc
R² = 0.74
Stratigraphic height (m, by bed)
δ13C (‰, VPDB)

Figure 10

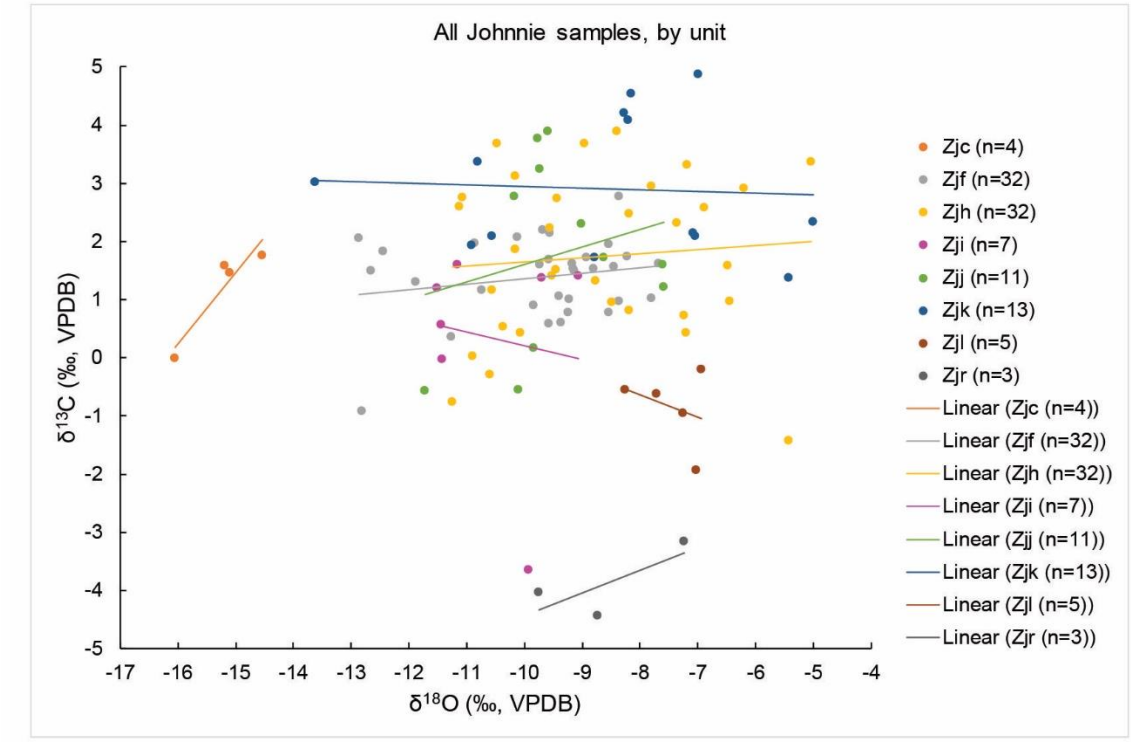
All Johnnie samples, by unit
δ13C (‰, VPDB)
δ18O (‰, VPDB)
5
4
3
2
1
0
-1
-2
-3
-4
-5
-17
-16
-15
-14
-13
-12
-11
-10
-9
-8
-7
-6
-5
-4
Zjc (n=4)
Zjf (n=32)
Zjh (n=32)
Zji (n=7)
Zjj (n=11)
Zjk (n=13)
Zjl (n=5)
Zjr (n=3)
Linear (Zjc (n=4))
Linear (Zjf (n=32))
Linear (Zjh (n=32))
Linear (Zji (n=7))
Linear (Zjj (n=11))
Linear (Zjk (n=13))
Linear (Zjl (n=5))
Linear (Zjr (n=3))

Figure 11

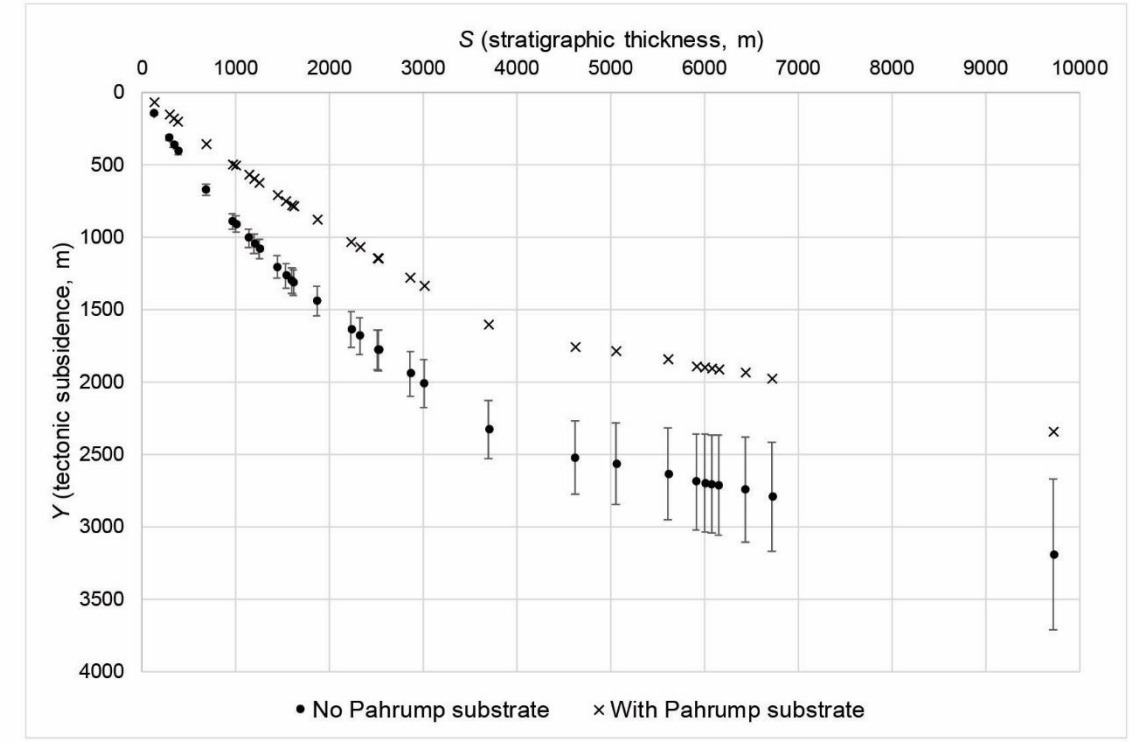
S (stratigraphic thickness, m)
0
1000
2000
3000
4000
5000
6000
7000
8000
9000
10000
Y (tectonic subsidence, m)
0
500
1000
1500
2000
2500
3000
3500
4000
• No Pahrump substrate
× With Pahrump substrate

Figure 12

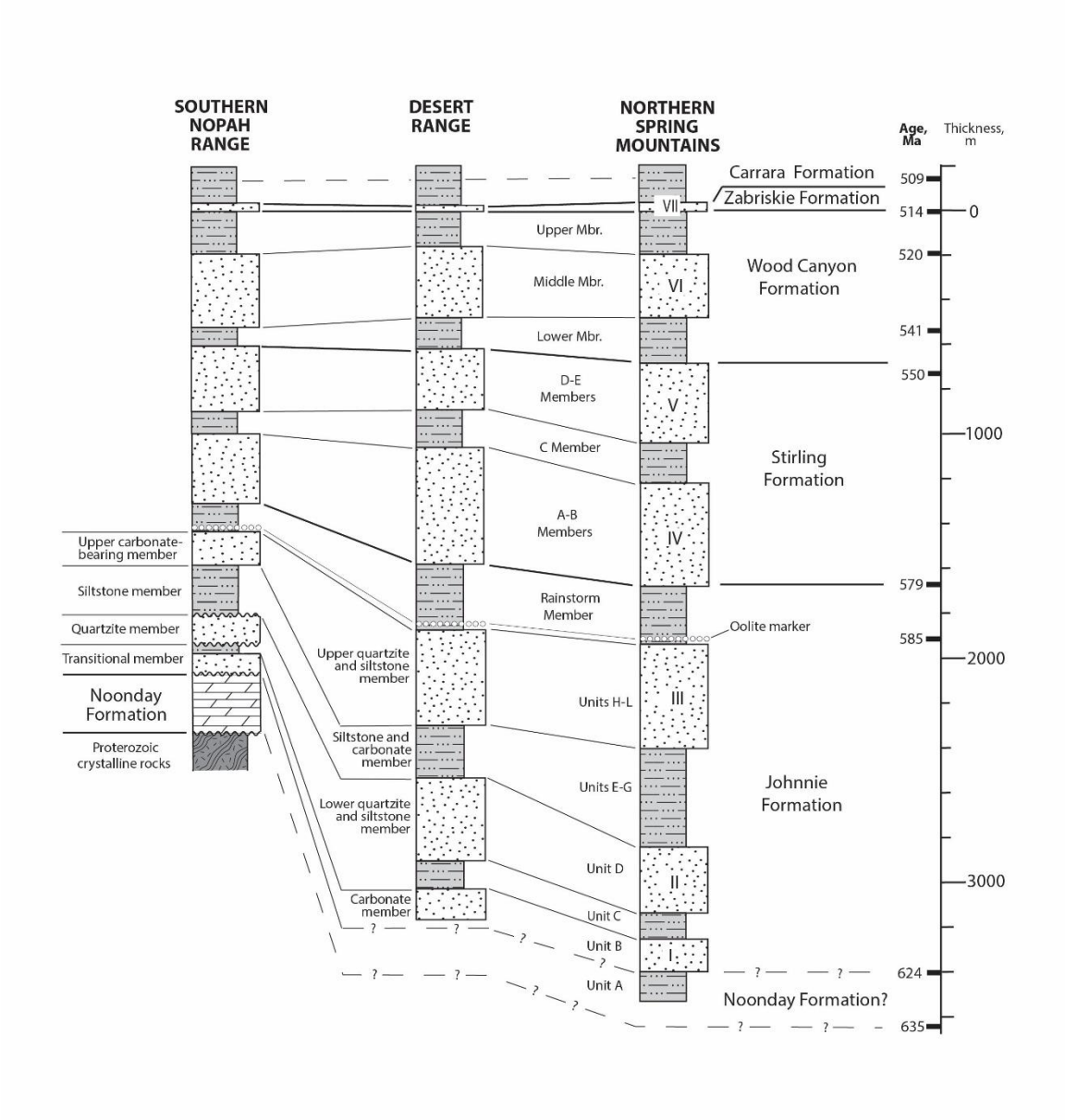
SOUTHERN NOPAH RANGE
DESERT RANGE
NORTHERN SPRING MOUNTAINS
Age, Ma
Thickness, m
Carrara Formation
Zabriskie Formation
Upper Mbr.
Middle Mbr.
Lower Mbr.
D-E Members
C Member
A-B Members
Rainstorm Member
Oolite marker
Upper quartzite and siltstone member
Siltstone and carbonate member
Lower quartzite and siltstone member
Carbonate member
Units H-L
Units E-G
Unit D
Unit C
Unit B
Unit A
Wood Canyon Formation
Stirling Formation
Johnnie Formation
Noonday Formation?
VII
VI
V
IV
III
II
I
Upper carbonate-bearing member
Siltstone member
Quartzite member
Transitional member
Noonday Formation
Proterozoic crystalline rocks
509
514
520
541
550
579
585
624
635
0
1000
2000
3000

Figure 13

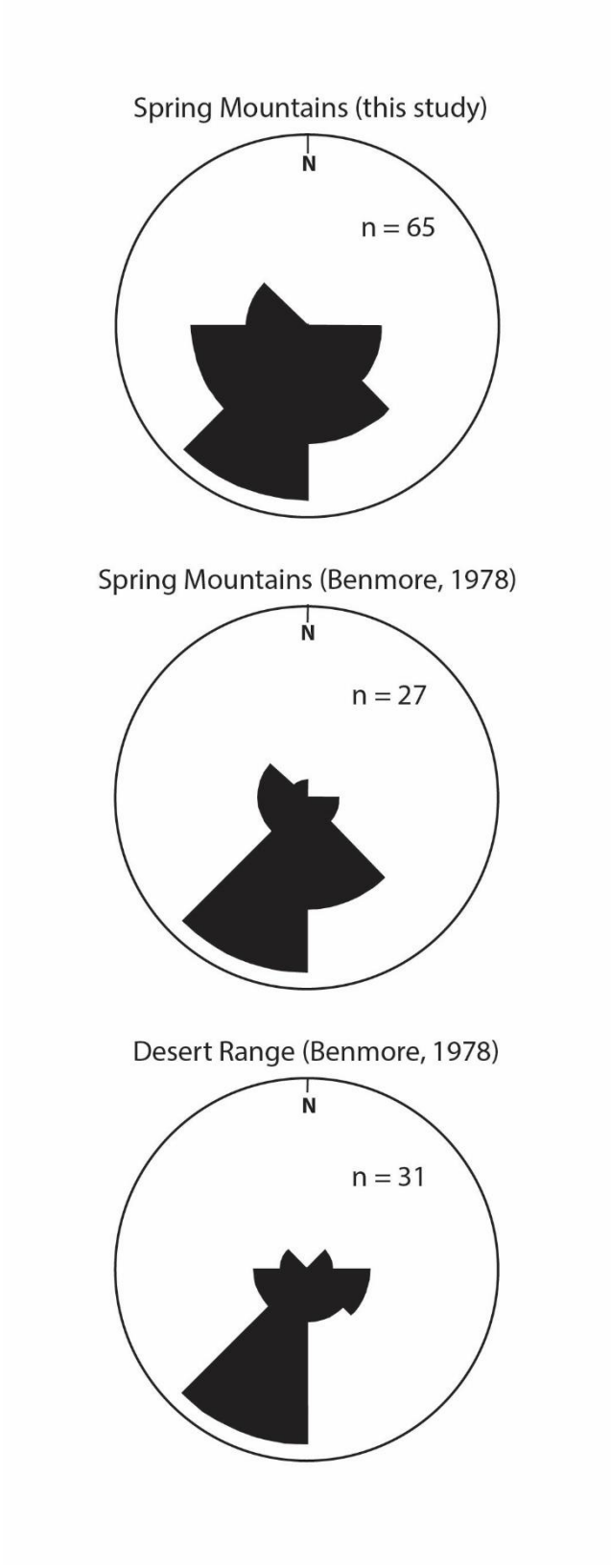
Spring Mountains (this study)
N
n = 65
Spring Mountains (Benmore, 1978)
N
n = 27
Desert Range (Benmore, 1978)
N
n = 31

Figure 14

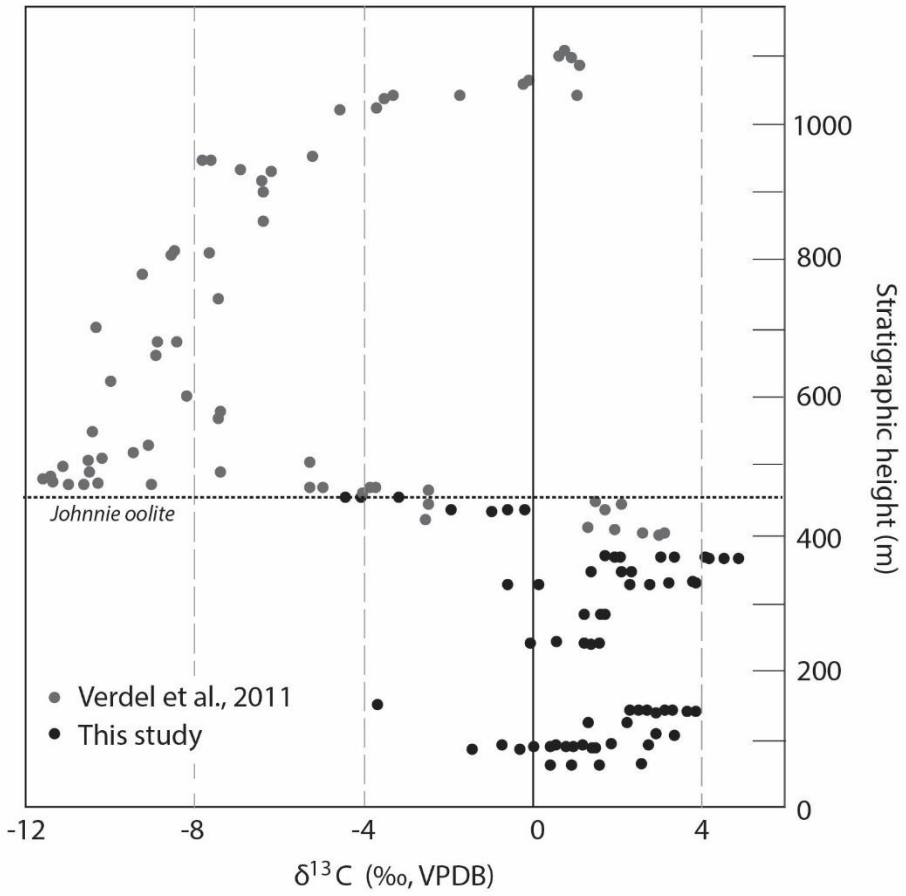
1000
800
600
400
200
0
Stratigraphic height (m)
Johnnie oolite
Verdel et al., 2011
This study
-12
-8
-4
0
4
δ13C (‰, VPDB)

Figure 15

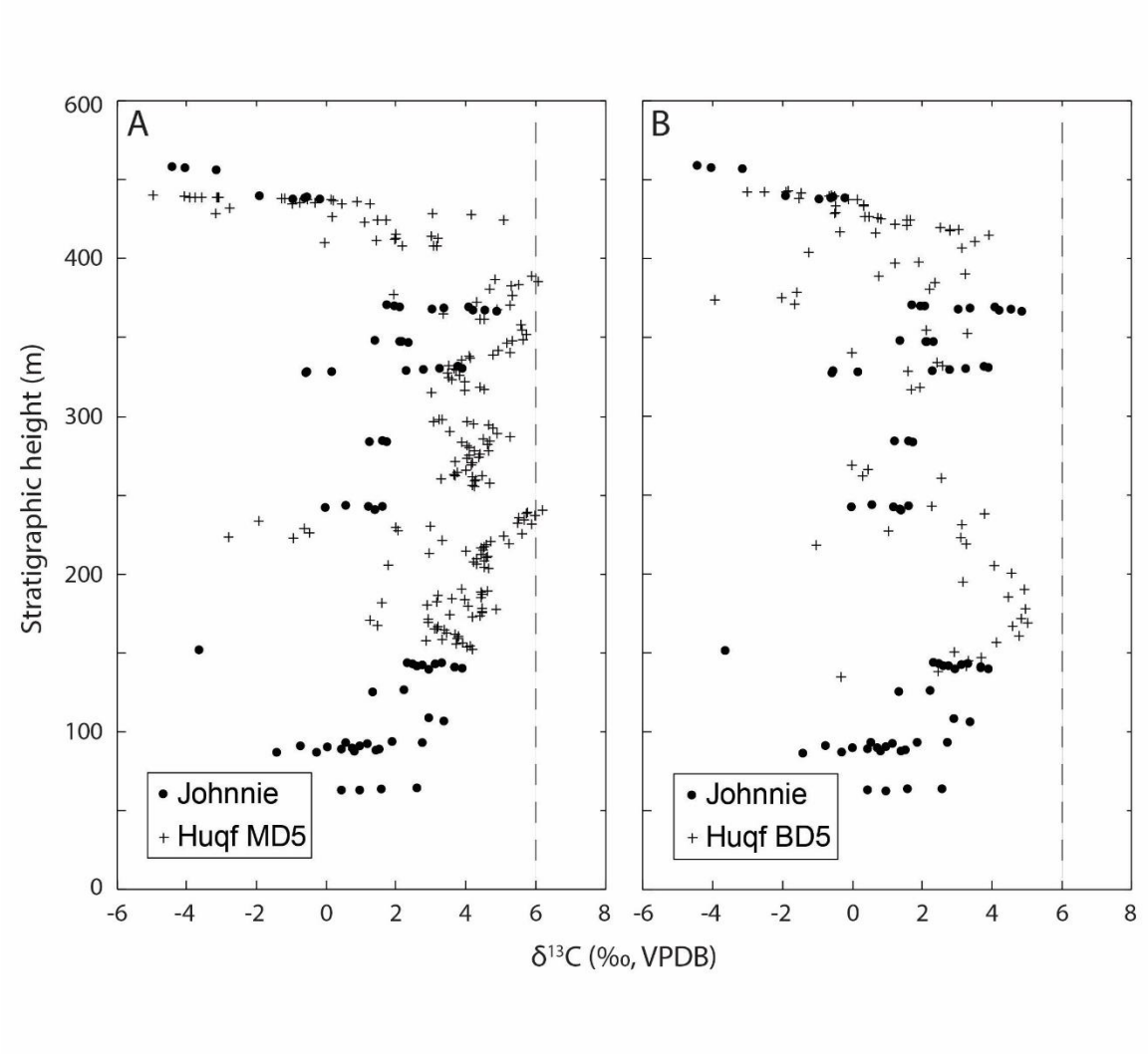
A
B
Stratigraphic height (m)
600
400
300
200
100
0
-6
-4
-2
0
2
4
6
8
Johnnie
Huqf MD5
Johnnie
Huqf BD5
δ13C (‰, VPDB)

Figure 16

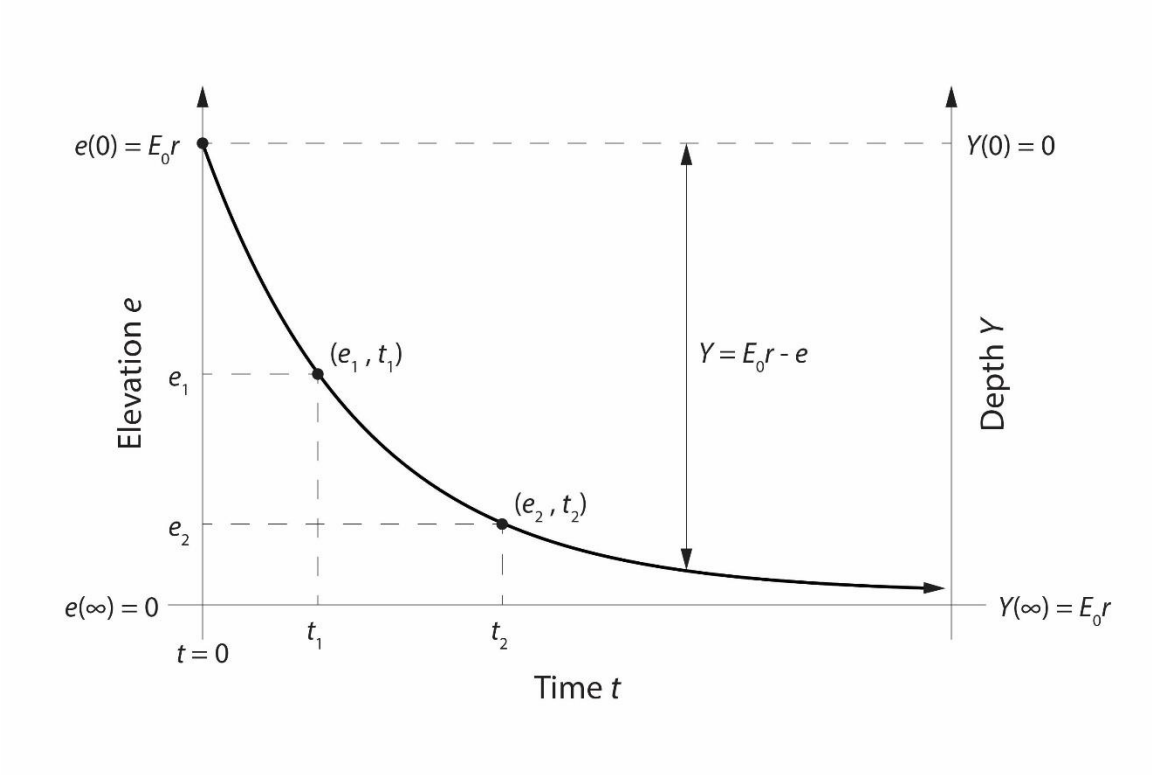
e(0) = E0r
Y(0) = 0
Elevation e
Depth Y
(e1 , t1)
Y = E0r - e
e1
(e2 , t2)
e2
e(∞) = 0
Y(∞) = E0r
t = 0
t1
t2
Time t

Figure 17

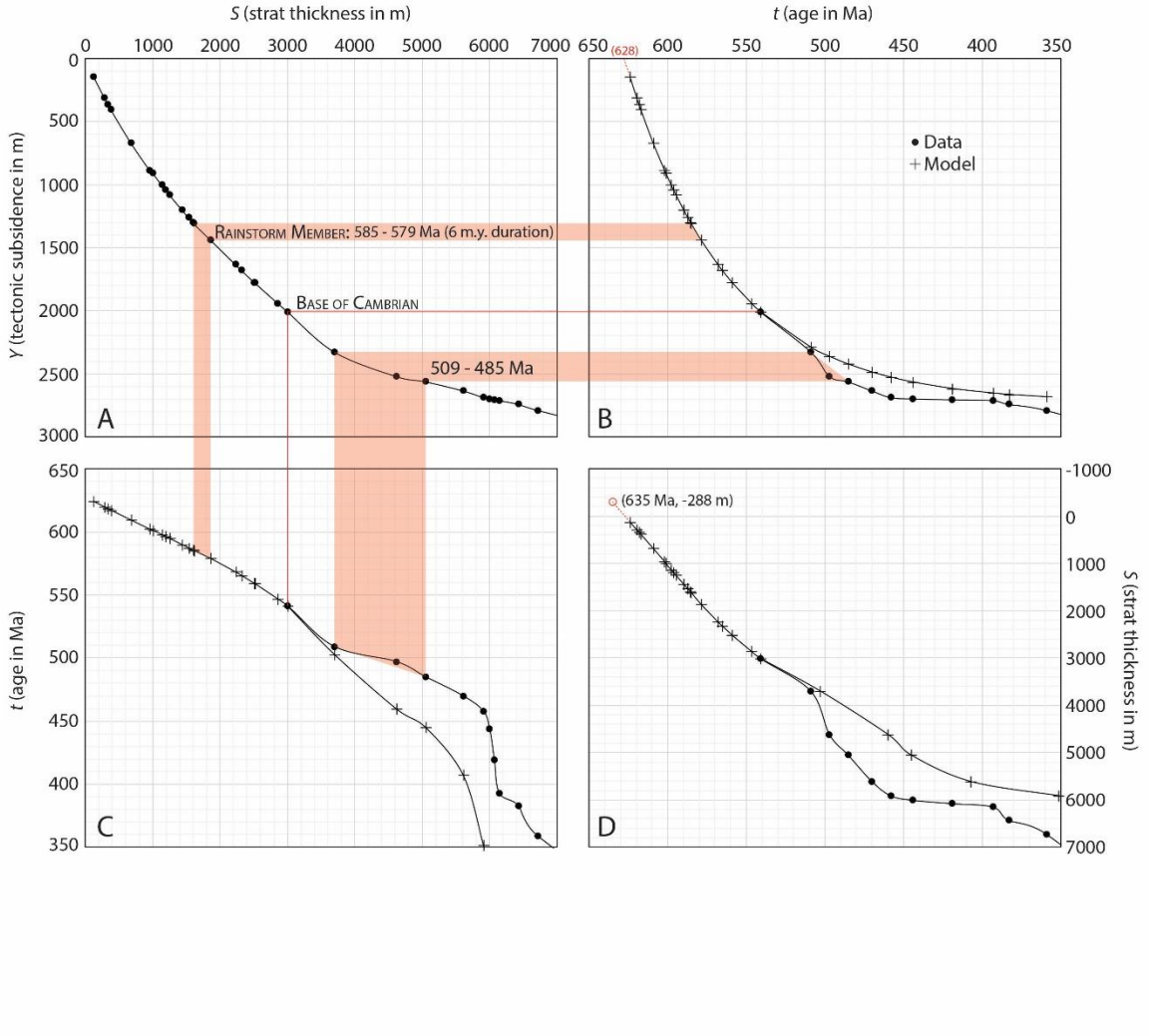
S (strat thickness in m)
t (age in Ma)
Y (tectonic subsidence in m)
RAINSTORM MEMBER: 585 - 579 Ma (6 m.y. duration)
BASE OF CAMBRIAN
509 - 485 Ma
• Data
+ Model
(628)
(635 Ma, -288 m)
A
B
C
D

Figure 18

SUPPLEMENTAL ITEMS

Figure Captions

Figure S1 (p. 114): (A) Google Earth image looking c. 60° down-dip to the east along section B - B' in Figure 3, showing traces of mapped unit boundaries (dashed lines) for units E through L and the Rainstorm Member, using unit designations from the Appendix. Width of view at level of Zji is c. 400 m. (B) Google Earth image looking c. 40° down-dip to the east along section A - A' in Figure 3, showing traces of mapped unit boundaries for units A through I. Width of view at unit D/E boundary is c. 1200 m.

Figure S2 (pp. 115-130): Plots of $\delta^{13}C$ and $\delta^{18}O$ versus stratigraphic position with side-by-side cross plots of $\delta^{18}O$ versus $\delta^{13}C$, for each individual carbonate interval designated in Figure 10 of the main text.

Figure S3 (pp. 131-138): Chemostratigraphic profiles comparing carbon isotopic data from the Johnnie Formation from unit H through the lowermost Rainstorm Member (ending at the top of the oolite marker bed, Figure 7) with profiles from the Buah Dome (BD1, BD4, BD5, BD6); Khufai Dome (KDW); and Mukhaibah Dome (MD5, MD6, MDE) areas of Oman (Osburn et al., 2015). Vertical axis shows measured stratigraphic height, from the Mt. Schader section, in all profiles.

Figure S4 (p. 139): Plot showing tectonic subsidence data and models as a function of age (small points and curves, respectively), showing the effect of varying sediment grain density on estimates for the age and duration of the Shuram excursion (large points). Red: high-density; blue: intermediate density; green: low density.

Figure S5 (p. 140): Plot showing tectonic subsidence data and models as a function of age (points and curves, respectively), showing the effect of varying the exponential time constant τ. Models are fit to the 541 Ma data point and assume intermediate sediment grain density.

Figure S6 (p. 141): Plot showing calculated tectonic subsidence Y as a function of observed stratigraphic thickness S for the backstripping and delithification model that includes a hypothetical Pahrump Group substrate below the lowest exposed Johnnie Formation strata (unit A) in the Spring Mountains section. Error bars show range of estimates of Y produced by a ±5 % variation in sediment grain density.

Tables

Table S1: Chemostratigraphy results						
Unit	Sample	Stratigraphic position (m)	Bed position (m)	$\delta^{13}C$ (‰, VPDB)	$\delta^{18}O$ (‰, VPDB)	Notes
Zjc collection site* located at 36°30'35.05" N, 116°00'58.55" W (within rectangle labeled "Locality A" in Figure 2A)						
Zjc	J72	-	0.00	1.8	-14.5	
	J73	-	1.00	1.6	-15.2	
	J74	-	2.00	1.5	-15.1	
	J75	-	3.00	0.0	-16.0	
Zjf collected along a transect beginning at 36°28'53.96" N, 116°01'30.13" W; ending at 36°28'53.79" N, 116°01'28.97" W (at the beginning of cross section line B-B' in Figure 3: Johnnie Wash geologic map)						

Zjf	J76	-	0.00	2.1	-10.1	
	J77	-	0.50	2.0	-10.9	
	J78	-	1.00	2.1	-9.6	
	J79	-	2.00	2.2	-9.7	
	J80	-	2.50	1.2	-10.7	
	J81	-	3.00	1.7	-9.6	
	J82	-	3.50	1.6	-9.2	
	J83	-	4.00	1.7	-8.9	
	J84	-	6.00	1.6	-8.4	
	J85	-	8.00	1.9	-8.5	
	J86	-	11.00	-0.9	-12.8	
	J87	-	11.50	1.3	-11.9	
	J88	-	12.00	1.5	-8.8	
	J89	-	13.50	1.5	-9.2	
	J90	-	14.00	1.6	-9.7	
	J91	-	14.50	1.7	-8.2	
	J92	-	15.00	1.5	-9.1	
	J93	-	15.50	1.0	-9.2	
	J94	-	16.50	0.8	-9.2	
	J95	-	19.00	1.0	-8.4	
	J96	-	19.50	0.8	-8.5	
	J97	-	20.00	1.1	-9.4	
	J98	-	20.50	0.9	-9.8	
	J99	-	21.00	1.0	-7.8	
	J100	-	21.50	0.6	-9.4	
	J101	-	22.00	0.6	-9.6	
	J102	-	22.50	1.6	-7.7	
	J103	-	23.00	0.4	-11.3	
	J104	-	23.50	2.8	-8.4	
	J105	-	26.00	1.5	-12.7	
	J106	-	27.00	1.8	-12.4	
	J107	-	28.00	2.0	-12.9	
Transect a-a’ in Figure 6: Mt. Schader geologic map (begins at 36°27'31.70" N, 116°05'43.38" W; ends at 36°27'30.30" N, 116°05'33.92" W)						
Zjh	J1	63.00	0.00	1.0	-6.5	
	J2	63.50	0.50	0.4	-7.2	
	J3	64.00	1.00	1.6	-6.5	
	J4	64.50	1.50	2.6	-6.9	
	J5	87.00	0.00	-1.4	-5.4	
	J6	87.50	0.50	-0.3	-10.6	
	J7	88.00	1.00	0.8	-8.2	
	J8	88.50	1.50	1.4	-9.5	
	J9	89.00	2.00	1.5	-9.5	
	J10	89.50	2.50	0.4	-10.1	
	J11	90.00	3.00	0.7	-7.2	
	J12	90.50	3.50	0.0	-10.9	
	J13	91.00	4.00	1.0	-8.5	
	J14	91.50	4.50	-0.8	-11.2	
	J15	93.00	6.00	1.2	-10.6	
	J16	93.33	6.33	2.7	-9.4	
	J17	93.66	6.66	0.5	-10.4	

	J18	94.00	7.00	1.9	-10.2	
	J19	107.00	-	3.4	-5.0	
	J20	109.00	-	2.9	-6.2	
	J21	125.75	-	1.3	-8.8	
	J22	126.75	-	2.2	-9.6	
	J23	140.00	0.00	2.9	-7.8	
	J24	140.50	0.50	3.9	-8.4	
	J25	141.00	1.00	3.7	-9.0	
	J26	141.50	1.50	3.7	-10.5	
	J27	142.00	2.00	2.6	-11.1	
	J28	142.50	2.50	2.7	-11.1	
	J29	143.00	3.00	3.1	-10.2	
	J30	143.33	3.33	2.5	-8.2	
	J31	143.66	3.66	3.3	-7.2	
	J32	144.00	4.00	2.3	-7.4	
Transect b-b’ in Figure 6: Mt. Schader geologic map (begins at 36°27'18.37" N, 116°05'39.60" W; ends at 36°27'17.54" N, 116°05'33.18" W)						
Zji	J33	152.00	-	-3.7	-9.9	
	J34	241.00	0.00	1.4	-9.1	
	J35	241.50	0.50	1.4	-9.7	
	J36	242.75	1.75	0.0	-11.4	
	J37	243.25	2.25	1.2	-11.5	
	J38	243.50	2.50	1.6	-11.2	
	J39	244.00	3.00	0.6	-11.4	
Transect c-c’ in Figure 6: Mt. Schader geologic map (begins at 36°26'50.85" N, 116°05'53.02" W; ends at 36°26'45.94" N, 116°05'46.85" W)						
Zjj	J40	284.00	0.00	1.7	-8.6	
	J41	284.50	0.50	1.2	-7.6	
	J42	285.00	1.00	1.6	-7.6	
	J43	328.00	0.00	-0.6	-11.7	
	J44	328.50	0.50	0.2	-9.8	
	J45	329.00	1.00	-0.6	-10.1	
	J46	329.50	1.50	2.3	-9.0	
	J47	330.00	2.00	2.8	-10.2	
	J48	330.50	2.50	3.2	-9.7	
	J49	331.00	3.00	3.9	-9.6	
	J50	332.00	4.00	3.8	-9.8	
Zjk	J51	347.50	0.00	2.3	-5.0	
	J52	347.75	0.25	2.1	-7.0	
	J53	348.00	0.50	2.1	-7.1	
	J54	348.50	1.00	1.4	-5.4	
	J55	367.00	0.00	4.9	-7.0	
	J56	367.50	0.50	4.2	-8.3	
	J57	368.00	1.00	4.5	-8.2	
	J58	368.50	1.50	3.0	-13.6	
	J59	369.00	2.00	3.4	-10.8	
	J60	369.50	2.50	4.1	-8.2	
	J61	370.00	3.00	2.1	-10.6	
	J62	370.50	3.50	1.9	-10.9	
	J63	371.00	4.00	1.7	-8.8	

Transect d-d' in Figure 6: Mt. Schader geologic map (begins at 36°27'28.71" N, 116°05'16.42" W; ends at 36°27'24.47" N, 116°05'10.44" W)						
Zjl	J64	438.00	0.00	-1.0	-7.3	
	J65	438.50	0.50	-0.2	-6.9	
	J66	439.00	1.00	-0.6	-7.7	
	J67	439.50	1.50	-0.6	-8.3	
	J68	440.00	2.00	-1.9	-7.0	
Zjr	J69	457.00	0.00	-3.2	-7.2	Johnnie oolite
	J70	458.00	1.00	-4.0	-9.8	
	J71	459.00	2.00	-4.4	-8.7	
*All locations recorded using GPS with the WGS84 coordinate system						

Table S2: All ages modeled using hypothetical Pahrump Group substrate										
		Model ages (Ma)								
		τ = 55 my			τ = 60 my			τ = 65 my		
Unit	Age (Ma)	Min	Int	Max	Min	Int	Max	Min	Int	Max
MzPzco	~243	-	-	-	-	-	-	-	-	-
Ddg	359	-	-	-	-	-	-	-	-	-
Dn	383	-	-	-	-	-	-	-	-	-
Dl	393	342	327	288	324	307	265	306	288	242
Sl	419	364	349	310	348	332	289	331	314	268
Oes	444	378	365	318	363	349	298	348	333	278
Oe	458	393	379	332	380	364	313	366	350	294
Op1	470	436	429	413	427	419	401	417	409	390
OЄn1	485	468	460	440	461	452	431	454	445	422
Єbk1	497	481	470	442	475	464	433	470	457	424
Єc1	509	513	507	492	511	504	488	508	501	483
ЄZwc1	541	541	541	541	541	541	541	541	541	541
Zse	-	545	546	547	546	546	548	546	547	548
Zsd	-	554	556	560	556	558	561	557	559	563
Zsc	-	554	556	560	556	558	562	557	559	563
Zsb	-	559	562	566	561	563	568	562	565	571
Zsa	-	561	564	569	563	566	571	565	568	574
Zjr2	-	569	572	579	571	575	582	574	578	585
Zjr1	-	573	577	584	576	580	588	579	584	592
Zjl	-	574	577	584	577	581	588	580	584	592
Zjk	-	575	579	586	578	582	590	581	586	594
Zjj	-	577	581	588	580	584	592	583	588	596
Zji	-	580	585	592	584	589	597	587	592	602
Zjh	-	581	586	594	585	590	598	588	594	603
Zjg	-	582	587	595	586	591	600	590	595	605
Zjf	-	584	589	598	588	594	603	592	598	608
Zje	-	585	590	598	589	594	603	593	599	608
Zjd	-	590	595	604	594	600	609	598	605	615
Zjc2	-	594	600	609	599	605	616	604	611	622
Zjc1	-	595	601	610	600	606	617	605	612	623
Zjb	-	596	602	611	601	607	618	606	613	624
Zja	-	598	604	614	603	610	621	609	616	627
Zjt	-	600	606	616	605	612	623	611	618	630
Zkpw	635	602	608	618	607	614	625	613	620	632
Zkpth	-	603	609	620	609	615	627	614	622	634
Zkpmg	-	604	610	621	610	617	628	615	623	635
Zkpsmp	-	605	612	622	611	618	630	617	625	637
Zkpls	-	608	615	626	615	622	634	621	629	641
Zbs	-	614	621	633	621	628	641	627	636	649
Zhs	<787	616	623	635	623	631	643	630	638	652
Ycs2	>1087	619	627	638	626	634	647	633	642	656
Ycs1	-	621	629	641	629	637	650	636	645	659
(base)	-	628	637	649	636	645	659	644	654	669

Figures

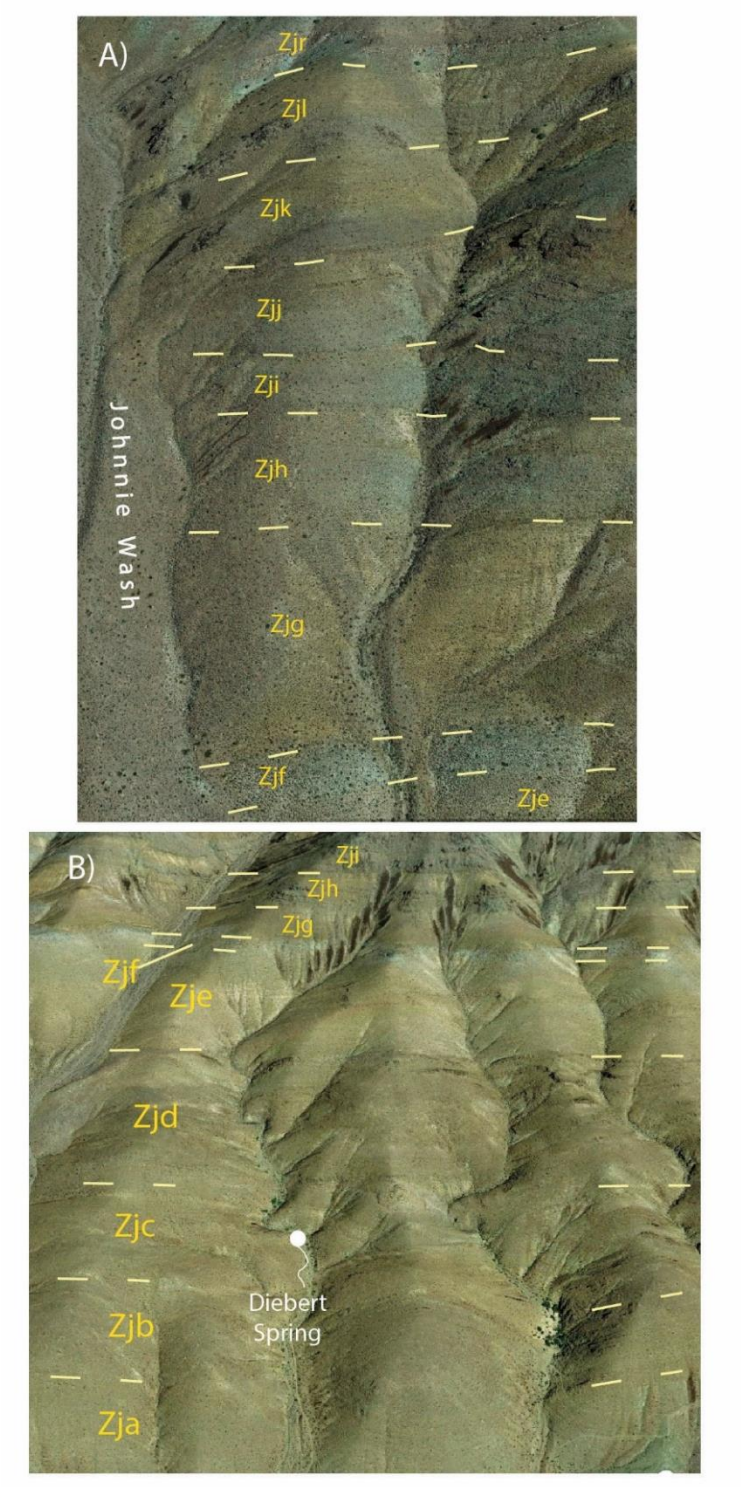

Figure S1

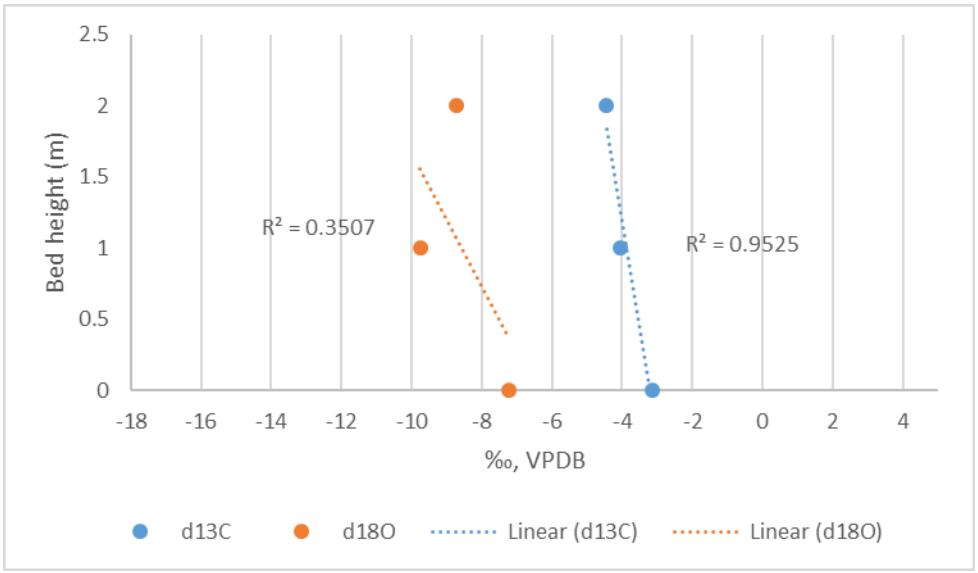

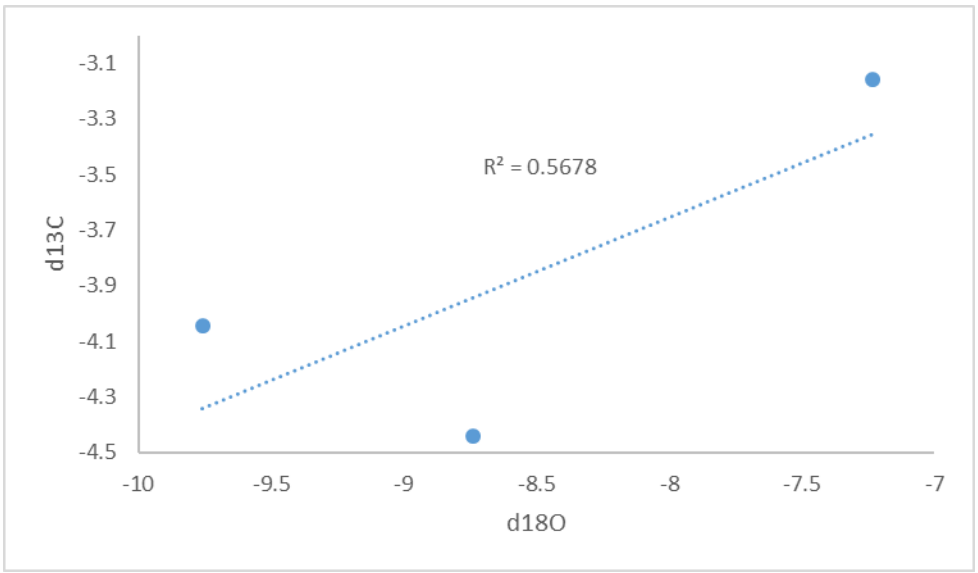

Figure S2: Zjr (j69-71)

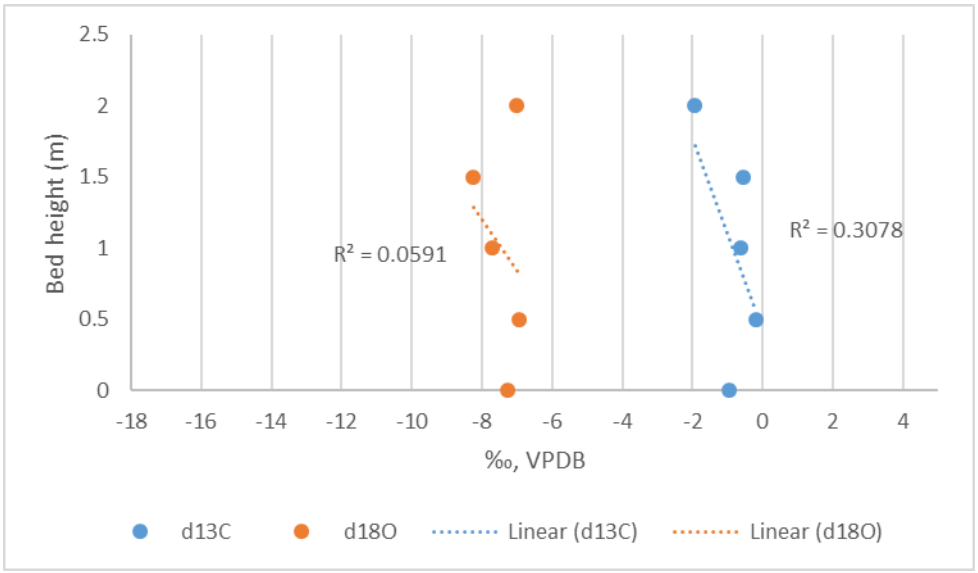

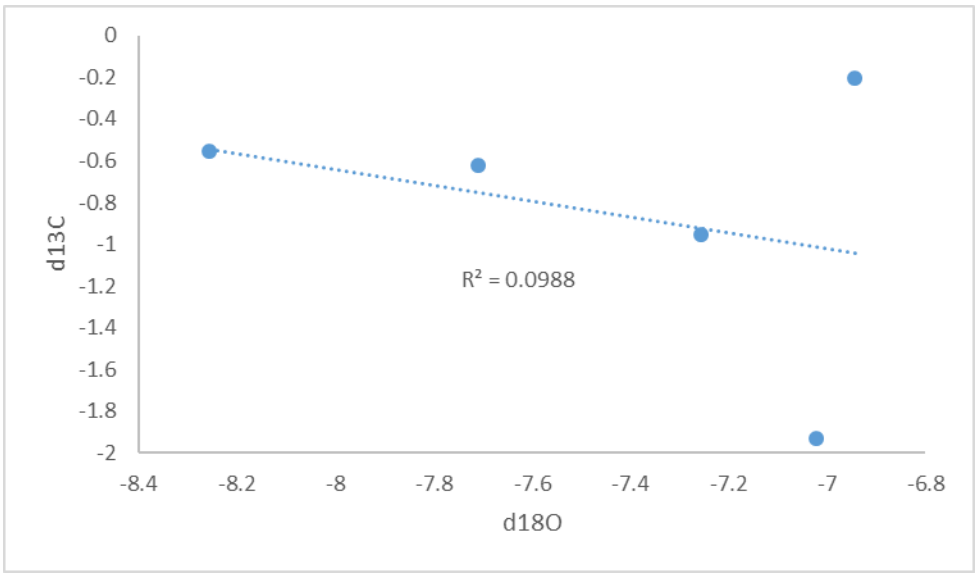

Figure S2: Zjl (j64-68)

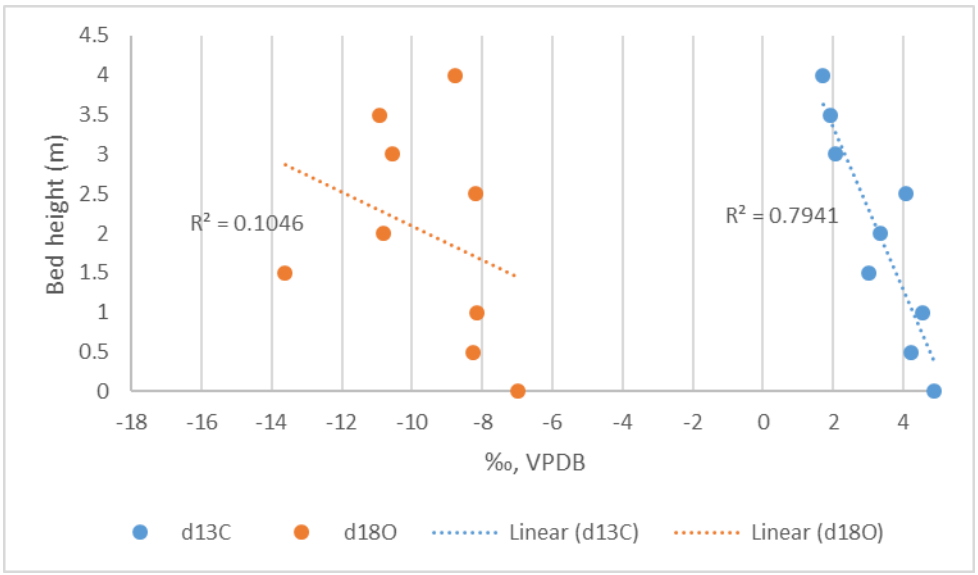

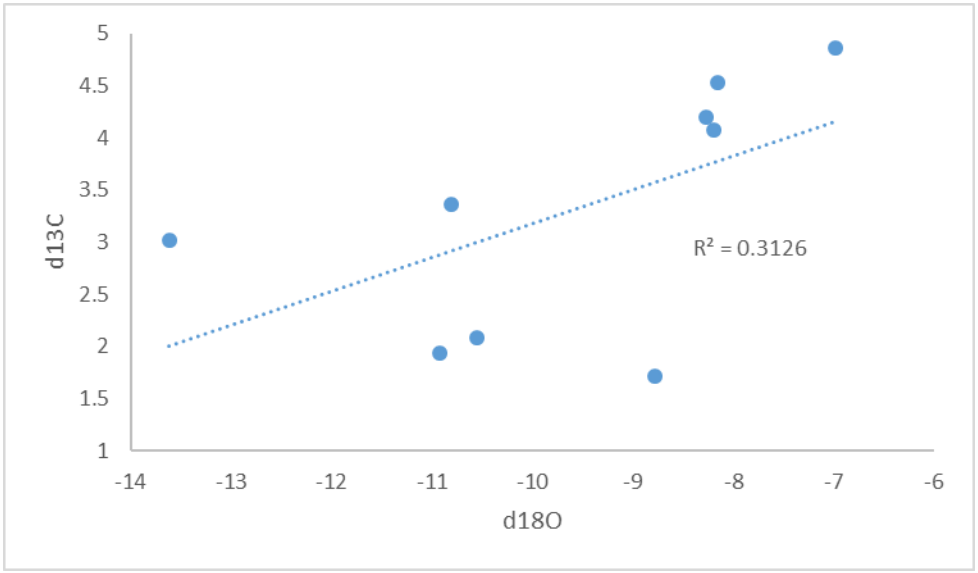

Figure S2: Zjk2 (j55-63)

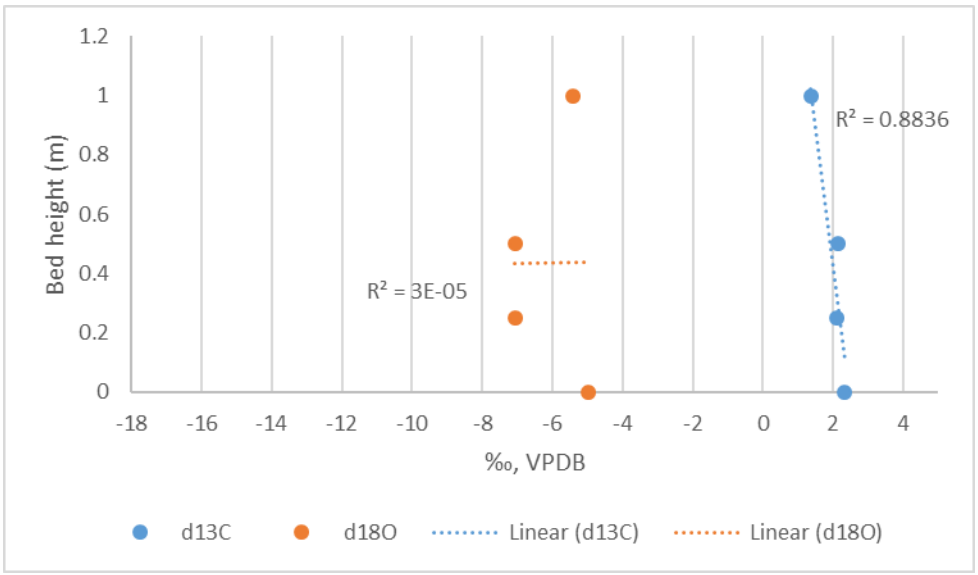

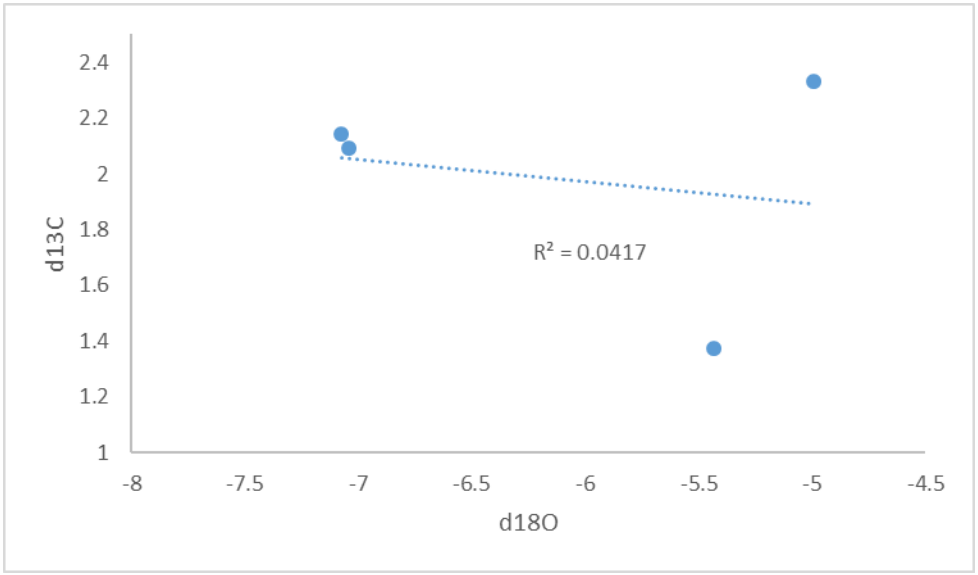

Figure S2: Zjk1 (j51-54)

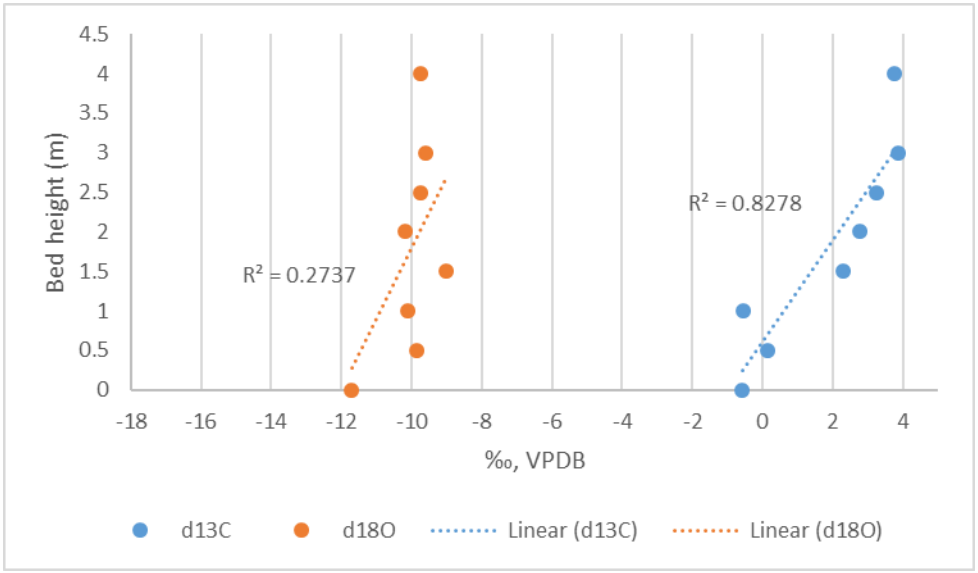

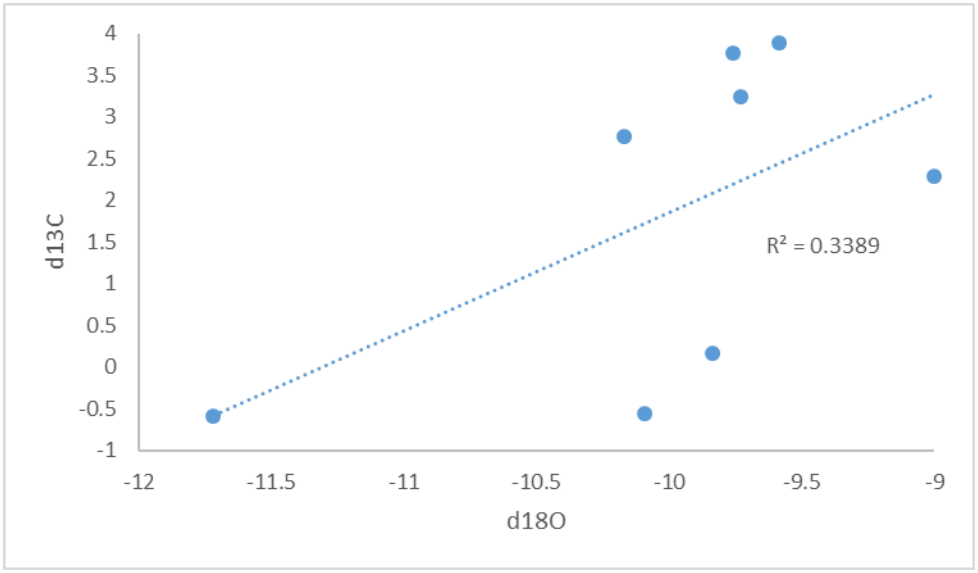

Figure S2: Zjj2 (j43-50)

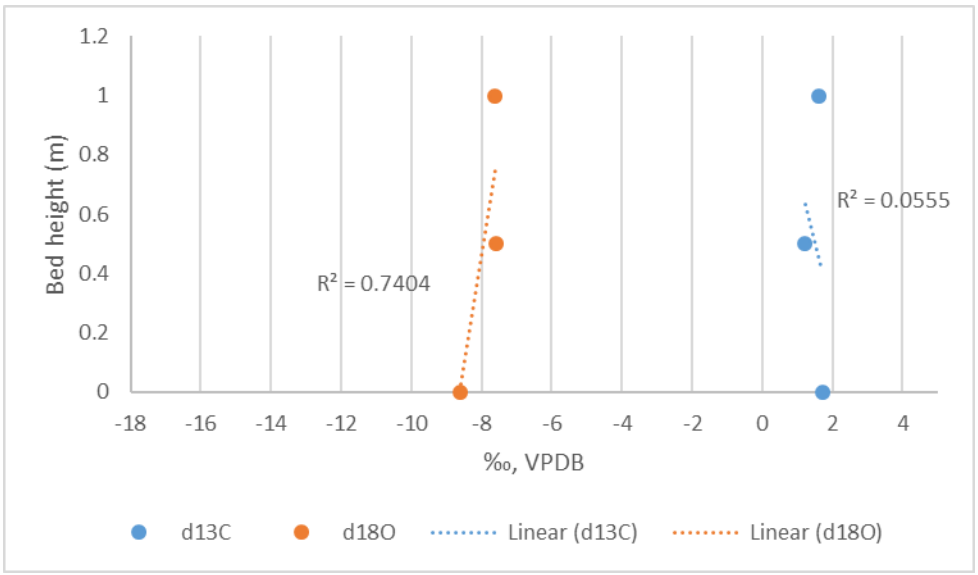

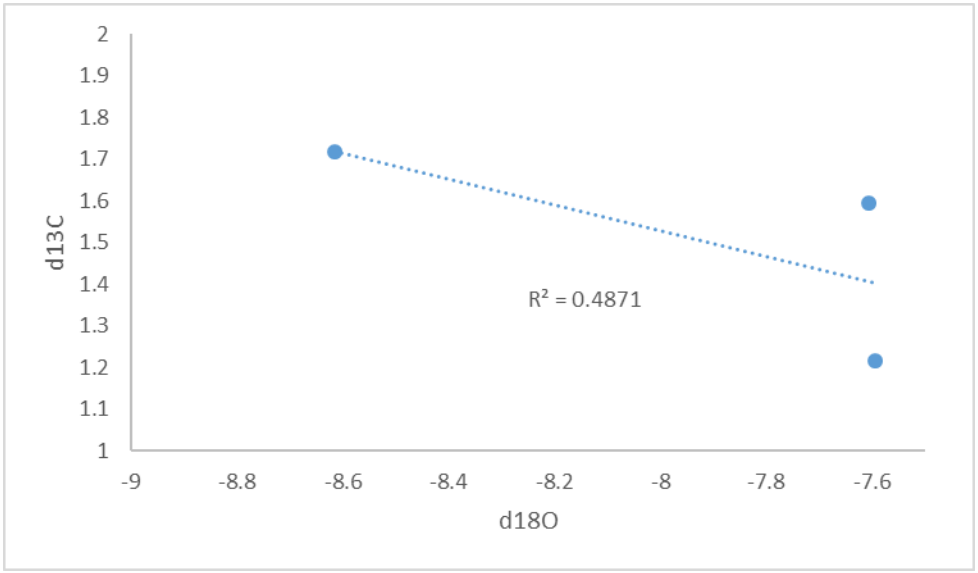

Figure S2: Zjj1 (j40-42)

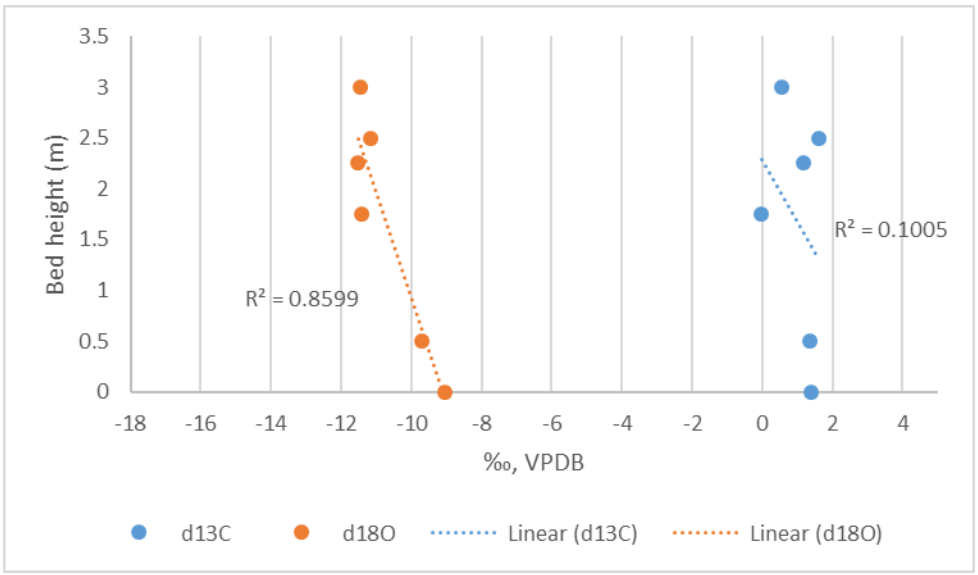

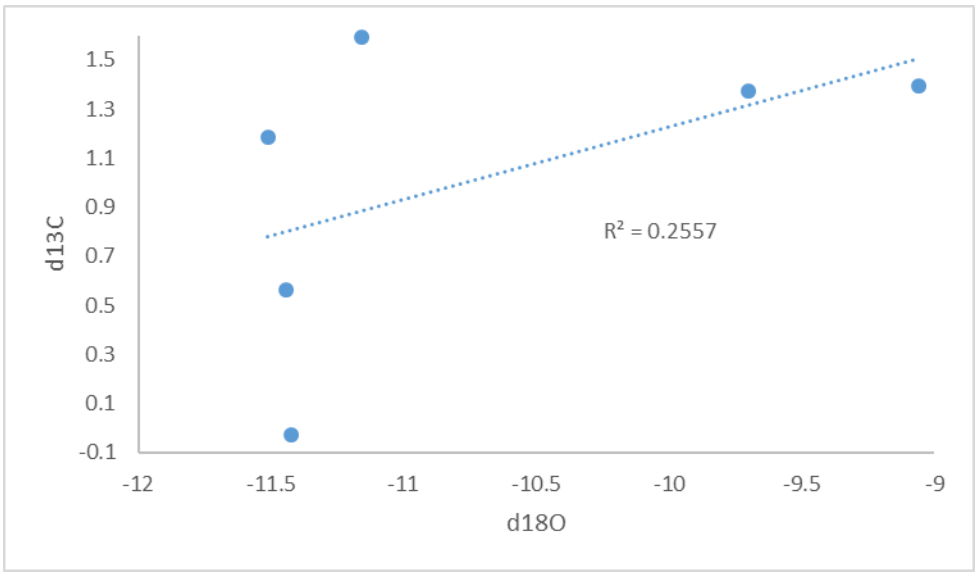

Figure S2: Zji2 (j34-39)

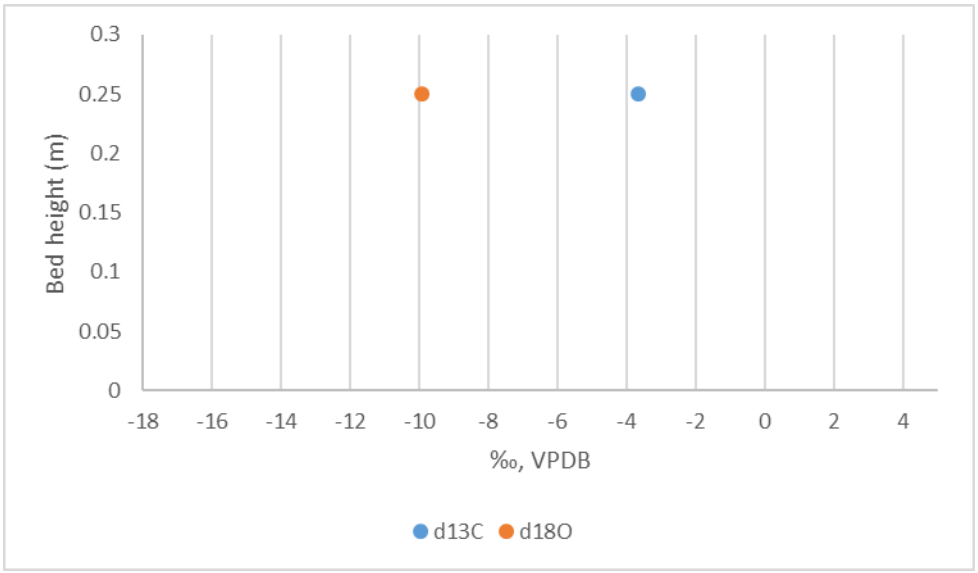

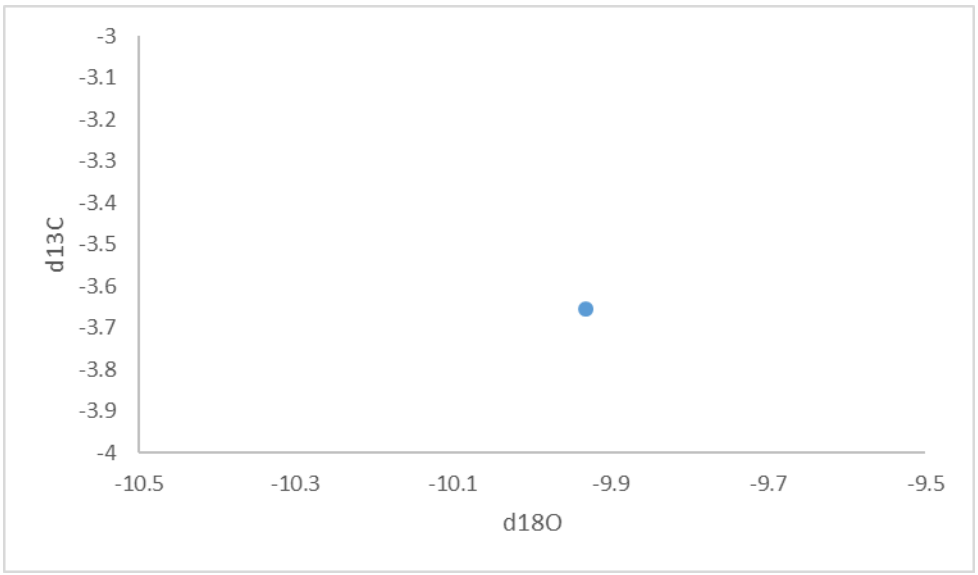

Figure S2: Zji1 (j33)

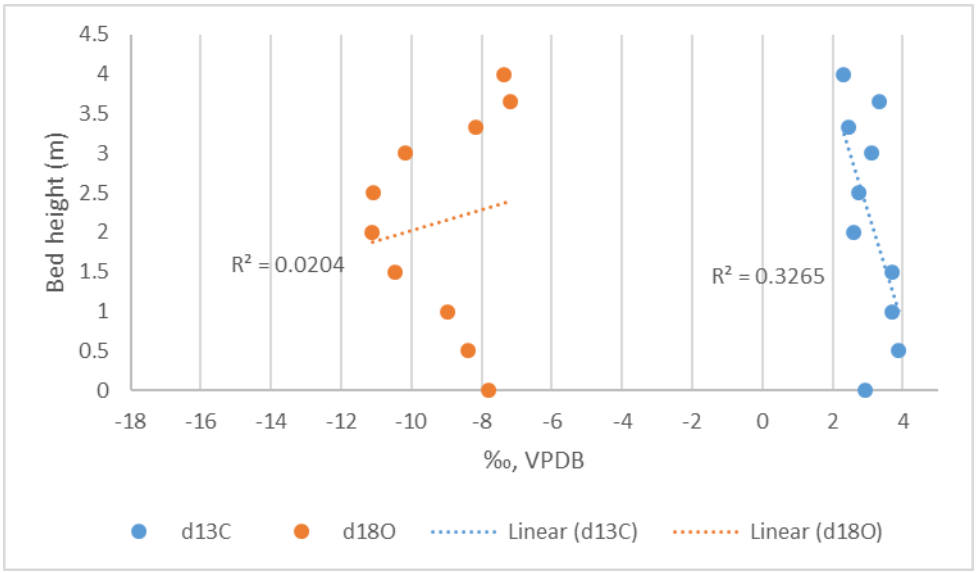

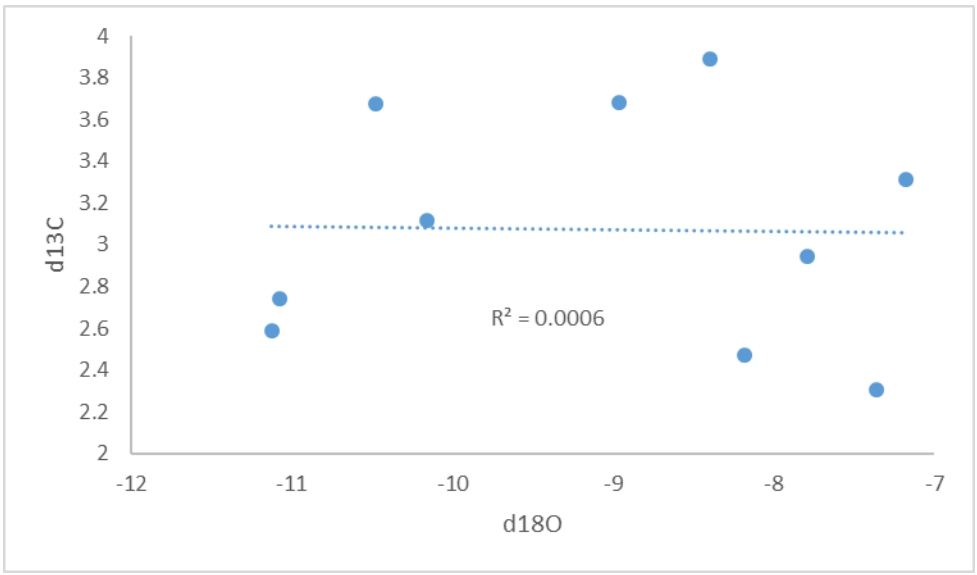

Figure S2: Zjh6 (j23-32)

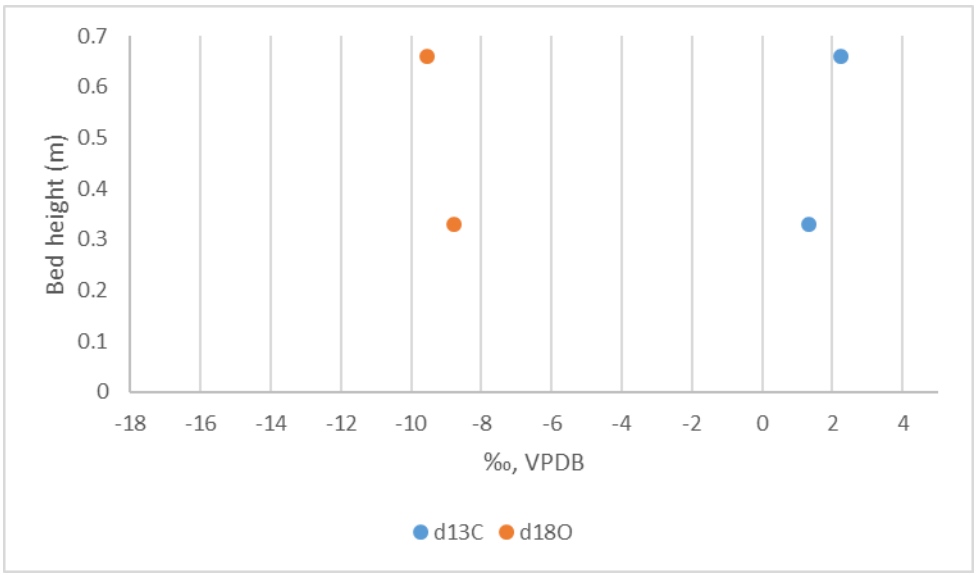

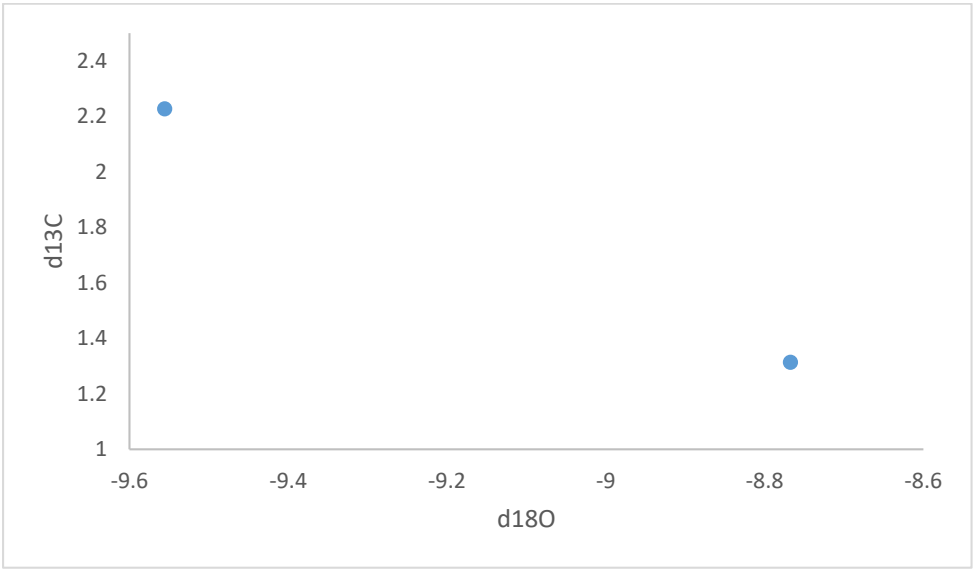

Figure S2: Zjh5 (j21-22)

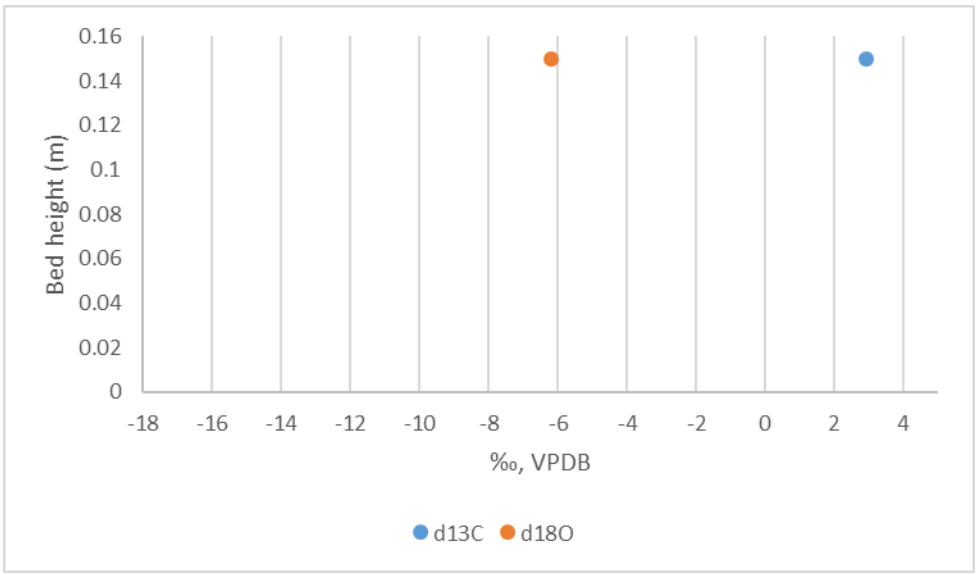

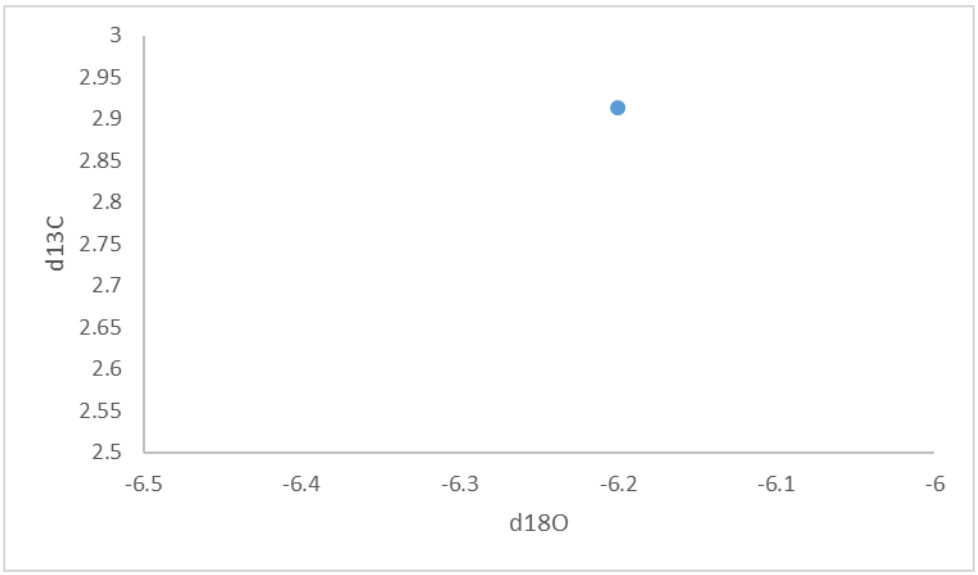

Figure S2: Zjh4 (j20)

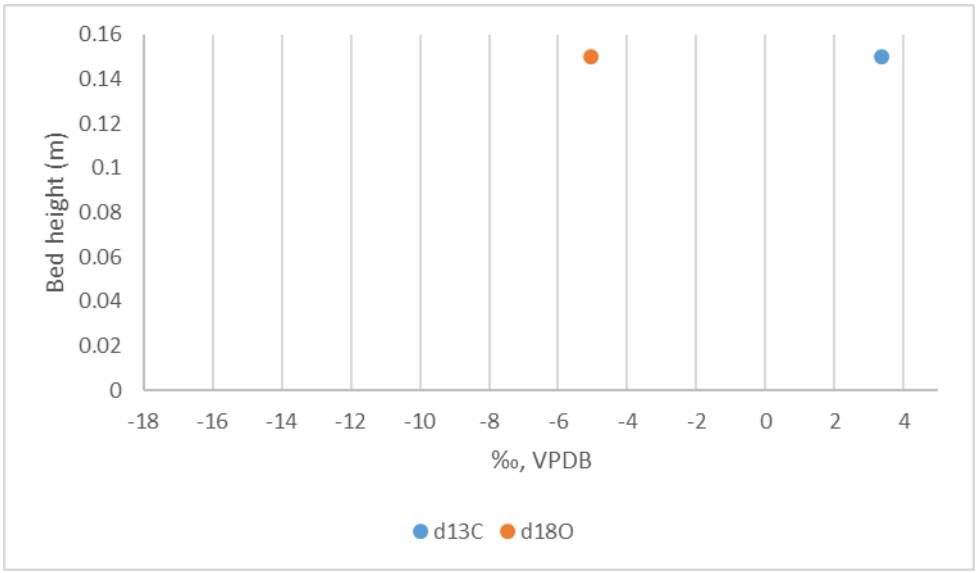

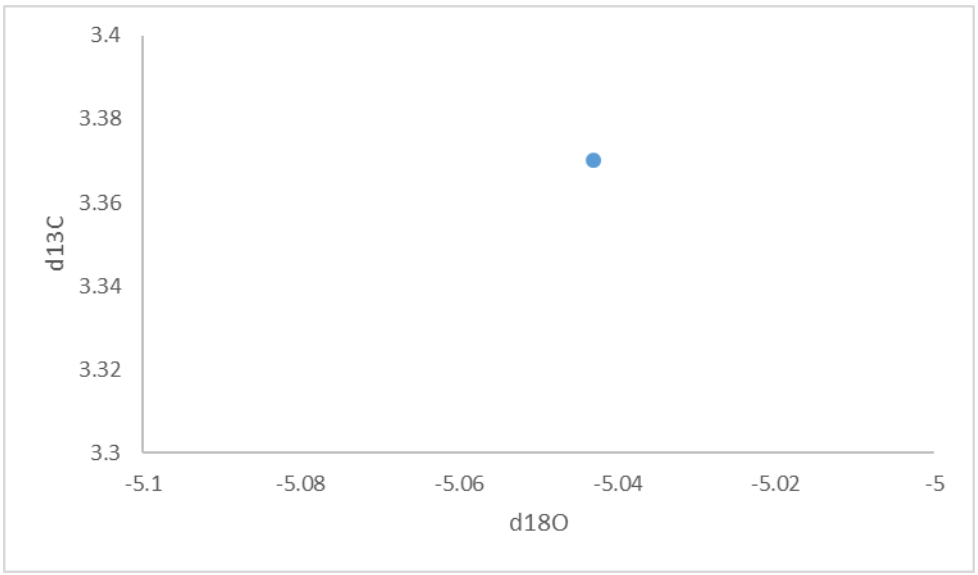

Figure S2: Zjh3 (j19)

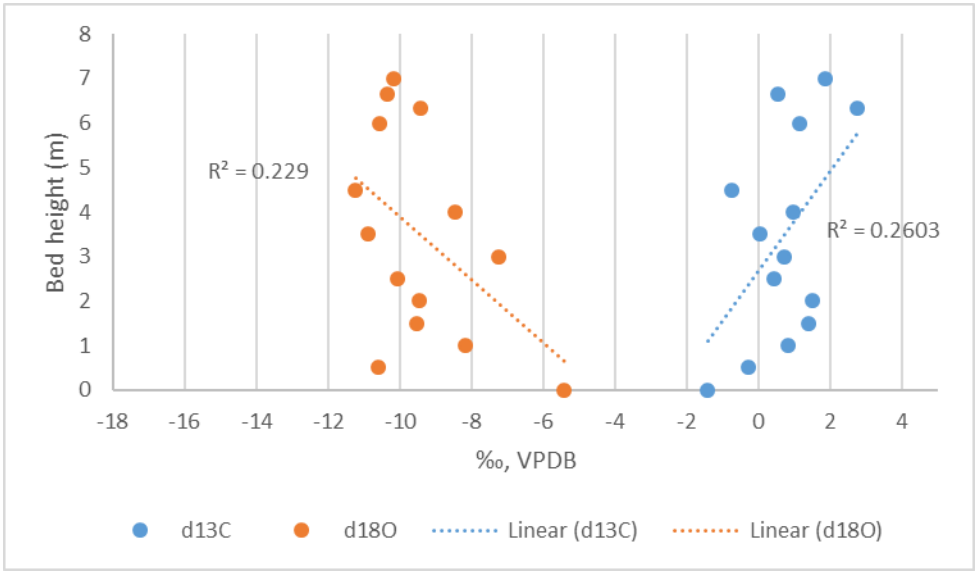

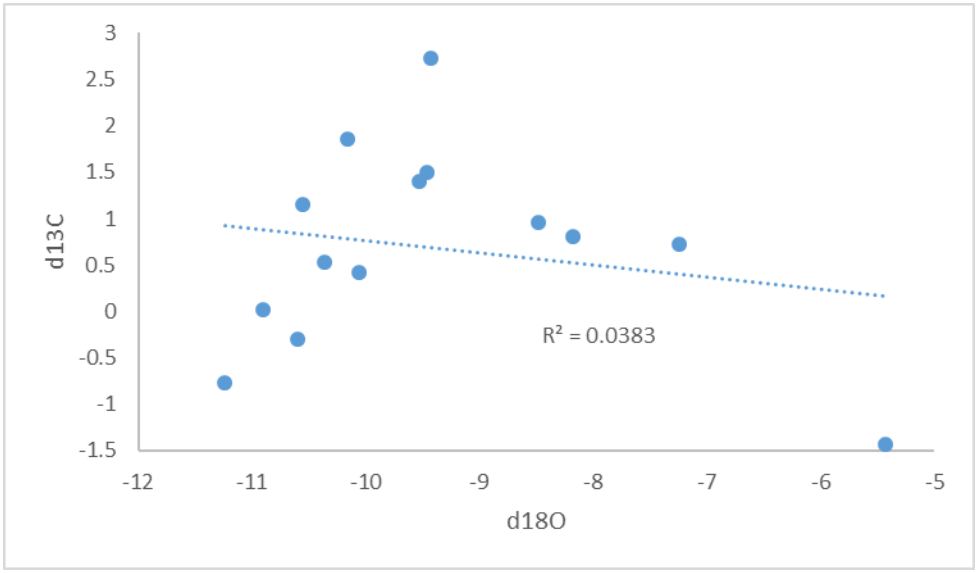

Figure S2: Zjh2 (j5-18)

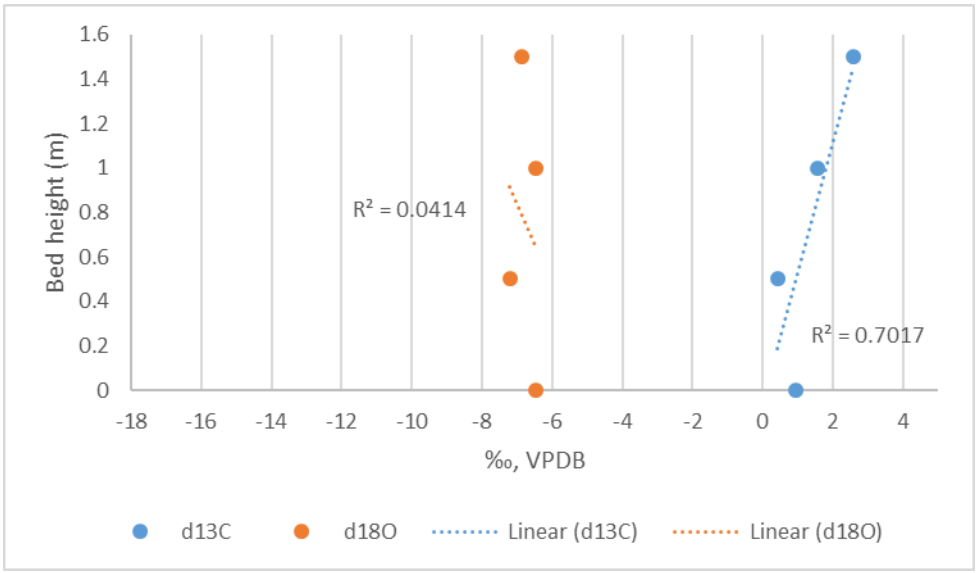

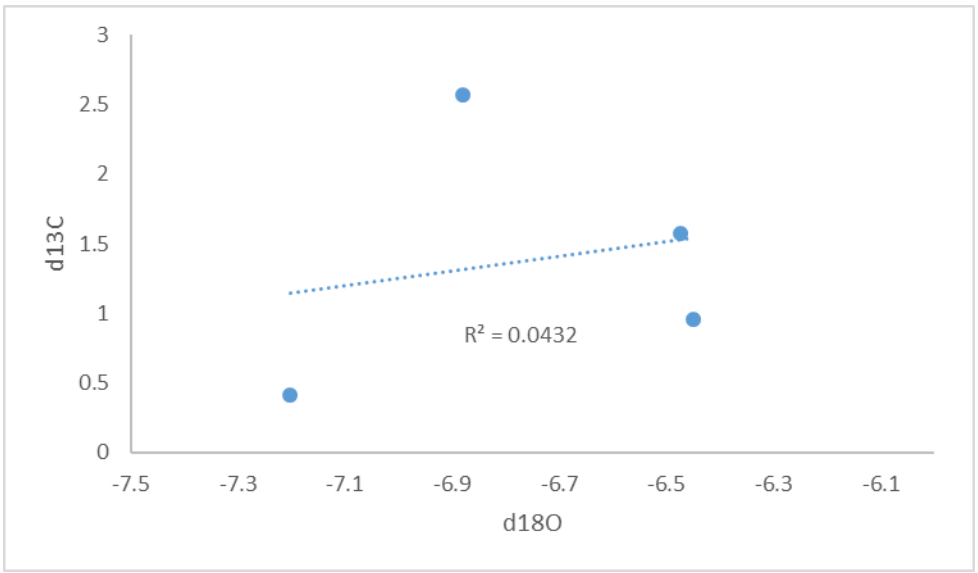

Figure S2: Zjh1 (j1-4)

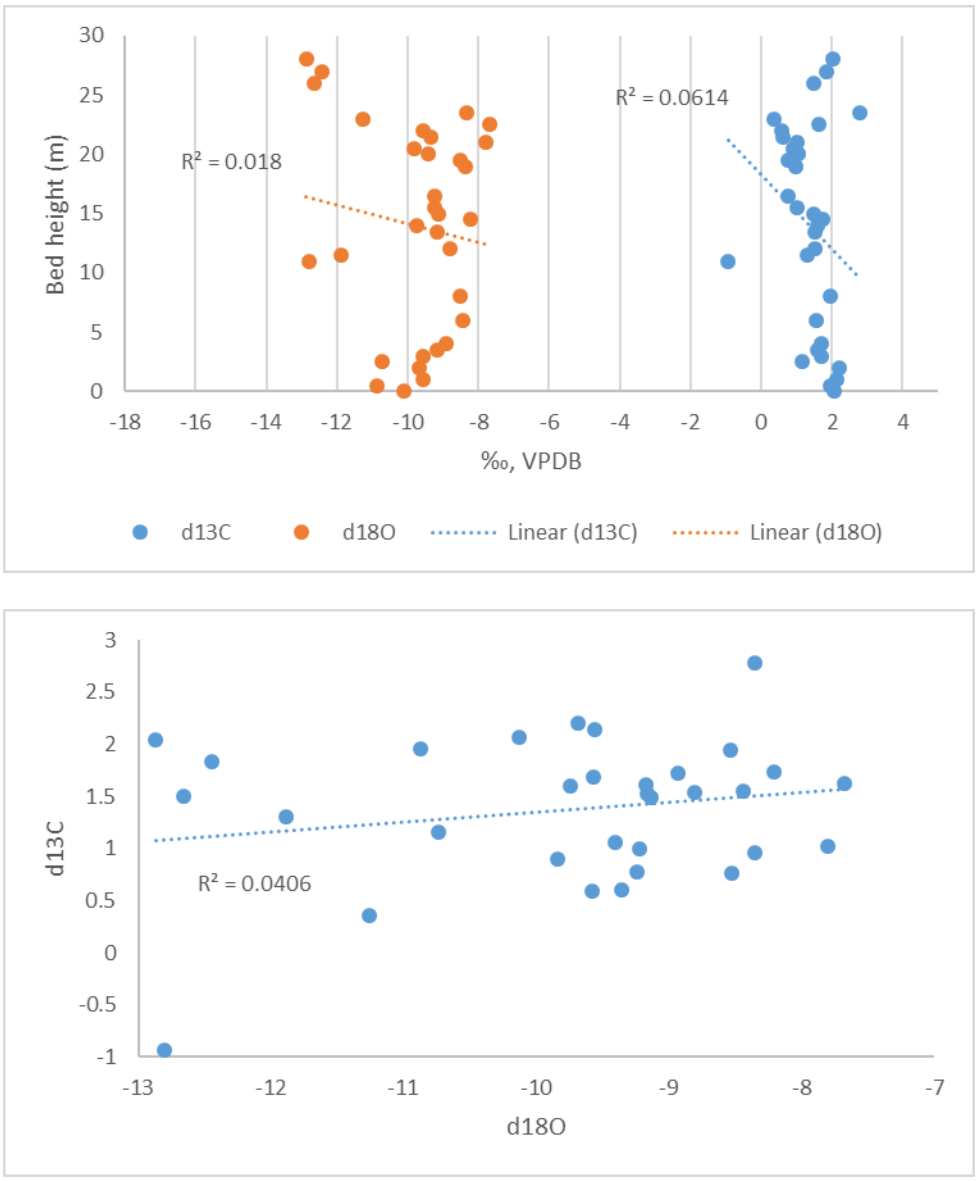

Figure S2: Zjf (j76-107)

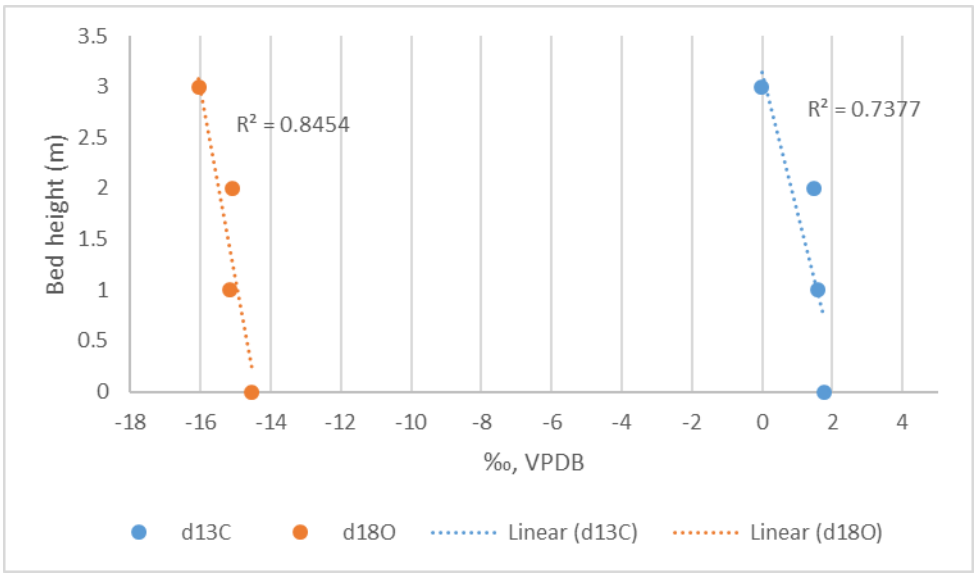

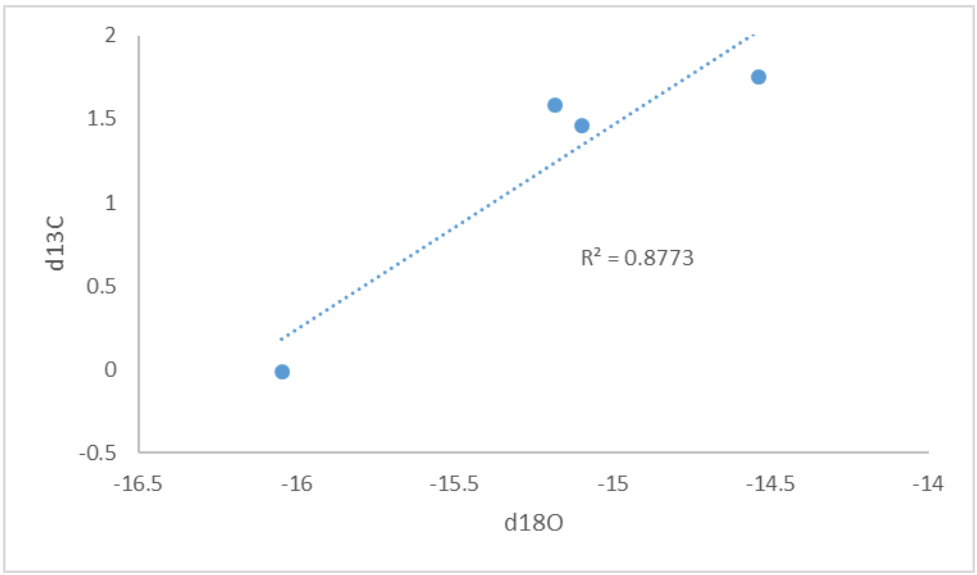

Figure S2: Zjc (j72-75)

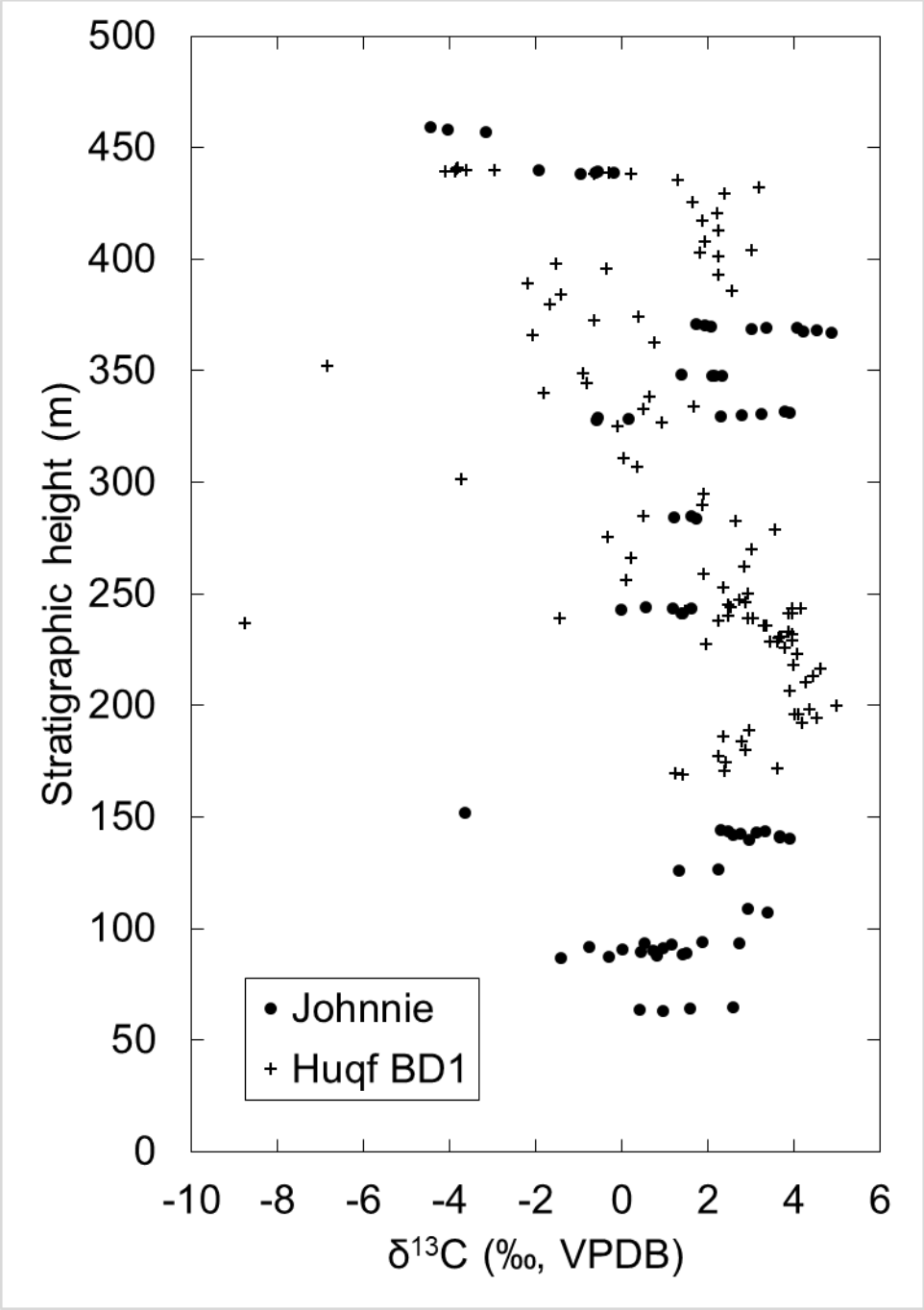

Figure S3: BD1

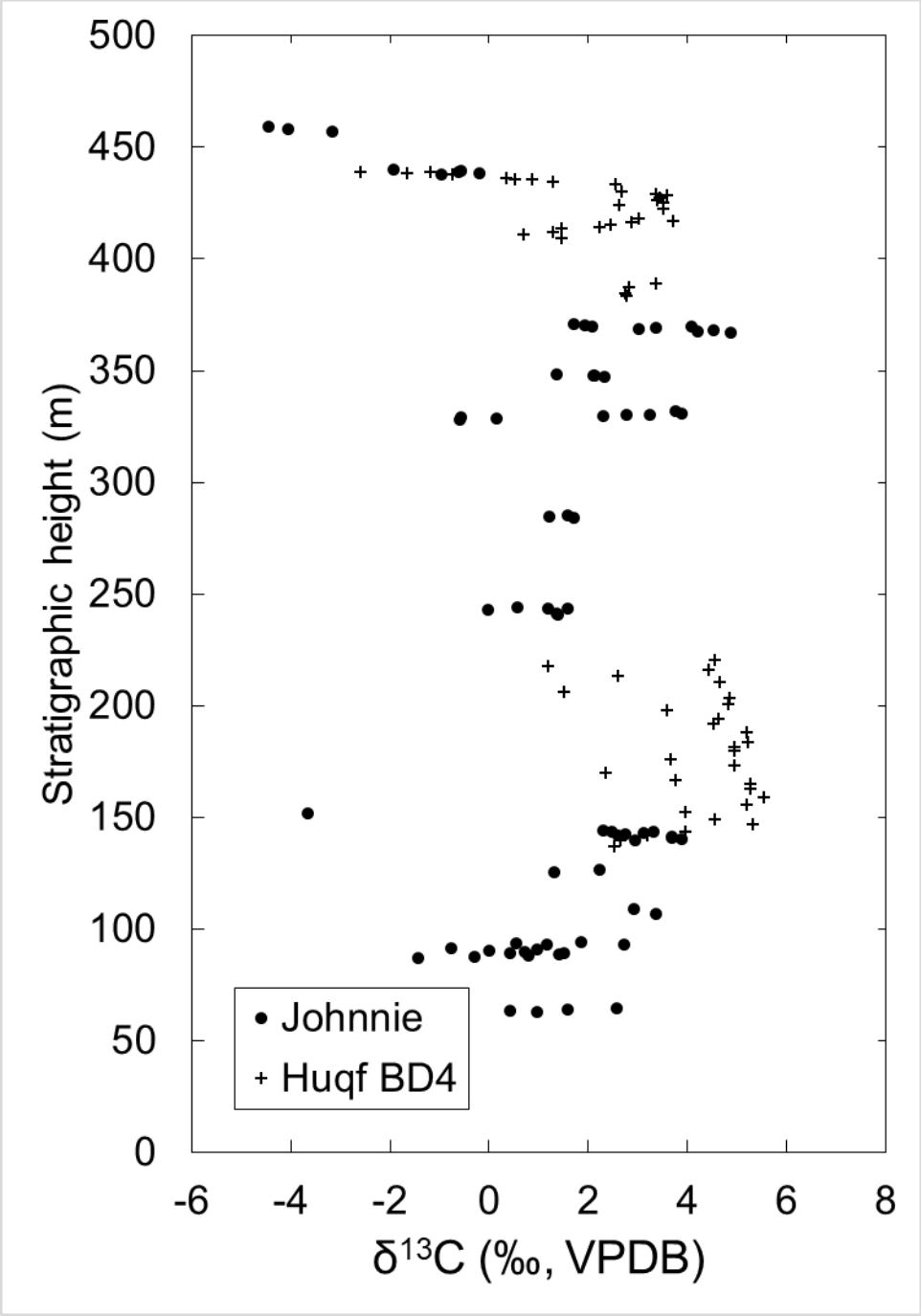

Figure S3: BD4

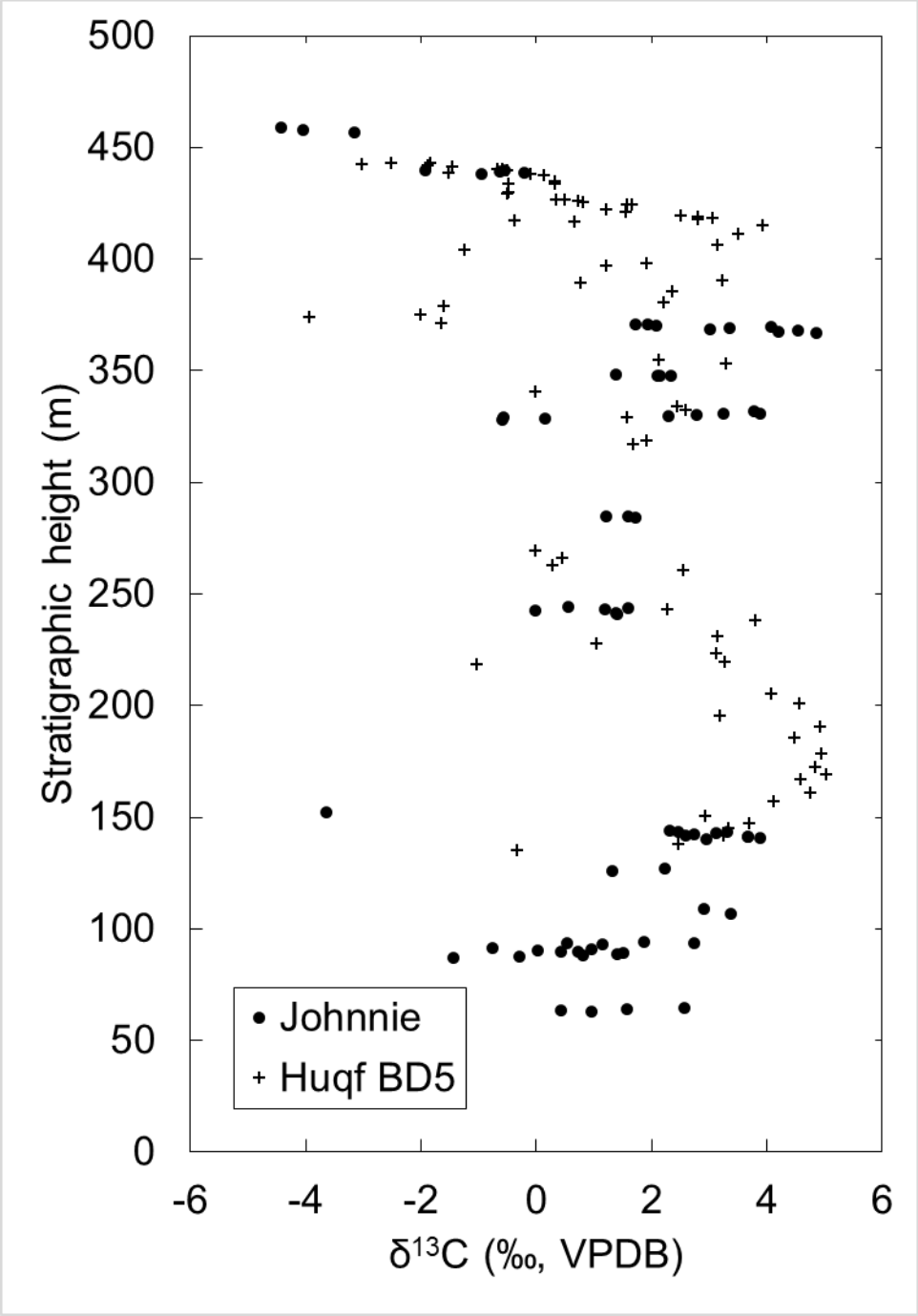

Figure S3: BD5

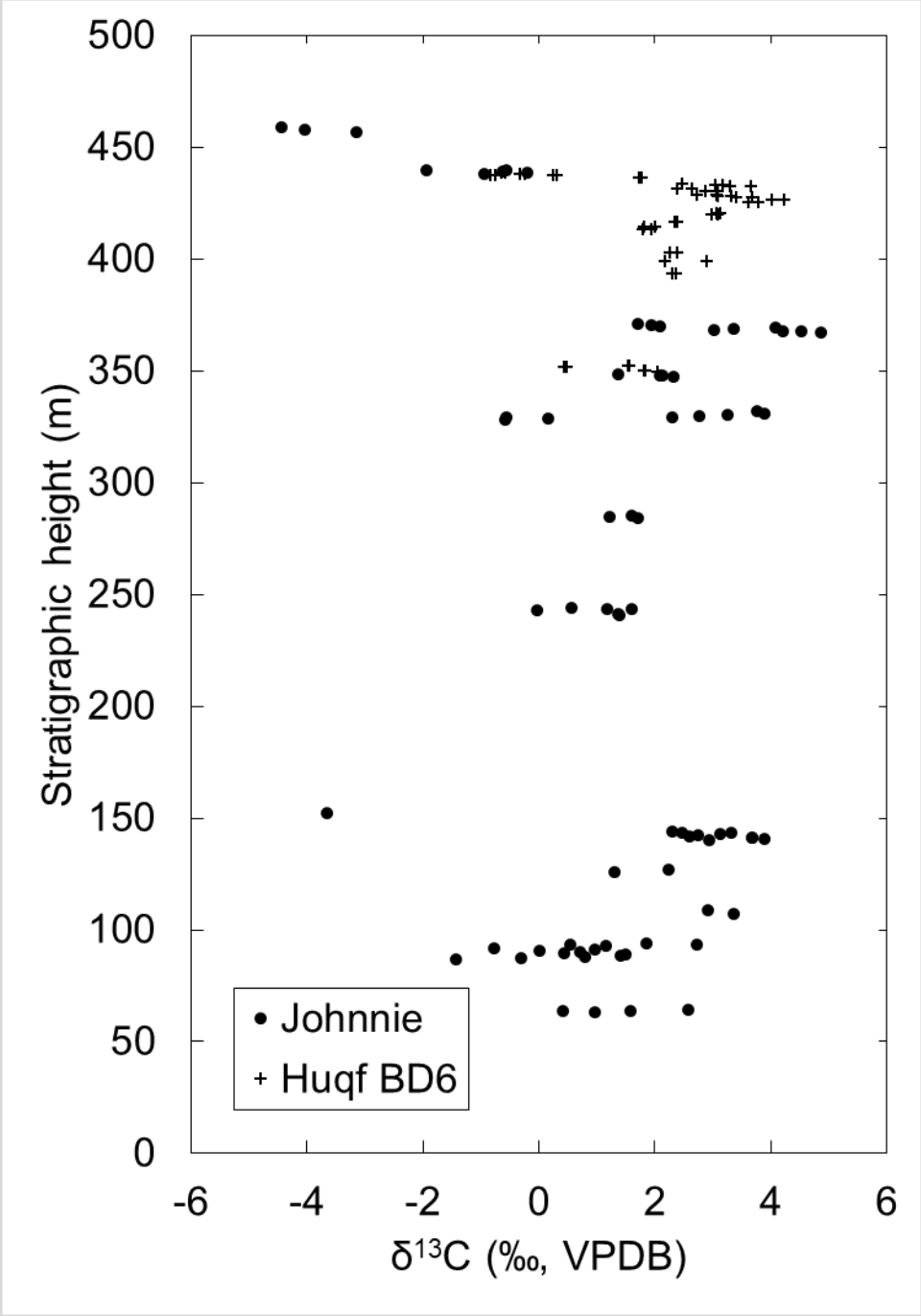

Figure S3: BD6

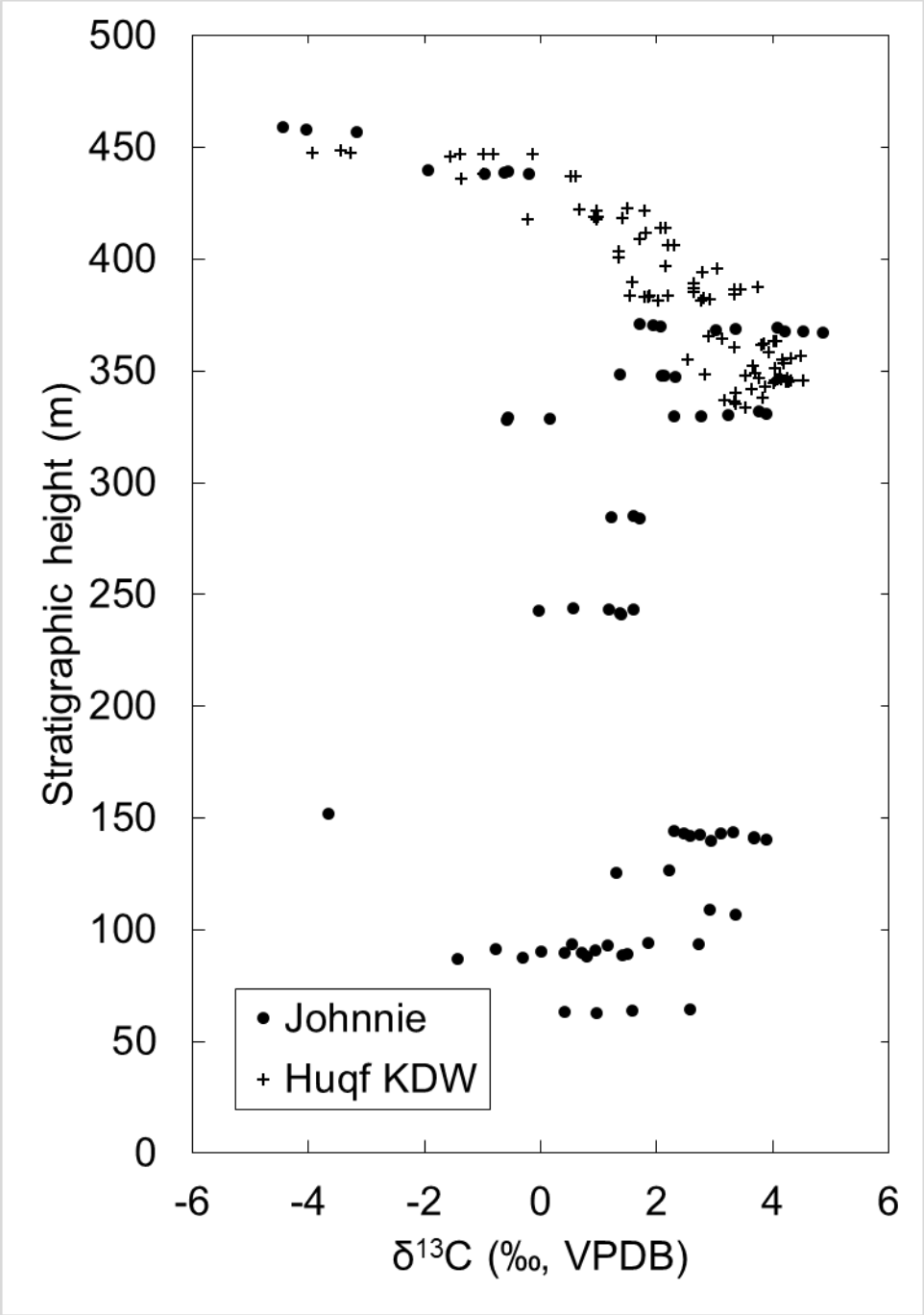

Figure S3: KDW

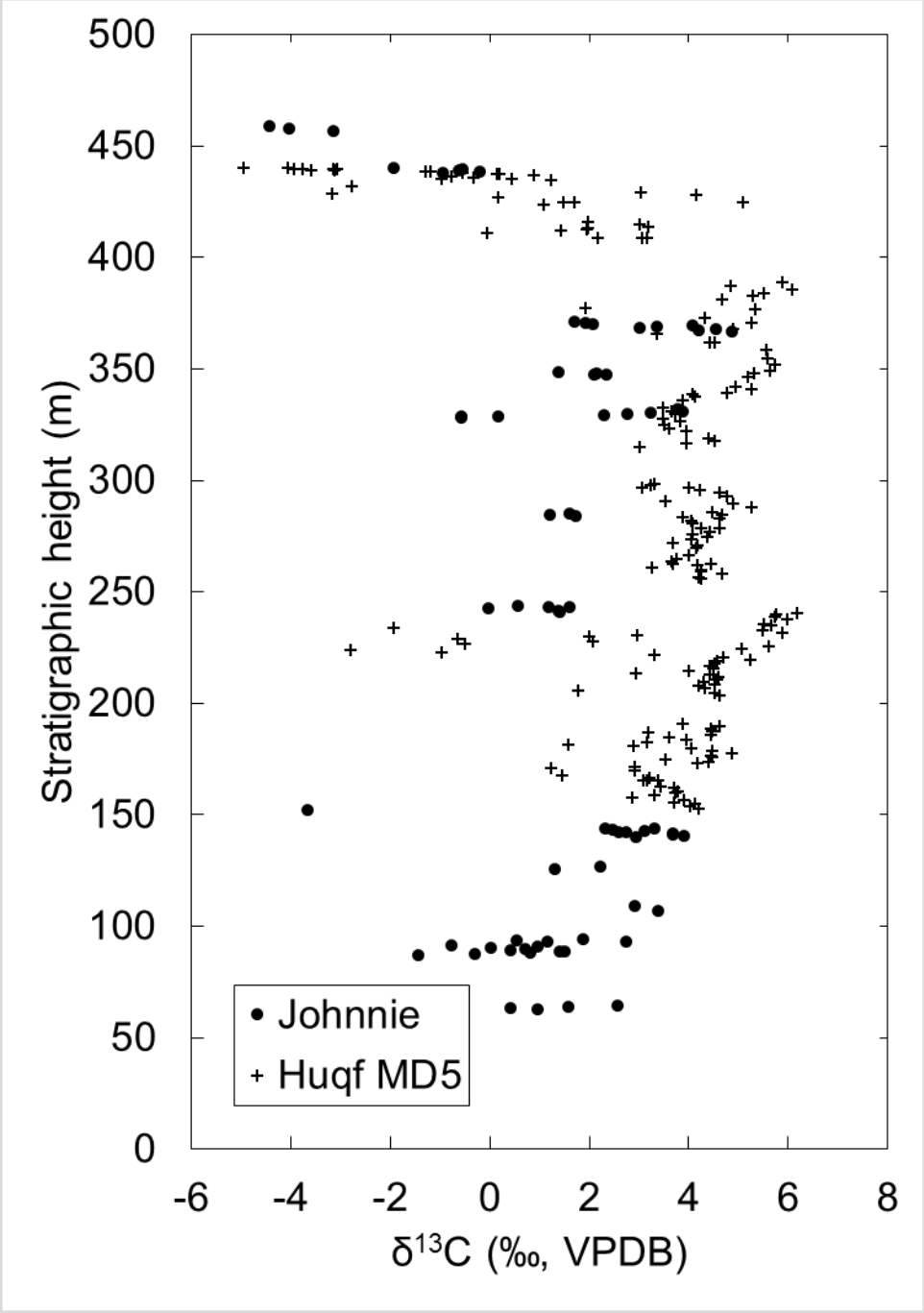

Figure S3: MD5

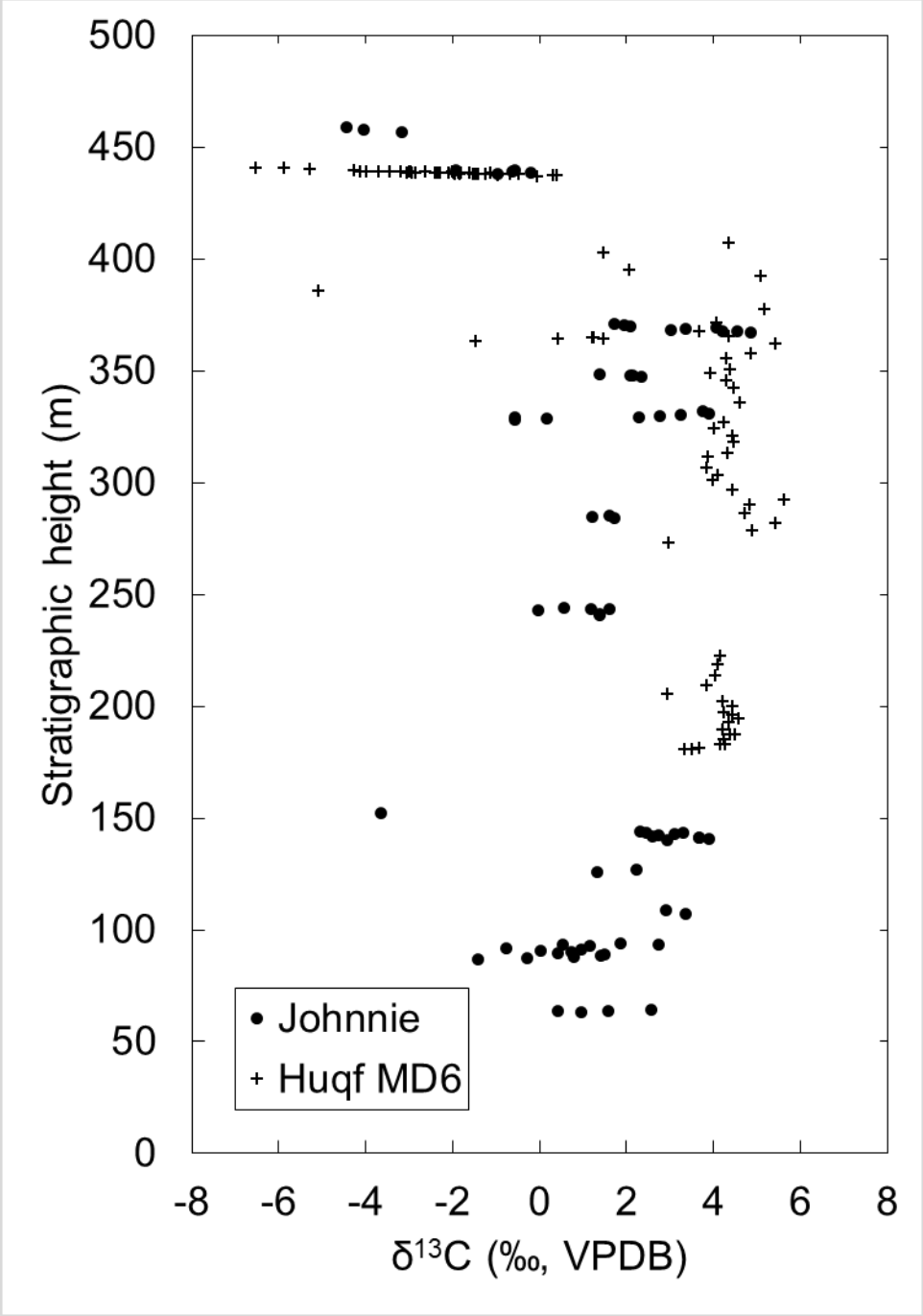

Figure S3: MD6

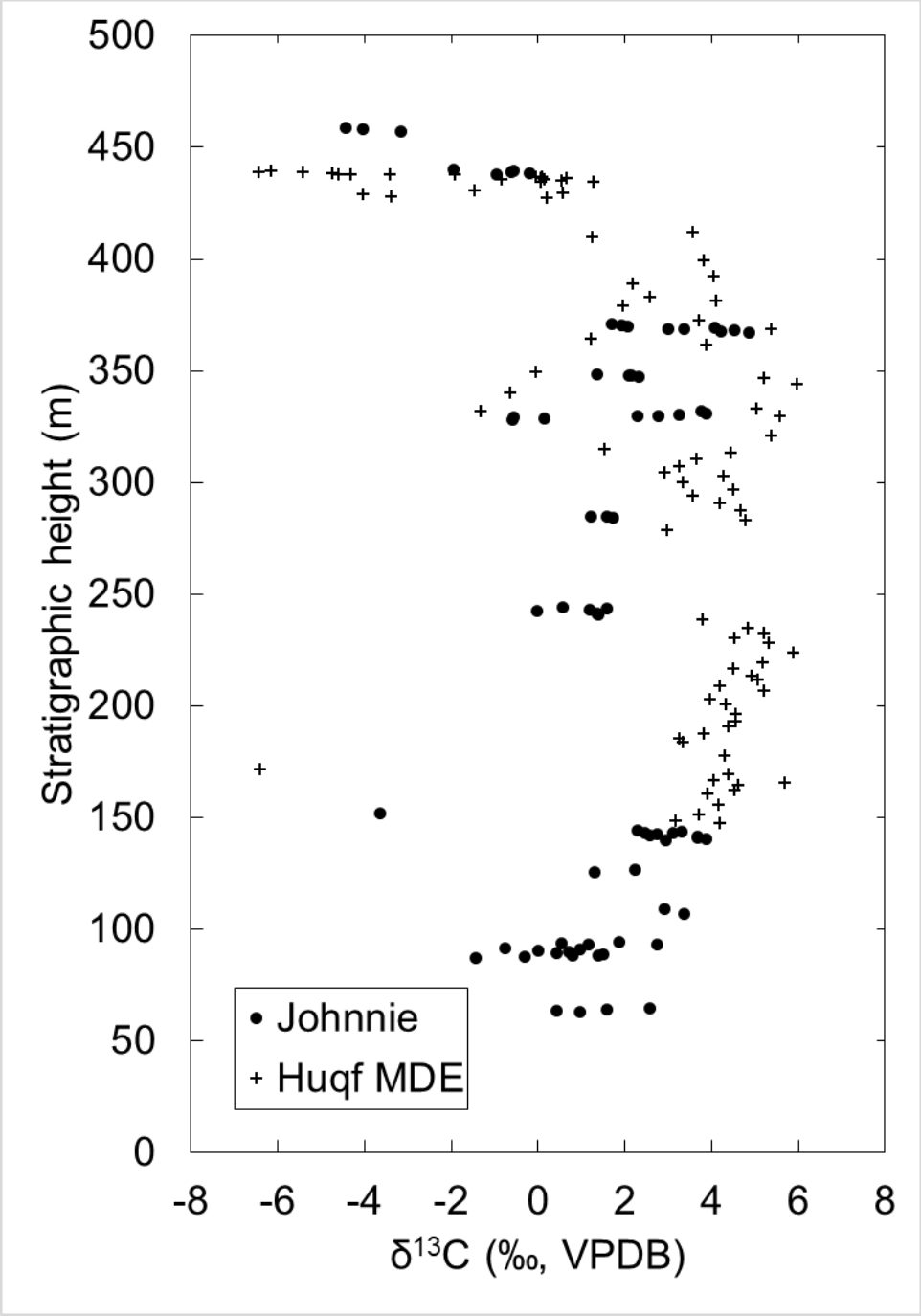

Figure S3: MDE

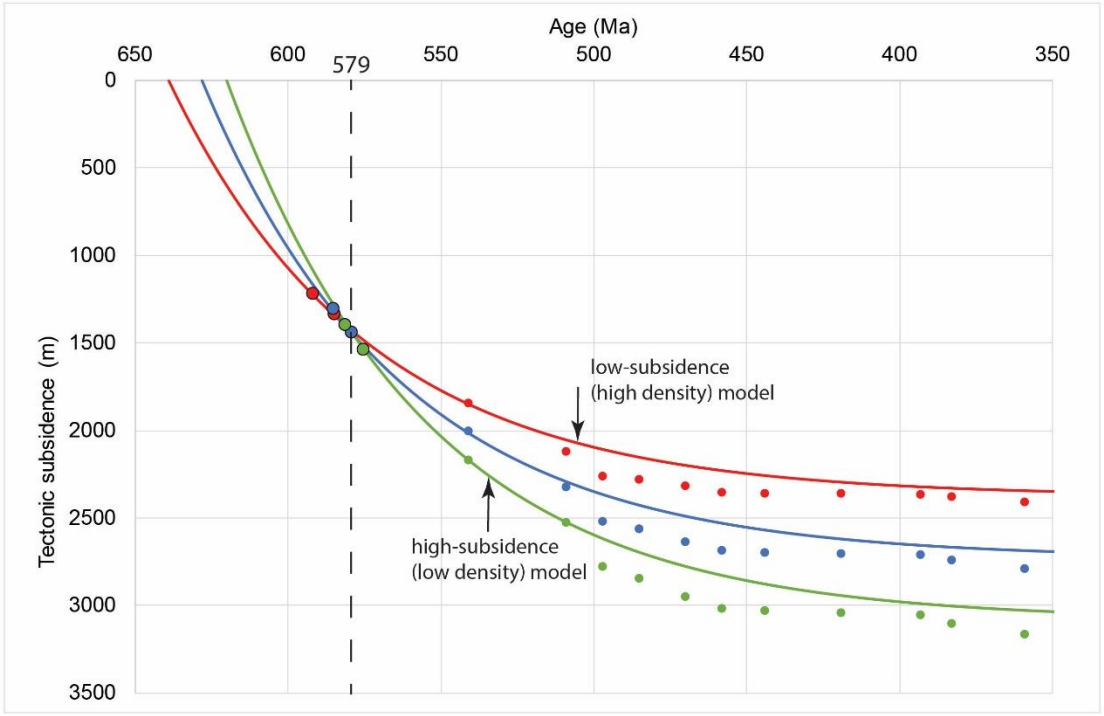
Age (Ma)
650
600
579
550
500
450
400
350
0
500
1000
1500
2000
2500
3000
3500
Tectonic subsidence (m)
low-subsidence
(high density) model
high-subsidence
(low density) model

Figure S4

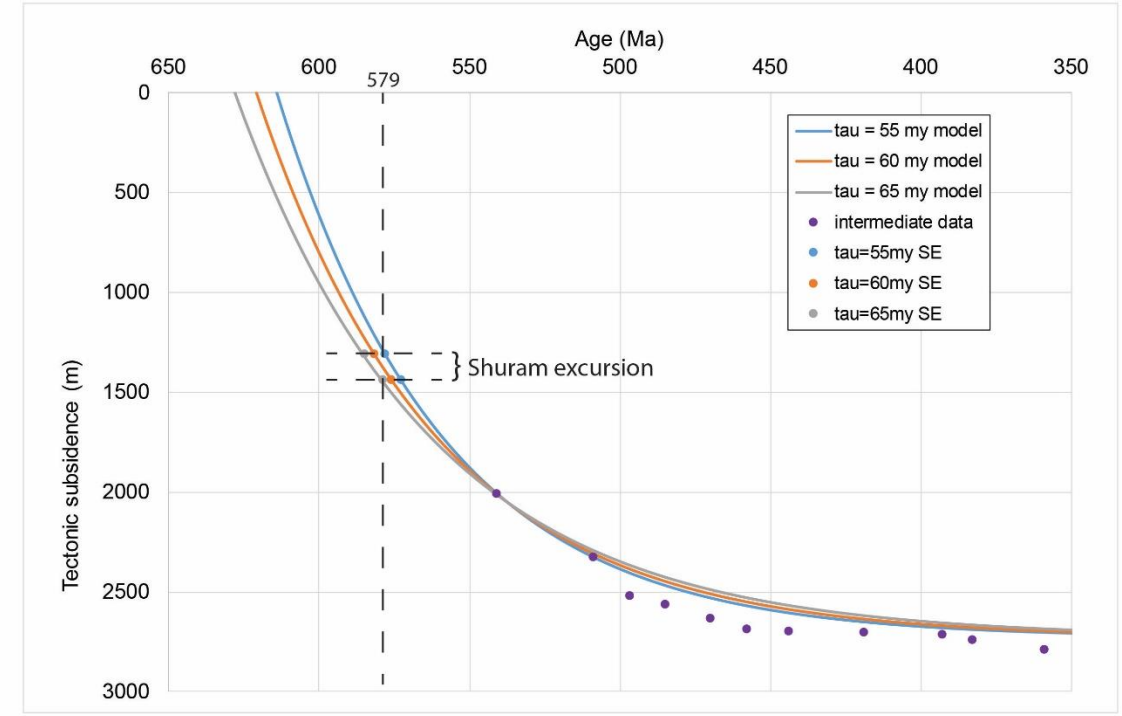
Age (Ma)
650
600
579
550
500
450
400
350
0
500
1000
1500
2000
2500
3000
Tectonic subsidence (m)
tau = 55 my model
tau = 60 my model
tau = 65 my model
intermediate data
tau=55my SE
tau=60my SE
tau=65my SE
} Shuram excursion

Figure S5

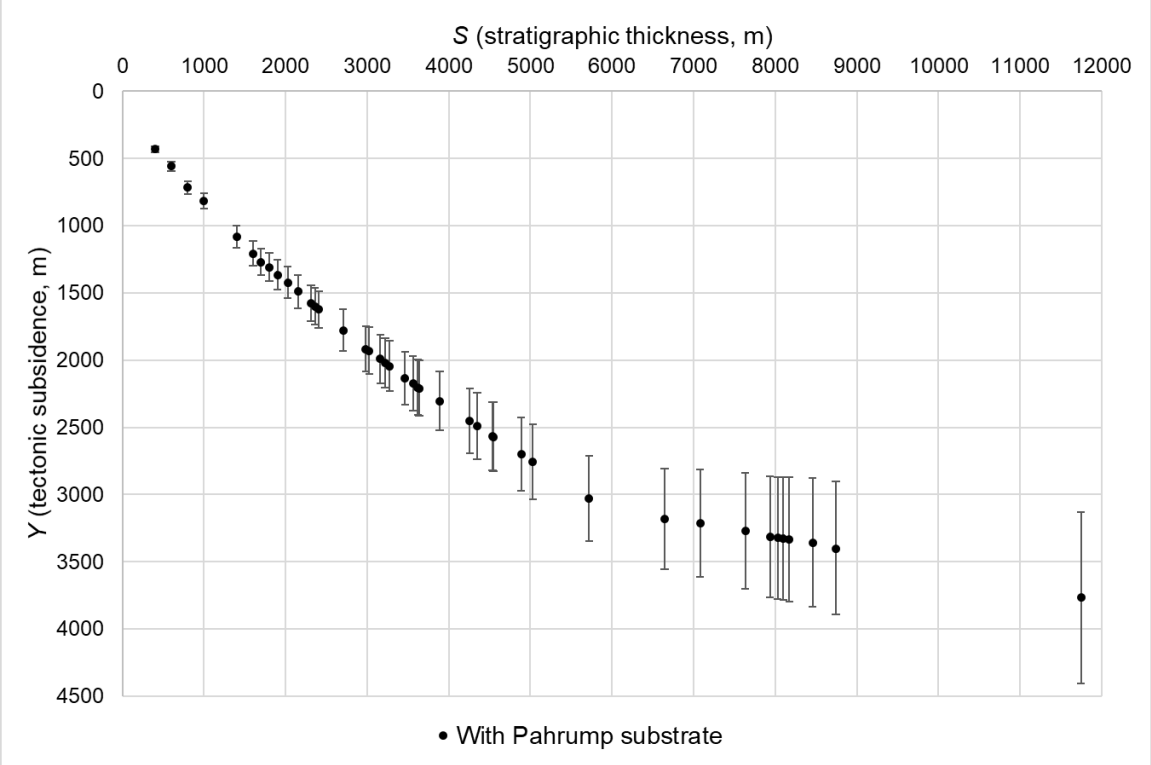
S (stratigraphic thickness, m)
0
1000
2000
3000
4000
5000
6000
7000
8000
9000
10000
11000
12000
Y (tectonic subsidence, m)
0
500
1000
1500
2000
2500
3000
3500
4000
4500
With Pahrump substrate

Figure S6

Supplemental Text

Lithologic descriptions regarding the Mt. Schader stratigraphic section for the Ediacaran Johnnie Formation, Montgomery Mountains, Nevada

Thickness of stratigraphic units were measured with a Jacob's staff and recorded to the nearest 1/4 or 1/3 of a meter. Care was taken to avoid structural complexities (i.e. by moving to locations where faults and/or folds are not present). Color names and numerical designations were recorded using a Geological Society of America Rock Color Chart with genuine Munsell® color chips. Grain sizes were recorded using an American/Canadian Stratigraphic reference card. Bed thicknesses use the following general designations: thin, <20 centimeters; medium, >20 centimeters; and thick, >50 centimeters. Total thickness of section measured is 538 meters for the Johnnie Formation, and 54 meters for the Stirling Quartzite (grand total of 592 meters).

Locality 1 (section 4, d-d')

Northeast part of Montgomery Mountains, measured about 3 kilometers west/southwest of Mt. Schader, starting at UTM zone 11S 0581729 m E 4035133 m N, and ending at UTM zone 11S 0581879 m E 4035004 m N.

Stirling Quartzite (incomplete):

Zsa member (incomplete):

Meters

48. Breccia and conglomerate. Breccia and conglomerate are very pale orange (10YR 8/2); weather to dark yellowish orange (10YR 6/6) and grayish black (N2); grains are poorly sorted coarse sand, pebbles, gravel; massive bedding; irregular cliff-forming protrusions; slickenlines on slickensided surfaces. Samples 20BW15 (590 m breccia) and 21BW15 (591 m). Incomplete measurement of bed.

4

47. Massive orthoquartzite. Orthoquartzite is pinkish gray (5YR 8/1); weathers to moderate yellowish orange (10YR 7/6); medium-coarse well-sorted grains; massive bedding with conjugate fractures; some cliff-forming protrusions on mostly recessive slopes. Sample 19BW15 (583 m-orthoquartzite).

14

144

46. Dolomitic sandstone. Dolomitic sandstone is grayish orange pink (5YR 7/2); weathers to grayish brown (5YR 3/2); fine-grained; laminated medium beds; trough cross strata; resistant cliff-forming unit.

8

45. Orthoquartzite and carbonate cemented sandstone. Orthoquartzite is very pale orange (10YR 8/2); weathers to dark yellowish orange (10YR 6/6); fine- to medium-grained; thick bedded; some laminations with fractures both along laminations and sub-orthogonal to laminations; channel fill with normal grading near base. Carbonate cemented sandstone is pale reddish brown (10R 5/4); weathers to olive black (5Y 2/1); fine-grained; medium-thick bedded; sometimes laminated.

28

Total of incomplete Zs member 54

Total of incomplete Stirling Quartzite 54

Johnnie Formation (incomplete):

Zjr member:

44. Sandstone and siltstone in ball-and-pillow structure, and dolostone. Ball-and-pillow structure is 1-2 m thick; light brown (5YR 6.4); weathers to dusky yellowish brown (10YR 2/2); sandstone is fine- to medium-grained; siltstone casted around sandstone. Other sandstone is pale red (5R 6/2); weathers to dark yellowish orange (10YR 6/6); fine-grained; medium bedded. Siltstone is typical VSS with additional new hue of pale red (5R 6/2); weathers to light greenish gray (5GY 8/1); speckled by 1 mm hematite grains; laminated. Dolostone is medium light gray (N6); weathers to yellowish orange (10YR 6/6) and light brown (5YR 6/4). Base of dolomitic sandstone is moderate yellowish brown (10YR 5/4); weathers to dusky yellowish brown (10YR 2/2) medium grains; some south-dipping foresets.

4

43. VSS and calcite-cemented sandstone. VSS as previous. Sandy limestone is pale red (10R 6/2); weathers to pale reddish brown (10R 5/4); very fine-grained; thin lenses of flaser beds.

8

42. Limestone breccia and sucrosic limestone. Limestone breccia is light gray (N7); weathers to light olive gray (5Y 5/2). Sucrosic limestone is pale red (10R 6/2); weathers to pale reddish brown (10R 5/4). Sandy limestone and calcite cemented sandstone with

laminated thin interbeds of sucrosic limestone; recessive, slope-forming unit.

24

41. Mixed siltstone and carbonate-rich sandstone. Siltstone as VSS; finely laminated. Sandstone is pale red (10R 6/2); weathers to dark yellowish brown (10YR 4/2); fine-grained, thin- to medium-bedded. Siltstone and sandstone form recessive slope-forming unit.

18

40. Argillite and limestone. Argillite is medium dark gray (N4); weathers to medium gray (N5); very fine mica, phyllitic texture. Limestone is laminated, as in unit 38.

5

39. Folded limestone. Same as liver limestone (38): pale reddish brown (10R 5/4); weathers to grayish red (10R 4/2); varnish is very dusky red (10R 2/2); folded top to west, pitted dissolution surfaces.

1

38. Liver limestone. Limestone is pale reddish brown (10R 5/4); weathers to grayish red (10R 4/2). Fine-grained with interspersed quartz grains; thinly to medium bedded, massive to laminated beds; occasional brecciation near top.

11.5

37. Carbonate-rich sandstone. Sandstone is grayish red (10R 4/2); weathers to pale reddish brown (10R 5/4) and dark yellowish

orange (10YR 6/6) and various similar hues; fine-medium grains**;** thinly bedded and finely laminated with rare north-dipping foresets.

7.5

36. Dolomitic oolite; “Johnnie Oolite”. Oolite is pale yellowish brown (10YR 6/2); weathers to grayish orange (10YR 7/4); very coarse-grained.

2

35. VSS. VSS is finely laminated, occasionally phyllitic, with rare N-dipping foresets and occasional quartz veins.

17

Total of Zjr member 98

Zjl member (combine with Zjl from section 3):

34. Laminated dolostone. Dolostone is pale yellowish brown (10YR 6/2); weathers to moderate yellowish brown (10YR 6/4); thick, laminated beds.

2

33. VSS and dolomitic sandstone (incomplete). VSS as previous. Dolomitic sandstone is medium gray (N5); weathers to moderate yellowish orange (10YR 5/6); fine-grained. Beds are massive with varnish of dark gray (N3).

6

Locality 1 (section 3, c-c')

Northeast part of Montgomery Mountains, measured about 3 kilometers west/southwest of Mt. Schader, starting at UTM zone 11S 0580829 m E 4033958 m N (approximate), and ending at UTM zone 11S 0580984 m E 4033808 m N.

Meters

Johnnie Formation (incomplete):

Zjl member (combine with Zjl from section 4):

32. Orthoquartzite and siltstone (VSS) as in 31. Sample 18BW15 (430 m), medium-grained orthoquartzite (incomplete).

36

31. Orthoquartzite and minor siltstone. Light brownish gray (5YR 6/1); weathers to moderate brown (5YR 4/4) and grayish black (N2); siltstone is fine-medium grained; thin-thick parallel beds with some hummocky cross-strata.

12

30. Siltstone and fine sandstone with minor orthoquartzite. Siltstone and fine sandstone, as VSS, are variegated; bluish white (5B 4/1) weathers to blackish red (5R 2/2) and green (undocumented), thin

beds. Orthoquartzite is medium light gray (N6); weathers to moderate reddish brown (10R 4/6).

13

Total of Zjl member 69

Zjk member:

29. Dolostone with chert. Dolostone is medium gray (N5); weathers to light olive gray (5Y 5/2) and medium yellowish brown (10YR 6/4). Dolostone is medium bedded with chert in lower third of section. Chert is medium light gray (N6); weathers to grayish black (N2). Hummocky cross-stratified mounds with anastomosing laminations in middle of section. Samples J63 (371 m), J62 (370.5 m), J61 (370), J60 (369.5), J59 (369), J58 (368.5), J57 (368), J56 (367.5), and J55 (367).

4

28. Siltstone and orthoquartzite, mainly parallel bedded.

18

27. Dolostone. Medium gray (N5); weathers to moderate olive brown (5Y 4/4) and moderate yellowish brown (10YR 5/4). Medium bedded with basal sandy dolostone. Samples J54 (349 m), J53 (348.5 m), J52 (348 m), and J51 (347.5 m).

150

2

26. Siltstone and orthoquartzite. Siltstone is typical variegates sandstone and siltstone, bluish white (5B 4/1) and blackish red (5R 2/2) and green (undocumented color), thinly bedded with thin beds or orthoquartzite. Orthoquartzite is medium light gray (N6); weathers to moderate reddish brown (10R 4/6), ripple laminations.

15

Total of Zjk member 39

Zjj member (combine with Zjj from section 2):

25. Dolostone and sandy dolostone. Dolostone is medium-dark gray (N4); weathers to olive gray (5Y 4/1); medium-thick bedded; some hummocky cross-stratified structures. Sandy dolostone is medium gray (N6-N8); weathers medium yellowish brown (10 YR 5/4); medium-thick beds with pure dolostone blebs and no chert. Samples J50 (332 m), J49 (331.5 m), J48 (331 m), J47 (330.5 m), J46 (330 m), J45 (329.5 m), J44 (329 m), and J43 (328.5 m).

5

24. Orthoquartzite and Siltstone. 2-4 m thick orthoquartzite and siltstone beds in rhythmic sets every 5 m. Siltstone coarsens upward into top (final) orthoquartzite bed.

151

23

23. Siltstone and sandstone. Siltstone is variegated (variegated sandstone and siltstone=VSS); mainly bluish white (5B 4/1); weathers to blackish red (5R 2/2); also typically green (undocumented color); thinly bedded. Sandstone is orthoquartzite; medium light gray (N6); weathers to moderate reddish brown (10R 4/6); minor in abundance.

19

22. Dolomitic sandstone marker bed. Light olive gray (5Y 6/1); weathers to moderate brown (5YR 4/6); fine to medium sand; some hummocky cross stratification (HCS). Samples J42 (285 m), J41 (284.5 m), and J40 (284 m).

1

21. (combine with unit 21 in section 2) Orthoquartzite, sandstone and siltstone. Orthoquartzite is medium light gray (N6); weathers to moderate reddish brown (10R 4/6); fine sand; thickly bedded. Sandstone and siltstone are variegated (VSS); “both “green-brown” and “lt. blue-red” shades of variegation present in VSS”-green color undocumented; bluish white (5B 4/1); weathers to blackish red (5R 2/2); fine sand; thinly bedded; some hummocky cross stratification (HCS).

27

Locality 1 (section 2, b-b')

Northeast part of Montgomery Mountains, measured about 3 kilometers west/southwest of Mt. Schader, starting at UTM zone 11S 0581155 m E 4034809 m N, and ending at UTM zone 11S 0581315 m E 4034785 m N.

Meters

Johnnie Formation (incomplete):

Zjj member (combine with Zjj in section 3):

21. (combine with unit 21 in section 3) Orthoquartzite, sandstone and siltstone. Orthoquartzite is medium light gray (N6); weathers to moderate reddish brown (10R 4/6); fine sand; thickly bedded. Sandstone and siltstone are variegated (VSS); "typical green fine sand of VSS"-green color undocumented; thinly bedded. Samples 17-BW-15 (247 m-sandstone) and 16-BW-15 (246.5 m-siltstone). 13

Total of Zjj member 88

Zji member (also see Zji from section 1):

20. Dolomitic sandstone. Medium gray (N5); weathers to pale reddish-brown (10R 5/4) and moderate yellowish-brown (10YR 5/4); fine to medium sand; medium bedded. Hummocky cross stratification (HCS), with an east-west trend in one well-exposed hummock. Samples J39 (244 m), J38 (243.5 m), J37 (243.25 m), J36 (242.75), J35 (241.5 m), J34 (241 m), and 15-BW-15 (242 m-dolomitic sandstone).

3

19. Orthoquartzite and siltstone. Orthoquartzite is medium light gray (N6); weathers to moderate reddish brown (10R 4/6); fine sand; thickly bedded. Siltstone has some sandstone (~25%) and is variegated (VSS); mainly bluish white (5B 4/1); weathers to blackish red (5R 2/2); fine sand; medium bedded. Orthoquartzite and siltstone occur in relative abundances of 75%/25% (respectively) throughout this section. Hummocky cross stratification is very prominent at ~190 m (most sandstone beds involved) and good hummocks in cross section at ~184 m; sandstone is more commonly medium-grained and micaceous at ~210 m; conspicuous thickly bedded intervals in 5-10 m cycles begin at ~215 m and continue through ~240 m. Sample 14-BW-15 (210.5 m-orthoquartzite; light purplish gray (5P 8/1); weathers to dark yellowish brown (10YR 4/4) and dusky yellowish brown (10YR 2/2); medium sand; thickly bedded). Thickness is

154

approximate; contact is covered in talus; bed surfaces in the float contain asymmetric ripples.

63

18. Orthoquartzite and siltstone. Orthoquartzite is grayish red (5R 4/2); weathers to very dusky red (10R 2/2); fine to medium sand (borderline); bedding thickness unknown. Siltstone is variegated (VSS); mainly blush white (5B 4/1); weathers to blackish red (5R 2/2); thinly bedded. Siltstone occurs in decimeter partings on ~30-70 cm sandstone beds.

14

17. Sandstone (dolomitic at the base of this unit) and siltstone. Sandstone can be light bluish gray (Munsell code unknown), grayish red purple (5RP 4/2) where carbonate-poor, and light brown (5YR 5/6) where carbonate-rich; weathers to moderate yellowish brown (10YR 5/4) where carbonate-poor, and moderate/light brown (5YR 4/6) where carbonate-rich; fine to medium sand; medium to thickly bedded. Siltstone is variegated (VSS); mainly bluish white (5B 4/1); weathers to blackish red (5R 2/2); thinly bedded. Carbonate cement occurs in lowest 2-3 sand beds; some hummocks observed, mainly parallel laminations. Sample J33 (152 m).

20

Locality 1 (section 1, a-a')

Northeast part of Montgomery Mountains, measured about 3 kilometers west/southwest of Mt. Schader, starting at UTM zone 11S 0581057 m E 4035219 m N, and ending at UTM zone 11S 0581293 m E 4035178 m N.

Meters

Johnnie Formation (incomplete):

Zji member (also see Zji from section 2):

16. Orthoquartzite and siltstone. Orthoquartzite is light gray (N7); weathers to brownish black (5YR 2/1); fine to medium sand; thin to medium bedded, mainly low angle hummocky cross stratification and parallel lamination. Siltstone is variegated (VSS); mainly medium to light bluish gray (5B 6/1), moderate red (5R 4/3 or 5R 5/4?), grayish orange pink (5YR 7/2), and grayish orange (10YR 7/4); weathers to light greenish gray (5GY 8/1), and brownish gray (5YR 4/1); laminated to massive. At the bottom, mainly low angle hummock cross stratification and parallel lamination; at the top, unit forms uniform, fairly steep hillsides and is predominantly parallel bedded with some hummocky cross stratification. Sample 13-BW-15 (198 m-coarse orthoquartzite from highest thick bed).

156

Note: unit 16 is omitted because for section 2, we restart at the base of the Zji member and repeat the same stratigraphy.

(58)

Total of Zji member 100

Zjh member:

15. Dolostone; medium gray (N5) and dark gray (N3); weathers to moderate yellow brown (10YR 5/4) and medium gray (N5); fine-grained to sucrosic; thickly bedded. Some evidence of hummocky cross stratification, but not as pronounced as in lower carbonate. “Colors vary; reddish gray top and bottom from alteration; more conspicuous here than in most markers.” Samples J32 (144 m), J31 (143.66 m), J30 (143.33 m), J29 (143 m), J28 (142.5 m), J27 (142 m), J26 (141.5 m), J25 (141 m), J24 (140.5 m), and J23 (140 m).

5

14. Sandstone and siltstone. Sandstone is medium light gray (N6); weathers to brownish gray (5YR 4/1); fine sand; thin to medium bedded. Siltstone is variegated (VSS); mainly medium to light bluish gray (5B 6/1), moderate red (5R 4/3 or 5R 5/4?), grayish orange pink (5YR 7/2), and grayish orange (10YR 7/4); weathers to

light greenish gray (5GY 8/1), and brownish gray (5YR 4/1); laminated to massive. Mainly parallel bedding.

12.25

13. Sandy limestone; medium reddish brown (10R 4/6) and moderate yellowish brown (10YR 5/4); weathers to moderate brown (10YR 5/4); fine sand; medium bedded. No well-developed lamination or internal structure. Samples J22 (126.75 m), and J21 (125.75 m).

1

12. Very fine sandstone (vfs) and siltstone. Very fine sandstone is medium light gray (N6); weathers to dusky yellowish brown (10YR 2/2); thinly bedded. Siltstone has several "modes": brown and light green (Munsell codes unknown); pale red and light green (Munsell codes unknown). Photo of light green and red vfs at ~118 m.

14.75

11. Sandstone with minor carbonate (carbonate occurs in two separate decimeter-scale beds). Sandstone is light bluish gray (5B 7/1); weathers to grayish orange (10YR 7/4) or light brown (5YR 5/6); fine sand; thinly to medium bedded. Carbonate is grayish red (5R 4/2); weathers to grayish red (10R 4/2); fine sand; thinly to medium bedded. Overall, this unit forms a resistant interval; mostly parallel bedded with some cross stratification; intense hummocky cross stratification (HCS); hummocks are apparently cross-

stratified with decimeter-scale “mounds” similar to unit 9 carbonates. Samples J20 (109 m; moderate yellowish brown (10YR 5/4); weathers to moderate brown (5YR 5/4)), and J19 (107 m).

7

10. Very fine/fine sandstone and siltstone. Very fine/fine sandstone is pale yellowish brown (10YR 6/2); weathers to dark yellowish brown (10YR 4/2); thinly bedded. Siltstone is variegated (VSS); mainly light bluish gray (5B 6/1), moderate red (5R 4/3 or 5R 5/4?), grayish orange pink (5YR 7/2), and grayish orange (10YR 7/4); weathers to light greenish gray (5GY 8/1), and brownish gray (5YR 4/1); laminated to massive. Photo of “brown-light green VSS” at ~96 m.

10

9. Stromatolitic dolostone; light olive gray (N4 or 5Y 6/1) or grayish red (10R 4/2); weathers to light olive gray (N5) or moderate yellowish brown (10YR 5/4); “macroscopically, unit tends to whether brown, lesser olive gray”; fine-grained/very fine-grained to micritic; medium to thickly bedded. Dolostone is laminated with variably steep-sided mound structures ~0.5-1 m across (three photos at ~89 m and ~92 m). Truncations of mounds observed at bedding interfaces. Samples J18 (94 m), J17 (93.66 m), J16 (93.33 m), J15 (93 m), J14 (91.5 m), J13 (91 m), J12 (90.5 m), J11 (90 m),

J10 (89.5 m), J9 (89 m), J8 (88.5 m), J7 (88 m), J6 (87.5 m), and J5 (87 m).

7

8. Sandstone; thin to medium beds are medium light gray (N6), and weather to medium dark gray (N4) or moderate yellowish brown (10YR 6/4); basal bed is light greenish gray (5GY 6/1), and weathers to dark greenish gray (5GY 4/1); fine to medium sand. Inconspicuous orthoquartzites, sandstone, and variegated sandstones and siltstones (VSS) occur near the top of this unit; near the bottom, sands are thinly bedded with no/minor cross stratification (not orthoquartzite, somewhat friable and porous in places).

18.5

7. Very fine sandstone and siltstone. Very fine sandstone is light purplish blue (5PB 8/1), or "white"; weathers to dark reddish brown (10R 4/4); thinly to medium bedded. Siltstone is variegated (VSS); mainly light bluish gray (5B 6/1), moderate red (5R 4/3 or 5R 5/4?), grayish orange pink (5YR 7/2), and grayish orange (10YR 7/4); weathers to light greenish gray (5GY 8/1), and brownish gray (5YR 4/1); laminated.

4

6. Dolostone; dark gray (N3); weathers to moderate yellowish brown (10YR 5/4); fine-grained; medium bedded with laminations

and thin (~1-2 cm) siliceous stringers; some dispersed quartz grains; complex structures; disruptions in laminations. Samples J4 (64.5 m), J3 (64 m), J2 (63.5 m), and J1 (63 m).

1.5

5. Very fine sandstone and siltstone. Very fine sandstone is light purplish blue (5PB 8/1), or "white"; weathers to dark reddish brown (10R 4/4); thinly to medium bedded; interbeds are massively textured, with a fair degree of induration. Siltstone is variegated (VSS); mainly light bluish gray (5B 6/1), moderate red (5R 4/3 or 5R 5/4?), grayish orange pink (5YR 7/2), and grayish orange (10YR 7/4); weathers to light greenish gray (5GY 8/1), and brownish gray (5YR 4/1); laminated. Overall, this is a recessive, slope-forming unit.

17.5

4. Orthoquartzite and very fine sandstone/siltstone. Orthoquartzite is medium light gray (N6); weathers to medium gray (N5); fine to medium sand; thickly bedded at base, medium to thinly bedded higher in unit; heavy desert varnish and cross-stratified higher in unit; silty "caps" on sandstone beds have abundant grooves/tool-markings, and small current ripples. Very fine sandstone/siltstone can be moderate red/grayish red (5R 4/3), light brown (5YR 5/6), or medium light bluish gray (5B 6/1); weathers to moderate red/grayish red (5R 4/3), moderate brown (5YR 4/4), or light

161

greenish gray (5GY 8/1) and darker hues. Generally, orthoquartzite is resistant, while very fine sandstone is recessive.

6.5

Total of Zjh member 105

Zjg member (incomplete)

3. Interstratified variegated sandstone and siltstone (VSS), and orthoquartzite. Siltstone has various hues and is “patchy” or “pinstriped”; hues include medium light bluish gray (5B 6/1), grayish orange pink (5YR 7/2), and grayish orange (10YR 7/4); weathers to brownish gray (5YR 4/1), light greenish gray (5GY 8/1), and darker hues. Sandstone is moderate red to grayish red (5R 4/3); weathers to moderate red/grayish red (5R 4/3); fine-grained. VSS is interstratified on the cm-scale. Orthoquartzite is medium gray (N6); weathers to medium dark gray (N4); thinly to medium bedded; 0.5 m foresets with steeply truncated laminatiosn observed near base at ~16 m. VSS is generally recessive and slope-forming unit; orthoquartzite beds are resistant.

22

2. Orthoquartzite; medium light gray (N6); weathers to medium dark gray (N4); thinly bedded. Thickness of this unit is certainly >2 m because there is a minor break in section (due to poor exposure).	162
1. Interstratified variegated sandstone and siltstone (VSS), and orthoquartzite. Sandstone is light brown (5YR 5/6); weathers to moderate brown (5YR 4/4); medium to fine sand; thinly to medium bedded. Siltstone is medium to light bluish gray (5B 6/1); weathers to light greenish gray (5GY 8/1) and darker hues; laminated to massive. Orthoquartzite is medium gray (N6); weathers to medium dark gray (N4); medium sand; thin to medium parallel bedding, with low-angle trough cross stratification observed at ~3 m.	2
	15

Total of incomplete Zjg member	39

Total of incomplete Johnnie Formation	538

Chapter 3

THE LAVIC LAKE FAULT: A LONG TERM CUMULATIVE SLIP ANALYSIS VIA COMBINED FIELD WORK AND THERMAL HYPERSPECTRAL AIRBORNE REMOTE SENSING

Rebecca A. Witkosky[1], Joann M. Stock[1], David M. Tratt[2], Kerry N. Buckland[2], Paul M. Adams[2], Patrick D. Johnson[2], David K. Lynch[2], and Francis J. Sousa[3]

[1]*California Institute of Technology, Division of Geological and Planetary Sciences, 1200 E. California Blvd., MC 170-25, Pasadena CA 91125*

[2]*The Aerospace Corporation, 2310 E. El Segundo Blvd., El Segundo CA 90245*

[3]*Oregon State University, College of Earth, Ocean, and Atmospheric Sciences, 104 CEOAS Administration Building, Corvallis, OR 97331-5503*

ABSTRACT

The 1999 Mw 7.1 Hector Mine earthquake was a major surface-rupturing event in the Mojave Desert region of eastern California, with coseismic right-lateral slip in excess of 5 m along the Lavic Lake fault. The cumulative long-term bedrock offset and geologic slip rate of this fault are not well defined, which inhibits tectonic reconstructions of the Eastern California shear zone (ECSZ). Furthermore, access to the fault is restricted, which complicates field work to study the fault's geological history. We gained access to the area in 2012 and 2014 to collect new field data, and in 2013, we collected new thermal

hyperspectral airborne imagery with a 2 m pixel size. With this new data, and auxiliary information from older geologic maps, we created lithologic maps of the area using supervised and unsupervised classifications of the remote sensing imagery. Based on our own field observations, we defined end member rock classes for the supervised classifications over a small test area. The high spatial and spectral resolution of the airborne sensor, along with a lack of significant vegetation, allowed us to optimize a data processing sequence for supervised classifications, resulting in lithologic maps of the test area with an overall accuracy of 71 ± 1%. For the unsupervised classifications, we first relied on an algorithm to define classes based on spectral information within the complete swath of remote sensing imagery, and then assigned rock types to these classes using information from a previous map of the area. To identify bedrock offset by the fault, we used the unsupervised lithologic classification map. A boundary between units in our unsupervised classification map correlated very well with a lithologic boundary that is displaced by the fault in a previously published geologic map. The lithologic boundary, a depositional contact between two volcanic units, pre-dates the Lavic Lake fault, thus capturing the entire cumulative long-term offset. We used the displaced depositional contact to calculate the vertical component of slip along the main Lavic Lake fault, and an older cross fault to measure the horizontal component of slip along the main fault. We then combined the vertical and horizontal components to derive a net fault slip of 960 +70/-40 m. We interpret that value as a maximum due to uncertainty in the dip angle of the cross fault. Our value is significantly less than a previous estimate of cumulative offset (3.4 ± 0.8 km) that was based on an offset magnetic feature, which we suggest may be partially due to off-fault deformation along proximal, smaller ECSZ structures. Our data corroborate past suggestions that transient tectonic

activity in the ECSZ may be responsible for the observed discrepancy between the higher current, measured geodetic slip rate and the total geologic rate since ~750 ka.

INTRODUCTION

The 1992 Mw 7.3 Landers and 1999 M_w 7.1 Hector Mine earthquakes resulted in two major surface ruptures in the Mojave Desert region of eastern California (Figure 1). The faults that ruptured in the 1992 Landers event were mostly located on publicly accessible land, allowing considerable subsequent geologic investigation (e.g. Sieh et al., 1993; Johnson et al., 1993; Arrowsmith and Rhodes, 1994; Unruh et al., 1994; Spotila and Sieh, 1995; Zachariasen and Sieh, 1995; Savage and Svarc, 1997; McGill and Rubin, 1999; Rockwell et al., 2000). However, faults that ruptured in the 1999 Hector Mine event (Figure 1), which include the Lavic Lake fault, and portions of the Calico-Hidalgo, Mesquite Lake, Pisgah-Bullion faults (Figure 2A), lie within the United States Marine Corps Air Ground Combat Center (MCAGCC), Twentynine Palms, and therefore received only limited field-based study (Treiman et al., 2002).

Remote sensing methods can yield additional useful data for studying these faults. The coseismic slip of the 1999 Hector Mine earthquake has been investigated with several remote sensing methods: InSAR from Fialko and Simons (2001); InSAR from Sandwell et al. (2002); InSAR and GPS from Simons et al. (2002); lidar-based offset measurements from Hudnut et al. (2002); lidar-based offset measurements from Chen et al. (2015); lidar-based (as well as field-based) offset measurements from Sousa (2016). Results of these studies generally concur with the principal field-based slip measurements (Treiman et al., 2002).

In this paper we use a new and more detailed remote sensing data set, thermal hyperspectral airborne imagery, to produce a geologic swath map and estimate the cumulative long-term tectonic offset of bedrock along the Lavic Lake fault. With this imagery, it is possible to differentiate various minerals and lithology within a scene by comparison of their spectra via supervised and unsupervised classifications. These are algorithmic classification methods for grouping pixels in an image by quantifying and comparing spectral similarity. We first used supervised classifications, which require the user to have some knowledge of ground cover (for lithologic mapping, the composition of rocks exposed at the surface) over an area to "train" the algorithm by deciding a priori what end member components will be mapped within an image. These classifications allow the user to quantify the accuracy of the mapping algorithm through comparison with ground-truth data. Ultimately, we also used unsupervised classifications that do not require any knowledge of ground cover but still group and map pixels into classes based on spectral similarity. Unsupervised classifications are more subjective and exploratory, but a quantitative accuracy analysis is not possible without ground truth data. We took a hybrid approach to exploit the advantages of both methods, by mapping a small example site in the field and then using supervised classifications to find the optimum hyperspectral image data processing sequence. This allowed us to use our dataset for remote geologic mapping via unsupervised classifications over a much larger area.

The thermal infrared wavelength range, λ = 8-15 μm, is appropriate for mapping volcanic lithologies, such as those along the Lavic Lake fault, due to a silica absorption feature known as the Reststrahlen band. The Reststrahlen band appears as a minimum in emissivity spectra for silicate rocks and minerals and shifts to longer wavelengths as the

degree of silica polymerization in a rock or mineral decreases (Launer, 1952). The base unit in silicate minerals is the silica tetrahedron (SiO_4). Polymerization occurs as silica tetrahedra in a crystal structure share an increasing number of oxygen ions, which increases the Si:O ratio and resultant weight percent silica. The Reststrahlen band is positioned at a longer wavelength for olivine (found in basaltic or ultramafic rocks), a silicate mineral that lacks Si:O polymerization, than for quartz (found in rhyolite or granite), in which polymerization and resultant weight percent silica is maximized. Since differences in volcanic lithology are defined by variations in weight percent silica (e.g., Le Bas et al., 1986), the shift in the Reststrahlen band can be used to map geochemical variation in volcanic rocks (Hook et al., 2005). Therefore, spectra measured in the thermal infrared are ideal for categorizing and mapping the volcanic lithologies present along the Lavic Lake fault.

Our goal in mapping the geology and total tectonic offset of the Lavic Lake fault is to expand and improve the information relevant to active tectonics and related seismic hazards in southern California. The fault is located in the Bullion Mountains of the Mojave Desert, California, but there is limited information on the geology of this area. The long-term cumulative offset along the Lavic Lake fault is not well resolved; in older maps, the Lavic Lake fault had not been formally named, the sense of displacement was unknown, and much of the fault's surface trace was only mapped as an approximate location (Kupfer and Bassett, 1962; Dibblee, 1966 (republished in 2008); Dibblee, 1967a; 1967b; 1967c).

The 1999 earthquake and surface rupture provided key new information about this fault and also motivated additional studies. Treiman et al. (2002) were able to map the surface trace and determine that the fault slip was generally right lateral. The Hector Mine Earthquake Geologic Working Group (1999) formally named the fault after the Lavic Lake

playa, a geographic feature crossed by the northern end of the fault (Figure 2A). A cumulative offset measurement for the Lavic Lake fault was then determined via geophysical methods: Jachens et al. (2002) estimated 3.4 ± 0.8 km of dextral offset from offset magnetic anomaly pairs within the Bullion Mountains. Because the age of these offset magnetic anomaly pairs is unknown, a geologic slip rate could not be calculated. The geologic slip rate would be useful because of the discrepancy between integrated geologic fault slip rates and current geodetic crustal motion (~6 and 12 mm/yr, respectively) in eastern California (Oskin et al., 2008). Long-term average geologic slip rates for the eastern California shear zone (ECSZ) range from 8.3 ± 1 mm/yr since 12 Ma (McQuarrie and Wernicke, 2005), to ≤6.2 ± 1.9 mm/yr since ~750 ka (Oskin et al., 2008). While Oskin et al. (2008) refer to their value as "geologic" rate, it could instead be considered a "geomorphic" rate, since it is averaged over a time interval of 10^3-10^6 years (e.g, see Table 2 in Friedrich et al. (2003), where "geologic" rates are defined as averages over 10^6-10^7 years). The discrepancy between geologic and geodetic slip rates in the eastern California shear zone could be minimized by including more accurate active fault slip rates into the total.

Paleoseismology on the Lavic Lake fault in the playa area following the 1999 earthquake also yielded several important results: the surface trace of the 1999 event had not previously ruptured for at least 7000 years, but another strand with geomorphic evidence (vegetation lineaments and uplifted basalt exposures) for recent activity ruptured sometime within the past ~1750 years (Rymer et al., 2002). Rymer et al. (2002) suggested that deformation has not yet been fully localized onto a single strand, suggesting that the Lavic Lake fault is relatively young. Since fault roughness and cumulative offset vary with age, a young fault provides an important data point for evaluating seismic hazard as a function of

fault maturity. Our objective is to measure the cumulative offset, which can be combined with bedrock ages to calculate a minimum geologic slip rate, and can also be used for palinspastic reconstructions of eastern California (e.g., McQuarrie and Wernicke, 2005).

GEOLOGIC SETTING

The Lavic Lake and Bullion faults are located in the Bullion Mountains, Mojave Desert, California. The Bullion Mountains have some 200 to 400 meters of topographic relief in bedrock outcrops. These include extrusive Tertiary and Quaternary igneous rocks, and underlying hypabyssal and intrusive lithologies of pre-Tertiary age (Kupfer and Bassett, 1962). Surficial weathering of the volcanic bedrock has resulted in alteration to abundant clay and zeolite minerals, and erosion has created Quaternary surficial deposits of colluvium and fanglomerate. In the northwest portion of the Bullion Mountains where Miocene (?) to Oligocene igneous extrusive rocks crop out, the 1999 Hector Mine earthquake surface rupture along the Lavic Lake fault (Figures 1 and 2) reached a maximum right-lateral displacement exceeding 5 m (Treiman et al., 2002). Lithologic composition ranges from andesitic to basaltic, with massive and porphyritic textures (Dibblee, 1966). Bedding is right-side up in this area, and attitudes generally strike northwest with $\leq 30°$ dip to the northeast. Many small faults are present that strike approximately northwest and show some right-lateral separation, and there are also faults that strike generally east-west, with either left-lateral or unknown sense of motion (Kupfer and Bassett, 1962). The other major named structure in the area, the Bullion fault, strikes approximately northwest and bounds the southwestern extent of the Bullion Mountains. This fault is sometimes combined with others

to define the Bullion-Rodman-Pisgah fault (e.g., Richard, 1993) with net slip estimates that range from 6.4-14.4 km (Dokka, 1983), up to 20-40 km (Garfunkel, 1974).

Immediately north of the Bullion Mountains lies the Lavic Lake playa, which is composed mainly of hard packed clay (Kupfer and Bassett, 1962) and contains decameter-scale surficial fractures and fissures that are linear and polygonal in shape. The fractures persist through multiple rainy seasons, and are likely caused by some combination of desiccation and crustal deformation (some from the 1999 Hector Mine earthquake). Farther north, the 22.5 ± 1.3 ka Pisgah basalts (Phillips, 2003) are in contact with Lavic Lake playa deposits. Paleoseismic trenching and dating of Lavic Lake playa strata (Rymer et al., 2002) show that the shallowest sediments postdate the Pisgah lavas. But because the thicknesses of these units are unknown, an interfingering contact between these two units cannot be ruled out.

The Lavic Lake fault is one of many faults comprising a tectonic province formally named the Eastern California shear zone (ECSZ) by Dokka and Travis (1990a; 1990b). Estimates for the inception age of ECSZ faulting vary widely, but some straightforward constraints come from cross-cutting field relationships. A minimum age for the onset of at least some ECSZ faulting is provided by a 3.77 ± 0.11 Ma basaltic lava that drapes over a fault scarp in the Black Mountains, near the Garlock fault (Oskin and Iriondo, 2004). Schermer et al. (1996) found that <11.7 Ma Miocene fan deposits and their older substrate are cut and displaced the same amount by component faults in the northeastern Mojave Desert with left-lateral offset. A palinspastic restoration model of mountain ranges in the southwestern United States concurs with the upper age limit of Schermer et al. (1996), finding ECSZ right-lateral displacement along faults oriented on average N25°W, since c.

12 Ma (McQuarrie and Wernicke, 2005). Several other estimates of ECSZ inception age utilize disparate methods, but all fall in the range of 5-6 Ma. Regional deformation in eastern California transitioned from extensional to right-lateral shear from 6-8 Ma (Snow and Wernicke, 2000), and this generalized right-lateral shear occurs from the Death Valley region across the Garlock fault into the northern extent of the ECSZ. Modeling the deflection of the Garlock fault suggests that right-lateral shear has deformed the region since 5.0 ± 0.4 Ma (Gan et al., 2003). Miller and Yount (2002) suggest that the proliferation of east-west striking left-lateral faults within the ECSZ controlled topography and consequently the flow direction of 5-6 Ma basaltic lavas. Woodburne (2015) couples ECSZ inception with, or possibly as a byproduct of, the opening of the Gulf of California at c. 6 Ma (Atwater, 1992; Atwater and Stock, 1998; Oskin and Stock, 2003; Bennett et al., 2015), and also cites a period of non-deposition in the Mojave Desert region until c. 6 Ma to strengthen the argument of tectonic quiescence prior to that time. Constraints for the age of inception of the ECSZ are summarized in Table 1.

In compiling the tectonic history of the ECSZ, the addition of cumulative net slip across all faults can be combined with age of inception to infer long-term geologic slip rates across the region. Earlier estimates of cumulative net slip across all right-lateral faults, striking approximately northwest, generally varied between 25-65 km (Dokka, 1983; Dokka and Travis, 1990a; Jagiello, 1991; Richard, 1993), but more recent estimates increase to about 100 km (McQuarrie and Wernicke, 2005; Bennett et al., 2016). The models used to derive net slip typically invoke clockwise rotation of fault blocks or considerable off-fault, continuous strain (Richard, 1993; McQuarrie and Wernicke, 2005), as this also can explain left-lateral slip along east-west striking faults within the ECSZ (e.g., see the model of

Luyendyk et al., 1980), although some opposing views imply counter clockwise rotation of the fault blocks bounded by right-lateral faults (Garfunkel, 1974; Dokka and Travis, 1990a). Although some groups (Golombek and Brown, 1988; Ross et al., 1989) have shown compelling paleomagnetic evidence for early Miocene clockwise rotation of some areas in the Mojave Desert, MacFadden et al. (1990a; 1990b) also pointed out that paleomagnetic results can vary locally and temporally, showing that caution is required in invoking a single generalized model of uniform rotation across the entire region.

Tallied net slips have been combined with age of inception to calculate the long-term geologic slip rate across the entire region, but results vary widely, anywhere from 3-12 mm/yr since the Early, Middle, or Late Miocene (Dokka and Travis, 1990b). A more recent and precise approach, however, involves extensive field work to find dateable offset piercing points along as many of the active faults in the region as possible, then integrating these results into a single value. Such an approach was undertaken by Oskin et al. (2008), who combined geologic slip rates from six major faults with Quaternary slip to arrive at a "sum geologic Mojave ECSZ slip rate" of $\leq 6.2 \pm 1.9$ mm/yr since ~750 ka. The inequality marker indicates that they used maximum possible offset values (and subsequent rates) for six specific faults to derive the summed rate. But in another sense, the value also represents a minimum, since data do not exist for every single active fault strand within the area of the integration, and do not account for continuous, off-fault strain (e.g., McQuarrie and Wernicke, 2005). Nonetheless, this result highlights a discrepancy between results from geology and geodesy, whose scientists often collaborate to study earthquake science and seismic hazards in southern California. With GPS tracking of tectonic motion, geodetic slip rate estimates across the ECSZ are usually >10 mm/yr (Sauber et al., 1994; Dixon et al.,

1995; Miller et al., 2001; McClusky et al., 2001; Becker et al., 2005; Spinler et al., 2010; McGill et al., 2015), much faster than the sum geologic rate from Oskin et al. (2008). Some geodetic slip rates are <10 mm/yr and more closely agree with the summed geologic rate, but they are either based on older data (Sauber et al., 1986; Savage et al., 1990), alternative methods (Peltzer et al., 2001), or are modeled with greatest effort to agree with and thus solve the discrepancy between the sum geologic rate (e.g. Chuang and Johnson, 2011). Meade and Hager (2005), Oskin et al. (2008), and Spinler et al. (2010) have all pointed out that although there may have been a post-seismic flare-up following the 1992 Landers and 1999 Hector Mine earthquakes, this does not explain the discrepancy, because a relatively fast geodetic rate (Sauber et al., 1994) had already been observed prior to those two major events. Another explanation for the discrepancy is the incorporation of off-fault deformation into either the sum geologic rate, the geodetic model used, or both. In this case much of the shear strain in the ECSZ could be distributed over the entire region and not confined to the fault segments portrayed in models. Analyses that considered off-fault deformation have minimized the discrepancy significantly (e.g., McQuarrie and Wernicke, 2005; Bird, 2009; Shelef and Oskin, 2010; Johnson, 2013). The assumption that some of the fault slip is absorbed by distributed shear (i.e., off fault deformation) increases the geologic rate (e.g., Chuang and Johnson, 2011). Analogously, designing the geodetic data inversion model to incorporate off-fault deformation decreases the geodetic rate (Herbert et al., 2014). In the end, both approaches minimize the discrepancy. Even with these approaches, though, a discrepancy of a few mm/yr often remains (depending on which values are compared). Therefore, there must still be more unaccounted-for active faults with geologic slip rates that should be integrated into the sum geologic slip rate, taking into account strain compatibility with the surrounding

region, before comparing with geodetic results (McQuarrie and Wernicke, 2005). The Lavic Lake fault, having the largest and most recent surface rupturing event in the ECSZ, is a good candidate to consider, making a logical starting point for this type of analysis.

METHODS

Hyperspectral data collection

Hyperspectral airborne imagery was collected on 27 August 2013 (at 11:00 am Pacific daylight savings time) using Mako, a whiskbroom-type sensor developed by The Aerospace Corporation. Mako measures emitted surface radiance in the thermal infrared at 128 bands covering wavelengths from 7.6-13.4 μm (Hall et al., 2011; Buckland et al., 2017). We used a 1.8 km wide, 11 km long swath with 2 m pixel resolution, from a flight at 12000 feet above ground level (c. 15000 feet altitude). The footprint of the swath was centered along the Lavic Lake fault and covered the 1999 maximum slip zone of the earthquake in the Bullion Mountains (Figure 2A, 2B).

Mako sensor calibration

The Mako airborne hyperspectral infrared sensor underwent radiometric and wavelength calibration. For radiometric calibration, two onboard blackbody sources were observed immediately before and after the scene was acquired. These were stabilized at different temperatures that spanned the expected radiance values of the scene. A linear

relation between the known blackbody radiance input and the digital counting output was assumed so that the sensor response could be modeled with multiplicative gain and additive offset terms. The gain and offset terms for the pre- and post-collect calibrations were then time-interpolated to match the actual collection time of the data.

The wavelength calibration was done by observing blackbody sources covered by National Institute of Standards and Technology (NIST) traceable transparent polymer films (with calibrated absorption features), and performing a least-squares fit across the full extent of the focal plane array. For more detailed descriptions of the calibration processes, see Hall et al. (2011) and Buckland et al. (2017).

Ground truth field mapping of the Red Flake site

Using a specific field site, we quantified the accuracy to which lithology along the Lavic Lake fault can be mapped with pixel-based image classifications (Figures 2B-2F, 3, and 4A). Limited access to the field site was granted by the Marine Corps Air Ground Combat Center (MCAGCC) in December 2012 and April 2014 (Figure 3A-3C). The ground truth site was c. 5000 m^2 in size, and centered at 34.586078° north, 116.288492° west. We refer to it as the "Red Flake" site after the presence of a prominent, 1-m-tall scarp of red feldspar porphyry that protrudes from the 1999 earthquake surface rupture (Figure 3C). The site was well suited for remote sensing due to the variety of geologic units that are very well exposed with little vegetative overgrowth. We identified primary mineralogy and mapped out the contacts between distinct lithologic units. The lithologic contacts between units are diffuse over a scale smaller than the hyperspectral image pixel size (2 m), making conditions

favorable for unequivocally identifying the boundaries between distinct units with remote sensing classification methods. At the Red Flake site, we identified and mapped the following four lithologic units to guide a supervised classification: 1) tuff (and tuff breccia), 2) detritus (colluvium), 3) feldspar porphyry, and 4) microcrystalline lava (Figure 4A).

While mapping the Red Flake site, hand samples were also collected for laboratory methods: x-ray diffraction (XRD) mineral identification, and laboratory thermal infrared spectroscopy. XRD was performed with a PANalytical X'Pert Pro MPD diffractometer using copper radiation and an X'Celerator strip detector in theta 2-theta mode. Thermal infrared laboratory spectra were taken from the upward-facing weathered surfaces of the sample chips using the biconical reflectance method. Reflectance spectra were measured using a Thermo-Nicolet 6700 FTIR Spectrometer, with a Harrick Scientific "Praying Mantis" diffuse reflection accessory. All laboratory spectra were measured with a spot size of 1-2 mm, and each final spectrum was an average of 150 scans taken over 4-6 minutes. The laboratory spectra were converted to emissivity using Kirchhoff's law (Robitaille, 2009) and are shown in Figure 5. Although Kirchhoff's law cannot be used to convert biconical reflectance spectra to emissivity for quantitative purposes (Salisbury and Walter, 1989; Christensen and Harrison, 1993; Salisbury et al., 1994), the same qualitative shape results when compared to direct spectral emissivity measurements (e.g., Figure 3b in Christensen and Harrison, 1993; Figure 4 in Christensen et al., 2000).

Supervised classification of the Red Flake site

We developed the following image processing sequence to create a final supervised classification with the highest possible accuracy (Figure 6, left hand path). All processing steps, unless otherwise specified, were completed using the Environment for Visualizing Images Software, version 4.8 (ENVI, Exelis Visual Information Solutions, Boulder, Colorado). We began with data cubes of airborne thermal hyperspectral imagery that had undergone radiometric and wavelength calibration, bad pixel replacement, and spectral smile removal.

In regard to the terminology used herein regarding hyperspectral image data from the Mako whiskbroom sensor, each single whisk is a single data cube, so the words "whisk" and "data cube" are used interchangeably. The spatial extent of a single whisk relative to the complete image swath can be seen in Figure 7: in the c. 100 m-scale sawtooth pattern along the side of the image swath, the point of each tooth is the boundary between two whisks (two adjacent whisks generally have a small amount of overlap). When multiple data cubes (or whisks) are concatenated, the set of combined data cubes can be called a "super cube." Although a set of combined super cubes can still be called a super cube, the full hyperspectral imagery data set presented here consists of two super cubes with different flight line azimuthal directions (to accommodate the change in strike of the Lavic Lake fault's surface trace), and when those two super cubes are combined, we call this the "complete image swath."

For the hyperspectral image data presented here, we also removed the bands that covered wavelengths from 7.6-8.4 μm because they were dominated by noise. At this point, under normal circumstances, we would concatenate as many data cubes (whisks) as necessary to cover the area of interest and carry out the subsequent processing steps in bulk;

however, this was not necessary for the Red Flake site because the extent of the area was imaged in a single whisk. Next, we performed an in-scene atmospheric compensation (ISAC algorithm from Young et al., 2002), setting the regression pixels to maximum hit, the fitting technique to normalized regression, and using for the noise equivalent spectral radiance (NESR), the median value for the data cube(s). Then, we did a principal component analysis (PCA) to identify any variance throughout the image that resulted from noise or data artifacts (Richards, 2013). A gradation through each individual data cube was present along the flight direction, producing a spurious spectral signal that we discarded in a PCA inverse transformation (Richards, 2013). Next, we converted the data from at-sensor radiance to emissivity with the emissivity normalization method (Kealy and Hook, 1993).

We then performed the supervised classification on emissivity spectra using the spectral angle mapper (SAM, described in Kruse et al., 1993). To remain objective, "end member" spectra for each class were defined by randomly choosing 2% of the pixels from each lithologic area in the geologic map and averaging their spectra (Figure 4B, 4C). For the SAM, we imposed a maximum angle threshold of 0.1 radian, leaving very few pixels unclassified. Post-classification, we used the "sieve" and "clump" functions in ENVI (i.e, replace single pixels that were classified differently from surrounding pixels) to correct for pixel classification errors due to small desert scrub or transported lithology. We repeated this procedure ten times. The ten results were tallied via error matrices (Congalton, 1991), and then used to calculate a mean and standard deviation for classification accuracy values (Tables 2 and 3). For more detailed information about supervised classifications, see Appendix: 'Background on supervised classifications and how they were applied to this work,' and 'Guide for interpreting error matrices.'

Unsupervised classification of the complete image swath

The data processing flow chart for our hyperspectral airborne image unsupervised classification is shown in Figure 6, right-hand path. For the unsupervised classification, we first concatenated the 70 data cubes (whisks) that made up the complete aerial image swath into a single super cube, and then performed the ISAC. Then, instead of performing a PCA like we did for the supervised classification, we used a minimum noise fraction (MNF) transformation (Green et al., 1988; note that it is called a "maximum noise fraction" in that paper; also, see Lee et al., 1990). The MNF transformation involves a PCA that is performed on the data set after: 1) the noise in the data is estimated (or if known, the noise can be declared); 2) any correlations between bands are removed; and 3) the data noise variance is normalized (Kruse, 1996). The resulting principal components are then ordered by decreasing signal-to-noise ratio (as opposed to decreasing variance, as in the standard PCA). MNF performed better than PCA here, possibly due to improved noise statistics when using the entire image swath versus a single data cube for supervised classifications of the Red Flake site (where PCA was used in place of MNF because the former resulted in a higher overall classification accuracy). Figure 7 shows the complete image swath of MNF components in false color.

We found that unsupervised classifications on the complete image swath worked qualitatively better when classifying the MNF components directly without inverting back to radiance and then converting to emissivity (we still discarded any components clearly dominated by noise or data artifacts). For classifying, we used the K-Means clustering

algorithm (described in Tou and Gonzalez, 1974) with a change threshold of 5%. To ensure that every pixel would be classified, we applied no value to the "maximum standard deviation from mean" and "maximum distance error" parameters. The cluster centers stabilized below our indicated change threshold after seven iterations. Finally, we used information from Dibblee (1966) to identify the lithology that each class represented, and to superimpose lithologic contact lines for a qualitative comparison with our class boundary lines.

Within our hyperspectral image footprint, Dibblee (1966) mapped twelve separate lithologic units. While we could have used Dibblee's lithologic units as "ground truth" to perform supervised classifications (like at the Red Flake site) on the complete image swath, we wanted to pursue a more objective and exploratory method for the larger area, that could potentially identify details that had not yet been discovered. Using the same number of classes (or more) as lithologic units from Dibblee (1966) would have been ideal, but as we experimented with increasing the number of classes with the K-Means classification algorithm, the product generally became more difficult to interpret. Ultimately, we settled on using six classes (Table 4). Using six classes yielded a clear distinction between the main bedrock units in the image without making our map overly detailed, to the extent that it would be impossible to generalize broadly and interpret.

RESULTS

Ground truth field mapping of the Red Flake site

A geologic map for the Red Flake site is shown in Figure 4A, and laboratory spectra for the hand samples are shown in Figure 5. The lithologic descriptions that follow are based on a combination of field identification, hand sample description, and laboratory XRD analyses. Note that the lithologic units we identified and used for these supervised classifications are from our own on-site geologic mapping, and therefore do not necessarily correlate with any specific lithologic units from the geologic maps of Dibblee (1966; 1967a; 1967b; 1967c; 2008), which will be referenced and discussed further in subsequent sections.

Tuff (and tuff breccia)

The tuff and tuff breccia are generally white- to tan-colored, containing <1 mm grains of biotite, hornblende laths, and quartz in a microcrystalline matrix of silicate ash. Additional minerals identified with XRD are plagioclase feldspar solid solutions (andesine), potassium feldspar solid solutions (sanidine and possibly microcline), zeolites (clinoptilolite), and the high-temperature quartz polymorph cristobalite (exact quantity not determined with our methods). Laboratory spectra for the tuff and tuff breccia are shown in Figure 5A.

Detritus (colluvium)

A portion of the Red Flake site is covered in a thin veneer of detrital material. We define this as a ground truth unit because in attempts at identifying lithology from an airborne platform, only the immediate surficial material can be observed and classified. The detritus is a heterogeneous mixture of volcaniclastic sand and gravel derived from proximal lithologic

units: primarily quartz and other weathering-resistant minerals with clasts ranging from <1 mm up to 2 mm in diameter, and also some larger cobbles and boulders up to 50 cm. Additional minerals identified with XRD are calcite, plagioclase feldspar solid solutions (albite and andesine), potassium feldspar solid solutions (sanidine), and cristobalite. A laboratory spectrum for the detritus is shown in Figure 5B.

Feldspar porphyry

The feldspar porphyry may be massive or banded, and has a pinkish to dark red fine-grained matrix, with 1-10 mm phenocrysts of feldspar, occasional biotite, and rare quartz. Additional minerals identified with XRD are plagioclase feldspar solid solutions (albite), potassium feldspar solid solutions (sanidine), and cristobalite. Laboratory spectra for the feldspar porphyry are shown in Figure 5C.

Microcrystalline lava

The microcrystalline lava can be massive or banded. This unit has a very dark purple to grayish-brown microcrystalline matrix with some feldspar, glass, and vesicles up to 3 mm (vesicles can be calcite-, quartz-, or zeolite-filled). Additional minerals identified with XRD are pyroxene solid solutions (augite and diopside), and plagioclase feldspar solid solutions (andesine, bytownite, and anorthite). Laboratory spectra for the microcrystalline lava are shown in Figure 5D.

Thermal infrared laboratory spectra

We can use the Reststrahlen position (minimum in an emissivity spectrum) to compare relative silica weight percent for each of the lithologies at the Red Flake site (e.g., Launer, 1952; Hook et al., 2005. Emissivity minima wavelength positions for laboratory spectra from Red Flake site lithologies descend in the following order (followed in parentheses by the average, with one standard deviation, wavelength positions from Figure 5): microcrystalline lava (9.56 ± 0.06 μm, n = 2), detritus (9.50 ± 0.00 μm, n = 1), tuff and tuff breccia (9.26 ± 0.02 μm, n = 4), and feldspar porphyry (9.17 ± 0.44 μm, n = 3). Therefore, it is likely that the silica weight percent increases in the same order for the suite of Red Flake site lithologies. This interpretation could be complicated by weathering, alteration, and/or surficial coatings (e.g. desert varnish), since the spectra were collected from the upward-facing weathered surfaces of the sample chips.

Supervised classification of the Red Flake site

The results for the ten supervised classifications we performed are shown in Figure 8. Mean and standard deviation (one sigma) accuracy percentage values (all rounded to the nearest integer), for each lithology we defined in the field, were calculated using error matrices from the ten supervised classifications we performed, each with its own randomly generated set of end member spectra (see Figure 4B for example). The ground truth in this case was our geological map from field work (Figures 2C-2F, 3, and 4). Producer's, user's and overall accuracies are tallied in error matrices and summarized in Tables 2 and 3 (also

see Appendix: 'Background on supervised classifications and how they were applied to this work,' and 'Guide for interpreting error matrices'). The statistical spread for overall accuracy of the final supervised classification analysis was 71 ± 1% (1σ, n = 10). The microcrystalline lava had the smallest difference between producer's and user's accuracies at 89 ± 3% and 86 ± 1% respectively (Table 3). This means that on average, the method correctly classified 89% of the pixels labeled microcrystalline lava on our geologic map, and 86% of the pixels classified as microcrystalline lava across the entire Red Flake site fell within our lithologic boundaries for the unit. In contrast, the detritus had the largest difference between producer's and user's accuracies, with 71 ± 24% and 19 ± 6% respectively. Again, the method correctly classified 71% of the pixels labeled detritus on our geologic map, but only 19% of the pixels classified as detritus across the entire Red Flake site fell within our lithologic boundaries for the unit. The accuracy ratings for the tuff, and feldspar porphyry were often <50%.

Unsupervised classification of the complete image swath and interpretation as a geologic map

The complete (unsupervised classification) geologic swath map is shown in Figure 9. With the unsupervised classification, our main goal was to identify features suitable for cumulative offset measurements. Thus, we were concerned with discerning the apparent contact lines between units as revealed by the classification map. To facilitate this analysis, we took into account lithologic contact lines from published geologic maps (Dibblee, 1966; 1967a; 1967b; 1967c; 2008). Note that in this section, references to the work of Dibblee include all of those publications, but the primary reference is the 1966 map. We

superimposed the lithologic contacts from Dibblee onto our classification map, to visually check by inspection whether lithologic boundaries apparent in the unsupervised classification were true. We also added Dibblee's approximate surface trace for the Lavic Lake fault because it provided a single line for annotation that approximates the highly detailed line set of the 1999 earthquake surface rupture (Treiman et al., 2002) very well. We qualitatively evaluated the unsupervised classification evaluated by visual inspection and comparison with the lithologic contacts from the Dibblee maps, so some of these results required broad generalizations and interpretation.

We used Dibblee's maps to define lithologic compositions for our unsupervised classification units, and to compare our class boundaries with the lithologic contacts. In some areas, the class boundaries we observed in our classification map correlate very well with the lithologic contacts, but in other places they did not. A lithologic contact line between a tuff breccia and a basalt correlates well with a boundary between two of the classes from our unsupervised classification map (west-central portion of zoom inset in Figure 9, Figures 10, 11, and Table 4). The unsupervised classification also produced a unique class that spatially correlated with a felsite unit (east-central portion in Figure 9). In this case, the felsite unit also forms a topographic ridge (labeled with white arrow in main part of Figure 9), and the class extends a few hundred meters to the west and south beyond the felsite contact. The mismatch in spatial correlation is probably due to erosion and transport of rocks away from the ridge, akin to accuracy issues we described previously for the detritus in the supervised classification.

We found that in general, each one of Dibblee's bounded lithologic units contained a range of our classes (Figure 9). This was also the case for the multi-lithologic Red Flake

supervised classification site, the majority of which was more broadly mapped as andesite by Dibblee. It is possible that one or more of the lithologic units at the Red Flake site are andesitic in composition, but the precise geochemical measurements required to apply that name correctly (e.g., Le Bas et al., 1986) were outside of the scope of this study. The occurrence of multiple lithologic classes from our map included within a single one of Dibblee's bounded lithologic units could be due to topography coupled with erosion and transport of lithologic material beyond the bedrock contact lines that Dibblee mapped. Similarly, each of our classes correlated with more than one of Dibblee's lithologic units throughout the maps (Table 4), but we expected this since we used fewer classes than the number of units that he mapped in our scene. In summary, our final product is limited by the extent to which bedrock is exposed at the Earth's surface and not concealed by eroded and transported detrital material.

Ground truth lithologic units from the Red Flake site that also ended up being classes in the unsupervised analysis were the tuff and tuff breccia ("tuff breccia" in the unsupervised classification), and the detritus or colluvium ("alluvium" in the unsupervised classification). Therefore, it was possible to quantify the producer's and user's accuracies in an error matrix for those lithologic classes in the unsupervised classification at the Red Flake site. The unsupervised classification error matrix for the Red flake site is in Table 5. While the producer's accuracies in this analysis were both relatively noteworthy at >70 %, the user's accuracies were both <30 %, and the overall accuracy was 60%.

DISCUSSION

Supervised classification of the Red Flake site

The Red Flake site was chosen for the supervised classification analysis because it has excellent bedrock exposure and lacks significant vegetation. In general, lithologic alteration, erosional transport, and vegetation can create mixtures of materials for larger ground sampling distances, resulting in lower accuracy ratings for supervised classification maps. The Mako thermal airborne sensor has a pixel size of 2 m, and hyperspectral resolution (Hall et al., 2011; Buckland et al., 2017), which also helped minimize problems with the error sources that could result from spectra collected over a larger pixel size. Larger pixel sizes, with their larger ground sampling distances, can inherently incorporate greater heterogeneity of materials and create more complex spectral mixtures. Hyperspectral resolution allows for greater detail in the spectral signatures of the materials, which increases the uniqueness of spectra.

For the supervised classifications presented here, some disparities exist between the producer's and the user's accuracy ratings for individual lithologies (see Table 3, and Appendix: 'Background on supervised classifications and how they were applied to this work,' and 'Guide for interpreting error matrices'). The highest disparity between accuracies found for a single lithology occurred with the detritus class. The low user's accuracy for the detritus class may be caused by transported sediment if surficial deposits of detrital material are large enough to dominate the spectra for groups of pixels that we mapped as exposed outcrop of other classes. The heterogeneity of the detritus may also contribute to its internal inconsistency in the producer's accuracy, as it is intrinsically produced by weathering, transport, and mixing of adjacent units. Geometric surface roughness and erosion to smaller

grain sizes can also suppress spectra for pure end members by reducing spectral contrast (Cooper and Mustard, 1999; Kirkland et al., 2001; Horgan et al., 2009), weakening signatures and further decreasing accuracy. Therefore, a primary conclusion from the supervised classification analysis is that the presence of detrital material (e.g., colluvium/alluvium/etc.), which is inevitable in natural settings, will lower the accuracy of lithologic classification maps.

Average values for the producer's accuracies of the tuff and tuff breccia (38 ± 16 %), and of the feldspar porphyry (34 ± 4 %), are both <50% (Table 3). The tuff is often incorrectly classified as detritus, and the feldspar porphyry is often incorrectly classified as microcrystalline lava. The incorrect classifications could be due to compositional similarity between lithologies. The average value for the user's accuracy of the tuff and tuff breccia (25 ± 5 %) is also <50%, but the feldspar porphyry has a user's accuracy (62 ± 6 %) that is nearly double its producer's accuracy. For practical applications, the user's accuracy can be a more important statistic, given that it is the probability that a material, when field-checked, will actually be what the map claims that it is (e.g., Congalton, 1991).

The performance of the microcrystalline lava is generally excellent with both producer's and user's accuracies (89 ± 3 % and 86 ± 1 %, respectively) >85%. Given the classification performance problems described above with respect to weathering, it is possible that the microcrystalline lava was classified better due to the unit being relatively less susceptible to erosion. Overall, our statistics show that out of the four lithologic units that we used as ground truth, the microcrystalline lava is probably the most dependable for classification mapping.

Lavic Lake fault piercing lines and cumulative offset

To estimate the cumulative long-term offset along the Lavic Lake fault, we needed to identify a piercing line within older bedrock units that was subsequently cut by the fault. The intersection of the piercing line with the fault then defines a piercing point, which then can be used to define the net slip. Piercing lines such as offset stream channels are often used for measuring coseismic displacement from earthquakes that occur in the present time, but such ephemeral features do not capture long-term offset that has accumulated since inception of the Lavic Lake fault. In offset bedrock units, linear geologic features are relatively rare, but the intersections between two planar features that can be confidently correlated across the fault are typically used. For example, the intersection of a lithologic contact (or specific bedding plane) with an igneous dike, the hinge surface of a fold, or a fault that clearly pre-dates the fault offset in question, are typically used. For our purposes, we looked for a lithologic contact and older fault plane that could be clearly identified on both sides of the Lavic Lake fault. This was the primary motivation for discerning the apparent boundaries between lithologic units as revealed by our classification maps. Superimposing Dibblee's (1966) lithologic contacts onto our remote sensing imagery products served as a qualitative assessment to reinforce the validity of any lithologic boundaries apparent in the unsupervised classification. As discussed below, two such intersections or piercing lines were identified that may serve as displaced features to constrain the net slip vector, which gives the magnitude of displacement.

Our analysis is based on some key observations from the geologic maps (Figures 9, 10, 11, and also see Table 4), high-resolution satellite imagery (Figure 12), and ground-based

field photographs (Figure 13). Of primary importance in the volcanic stratigraphy are a tuff breccia (Dibblee's "Tt," see Figures 9, 10, 11C, and Table 4) and a basalt (Dibblee's "Tb," see Figures 9, 10, 11C, and Table 4). Note that these units are designated and referenced from the combined analysis of our unsupervised classification with Dibblee's (1966) geologic map, rather than any similar or identically-named units from our supervised classification analysis at the Red Flake site. We determined that bedding in Tt and Tb is right-side up, based on attitudes plotted on the Dibblee map (Figure 10) for crude bed forms within these units that are apparent in the oblique view satellite imagery (Figure 12), and field photographs (Figure 13). In true color, Tt is a very light shade of tan, and Tb is an overlying, very dark brown to black shade (Figures 12 and 13). Thus, Tt is older than Tb by stratigraphic superposition.

We were interested in using the lithologic depositional contact between Tt and Tb as part of an offset piercing line, so hereafter, we refer to this feature as the "Tt/Tb contact," after the abbreviated lithologic letter codes from the Dibblee (1966) map. In our unsupervised classification map (Figure 9, see lower left zoom inset, and Figure 11B), the Tt/Tb contact is revealed as a generalized boundary between the green-color-coded "tuff breccia" (Tt) and the blue-color-coded "basalt" (Tb). With Dibblee's lithologic contacts superimposed onto our unsupervised classification (Figures 9, 10, and 11), the general designation between the tuff breccia and basalt becomes more evident (also see Figure 7), albeit somewhat obfuscated by scattered alluvium and other lithologies (i.e., weathering, erosion, and transport of the various rock types that coexist in proximity to one another). Tt and Tb strata, and their contact boundary, generally dip 15-30º east/northeast (Figure 10 and 11C). At the location where we used the maps to measured fault offset (west-central portion of zoom inset of Figure 9, and

Figures 10 and 11), a younger lithologic unit, the fanglomerate of andesitic detritus (Dibblee's "Tfa," see Figure 10 and Table 4), overlies Tb in angular unconformity. Tfa's base appears relatively flat, as indicated by the fact that its basal contact with older units follows topographic contours. This relationship between Tb and Tfa is also clearly defined on Dibblee's map at a location some 5 km west of the location shown in Figure 10.

Another younger lithologic unit overlies the volcanic bedrock (including Tt, Tb, and their depositional contact) in angular unconformity, a rhyolitic felsite (Dibblee's "QTr," see Table 4). QTr's base also appears relatively flat, because its basal contact also follows topographic contours. Note that QTr is not the same lithology as the felsite class shown in Figure 9; that felsite is correlated with an intrusive felsite (Dibblee's "Tif," see Table 4). One bedrock exposure labeled "QTr" in Dibblee's maps is now known to be Peach Spring Tuff (Wells and Hillhouse, 1989), which has implications for age control on aspects of the system we are considering here. The age of the Peach Spring Tuff is 18.78 ± 0.02 Ma (Ferguson et al., 2013). ECSZ age of inception is generally considered to be 5-10 Ma (Table 1), much younger than the Peach Spring Tuff. Thus, the Peach Spring Tuff is older than the ECSZ and the Lavic Lake fault. Therefore, we are confident that the Tt/Tb depositional contact pre-dated inception of the Lavic Lake fault, so using the contact as a component plane of our piercing line captures the complete offset of the Lavic Lake fault.

Displaced Tt/Tb contact: the vertical component of slip

On the west side of the main Lavic Lake fault, the Tt/Tb contact appears in our remote sensing maps (Figures 7, 9, and 11), Dibblee's mapped lithologic contacts (Figure 10), and

also an additional published geologic map (Kupfer and Bassett, 1962). Although the displaced Tt/Tb contact has apparent right-lateral map-view separation in Dibblee's map (Figure 10), because the contact is a planar geologic feature, it cannot, as a matter of definition, be used as an offset feature to measure net slip across the Lavic Lake fault. On the west side of the main Lavic Lake fault, Dibblee's Tt/Tb contact is depicted as depositional, but we discovered by using our ground-based field photographs and satellite imagery, that the contact line is actually a separate and distinct, smaller cross fault where the feature intersects the main fault (Figures 12 and 13). On the east side of the main fault, the Tt/Tb contact is also depositional, but does not clearly align with a distinct class boundary from our remote sensing map (Figure 9, southeast portion of the zoom inset, and Figure 11). This is partly because the Tt/Tb contact does not intersect the main fault on its east side, as depicted in Dibblee's map (Figure 10); instead, the contact is truncated by a separate and distinct, smaller cross fault. The smaller cross fault that truncates the Tt/Tb contact on the east side of the Lavic Lake fault is apparent in satellite imagery (Figure 12). The southernmost portion of the area mapped as Tt along the Lavic Lake fault on Dibblee's map (Figure 10) is mapped as basalt on another published geologic map, and shown in fault contact with Tt (Kupfer and Bassett, 1962). Figure 12 shows Dibblee's depiction of the Tt/Tb contact compared to our depiction of the same feature. In Figure 12B, Dibblee's Tt/Tb contact is depicted as wholly depositional, except where the two lithologic units are in fault contact along the main fault. Figure 12C shows our observations of the smaller additional structures that exist in relation to the Tt/Tb contact and the main fault. On the west side of the main fault, the contact is partly depositional and partly fault. On the east, the depositional contact is truncated by a distinct, smaller cross fault.

As noted above, the apparent horizontal separation of a planar feature is insufficient to indicate the true displacement vector of net fault slip. The separation of a stratigraphic plane, versus true net slip, is a classic problem in structural geology, because a linear feature can appear to have been tectonically displaced in a specific way when viewed in a two dimensional perspective (such as an overhead map view), but the three dimensional consideration shows that a given separation can result from a wide variation in net slip. For example, a dipping stratum can appear to be offset laterally by a fault in map view, but the observed separation can actually result from pure dip-slip (e.g., Figure 8.6 in Fossen, 2010; Figure 6.48 in Davis et al., 2012). The variety of possible spatial orientations and intersections between strata, contact boundaries, and fault planes will inevitably create ambiguity when considering separation versus slip.

Bedding attitudes given in the Dibblee maps show that the strike of Tt and Tb bedding (and by extension, their depositional contact) is fairly consistent in proximity to the main Lavic Lake fault (Figure 10). The angle of intersection between bedding and the fault is about 70 to 75°, and the map-view trace of the Tt/Tb depositional contact is mainly subparallel to the trend of the main fault trace (Figure 10). The subparallel geometry between the Tt/Tb contact trace and the main fault trace would lead to significant error if considering horizontal map-view separation of the contact versus true fault slip. The very low angle of intersection between the Tt/Tb depositional contact trace and the fault trace contributes to an exaggerated amount of perceived lateral separation, and the cross section that traverses the main fault at this location (line A-A' in Figure 10) shows that the Tt/Tb depositional contact has apparent vertical separation. The cross section reveals a solution that invokes a purely vertical offset of the Tt/Tb contact, but the map-view separation allows a purely horizontal

strike-slip offset also, depending on the dip direction of the contact prior to offset. The topographic relief and broad surface elevation are greater on the east side of the main Lavic Lake fault than on the west side, which we interpret to represent a component of cumulative and significant pre-1999 vertical fault displacement, with the east block upthrown relative to the west block (cross section A-A' in Figure 10).

The apparent vertical separation that we measured in the cross section (Figure 10) is 240 m. We derived an error range for that measurement by considering variability in the cross-section-projected dip of the Tt/Tb contact, and also a relatively small amount of variability in the dip of the main Lavic Lake fault (as described below). Average cross-section-projected dip domains on the west and east side of the Lavic Lake fault are 13º and 23º (both east/northeast), respectively, and this variation in dip affects the vertical separation estimate. We also considered variation in the dip of the Lavic Lake fault itself. Geodetic inversion models show that some portions of the Lavic Lake fault dip 75-90º east/northeast (Simons et al., 2002). With all of the data combined, we calculated the minimum apparent vertical separation by assuming that the Tt/Tb depositional contact had minimum cross-section-projected dip on both sides of the fault (13º east/northeast), and the fault had maximum dip (90º). We calculated the maximum by assuming that the contact had maximum cross-section-projected dip (23º east/northeast) and the fault had minimum dip (75º east/northeast). We derived the intermediate value by assuming the average cross-section-projected dip domains for the west and east sides of the main fault (13º and 23º, respectively), and that the fault had a 90º dip. The value for apparent vertical separation is: minimum 210 m, intermediate 240 m, and maximum 370 m, or 240 +130/-30 m.

We note that on the basis of the apparent vertical separation of the Tt/Tb contact alone, the vertical component of net slip cannot be resolved. For example, if the contact dipped northeast prior to faulting, then purely left-lateral net slip would produce a vertical separation of the contact with the east side upthrown. However, at the location in discussion, the strike of bedding in Tt/Tb is nearly parallel to the fault trace, or said in another way, the dip direction of the Tt/Tb contact is very close to perpendicular to the fault trace (Figure 10). With the very small acute angle (5-10º) between bedding strike and the trace of the Lavic Lake fault (Figure 10), left-lateral slip of at least a few kilometers would be required to produce the apparent vertical separation of 240 m. Left-lateral slip in that amount is very large and, and in the wrong sense of the coseismic slip of the 1999 earthquake. Furthermore, for any area where the fault trace and bedding strike are parallel, no amount of strike slip in either direction can produce a net vertical separation of the contact. If we assume that, like all of the other major northwest trending faults in the ECSZ, the Lavic Lake fault has net slip that is mainly right-lateral strike slip, then the vertical separation is probably the result of a true component of vertical slip. Thus, we interpreted the apparent vertical separation as the vertical component of the slip vector, which we then combined with a horizontal component, to solve for the magnitude of displacement.

Displaced cross fault: the horizontal component of slip

As stated previously, much of the Tt/Tb contact trace is depositional, but west of the main fault, the Tt/Tb contact intersects the main fault as a separate and distinct, smaller cross fault (Figures 12C and 13). In proximity to the main fault, on its west side, the Tt/Tb contact

trends along a 5-10º azimuth. However, at a point c. 200 m from the main fault trace, the contact line makes an abrupt 120º turn immediately before intersecting the main fault trace. There is not actually an abrupt change in azimuth along the Tt/Tb depositional contact right before it intersects the main fault; instead, we attribute the sudden and drastic change in azimuth to the smaller cross fault. The Tt/Tb fault contact here is further evidenced by the structural juxtaposition of older Tt on top of younger Tb. Figure 13B and 13D shows ground-based field photographs where this portion of the Tt/Tb contact is a smaller cross fault, as evidenced by how the older, light-hued Tt strikes at high-angle into, and structurally overlies, the younger, dark-hued Tb. While we interpreted this field relationship as a fault contact, we note the possibility that the Tt and Tb units interfinger with one another, as implied by Dibblee's interpretation, and by Kupfer and Bassett (1962).

On the east side of the Lavic Lake fault, the Tt/Tb depositional contact does not intersect the main fault as shown by Dibblee (southern center portion of Figure 10, Figure 11), because as noted above it is cut by a separate and distinct, smaller cross fault (Figure 12C; Kupfer and Bassett, 1962). The cross fault that truncates the Tt/Tb contact on the east side of the main fault could be the same fault as the cross fault on the west. This correlation is strengthened by the fact that both cross faults have a separation that is downthrown to the south, juxtaposing the younger basalt on the south side with the older tuff on the north side. If the two cross faults on each side of the main fault are indeed the same (that is, an older fault that pre-dates inception of the Lavic Lake fault) then the older cross fault has been cut and displaced by the main fault, and the older cross fault's surface trace defines a feature that is independent of offset of the Tt/Tb contact. Because the fault trace strikes at a high angle to the Lavic Lake fault, if it has a steep dip (see below), then its offset serves as a fairly

accurate estimate of horizontal displacement. Any purely dip slip solution for the net slip vector would require many kilometers of vertical displacement, which would violate the modest vertical separation defined by the shallowly dipping Tt/Tb contact. We therefore interpret the map-view lateral separation of the cross fault as an accurate estimate of the horizontal component of slip along the Lavic Lake fault.

The apparent map-view right-lateral separation of the cross fault by the main Lavic Lake fault is 930 m, and we estimate an error of ±30 m based on possible variation of its precise intersection lines with the main fault. The cross fault on the east appears to have steep dip, based on its relatively straight surface trace. The cross fault on the west, though, could have a low dip angle, as suggested by its highly meandering surface trace (Figure 12C). While it is possible that the cross faults are not correlative (which would completely invalidate the horizontal separation measurement), tectonic deformation by the main fault could have resulted in different dip angles for the cross fault's displaced, complementary components. But if the cross fault originally had, or does have a shallow dip, then we again encounter the nonuniqueness in the separation versus slip problem, where a small amount of vertical fault motion along the main fault could have produced significant apparent lateral separation of the cross fault's surface trace. We do not have any subsurface or other data to determine if the cross fault has a low dip, but we can assign the horizontal separation as a maximum value, where less total slip can be inferred to the extent that the fault dip is very shallow.

Slip vector and off-fault deformation

We used our estimates of the horizontal and vertical separation components (both at the same location) to estimate a total slip vector and solve for the magnitude of displacement. The vertical separation of the Tt/Tb contact is 240 +130/-30 m down on the west, and the horizontal separation of the cross fault is 930 ± 30 m right-lateral. By the Pythagorean theorem, we therefore estimate the net slip to be 960 +70/-40 m (error range from solving for the maximum/minimum vertical and horizontal values).

We assumed that the Lavic Lake fault as a whole has predominantly experienced strike-slip displacement since its inception, similar to other components of the ECSZ that have locally large components of dip slip (e.g., Spotila and Sieh, 1993), and concluded that the slip vector and displacement magnitude presented here represent the cumulative long-term offset of bedrock. Unresolvable uncertainties remain regarding prehistoric slip on the main fault (e.g., lateral/strike slip versus dip slip) and structural geometry of the cross fault (e.g., the dip angle), so we consider the cumulative offset value presented here to be a maximum (since ECSZ inception at 5-10 Ma, see above, and Table 1). Our value of <1 km is significantly less than the magnetic gradient offset estimate of 3.4 ± 0.8 km (Jachens et al., 2002), but our measurement is from a different location that is 3-5 km away to the north from theirs. We are confident that we captured the entire cumulative offset recorded at the surface by the Lavic Lake fault, because the Lavic Lake fault is younger than the piercing lines (Tt/Tb contact is >18.78 ± 0.02 Ma from overlying QTr = Peach Spring Tuff, see above) that we used to derive the slip vector. The difference between our surface measurement and the magnetic measurement, then, may be due to factors of 3D basement geometry, as well as off-fault continuous deformation, or tectonic displacement along discrete, smaller adjacent structures.

Off-fault deformation has been cited as a potentially significant source of error in considering the discrepancy between long-term geologic and current geodetic slip rates (Bird, 2009; Shelef and Oskin, 2010; Chuang and Johnson, 2011; Johnson, 2013; Herbert et al., 2014). Off-fault continuous deformation is more likely to occur in unconsolidated sediments (e.g., the Lavic Lake playa to the northwest, or alluvium to the southeast), than in the bedrock where we performed a cumulative slip analysis. In alluvium to the southeast of the cumulative offset area presented in this study, Treiman et al. (2002) observed off-fault continuous deformation: 7 cm of right-lateral offset in a 7-m wide zone. Smaller, discrete adjacent faults can also contribute to off-fault deformation. For example, in the southernmost portion of the 1999 earthquake surface rupture, where offset was recorded along three distinct fault traces, up to ~2 m of fault-parallel lateral displacement was recorded in the field on secondary structures (Figure 3 in Treiman et al., 2002).

While the cumulative long-term offset along smaller faults are unlikely to be as large as that of the main Lavic Lake fault, if there are a number of these smaller faults, their integrated displacements could be significant. However, the uncertainties associated with smaller, ambiguous structures might be so high as to render such measurements meaningless. Also, it is possible that considering increasingly smaller features with increasingly smaller displacements would yield diminishing returns, akin to the Gutenberg-Richter Law, which shows the contribution of smaller earthquakes to cumulative seismic moment. For all of the reasons cited above, it is unlikely that off-fault deformation contributes significantly to the cumulative offset measurement presented here for the Lavic Lake fault.

Relative merits of the remote sensing methods used in this study

The supervised classifications we did were at a location (the Red Flake site) distant from the cumulative fault offset analysis area, but the supervision process helped us accomplish the goals in this study by allowing us to experiment with the processing sequence for quantifying and maximizing lithologic mapping accuracy values. The supervised classification overall accuracy was maximized at 71 ± 1%, by classifying the bands with wavelengths from 8.4-13.1 μm, on the emissivity data product. However, we also attempted supervised classifications on other products of the same data, including with atmospheric compensation only, the PCA components, the MNF components, and subsets of bands from those data products. The supervision process did not directly contribute to the cumulative fault offset analysis, but due to the limited access to the area for field work, experimenting with the processing sequence gave us experience and knowledge about how effectively we could differentiate some of the volcanic rocks in the area with remote sensing data and methods. We could have gone on to attempt supervised classifications of the complete image swath, using lithologic identifications and contact line work from the Dibblee (1966) map as ground truth. However, we chose to instead perform unsupervised classifications on the complete image swath because we were interested in using a more exploratory method that had the potential to highlight any features that had not been previously discovered, and could potentially assist in our cumulative fault offset analysis. Still, including the supervision process (if possible) could be an integral component to future studies that use remote sensing for geologic mapping.

In mapping the lithology along the complete image swath, we could have also opted to use the MNF false color image in a similar way to how we used the unsupervised

classification image to visually and qualitatively compare class boundaries with Dibblee's (1966) contact line work. The MNF image (Figure 7) is based on a continuous spectrum of false color to depict lithologic variation, whereas the unsupervised image (Figure 9) is based on discrete colors to represent a finite number of lithologic classes. With a finite number of discrete color assignments, the unsupervised classification method had the potential to simplify and clean up the MNF image by categorizing and sorting all of the lithologic material into a smaller set of units, which could assist in image interpretation for a more effective and synoptic summary.

Figure 11 shows a side-by-side comparison of the cumulative fault offset analysis area that we focused on for this study: the MNF components in false color (Figure 7), the unsupervised classification (Figure 9), and a portion of the Dibblee (1966) map (Figure 10). While each of the images has its own individual merits, it would not have been possible to accomplish the goals of this study without each of the three images used together. In the MNF components image, the Tt/Tb depositional contact is clearly visible on the west side of the Lavic Lake fault by a boundary between false color assignments. This boundary aligns almost perfectly with Dibblee's contact line from the 1966 map, and the lithologic descriptions from the 1966 map provided information about what type of rocks these are. However, the Tt/Tb depositional contact on the east side of the Lavic Lake fault, while depicted to be very straight forward in Dibblee's map, is not readily apparent in the MNF image. As stated above, performing the unsupervised classification provided an opportunity to simplify the MNF image into a data product that would be more straight forward to interpret. Since the unsupervised image did not yield that desired result in this case, the MNF image was optimal for the purposes of this study. In general, though, it is ideal to experiment

with and incorporate as many of the data products as possible (e.g., to see where they might agree/disagree with each other, and reveal/obscure features) into a more conclusive summary. This is why we also used the data from the Kupfer and Bassett (1962) map, which depicts the cross fault on the east side of the Lavic Lake fault. We verified the location of the east cross fault using true color Google Earth satellite imagery (Figure 12C), and went on to discover that the east cross fault is possibly correlative to the west cross fault that we verified from our field data (Figure 13), and therefore could be used as a cumulative offset marker along the Lavic Lake fault.

Implications for estimates of slip rate on the Lavic Lake fault

In regard to the discrepancy between ECSZ geologic (~6 mm/yr) and current geodetic (>10 mm/yr) slip rates, the c. 1 km cumulative displacement that we calculated is relatively small, and would not make a significant contribution to minimizing the difference. As noted above, the summed geologic ECSZ slip rate (based on six major faults across the Mojave Desert with Quaternary slip) is $\leq 6.2 \pm 1.9$ mm/yr since ~750 ka (Oskin et al., 2008), and most geodetic studies find an overall contemporary slip rate of >10 mm/yr (Sauber et al., 1994; Dixon et al., 1995; Miller et al., 2001; McClusky et al., 2001; Becker et al., 2005; Spinler et al., 2010). One of the more recent publications even cited a geodetic value of >15 mm/yr (McGill et al., 2015). The Lavic Lake fault would require a geologic slip rate of at least 4 mm/yr (i.e., bring the ~6 mm/yr total up to ~10 mm/yr) to make a significant contribution in minimizing the difference. With a slip rate hypothesized or determined, and the cumulative offset known from this study, the age of inception of the Lavic Lake fault can

be calculated. A 4 mm/yr slip rate with 1 km of cumulative offset suggests that inception of the Lavic Lake fault occurred c. 250 ka. Most of the research suggests that the ECSZ age of inception is >5 Ma (Table 1), so if the 4 mm/yr slip rate is correct, the Lavic Lake fault is a very young structure in the overall ECSZ architecture. Paleoseismological studies in the Lavic Lake playa area after the 1999 earthquake suggest that the Lavic Lake fault is a relatively young structure, with deformation that has not yet been fully localized onto a single strand (Rymer et al., 2002). A separate, proximal strand of the Lavic Lake fault that did not rupture in 1999 had ruptured within the past c. 1750 years (Rymer et al., 2002). If earthquakes occurred once every 1750 years for 250,000 years, each event with 5 m of slip, only c. 700 m of slip would accumulate (i.e., somewhat less than our estimate of c. 1 km).

If tectonic motion along the Lavic Lake fault initiated much earlier, though, for example at 1 Ma, then the geologic slip rate (using 1 km cumulative offset) would be 1 mm/yr. A 1 mm/yr slip rate for the Lavic Lake fault would be too low to significantly minimize the difference between geologic and geodetic slip rates. Furthermore, the Lavic Lake fault appears to be one of the few remaining major faults whose geologic slip rate is unknown and needs to be integrated into the summed geologic Mojave ECSZ rate. As this study on analyzing the geologic slip rate for an additional major structure in the ECSZ suggests, it seems unlikely that the discrepancy between geologic and geodetic slip rates can be resolved by simply finding and analyzing more faults for geologic slip rates to integrate.

Geologic slip rates are often minimum values, because of uncertainty in the time lag between the age of the displaced feature and inception of fault motion. Assuming this error source manifests consistently, that in itself could explain the discrepancy, because the true geologic rate would be larger than any value calculated with available methods. On the other

hand, if the geologic rates are accurate and the discrepancy really does exist, perhaps the ECSZ is currently experiencing some type of transient, or permanent, accelerated deformation rate.

CONCLUSIONS

Thermal hyperspectral airborne imagery and remote sensing techniques greatly supplemented our geologic field mapping within a restricted area along the Hector Mine earthquake surface rupture in the eastern Mojave Desert. We could not conduct an extended campaign for detailed field mapping along the entire Lavic Lake fault, but with supervised classifications over a small test site, we processed the remote sensing data to maximize accuracy in lithologic classification mapping of the volcanic rocks in the area. We also compared an unsupervised classification over the complete aerial image swath with a published geologic map of the same area. This served as a qualitative accuracy check for both the unsupervised classification map and the published geologic map. We were able to map generally the same variation and distribution of lithology with classification errors occurring mainly due to erosion and transport of heterogeneous detrital material, and possibly because the materials were similar in composition.

We used available geologic maps, along with satellite imagery, and field work to identify and measure the separations of planar features by the Lavic Lake fault. Some of the class boundaries in our remote sensing map displayed compelling correlation with lithologic contacts that were previously mapped. A mapped lithologic contact between a tuff breccia (Tt) and a basalt (Tb) correlated well with a boundary between two of the classes from our

remote sensing map. This Tt/Tb contact is cross cut and displaced by the Lavic Lake fault, with a vertical separation of 240 +130/-30 m. On the west side of the main Lavic Lake fault, the Tt/Tb contact intersects the main fault as a separate, smaller cross fault, and on the east side, the depositional contact is truncated by another separate, smaller cross fault. The right-lateral horizontal separation of this cross fault by the main Lavic Lake fault is 930 ± 30 m.

Neither the apparent vertical or horizontal separation measurements individually represent the cumulative slip along the Lavic Lake fault, but they occur at the same location, so we used them to construct the complete slip vector and calculate the magnitude of displacement. The magnitude of displacement is 960 +70/-40 m. This value is an upper limit, since some uncertainty exists regarding prehistoric slip and structural geometry. However, the magnitude of displacement that we calculate is much less than another independent cumulative offset estimate (~3 km) that was based on an offset magnetic gradient. The geologic features that we used to estimate the slip vector pre-date inception of the main Lavic Lake fault, so we are confident that the magnitude of displacement is the cumulative long-term offset of bedrock, expressed at the surface, along the main fault, since 18-19 Ma. The difference between our surface measurement and the magnetic measurement might be due to 3D basement geometry, as well as off-fault deformation accommodated by continuous strain or other smaller, discrete structures adjacent to the fault.

The magnitude of displacement that we calculate can assist in reconstructing fault histories in eastern California, and can be combined with bedrock ages to calculate the geologic slip rate. Fortunately, with its remote and inaccessible location, the Lavic Lake fault does not currently pose a major threat to society and infrastructure. Calculation of a geologic slip rate for the Lavic Lake fault may help in resolving the discrepancy between current

geodetically measured tectonic motion and integrated geologic slip rates over faults across eastern California, but based on the relatively small cumulative long-term slip that we infer, it does not appear that the Lavic Lake fault will contribute significantly to the sum geologic Mojave ECSZ slip rate.

ACKNOWLEDGEMENTS

This material is based upon work supported by the National Science Foundation (NSF) Graduate Research Fellowship Program under Grant No. 1144469 awarded to R. Witkosky, and also by Southern California Earthquake Center (SCEC) Award No. 14160 awarded to J. Stock This paper is SCEC Contribution No. 8898. SCEC is funded by NSF Cooperative Agreements EAR-1033462 & EAR-0529922, and United States Geological Survey Cooperative Agreements G12AC20038 & 07HQAG0008. Mako airborne hyperspectral imagery was acquired under the auspices of the Aerospace Corporation's Independent Research and Development program. We thank the Marine Corps Air Ground Combat Center in Twentynine Palms, California, for allowing access to the military base. We also thank Ken Hudnut, Janet Harvey, Kate Scharer, and Sinan Akçiz for their help and support in field work, performing this research, and preparing this manuscript.

APPENDIX

Background on supervised classifications and how they were applied to this work

After compiling our ground-truth data into a geologic map, we used this information to perform supervised classifications on the portion of the hyperspectral imagery that covers the Red Flake site. A supervised classification is a common remote sensing product where pixels in an image are organized into a set of classes defined a priori by a user who has knowledge of materials or land cover present in the image. In defining the classes, a few pixels are chosen to represent each class as "end members." Then, the other pixels in the image are each grouped with the end member with whom it shares the greatest spectral similarity. For our case, the classes are the four main lithologic units that we observed in the field.

After pixels are organized into classes, physical boundaries between classes are superimposed on the image in order to determine how many pixels in each area were assigned to their correct class. Results for correctly and incorrectly identified pixels are tabulated and offer a quantitative summary—as the percentage of pixels mapped correctly in relation to ground truth—for the accuracy to which the classes can be mapped using a remote sensing data set. For our purpose, the supervised classification was a test to establish how well spectral information embedded within the thermal airborne imagery allowed for differentiation of distinct lithologic units on the scale of the pixel size.

For further clarity, we present an example case: a lithologic unit is observed and its boundary mapped in the field. A remote sensing image completely covers the map view extent of this unit, so the lithologic boundary is digitized and superimposed on the image. Spectra from a few pixels within the boundary are chosen to represent the lithologic unit. In an ideal supervised classification, all of the other pixels within the boundary should be grouped, based on spectral similarity, with the chosen representative pixels. In the real world.

However, complications exist that make a 100% accuracy rating for a supervised classification highly unlikely. Compositional heterogeneity of surficial material due to alteration, vegetation, transport, and/or incomplete knowledge often results in mixtures of materials for each pixel. Geometric surface complexity (intrinsic roughness and/or erosion to small angular grains) can also complicate spectra for pure end members by reducing spectral contrast, resulting in weak signatures (Cooper and Mustard, 1999; Kirkland et al., 2001; Horgan et al., 2009). Nonetheless, our choice of sensor and site minimized these problems. The Mako sensor has a pixel size of 2 m, with hyperspectral resolution (Hall et al., 2011; Buckland et al., 2017), and the Red Flake site offers excellent bedrock exposure with a lack of significant erosion or vegetation.

The spectral angle mapping algorithm (SAM, described in Kruse et al., 1993) calculates the n-dimensional angle, where n is the number of bands, between the spectrum for each pixel and the spectrum for each end member using the geometric definition of an inner product. Each pixel is then classified as the end member for which the minimum angle is calculated. Finally, lithologic contacts from our geologic map were superimposed to assist in visualizing the classification accuracy, and we assessed the accuracy of the supervised classification via error matrices (Congalton, 1991). Figure 8 shows the results for the ten supervised classifications (labeled A through J), and the corresponding error matrices are in Table 2.

Guide for interpreting error matrices

Here we provide a detailed explanation, with examples, for how to interpret error matrices and calculate producer's, user's, and overall accuracies. All of the following explanations reference numerical values in the error matrix from supervised classification A (see Figure 8 and Table 2).

Reading down a column of the error matrix shows the distribution of classified pixels within each ground truth class. For example, the first column shows that in the bounded region that we mapped as tuff, 25 pixels were correctly classified as tuff, but 11, 13, and 13 pixels were incorrectly classified as detritus, feldspar porphyry, and microcrystalline lava, respectively. Thus, summing over a column gives the total number of pixels contained in each bounded ground truth area. The total number of pixels classified correctly as a fraction of the total number of pixels in a column gives the "Producer's accuracy." The name is in reference to a scenario where the producer of the classification map wishes to assign a grade to their product, so they simply quantify how many pixels are correct in each bounded class area. For the tuff, this is 25/62 = 0.40 or 40%.

Reading across a row of the error matrix shows how many pixels for each type of lithology were classified into each ground truth class. For example, the first row shows that 25 true tuff pixels were correctly classified as tuff, but 2 true detritus, 56 true feldspar porphyry, and 4 true microcrystalline lava pixels were incorrectly classified as tuff. Thus, summing over a row gives the total number of pixels classified as a given lithology throughout the entire classification map. The total number of pixels classified correctly as a fraction of the total number of pixels in a row gives the "User's accuracy." The name is in reference to a scenario where a user of the classification map field-checks every pixel and

then assigns a grade based on misclassified pixels across the entire scene, not just grading within the individual class boundaries. For the tuff, this is 25/87 = 0.29 or 29%.

Taking the sum of the diagonal of the error matrix gives the total number of pixels classified correctly in relation to ground truth. The total number of pixels classified correctly across all classes, as a fraction of the total number of pixels in the classification map gives the "Overall accuracy," which is the lowest entry to the right. For supervised classification A and its accompanying error matrix, this is 25 + 28 + 125 + 747 = 925, then 925/1297 = 0.71 or 71%.

REFERENCES CITED

Arrowsmith, J.R., and Rhodes, D.D., 1994, Original Forms and Initial Modifications of the Galway Lake Road Scarp Formed along the Emerson Fault during the 28 June 1992 Landers, California, Earthquake: Bulletin of the Seismological Society of America, v. 84, n. 3, pp. 511-527.

Atwater, T., 1992, Constraints from plate reconstructions for Cenozoic tectonic regimes of southern and eastern California, *in* Richards, S.M., ed., Deformation associated with the Neogene Eastern California Shear Zone, southwestern Arizona and southeastern California: San Bernardino County Museum Special Publication, v. 92-1, p. 1-2.

Atwater, T., and Stock, J., 1998, Pacific-North American plate tectonics of the Neogene Southwestern United States: An update: International Geology Review, v. 40, p. 375-402, doi:10.1080/00206819809465216.

Becker, T.W., Hardebeck, J.L., and Anderson, G., 2005, Constraints on fault slip rates of the southern California plate boundary from GPS velocity and stress inversions: Geophysical Journal International, v. 160, p. 634-650, doi: 10.1111/j.1365-246X.2004.02528.x.

Bennett, S.E.K., Oskin, M.E., Dorsey, R.J., Iriondo, A., and Kunk, M.J., 2015, Stratigraphy and structural development of the southwest Isla Tiburón marine basin: Implications for latest Miocene tectonic opening and flooding of the northern Gulf of California: Geosphere, v. 11, n. 4, doi: 10.1130 /GES01153.1.

Bennett, S.E.K., Darin, M.H., Dorsey, R.J., Skinner, L.A., Umhoefer, P.J., and Oskin, M.E., 2016, Animated tectonic reconstruction of the Lower Colorado River region: implications for Late Miocene to Present deformation, *in* 2016 Desert Symposium Field Guide and Proceedings, Zzyzx, California, California State University Desert Studies Center, p. 73-86.

Bird, P., 2009, Long-term fault slip rates, distributed deformation rates, and forecast of seismicity in the western United States from joint fitting of community geologic, geodetic, and stress direction data sets: Journal of Geophysical Research, v. 114, B11403, doi:10.1029/2009JB006317.

Buckland, K.N., Young, S.J., Keim, E.R., Johnson, B.R., Johnson, P.D., and Tratt, D.M, 2017, Tracking and quantification of gaseous chemical plumes from anthropogenic emission sources within the Los Angeles Basin: Remote Sensing of Environment, v. 201, p. 275- 296, doi: 10.1016/j.rse.2017.09.012.

Burbank, D.W., and Whistler, D.P., 1987, Temporally constrained tectonic rotations derived from magnetostratigraphic data: Implications for the initiation of the Garlock fault, California: Geology, v. 15, p. 1172-1175.

Carter, J.N., Luyendyk, B.P., and Terres, R.R., 1987, Neogene clockwise rotation of the eastern Transverse Ranges, California, suggested by paleomagnetic vectors: Geological Society of America Bulletin, v. 98, p. 199-206.

Chen, T., Akciz, S.O., Hudnut, K.W., Zhang, D.Z., and Stock, J.M., 2015, fault-slip distribution of the 1999 Mw 7.1 Hector Mine earthquake, California, estimated from postearthquake airborne LiDAR data: Bulletin of the Seismological Society of America, v. 105, no. 2A, p. 776-790, doi:10.1785/0120130108.

Christensen, P.R., and Harrison, S.T., 1993, Thermal infrared emission spectroscopy of natural surfaces: application to desert varnish coatings on rocks: Journal of Geophysical Research, v. 98, n. B11, p. 19819-19834.

Christensen, P.R., Bandfield, J.L., Hamilton, V.E., Howard, D.A., Lane, M.D., Piatek, J.L., Ruff, S.W., and Stefanov, W.L., 2000, A thermal emission spectral library of rock-forming minerals: Journal of Geophysical Research, v. 105, n. E4, p. 9735-9739.

Chuang, R.Y., and Johnson, K.M., 2011, Reconciling geologic and geodetic model fault slip-rate discrepancies in Southern California: Consideration of nonsteady mantle flow and lower crustal fault creep: Geology, v. 39; n. 7; p. 627-630, doi:10.1130/G32120.1.

Congalton, R.G., 1991, A review of assessing the accuracy of classifications of remotely sensed data: Remote Sensing of Environment, v. 37, p. 35-46, doi: 10.1016/0034-4257(91)90048-B.

Cooper, C.D., and Mustard, J.F., 1999, Effects of very fine particle size on reflectance spectra of smectite and palagonitic soil: Icarus, v. 142, p. 557-570, doi: 10.1006/icar.1999.6221.

Davis, G.A., and Burchfiel, B.C., 1973, Garlock fault, an intracontinental transform structure, southern California: Geological Society of America Bulletin, v. 84, p. 1407-1422, doi: 10.1130/0016-7606(1973)84<1407:GFAITS>2.0.CO;2.

Davis, G.H., Reynolds, S.J., and Kluth, C.F., 2012, Structural geology of rocks and regions, third edition: Hoboken, New Jersey, John Wiley & Sons, Inc., 839 p.

Dibblee, T.W., Jr., 1966, Geologic map of the Lavic quadrangle, San Bernardino County, California: U.S. Geological Survey Miscellaneous Geologic Investigations Map I-472, scale 1:62,500, 1 sheet.

Dibblee, T.W., Jr., 1967a, Geologic map of the Deadman Lake quadrangle, San Bernardino County, California: U.S. Geological Survey Miscellaneous Geologic Investigations Map I-488, scale 1:62,500, 1 sheet.

Dibblee, T.W., Jr., 1967b, Geologic map of the Emerson Lake quadrangle, San Bernardino County, California: U.S. Geological Survey Miscellaneous Geologic Investigations Map I-490, scale 1:62,500, 1 sheet.

Dibblee, T.W., Jr., 1967c, Geologic map of the Ludlow quadrangle, San Bernardino County, California: U.S. Geological Survey Miscellaneous Geologic Investigations Map I-477, scale 1:62,500, 1 sheet.

Dibblee, T.W., Jr., 2008, Geologic map of the Rodman Mountains and Lavic 15 minute quadrangles, San Bernardino County, California (edited by John A. Minch): Santa Barbara Museum of Natural History, Dibblee Geology Center Map #DF-378, scale 1:62,500, 1 sheet.

Dixon, T.H., Robaudo, S., Lee, J., and Reheis, M.C., 1995, Constraints on present-day Basin and Range deformation from space geodesy: Tectonics, v. 14, n. 4, p. 755-772, doi: 10.1029/95TC00931.

Dokka, R.K., 1983, Displacements on late Cenozoic strike-slip faults of the central Mojave Desert, California: Geology, v. 11, p. 305-308, doi: 10.1130/0091-7613(1983)11<305:DOLCSF>2.0.CO;2.

Dokka, R.K., and Travis, C.J., 1990a, Late Cenozoic strike-slip faulting in the Mojave Desert, California: Tectonics, v. 9, n. 2, p. 311-340, doi: 10.1029/TC009i002p00311.

Dokka, R.K., and Travis, C.J., 1990b, Role of the eastern California shear zone in accommodating Pacific-North American plate motion: Geophysical Research Letters, v. 17, n. 9, p. 1323- 1326, doi: 10.1029/GL017i009p01323.

Ferguson, C.A., McIntosh, W.C., and Miller, C.F., 2013, Silver Creek caldera-The tectonically dismembered source of the Peach Spring tuff: Geology, v. 41, n. 1, p. 3-6, doi:10.1130/G33551.1.

Fialko, Y., and Simons, M., 2001, The complete (3-D) surface displacement field in the epicentral area of the 1999 Mw 7.1 Hector Mine earthquake, California, from space geodetic observations: Geophysical Research Letters, v. 28, n. 16, p. 3063-3066, doi: 10.1029/2001GL013174.

Fossen, H. 2010, Structural geology: New York, Cambridge University Press, 463 p.

Friedrich, A.M., Wernicke, B.P., Niemi, N.A., Bennett, R.A., and Davis, J.L., 2003, Comparison of geodetic and geologic data from the Wasatch region, Utah, and implications for the spectral character of Earth deformation at periods of 10 to 10 million years: Journal of Geophysical Research, v. 118, n. B4, 2199, doi:10.1029/2001JB000682.

Gan, W., Zhang, P., and Shen, Z.-K., 2003, Initiation of deformation of the Eastern California Shear Zone: Constraints from Garlock fault geometry and GPS observations: Geophysical Research Letters, v. 30, n. 10, 1496, doi:10.1029/2003GL017090.

Garfunkel, Z., 1974, Model for the Late Cenozoic tectonic history of the Mojave Desert, California, and for its relation to adjacent regions: Geological Society of America Bulletin, v. 85, p. 1931-1944, doi: 10.1130/0016-7606(1974)85<1931:MFTLCT>2.0.CO;2.

Golombek, M.P., and Brown, L.L., 1988, Clockwise rotation of the western Mojave Desert: Geology, v. 16, p. 126-130, doi: 10.1130/0091-7613(1988)016<0126:CROTWM>2.3.CO;2.

Green, A.A., Berman, M., Switzer, P., and Craig, M.D., 1988, A transformation for ordering multispectral data in terms of image quality with implications for noise removal: IEEE Transactions on Geoscience and Remote Sensing, v. 26, no. 1, p. 65-74, doi: 10.1109/36.3001.

Hall, J.L., Boucher, R.H., Gutierrez, D.J., Hansel, S.J., Kasper, B.P., Keim, E.R., Moreno, N.M., Polak, M.L., Sivjee, M.G., Tratt, D.M., and Warren, D.W., 2011, First flights of a new

airborne thermal infrared imaging spectrometer with high area coverage, *in* Andresen, B.F., Fulop, G.F., and Norton, P.R., eds., Infrared Technology and Applications XXXVII, Proceedings of SPIE, v. 8012, p. 8012031-8012037, doi: 10.1117/12.884865.

Hector Mine Earthquake Geologic Working Group, 1999, Surface rupture, slip distribution, and other geologic observations associated with the M 7.1 Hector Mine earthquake of 16 October 1999 in AGU Fall Meeting Program, Dec. 13–17, 1999, p. 11.

Herbert, J.W., Cooke, M.L., Oskin, M., and Difo, O., 2014, How much can off-fault deformation contribute to the slip rate discrepancy within the eastern California shear zone?: Geology, v. 42, n. 1, p. 71-74, doi: 10.1130/G34738.1.

Hook, S.J., Dmochowski, J.E., Howard, K.A., Rowan, L.C., Karlstrom, K.E., and Stock, J.M., 2005, Mapping variations in weight percent silica measured from multispectral thermal infrared imagery—Examples from the Hiller Mountains, Nevada, USA, and Tres Virgenes-La Reforma, Baja California Sur, Mexico: Remote Sensing of Environment v. 95, p. 273-289, doi: 10.1016/j.rse.2004.11.020.

Horgan, B.H., Bell, J.F. III, Noe Dobrea, E.Z., Cloutis, E.A., Bailey, D.T., Craig, M.A., Roach, L.H., and Mustard, J.F., 2009, Distribution of hydrated minerals in the north polar region of Mars: Journal of Geophysical Research, v. 114, n. E01005, doi: 10.1029/2008JE003187.

Hudnut, K.W., Borsa, A., Glennie, C., and Minster, J.-B., 2002, High-resolution topography along surface rupture of the 16 October 1999 Hector Mine, California, earthquake (Mw 7.1) from airborne laser swath mapping: Bulletin of the Seismological Society of America, v. 92, n. 4, p. 1570-1576, doi: 10.1785/0120000934.

Jachens, R.C., Langenheim, V.E., and Matti, J.C., 2002, Relationship of the 1999 Hector Mine and 1992 Landers fault ruptures to offsets on Neogene faults and distribution of Late Cenozoic basins in the eastern California shear zone: Bulletin of the Seismological Society of America, v. 92, n. 4, p. 1592-1605, doi: 10.1785/0120000915.

Jagiello, K.J., 1991, Determination of horizontal separation on Late Cenozoic strike-slip faults in the central Mojave Desert, southern California [Ph.D. thesis]: Los Angeles, University of California, 293 p.

Johnson, A.M., Fleming, R.W., and Cruikshank, K.M., 1993, Broad belts of shear zones: The common form of surface rupture produced by the 28 June 1992 Landers, California, earthquake: United States Geological Survey Open-File Report 93-348, 29 p., doi: 10.2172/677052.

Johnson, K.M., 2013, Slip rates and off-fault deformation in southern California inferred from GPS data and models: Journal of Geophysical Research: Solid Earth, v. 118, p. 5643-5664, doi:10.1002/jgrb.50365.

Kealy, P.S., and Hook, S.J., 1993, Separating temperature and emissivity in thermal infrared multispectral scanner data: implications for recovering land surface temperatures: IEEE Transactions on Geoscience and Remote Sensing, v. 31, n. 6, p. 1155-1164, doi: 10.1109/36.317447.

Kirkland, L., Herr, K., Keim, E., Adams, P., Salisbury, J., Hackwell, J., and Treiman, A., 2001, First use of an airborne infrared hyperspectral scanner for compositional mapping: Remote Sensing of Environment, v. 80, p. 447-459, doi: 10.1016/S0034-4257(01)00323-6.

Kruse, F.A., Lefkoff, A.B., Boardman, J.W., Heidebrecht, K.B., Shapiro, A.T., Barloon, P.J., and Goetz, A.F.H., 1993, The Spectral Image Processing System (SIPS)-Interactive visualization and analysis of imaging spectrometer data: Remote Sensing of Environment, v. 44, p. 145-163, doi: 10.1016/0034-4257(93)90013-N.

Kruse, F.A., 1996, Geologic mapping using combined analysis of airborne visible/infrared imaging spectrometer (AVIRIS) and SIR-C/X-SAR data: Proceedings of SPIE, v. 2819, Imaging Spectrometry II, p. 24-35, doi: 10.1117/12.258078, event: SPIE's 1996 International Symposium on Optical Science, Engineering, and Instrumentation, Denver, Colorado, United States.

Kupfer, D.H., and Bassett, A.M., 1962, Geologic reconnaissance map of part of the southeastern Mojave Desert, California: United States Geological Survey Mineral Investigations Field Studies Map MF-205, scale 1:125,000.

Launer, P.J., 1952, Regularities in the infrared absorption spectra of the silicate minerals: American Mineralogist, v. 37, n. 9-10, p. 764-784, http://www.minsocam.org/ammin/AM37/AM37_764.pdf (accessed July 2018).

Le Bas, M.J., Le Maitre, R.W., Streckeisen, A., and Zanettin, B., 1986, A chemical classification of volcanic rocks based on the Total Alkali-Silica diagram: Journal of Petrology, v. 27, p. 745-750.

Lee, J.B., Woodyatt, S., and Berman, M., 1990, Enhancement of high spectral resolution remote- sensing data by a noise-adjusted principal components transform: IEEE Transactions on Geoscience and Remote Sensing, v. 28, n. 3, p. 295-304, doi: 10.1109/36.54356.

Luyendyk, B.P., Kamerling, M.J., and Terres, R., 1980, Geometric model for Neogene crustal rotations in southern California: Geological Society of America Bulletin, Part I, v. 91, n. 4, p. 211-217, doi: 10.1130/0016-7606(1980)91<211:GMFNCR>2.0.CO;2.

MacFadden, B.J., Woodburne, M.O., and Opdyke, N.D., 1990a, Paleomagnetism and Neogene clockwise rotation of the northern Cady Mountains, Mojave Desert of southern California: Journal of Geophysical Research, v. 95, n. B4, p. 4597-4608, doi: 10.1029/JB095iB04p04597.

MacFadden, B.J., Swisher, C.C. III, Opdyke, N.D., and Woodburne, M.O., 1990b, Paleomagnetism, geochronology, and possible tectonic rotation of the middle Miocene Barstow Formation, Mojave Desert, southern California: Geological Society of America Bulletin, v. 102, n. 4, p. 478-493, doi: 10.1130/0016-7606(1990)102<0478:PGAPTR>2.3.CO;2.

McClusky, S.C., Bjornstad, S.C., Hager, B.H., King, R.W., Meade, B.J., Miller, M.M., Monastero, F.C., and Souter, B.J., 2001, Present day kinematics of the eastern California shear zone from a geodetically constrained block model: Geophysical Research Letters, v. 28, n. 17, p. 3369-3372, doi: 10.1029/2001GL013091.

McGill, S.F., and Rubin, C.M., 1999, Surficial slip distribution on the central Emerson fault during the June 28, 1992, Landers earthquake, California: Journal of Geophysical Research, v. 104, n. B3, p. 4811-4833, doi: 10.1029/98JB01556.

McGill, S.F., Spinler, J.C., McGill, J.D., Bennett, R.A., Floyd, M.A., Fryxell, J.E., and Funning, G.J., 2015, Kinematic modeling of fault slip rates using new geodetic velocities from a transect across the Pacific-North America plate boundary through the San Bernardino Mountains, California: Journal of Geophysical Research: Solid Earth, v. 120, n. 4, doi:10.1002/2014JB011459.

McQuarrie, N., and Wernicke, B.P., 2005, An animated reconstruction of southwestern North America since 36 Ma: Geosphere, v. 1, n. 3, p. 147-172, doi: 10.1130/GES00016.1.

Meade, B.J., and Hager, B.H., 2005, Block models of crustal motion in southern California constrained by GPS measurements: Journal of Geophysical Research, v. 110, B03403, doi:10.1029/2004JB003209.

Miller, M.M., Johnson, D.J., Dixon, T.H., and Dokka, R.K., 2001, Refined kinematics of the eastern California shear zone from GPS observations, 1993-1998: Journal of Geophysical Research, v. 106, n. B2, p. 2245-2263, doi: 10.1029/2000JB900328.

Miller, D.M., and Yount, J.C., 2002, Late Cenozoic tectonic evolution of the north-central Mojave Desert inferred from fault history and physiographic evolution of the Fort Irwin area, California, *in* Glazner, A.F., Walker, J.D., and Bartley, J.M., eds., Geologic Evolution of the Mojave Desert and Southwestern Basin and Range: Boulder, Colorado, Geological Society of America Memoir 195, p. 173–197, doi: 10.1130/0-8137-1195-9.173.

Oskin, M., and Stock, J., 2003, Marine incursion synchronous with plate-boundary localization in the Gulf of California: Geology, v. 31, n. 1, p. 23-26, doi: 10.1130/0091-7613(2003)031<0023:MISWPB>2.0.CO;2.

Oskin, M., Perg, L., Shelef, E., Strane, M., Gurney, E., Singer, B., and Zhang, X., 2008, Elevated shear zone loading rate during an earthquake cluster in eastern California: Geology, v. 36, no. 6, p. 507-510, doi: 10.1130/G24814A.1.

Oskin, M., and Iriondo, A., 2004, Large-magnitude transient strain accumulation on the Blackwater fault, Eastern California shear zone: Geology, v. 32, n. 4, p. 313-316, doi: 10.1130/G20223.1.

Peltzer, G., Crampé, F., Hensley, S., and Rosen, P., 2001, Transient strain accumulation and fault interaction in the eastern California shear zone: Geology, v. 29, n. 11, p. 975-978, doi: 10.1130/0091-7613(2001)029<0975:TSAAFI>2.0.CO;2.

Phillips, F.M., 2003, Cosmogenic ^{36}Cl ages of Quaternary basalt flows in the Mojave Desert, California, USA: Geomorphology, v. 53, p. 199-208, doi:10.1016/S0169-555X(02)00328-8.

Plescia, J., and Henyey, T.L., 1982, Geophysical character of the proposed eastern extension of the Garlock fault and adjacent areas, eastern California: Geology, v. 10, p. 209-214, doi: 10.1130/0091-7613(1982)10<209:GCOTPE>2.0.CO;2.

QGIS Development Team, 2018, QGIS Geographic Information System, Open Source Geospatial Foundation Project: https://qgis.org/en/site/ (accessed September 2017).

Richard, S.M., 1993, Palinspastic reconstruction of southeastern California and southwestern Arizona for the Middle Miocene: Tectonics, v. 12, n. 4, p. 830-854, doi: 10.1029/92TC02951.

Richards, J.A., 2013, Remote Sensing Digital Image Analysis: An Introduction (Fifth Edition): Berlin, Germany, Springer-Verlag, 494 p., doi: 10.1007/978-3-642-30062-2.

Robitaille, P. -M., 2009, Kirchhoff's law of thermal emission: 150 years: Progress in Physics, v. 4, p. 3-13.

Rockwell, T.K., Lindvall, S., Herzberg, M., Murbach, D., Dawson, T., and Berger, G., 2000, Paleoseismology of the Johnson Valley, Kickapoo, and Homestead Valley faults: Clustering of earthquakes in the eastern California shear zone: Bulletin of the Seismological Society of America, v. 90, n. 5, p. 1200-1236, doi: 10.1785/0119990023.

Ross, T.M., Luyendyk, B.P., and Haston, R.B., 1989, Paleomagnetic evidence for Neogene clockwise tectonic rotations in the central Mojave Desert, California: Geology, v. 17, p. 470-473, doi: 10.1130/0091-7613(1989)017<0470:PEFNCT>2.3.CO;2.

Rymer, M.J., Seitz, G.G., Weaver, K.D., Orgil, A., Faneros, G., Hamilton, J.C., and Goetz, C., 2002, Geologic and paleoseismic study of the Lavic Lake fault at Lavic Lake playa, Mojave Desert, southern California: Bulletin of the Seismological Society of America, v. 92, n. 4, p. 1577-1591, doi: 10.1785/0120000936.

Salisbury, J.W., and Walter, L.S., 1989, Thermal infrared (2.5-13.5 μm) spectroscopic remote sensing of igneous rock types on particulate planetary surfaces: Journal of Geophysical Research, v. 94, n. B7, p. 9192-9202.

Salisbury, J.W., Wald, A., and D'Aria, D.M., 1994, Thermal-infrared remote sensing and Kirchhoff's law 1. Laboratory measurements: Journal of Geophysical Research, v. 99, n. B6, p. 11897-11911.

Sandwell, D.T., Sichoix, L., and Smith, B., 2002, The 1999 Hector Mine earthquake, southern California: Vector near-field displacements from ERS InSAR: Bulletin of the Seismological Society of America, v. 92, no. 4, p. 1341-1354, doi: 10.1785/0120000901.

Sauber, J., Thatcher, W., and Solomon, S.C., 1986, Geodetic measurement of deformation in the central Mojave Desert, California: Journal of Geophysical Research, v. 91, n. B12, p. 12,683-12,693, doi: 10.1029/JB091iB12p12683.

Sauber, J., Thatcher, W., Solomon, S.C., and Lisowski, M., 1994, Geodetic slip rate for the eastern California shear zone and the recurrence time of Mojave Desert earthquakes: Nature, v. 367, p. 264-266, doi: 10.1038/367264a0.

Savage, J.C., Lisowski, M., and Prescott, W.H., 1990, An apparent shear zone trending north-northwest across the Mojave Desert into Owens Valley, eastern California: Geophysical Research Letters, v. 17, n. 12, p. 2113-2116, doi: 10.1029/GL017i012p02113.

Savage, J.C., and Svarc, J.L., 1997, Postseismic deformation associated with the 1992 Mw = 7.3 Landers earthquake, southern California: Journal of Geophysical Research, v. 102, n.

B4, p. 7565-7577, doi: 10.1029/97JB00210.

Schermer, E.R., Luyendyk, B.P., and Cisowski, S., 1996, Late Cenozoic structure and tectonics of the northern Mojave Desert: Tectonics, v. 15, n. 5, p. 905-932, doi:10.1029/96TC00131.

Shelef, E., and Oskin, M., 2010, Deformation processes adjacent to active faults: Examples from eastern California: Journal of Geophysical Research, v. 115, B05308, doi:10.1029/2009JB006289.

Sieh, K., et al., 1993, Near-field investigations of the Landers earthquake sequence, April to July 1992: Science, v. 260, n. 5105, p. 171-176.

Simons, M., Fialko, Y., Rivera, L., 2002, Coseismic deformation from the 1999 Mw 7.1 Hector Mine, California, earthquake as inferred from InSAR and GPS observations: Bulletin of the Seismological Society of America, v. 92, no. 4, p. 1390-1402, doi: 10.1785/0120000933.

Snow, J.K., and Wernicke, B.P., 2000, Cenozoic tectonism in the central Basin and Range: magnitude, rate, and distribution of upper crustal strain: American Journal of Science, v. 300, p. 659-719.

Sousa, F.J., 2016, Tectonics of central and eastern California: Late Cretaceous to modern [Ph.D. thesis]: Pasadena, California Institute of Technology, 243 p., https://thesis.library.caltech.edu/9748/13/Sousa_Francis_2016_thesis.pdf (accessed July 2018).

Spinler, J.C., Bennett, R.A., Anderson, M.L., McGill, S.F., Hreinsdóttir, S., and McCallister, A., 2010, Present-day strain accumulation and slip rates associated with southern San Andreas and eastern California shear zone faults: Journal of Geophysical Research, v. 115, B11407, doi:10.1029/2010JB007424.

Spotila, J.A., and Sieh, K., 1995, Geologic investigations of a "slip gap" in the surficial ruptures of the 1992 Landers earthquake, southern California: Journal of Geophysical Research, v. 100, n. B1, p. 543-559, doi: 10.1029/94JB02471.

Stewart, J.H., 1983, Extensional tectonics in the Death Valley area, California: Transport of the Panamint Range structural block 80 km northwestward: Geology, v. 11, p. 153-157, doi: 10.1130/0091-7613(1983)11<153:ETITDV>2.0.CO;2.

Tou, J.T. and R. C. Gonzalez, 1974, Pattern Recognition Principles: Reading, Massachusetts, Addison-Wesley Publishing Company, 377 p.

Treiman, J.A., Kendrick, K.J., Bryant, W.A., Rockwell, T.K., and McGill, S.F., 2002, Primary surface rupture associated with the Mw 7.1 16 October 1999 Hector Mine

earthquake, San Bernardino County, California: Bulletin of the Seismological Society of America, v. 92, no. 4, p. 1171-1191, doi: 10.1785/0120000923.

Unruh, J.R., Lettis, W.R., and Sowers, J.M., 1994, Kinematic interpretation of the 1992 Landers earthquake: Bulletin of the Seismological Society of America, v. 84, n. 3, p. 537-546.

U.S. Geological Survey and California Geological Survey, 2006, Quaternary fault and fold database for the United States: http://earthquake.usgs.gov/hazards/qfaults/ (accessed September 2017).

Wells, R.E., and Hillhouse, J.W., 1989, Paleomagnetism and tectonic rotation of the lower Miocene Peach Springs Tuff: Colorado Plateau, Arizona, to Barstow, California: Geological Society of America Bulletin, v. 101, p. 846-863, doi: 10.1130/0016-7606(1989)101<0846:PATROT>2.3.CO;2.

Wessel, P., Smith, W.H.F, Scharroo, R., Luis, J., and Wobbe, F., 2013, Generic Mapping Tools: Improved Version Released: EOS, Transactions, American Geophysical Union, v. 94, no. 45, p. 409-410, doi: 10.1002/2013EO450001.

Woodburne, M.O., 2015, Mojave Desert Neogene tectonics and the onset of the eastern California shear zone, *in* Proceedings, 2015 Desert Symposium, Zzyzx, California, California State University Desert Studies Center, p. 153-199,

http://nsm.fullerton.edu/dsc/images/DSCdocs/DS%202015%20volume.pdf#page=153 (accessed July 2018).

Young, S.J., Johnson, B.R., and Hackwell, J.A., 2002, An in-scene method for atmospheric compensation of thermal hyperspectral data: Journal of Geophysical Research, v. 107, no. D24, p. 4774-4793, doi: 10.1029/2001JD001266.

Zachariasen, J., and Sieh, K., 1995, The transfer of slip between two en echelon strike- slip faults: A case study from the 1992 Landers earthquake, southern California: Journal of Geophysical Research, v. 100, n. B8, p. 15,281-15,301, doi: 10.1029/95JB00918.

FIGURE CAPTIONS

Figure 1 (p. 243): Overview map of the 1992 Mw 7.3 Landers and 1999 Mw 7.1 Hector Mine earthquake surface ruptures, and territory with access restricted by the MCAGCC (United States Marine Corps Air Ground Combat Center, Twentynine Palms) as of 1999 (solid line) and as of 2018 (dashed line). Other major faults shown are the Pinto Mountain fault (PMF) and the Mission Creek strand of the San Andreas fault (SAF). Base map is an SRTM 1 arc-second DEM hillshade (from the USGS Earth Resources Observation and Science website, https://eros.usgs.gov/, accessed on 09/02/2017). Faults are from U.S. Geological Survey and California Geological Survey (2006). Map was produced using QGIS software (QGIS, 2018).

Figure 2 (p. 244): (A) Overview of the Lavic Lake fault, mapped by its 1999 earthquake surface rupture. Arrows indicate relative fault motion, rectangular boxes are the extent of ground coverage of the hyperspectral airborne imagery used in this study, and LLP denotes the Lavic Lake playa, the geographic feature after which the fault is named (Hector Mine Earthquake Geologic Working Group, 1999). GIS data (base map and fault) is same as in Figure 1. Portions of other faults that ruptured in the 1999 earthquake are letter-coded as follows: CH- Calico-Hidalgo fault zone; ML- Mesquite Lake fault; BP- Bullion-Pisgah fault zone. (B) Overview of the portion of the Lavic Lake Fault covered by the hyperspectral airborne imagery footprints. "RF" denotes the Red Flake site, an area that was ground-truthed for supervised classifications. GIS data is same as in Figure 1. (C)-(F) Overview maps of the Red Flake site, centered at 34.586078° north, 116.288492° west. (C) Lidar 10 cm DEM hillshade (from the Open Topography website, http://www.opentopography.org/, accessed September 2017). Fault scarps from the 1999 earthquake are annotated by the dotted lines. (D) Polygon representing the area ground-truthed at the Red Flake site. Base map same as (C). (E) Elevation contour map of the Red Flake site (contour interval is 1 m). Polygon same as in (D). (F) Google Earth true color satellite image of the Red Flake site (imagery date: 2 January 2015). Polygon same as in (D). Maps in (A)-(E) were produced using QGIS software (QGIS, 2018).

Figure 3 (p. 245): Field photographs of the Red Flake site (located at 34.586078° north, 116.288492° west), an area where we ground-truthed the lithology as part of the supervised classification process. The lithologic variety at the Red Flake site is distinguishable by distinct differences in rock color, due to good exposure and little vegetative overgrowth. (A)

Overview facing west; circle denotes the location where the people seen in (C) are standing (photograph date / time / credit: 21 December 2012 / 9:49 am Pacific standard time / Joann Stock). (B) Overview facing north from helicopter; circle denotes location where the people seen in (C) are standing (photograph date / time / credit: 26 December 2012 / 1:14 pm Pacific standard time / Ken Hudnut). (C) View facing north of the 1999 earthquake fault scarp, showing the 1-m-tall protrusion of red feldspar porphyry (center of image, to right of scarp) from which the site derives its name. People on the horizon are circled for scale (photograph date / time / credit: 21 December 2012 / 10:30 am Pacific standard time / Ken Hudnut).

Figure 4 (p. 246): (A) Geologic map of the Red Flake site (located at 34.586078° north, 116.288492° west), with lithologic names and color assignments on the right. (B) Example of pixels randomly generated to produce end-member spectra for a supervised classification. Random generation is stratified (samples randomly chosen from individual classes) and proportionate to the area defined by a lithologic boundary (we used 2% of the area; e.g. if a certain lithology occupied 100 pixels of image area, two pixels would be randomly chosen for spectral sampling and averaged to define a representative end-member spectrum for said lithology. (C) Example remote sensing spectra derived from the randomly generated pixel selections shown in (B).

Figure 5 (p. 247): Thermal infrared laboratory spectra for lithologic hand samples collected at the Red Flake site. Spectra were measured on a Thermo-Nicolet 6700 FTIR Spectrometer using the biconical reflectance method. (A) Tuff and tuff breccia (four spectra), (B) detritus/colluvium (1 spectrum), (C) feldspar porphyry (3 spectra), and (D) microcrystalline

lava (2 spectra). All spectra were measured with a spot size of 1 - 2 mm, and each spectrum shown is an average of 150 scans taken over 4 - 6 minutes.

Figure 6 (p. 248): Data processing flowchart for our hyperspectral airborne image classifications. Based upon our knowledge of the site, we chose to perform standard classification techniques commonly available. We used the Environment for Visualizing Images Software, version 4.8 (ENVI, Exelis Visual Information Solutions, Boulder, Colorado). User-specified parameters are indicated by how they are input in dialogue boxes for each of the image processing steps. NESR- noise equivalent spectral radiance.

Figure 7 (p. 249): Overview of the complete hyperspectral airborne image swath, displayed in the following false color assignment: red, third MNF component; green, sixth MNF component; and blue, eighth MNF component. A subtle along-track gradation is present, and some clouds that were present during acquisition have been masked. The Red Flake site is annotated by a star, and located at 34.586078° north, 116.288492° west. Rectangular outline is the area shown in more detail in Figures 9, 10, and 11. GIS data is same as in Figure 1. Map was produced using QGIS software (QGIS, 2018).

Figure 8 (p. 250): (A)-(J) Ten supervised classifications of the Red Flake site (located at 34.586078° north, 116.288492° west). Lithologic contacts are superimposed for comparison with the ground-truthed geologic map (Figure 4A), and to visually assess the classification accuracy. Ground truth lithologic names, with color assignments, are shown at the bottom

for ready interpretation. Quantified results for the producer's, user's, and overall accuracies are in Tables 2 and 3, designated by the corresponding capital letters (A)-(J).

Figure 9 (p. 251): Geologic swath map of the Lavic Lake fault from an unsupervised classification of thermal hyperspectral airborne imagery. Thin lines are lithologic contacts; thick line is the approximate surface trace of the Lavic Lake fault (linework from Dibblee, 1966). Arrows indicate relative fault motion. Lithologic names shown in key are from correlating our classes with the units from Dibblee (also see Table 4). The Red Flake site is annotated by a star, and located at 34.586078° north, 116.288492° west. Upper right inset map (produced using Generic Mapping Tools, see Wessel et al., 2013) shows the footprint of the airborne imagery and the 1999 Hector Mine earthquake surface rupture (Treiman et al., 2002; U.S. Geological Survey and California Geological Survey, 2006). Lower left zoom inset (centered at 34.551116° north, 116.264804° west) shows a boundary between our classes that correlates well with a lithologic contact between tuff breccia and basalt (Dibblee, 1966). Note that some clouds that were present during image acquisition have been masked.

Figure 10 (p. 252): Portion of the Dibblee (1966) geologic map, zoomed to approximately the same area shown in the zoom inset of Figure 9. The map was modified by adding the line A-A' (with the representative cross section shown above the map), and also adding the asterisk symbol where the Tt/Tb contact was depicted as depositional, but is actually be a fault. The legend contains the relevant lithologic units and symbols featured here and discussed in the text. In the cross section, dip of the Tt/Tb depositional contact is from the

average of cross-section-projected dip domains on the east and west side of the Lavic Lake fault are 13º and 23º (both east/northeast), respectively.

Figure 11 (p. 253): Side-by-side comparison of the cumulative fault offset analysis area, as portrayed in (A) the MNF components in false color (from Figure 7), (B) the unsupervised classification (from Figure 9), and (C) the Dibblee (1966) map (from Figure 10). All panels are at the same scale (scale bar and north arrow in (A) apply to all three panels) and location (centered at 34.551116° north, 116.264804° west), with Dibblee's line work superimposed on the remote sensing imagery products in (A) and (B).

Figure 12 (p. 254): Oblique-view Google Earth satellite image (imagery date: 2 January 2015) of the location (centered at 34.551116° north, 116.264804° west) where we measured separation of piercing lines by the Lavic Lake fault (note that the scales are not accurate everywhere in the images, due to the oblique viewing geometry). (A) Image without annotation. (B) Thick black line is the Lavic Lake fault surface trace, thin red lines are Dibblee's Tt/Tb lithologic depositional contact, which separates the lighter-hued lithology (Tt, the older tuff breccia), from the darker-hued lithology (Tb, the younger basalt, which overlies Tt). (C) Thick black line is the Lavic Lake fault surface trace, thin green lines are the Tt/Tb depositional contact (modified from Dibblee's depiction), and the smaller cross faults are also depicted by a thick black line. We used the smaller cross faults to measure 930 m of horizontal, right-lateral map-view separation for the horizontal component of the slip vector. Note that the smaller cross fault on the west side of the Lavic Lake fault is depicted

in (B) as a portion of the Tt/Tb depositional contact. The yellow double-headed arrows white stars are the ground-based field photograph locations in Figure 13.

Figure 13 (p. 255): Ground-based field photographs of the cross fault (Tt/Tb fault contact) on the west side of the main Lavic Lake fault. Figure 12C shows the photograph locations as white stars. Person (Ken Hudnut) provides scale. (A) date: 3 April 2014; time: 4:09 pm Pacific daylight savings time; location: 34.556183º north, 116.267204º west; viewing direction: north/northwest; taken by Joann Stock. (B) date: 2 October 2012; time: 10:55 am Pacific daylight savings time; location: 34.557096º north, 116.266962º west; viewing direction: south/southwest; taken by Frank Sousa. (C) same as (A), but annotated with lithologic letter codes (see Table 4). (D) same as (B), but annotated with lithologic letter codes (see Table 4). In (A), bedding in Tt can be observed dipping to the east/northeast. In (C) and (D), note that the older Tt unit is structurally above the younger Tb unit.

TABLES

Table 1: ECSZ age of inception		
Author(s)	Age	Basis
Dokka and Travis (1990a; b)	6 - 10 Ma	Initiation of Garlock Fault c. 10 Ma (Burbank and Whistler, 1987), which is cut by younger ECSZ faults in the east (Davis and Burchfiel, 1973; Plescia and Henyey, 1982); age relations from Stewart (1983), which may indicate that some ECSZ faults initiated c. 6 Ma; Paleomagnetic data from Carter et al. (1987), which may indicate that regional deformation began after c. 6 Ma
Schermer et al. (1996)	<11.7 Ma	Fan deposits dated at 11.7 Ma have left lateral offset
Miller and Yount (2002)	>5 - 6 Ma	Left lateral faults controlled topography and subsequently the flow direction of 5-6 Ma basalts
Gan et al. (2003)	5.0 ± 0.4 Ma	Modeling the deflection of the Garlock Fault's once straight, but now curved surface trace
Oskin and Iriondo (2004)	>3.77 ± 0.11 Ma	Dated basalt flow that drapes a fault scarp in the Black Mountains
McQuarrie and Wernicke (2005)	c. 12 Ma	Right lateral shear, oriented N25°W since c. 12 Ma is based on palinspastic restoration modeling of mountain ranges in the southwestern U.S.A.
Woodburne (2015)	c. 6 Ma	Coupled with, or possibly as a byproduct of the opening of the Gulf of California (Atwater, 1992; Atwater and Stock, 1998; Oskin and Stock, 2003; Bennett et al., 2015); also cites a period of non-deposition in the Mojave Desert Region until c. 6 Ma to argue for tectonic quiescence up until that time.

Table 2: Red flake site supervised classification error matrices						
Classified	Ground truth				Total	User's accuracy
(A)	Tuff	Detritus	Feldspar porphyry	Microcrystalline lava		
Tuff	25	2	56	4	87	0.29
Detritus	11	28	69	3	111	0.25
Feldspar porphyry	13	0	125	89	227	0.55
Microcrystalline lava	13	0	112	747	872	0.86
Total possible	62	30	362	843	1297	
Producer's accuracy	0.40	0.93	0.35	0.89		Overall accuracy = 0.71
(B)						
Tuff	30	17	85	2	134	0.22
Detritus	2	3	12	0	17	0.18
Feldspar porphyry	18	10	161	121	310	0.52
Microcrystalline lava	12	0	105	719	836	0.86
Total possible	62	30	363	842	1297	
Producer's accuracy (%)	0.48	0.10	0.44	0.85		Overall accuracy = 0.70
(C)						
Tuff	41	6	97	24	168	0.24
Detritus	13	23	53	22	111	0.21
Feldspar porphyry	0	0	128	88	216	0.59
Microcrystalline lava	8	0	85	709	802	0.88
Total possible	62	29	363	843	1297	
Producer's accuracy (%)	0.66	0.79	0.35	0.84		Overall accuracy = 0.69
(D)						
Tuff	36	5	81	13	135	0.27
Detritus	4	24	43	1	72	0.33
Feldspar porphyry	9	0	114	68	191	0.60
Microcrystalline lava	13	0	124	761	898	0.85
Total possible	62	29	362	843	1296	
Producer's accuracy (%)	0.58	0.83	0.31	0.90		Overall accuracy = 0.72
(E)						
Tuff	13	2	26	7	48	0.27
Detritus	29	24	87	2	142	0.17
Feldspar porphyry	11	3	117	59	190	0.62

Microcrystalline lava	8	0	132	775	915	0.85
Total possible	61	29	362	843	1295	
Producer's accuracy (%)	0.21	0.83	0.32	0.92		Overall accuracy = 0.72
(F)						
Tuff	19	1	44	61	125	0.15
Detritus	28	24	103	5	160	0.15
Feldspar porphyry	1	5	124	45	175	0.71
Microcrystalline lava	14	0	92	731	837	0.87
Total possible	62	30	363	842	1297	
Producer's accuracy (%)	0.31	0.80	0.34	0.87		Overall accuracy = 0.69
(G)						
Tuff	28	1	70	36	135	0.21
Detritus	23	26	68	5	122	0.21
Feldspar porphyry	1	3	109	45	158	0.69
Microcrystalline lava	10	0	116	756	882	0.86
Total possible	62	30	363	842	1297	
Producer's accuracy (%)	0.45	0.87	0.30	0.90		Overall accuracy = 0.71
(H)						
Tuff	15	4	20	7	46	0.33
Detritus	22	16	86	3	127	0.13
Feldspar porphyry	10	10	133	63	216	0.62
Microcrystalline lava	15	0	124	769	908	0.85
Total possible	62	30	363	842	1297	
Producer's accuracy (%)	0.24	0.53	0.37	0.91		Overall accuracy = 0.72
(I)						
Tuff	15	1	27	22	65	0.23
Detritus	34	23	98	11	166	0.14
Feldspar porphyry	4	6	116	55	181	0.64
Microcrystalline lava	8	0	122	755	885	0.85
Total possible	61	30	363	843	1297	
Producer's accuracy (%)	0.25	0.77	0.32	0.90		Overall accuracy = 0.70
(J)						
Tuff	16	1	26	10	53	0.30
Detritus	22	20	83	6	131	0.15

Feldspar porphyry	9	8	101	37	155	0.65
Microcrystalline lava	15	0	152	790	957	0.83
Total possible	62	29	362	843	1296	
Producer's accuracy (%)	0.26	0.69	0.28	0.94		Overall accuracy = 0.72

Table 3: Red flake site supervised classification accuracy summary*				
Lithology	# of 4-m^2 pixels	Area (m^2)	Producer's accuracy (%)	User's accuracy (%)
Tuff (and tuff breccia)	62	248	38 ± 16	25 ± 5
Detritus (colluvium)	30	120	71 ± 24	19 ± 6
Feldspar porphyry	364	1456	34 ± 4	62 ± 6
Microcrystalline lava	845	3380	89 ± 3	86 ± 1
*Standard deviation = 1σ; all values rounded to nearest integer				

Table 4: Correlation of unsupervised classification units with lithologic units from the Dibblee (1966) geologic map[1]			
Class color	Lithologic name given here	Letter codes and lithologic names from Dibblee (1966)[2]	Class also includes these units[2]
Yellow	Alluvium	Qa: alluvium Qf: fan gravel Qoa: older alluvium Qof*: older valley sediments, fanglomerate and gravel	QTr: rhyolitic felsite, (and all others)
Red	Felsite	Tif: intrusive felsite	Ta, Tt
Magenta	Andesite	Ta*: andesite Tap: andesite porphyry Tfa: fanglomerate of andesitic detritus	Qof, QTr, Tif, Tb, Tt
Purple	Weathered basalt	Tb*: basalt Tib: intrusive basalt	Tt
Blue	Basalt	Tb*: basalt Tib: intrusive basalt	QTr, Ta, Tt
Green	Tuff breccia	Tt: tuff breccia	Qof, Tif, Ta

[1]See Dibblee (1966; 1967abc; 2008) for complete lithologic descriptions; correlations are broad generalizations that do not necessarily cover every possible detail/variation

[2]Q: Quaternary, T: Tertiary; when multiple units appear in column three, asterisks indicate the predominant correlative unit

Table 5: Unsupervised classification error matrix for the Red flake site					
Classified	Ground truth			Total	User's accuracy
	Tuff	Detritus	Other		
Tuff	41	7	99	147	0.28
Detritus	1	20	351	372	0.05
Other	13	0	631	644	0.98
Total Possible	55	27	1081	1163	
Producer's accuracy	0.75	0.74	0.58		Overall accuracy = 0.60

FIGURES

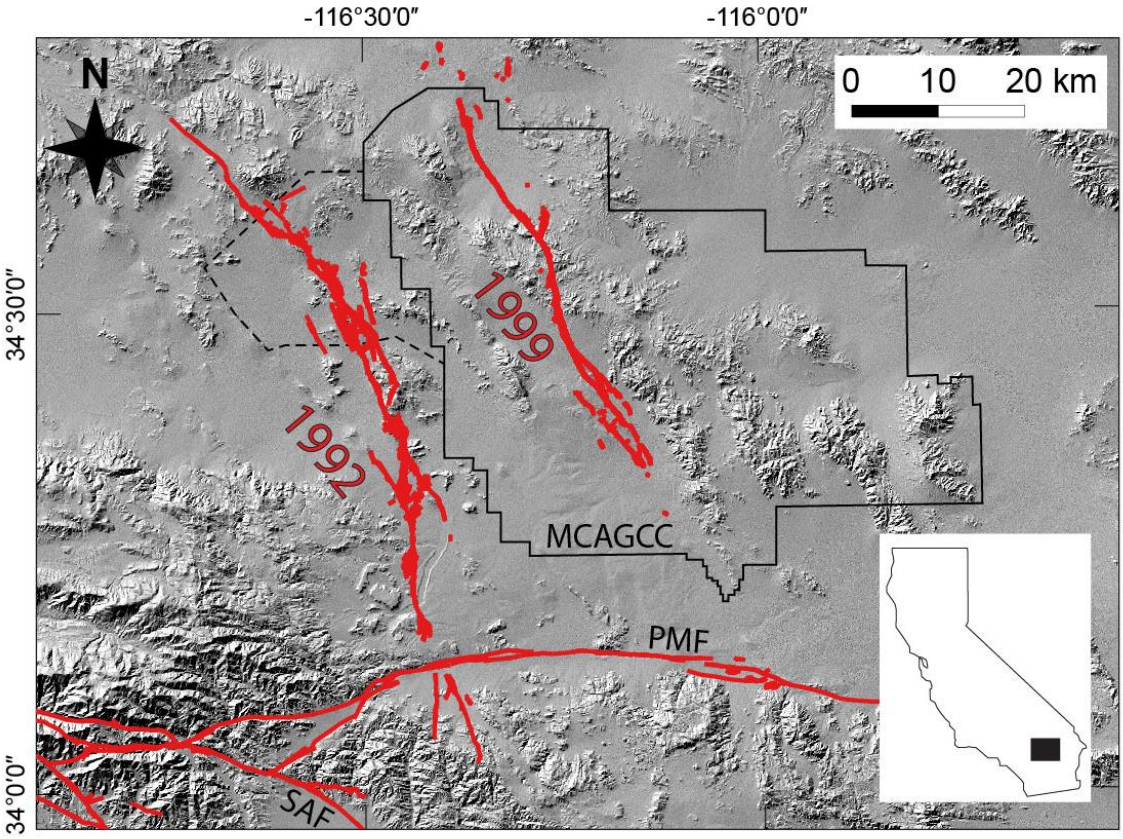

Figure 1

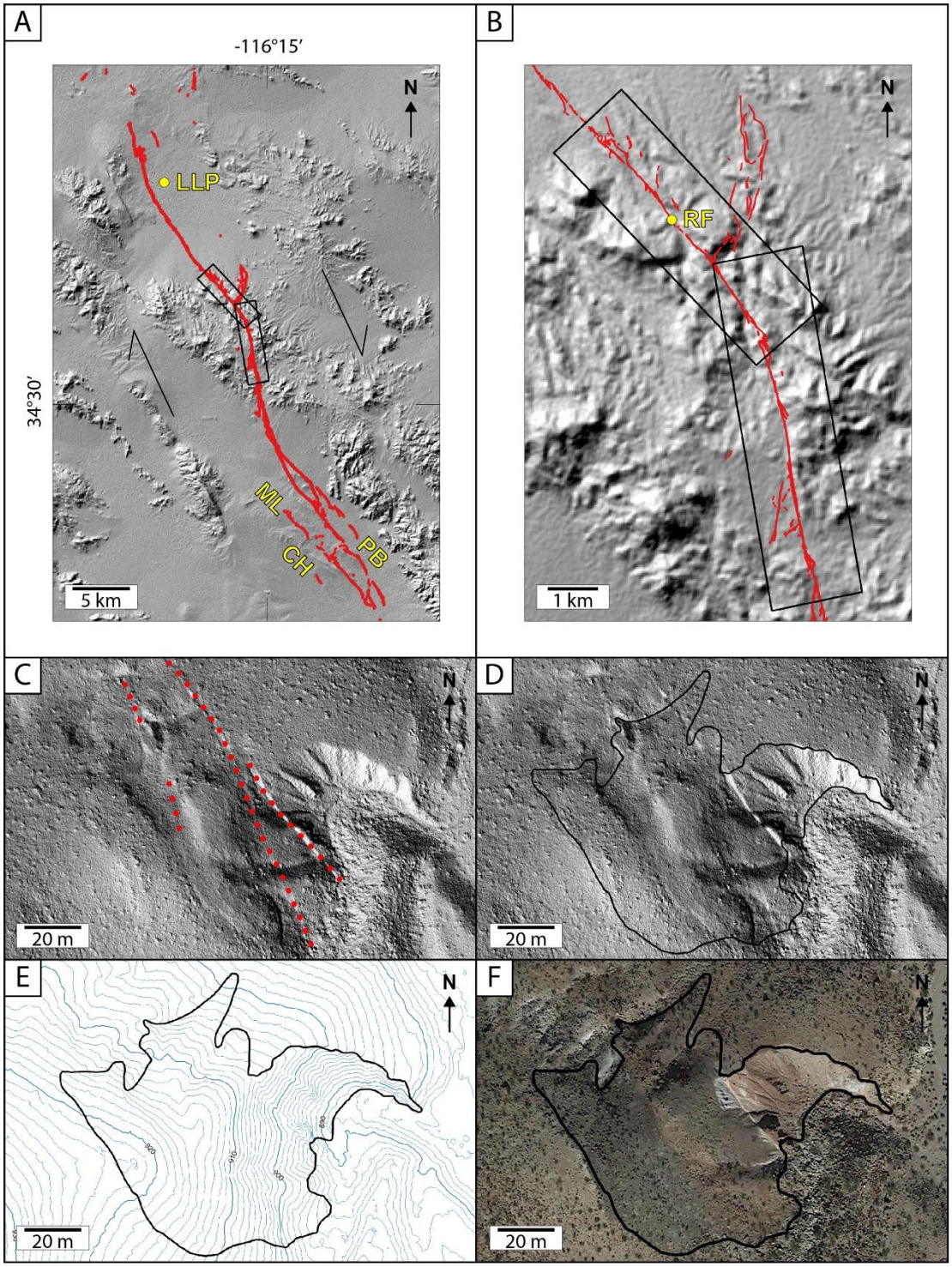
A
-116°15′
34°30′
N
LLP
ML
CH
PB
5 km
B
N
RF
1 km
C
N
20 m
D
N
20 m
E
N
20 m
F
N
20 m

Figure 2

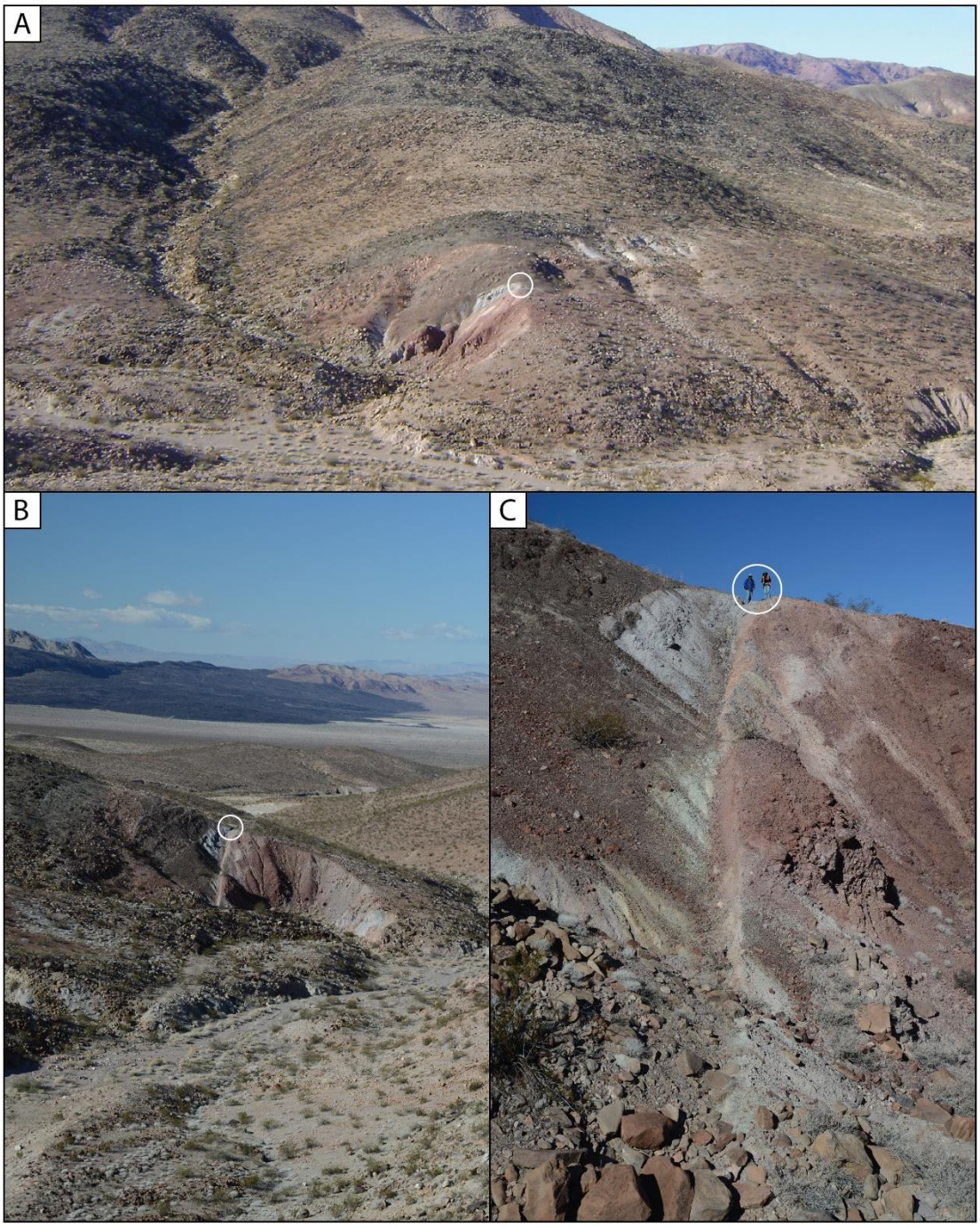

Figure 3

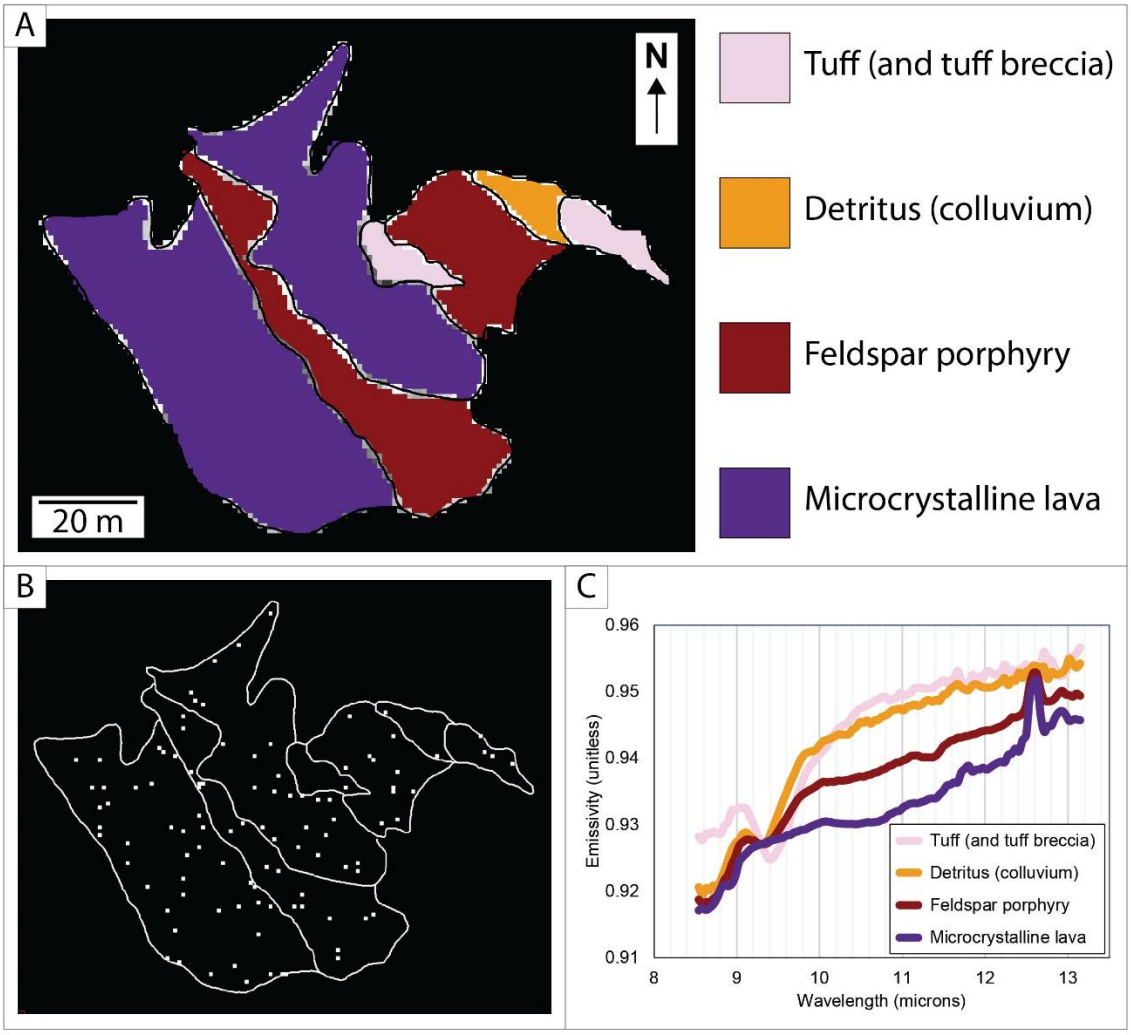
A
N
20 m
Tuff (and tuff breccia)
Detritus (colluvium)
Feldspar porphyry
Microcrystalline lava
B
C
0.96
0.95
0.94
0.93
0.92
0.91
Emissivity (unitless)
8
9
10
11
12
13
Wavelength (microns)
Tuff (and tuff breccia)
Detritus (colluvium)
Feldspar porphyry
Microcrystalline lava

Figure 4

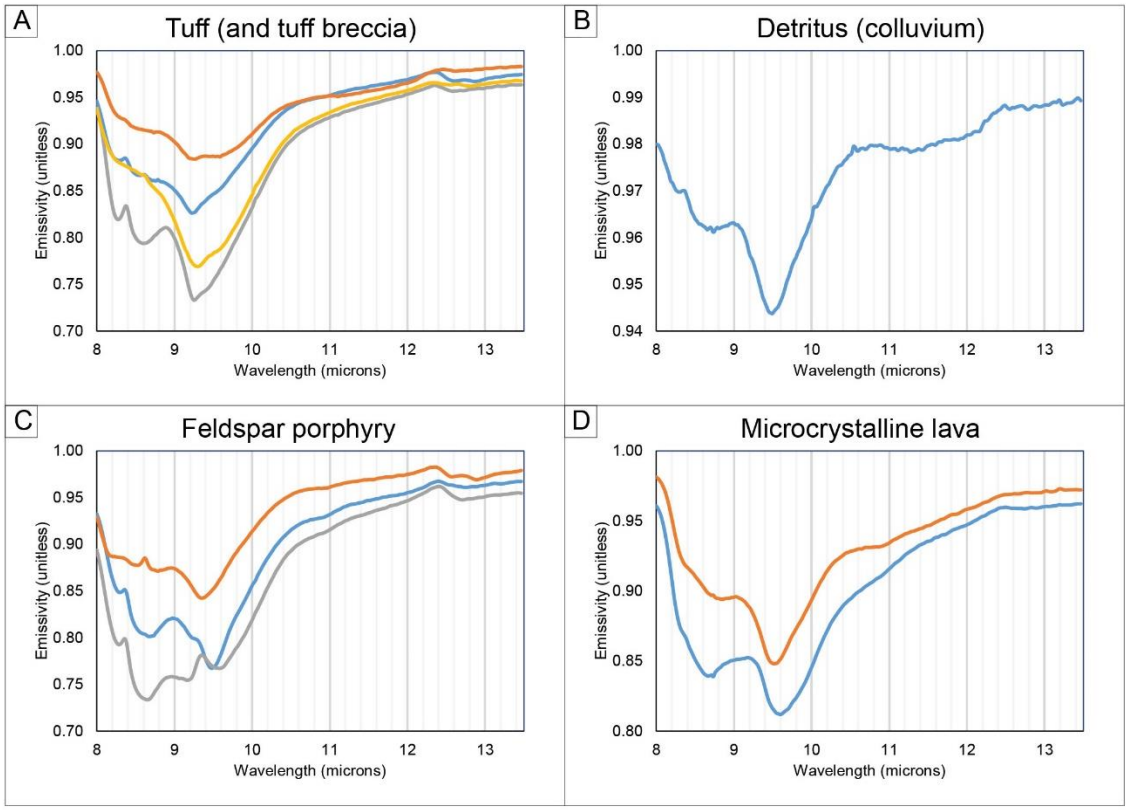
A
Tuff (and tuff breccia)
Emissivity (unitless)
1.00
0.95
0.90
0.85
0.80
0.75
0.70
8
9
10
11
12
13
Wavelength (microns)
B
Detritus (colluvium)
Emissivity (unitless)
1.00
0.99
0.98
0.97
0.96
0.95
0.94
8
9
10
11
12
13
Wavelength (microns)
C
Feldspar porphyry
Emissivity (unitless)
1.00
0.95
0.90
0.85
0.80
0.75
0.70
8
9
10
11
12
13
Wavelength (microns)
D
Microcrystalline lava
Emissivity (unitless)
1.00
0.95
0.90
0.85
0.80
8
9
10
11
12
13
Wavelength (microns)

Figure 5

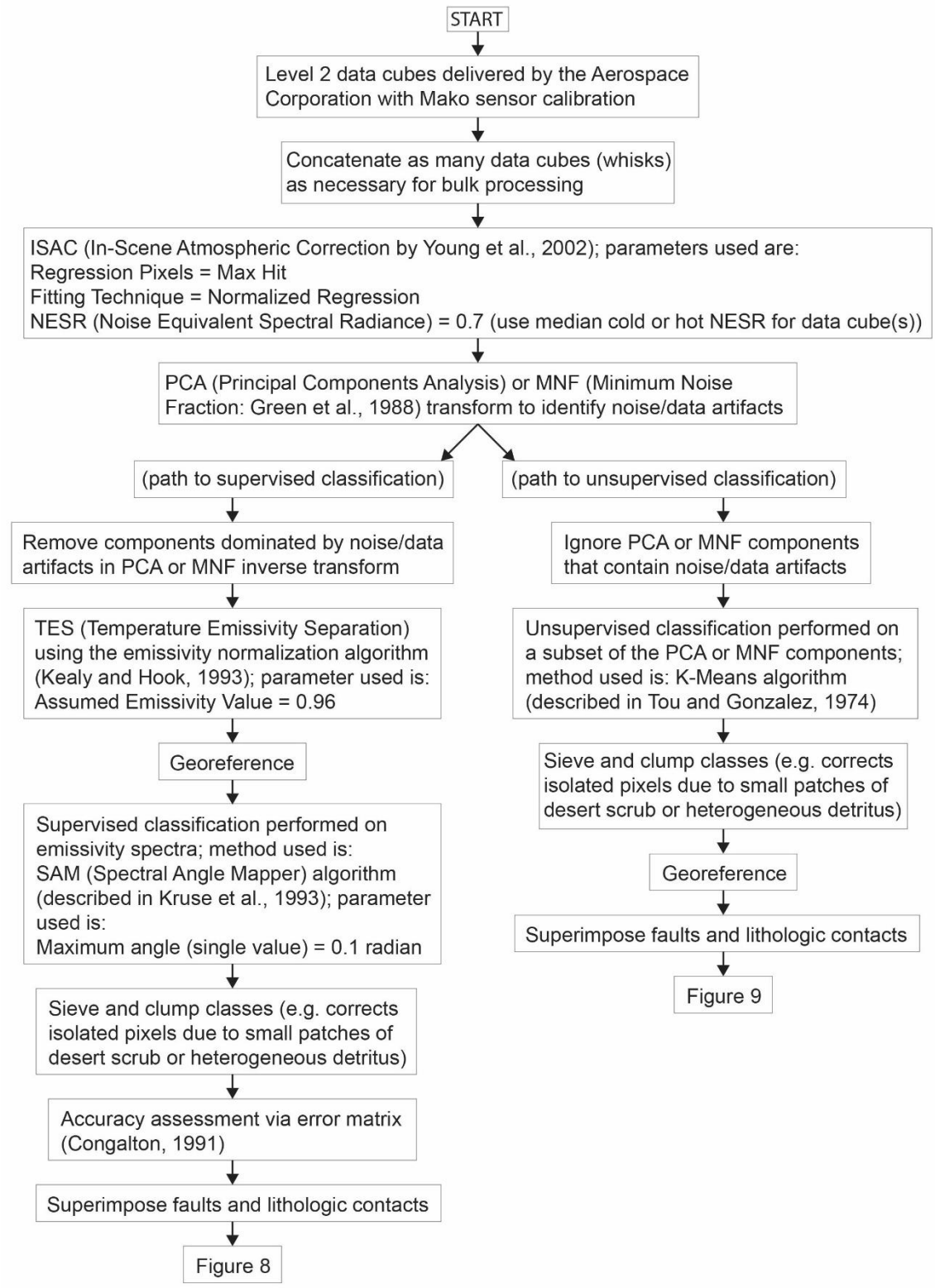
START
Level 2 data cubes delivered by the Aerospace Corporation with Mako sensor calibration
Concatenate as many data cubes (whisks) as necessary for bulk processing
ISAC (In-Scene Atmospheric Correction by Young et al., 2002); parameters used are:
Regression Pixels = Max Hit
Fitting Technique = Normalized Regression
NESR (Noise Equivalent Spectral Radiance) = 0.7 (use median cold or hot NESR for data cube(s))
PCA (Principal Components Analysis) or MNF (Minimum Noise Fraction: Green et al., 1988) transform to identify noise/data artifacts
(path to supervised classification)
(path to unsupervised classification)
Remove components dominated by noise/data artifacts in PCA or MNF inverse transform
Ignore PCA or MNF components that contain noise/data artifacts
TES (Temperature Emissivity Separation) using the emissivity normalization algorithm (Kealy and Hook, 1993); parameter used is:
Assumed Emissivity Value = 0.96
Unsupervised classification performed on a subset of the PCA or MNF components; method used is: K-Means algorithm (described in Tou and Gonzalez, 1974)
Georeference
Sieve and clump classes (e.g. corrects isolated pixels due to small patches of desert scrub or heterogeneous detritus)
Supervised classification performed on emissivity spectra; method used is:
SAM (Spectral Angle Mapper) algorithm (described in Kruse et al., 1993); parameter used is:
Maximum angle (single value) = 0.1 radian
Georeference
Sieve and clump classes (e.g. corrects isolated pixels due to small patches of desert scrub or heterogeneous detritus)
Superimpose faults and lithologic contacts
Accuracy assessment via error matrix (Congalton, 1991)
Figure 9
Superimpose faults and lithologic contacts
Figure 8

Figure 6

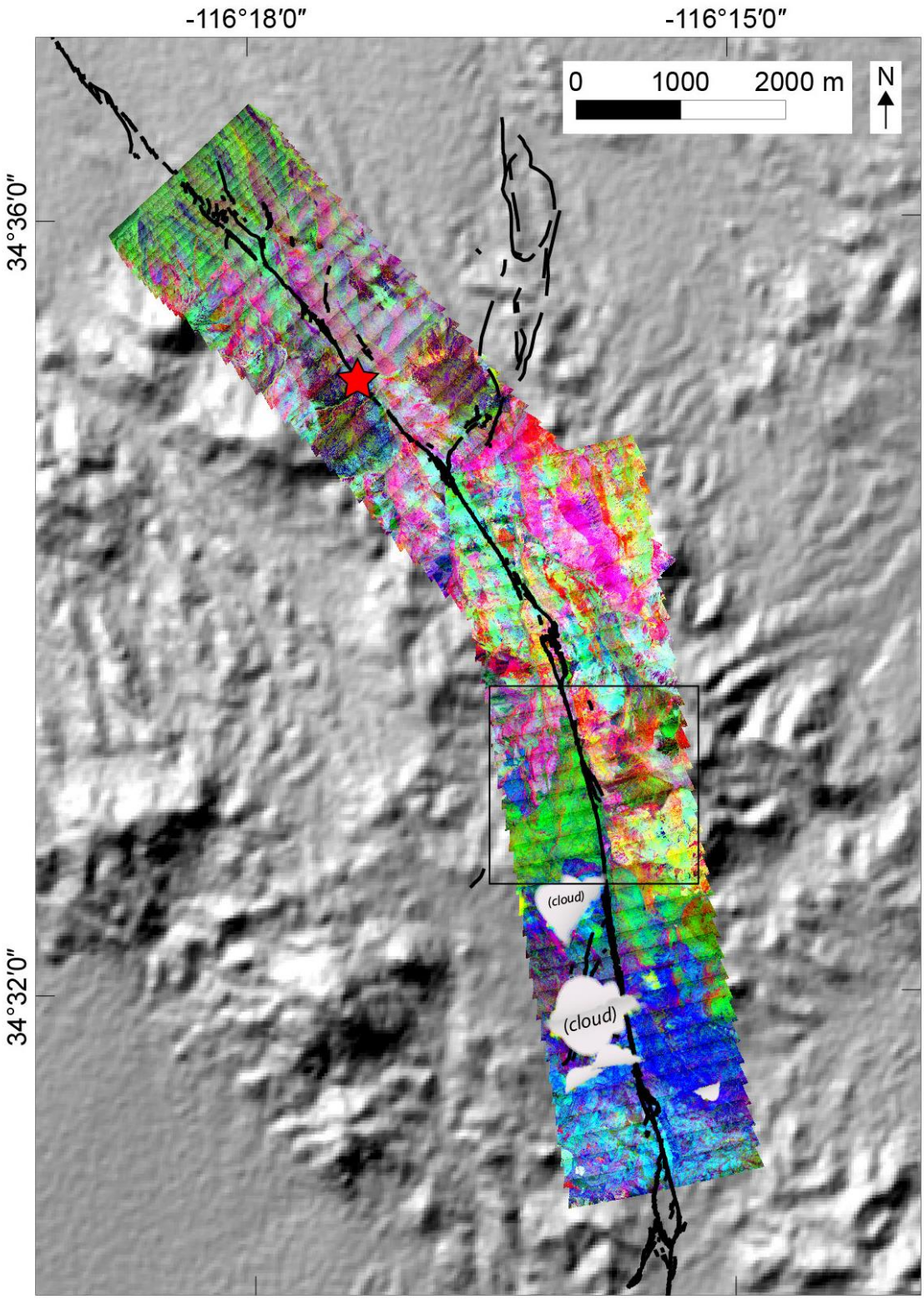

Figure 7

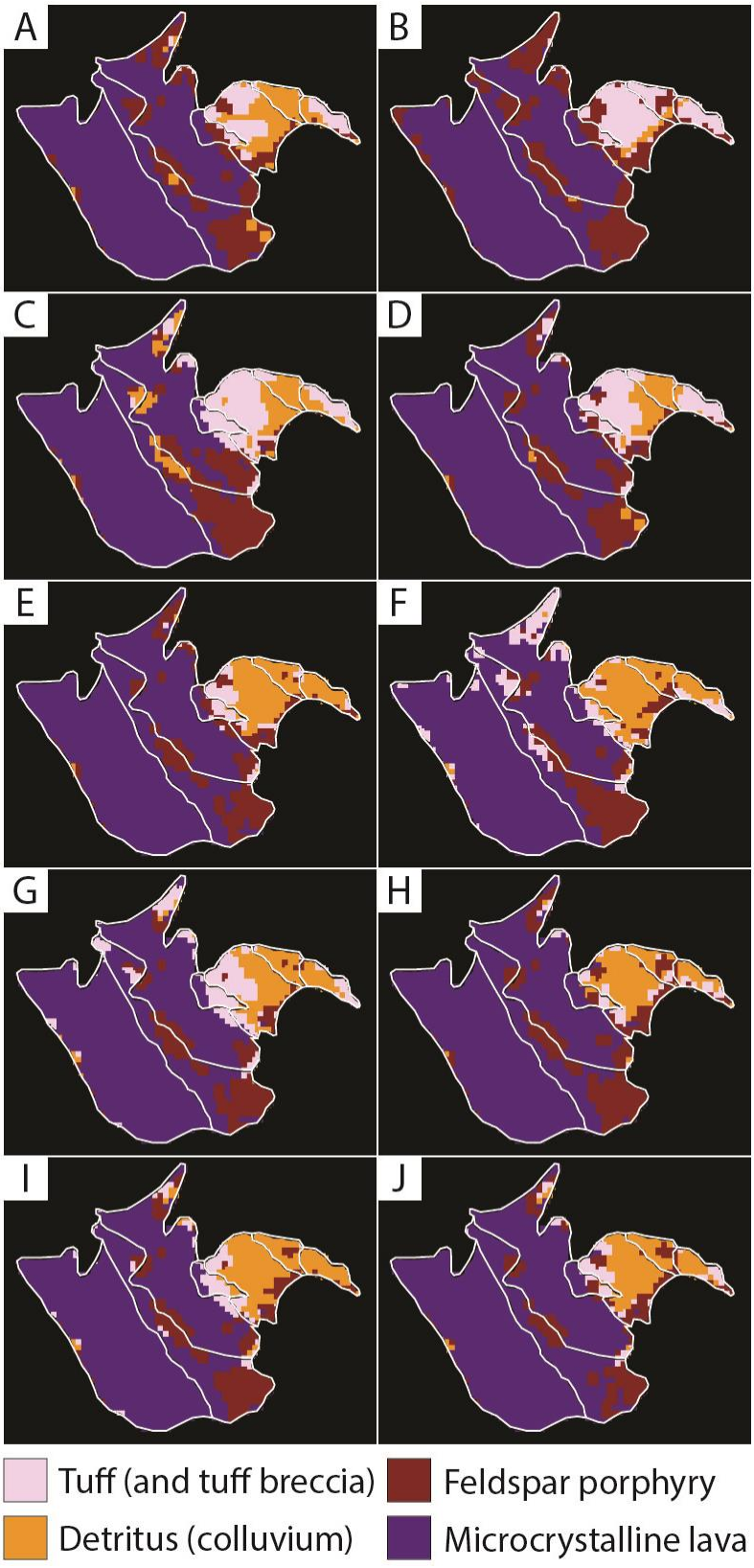
A
B
C
D
E
F
G
H
I
J
Tuff (and tuff breccia)
Feldspar porphyry
Detritus (colluvium)
Microcrystalline lava

Figure 8

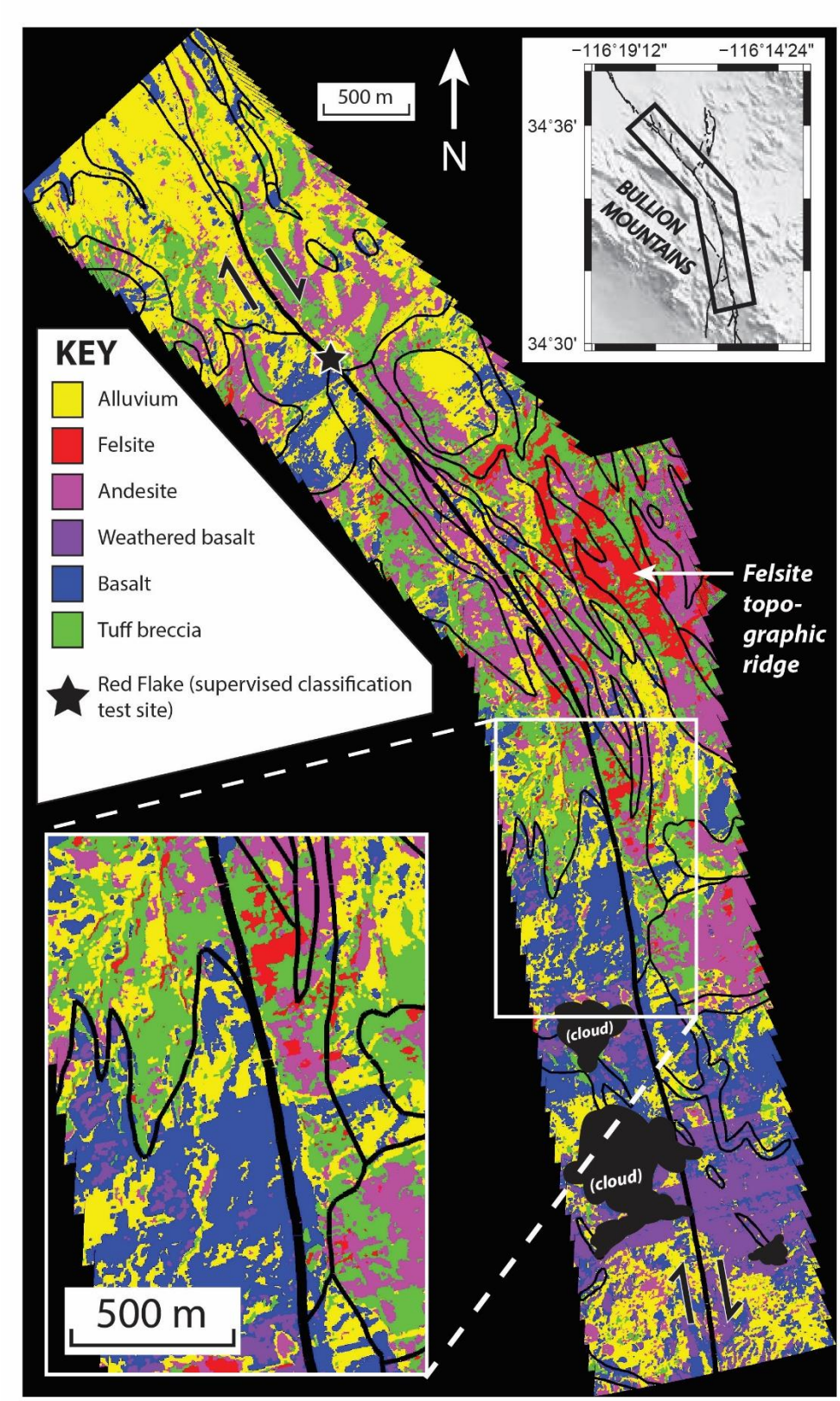
500 m
N
−116°19'12"
−116°14'24"
34°36'
34°30'
BULLION MOUNTAINS
KEY
Alluvium
Felsite
Andesite
Weathered basalt
Basalt
Tuff breccia
Red Flake (supervised classification test site)
Felsite topo-graphic ridge
(cloud)
(cloud)
500 m

Figure 9

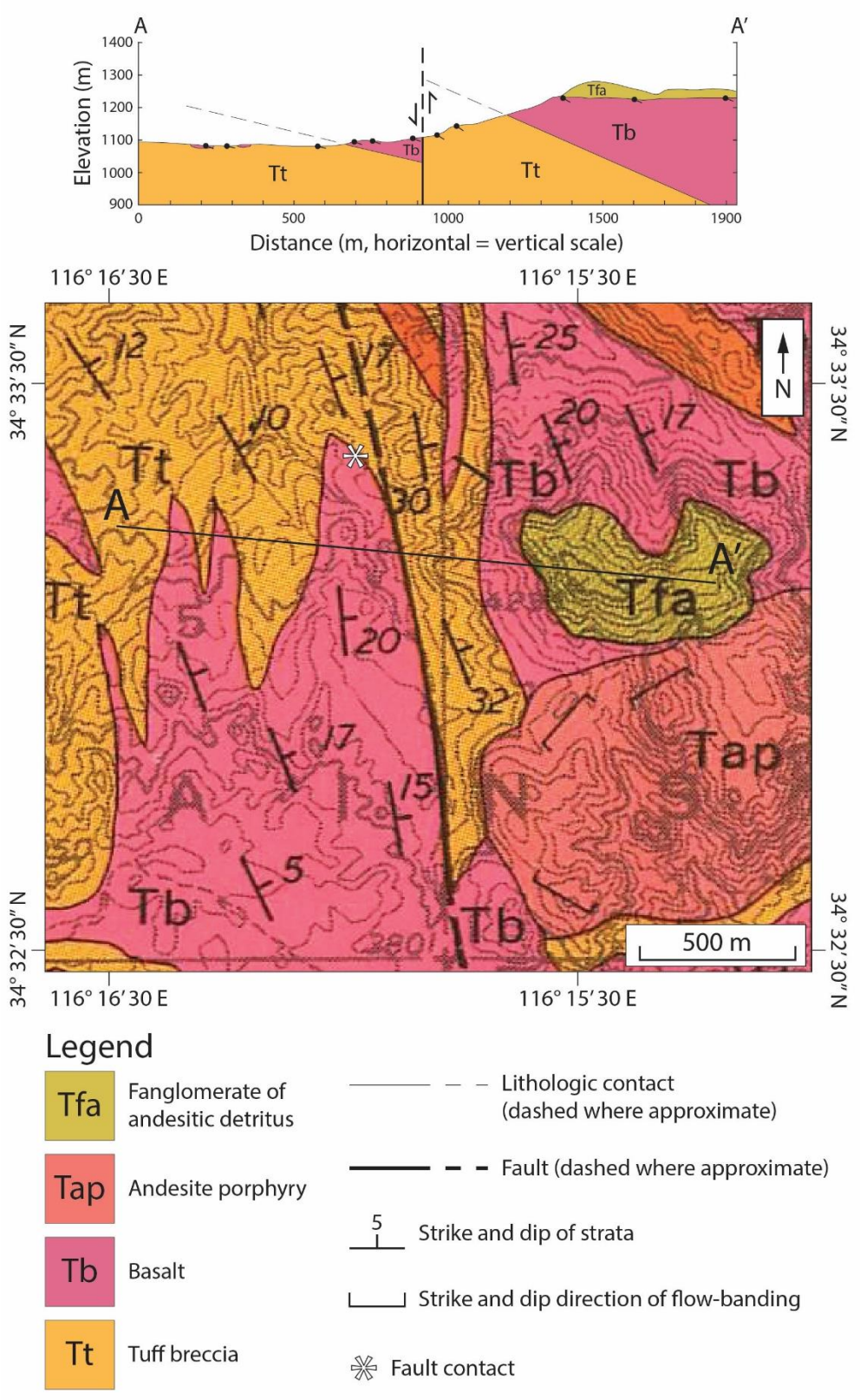
A
A′
Elevation (m)
1400
1300
1200
1100
1000
900
0
500
1000
1500
1900
Tfa
Tb
Tt
Tb
Tt
Distance (m, horizontal = vertical scale)
116° 16′ 30 E
116° 15′ 30 E
34° 33′ 30″ N
34° 32′ 30″ N
N
Tt
A
Tb
Tb
A′
Tfa
Tt
Tb
Tap
Tb
500 m
Legend
Tfa
Fanglomerate of andesitic detritus
Tap
Andesite porphyry
Tb
Basalt
Tt
Tuff breccia
Lithologic contact (dashed where approximate)
Fault (dashed where approximate)
5
Strike and dip of strata
Strike and dip direction of flow-banding
Fault contact

Figure 10

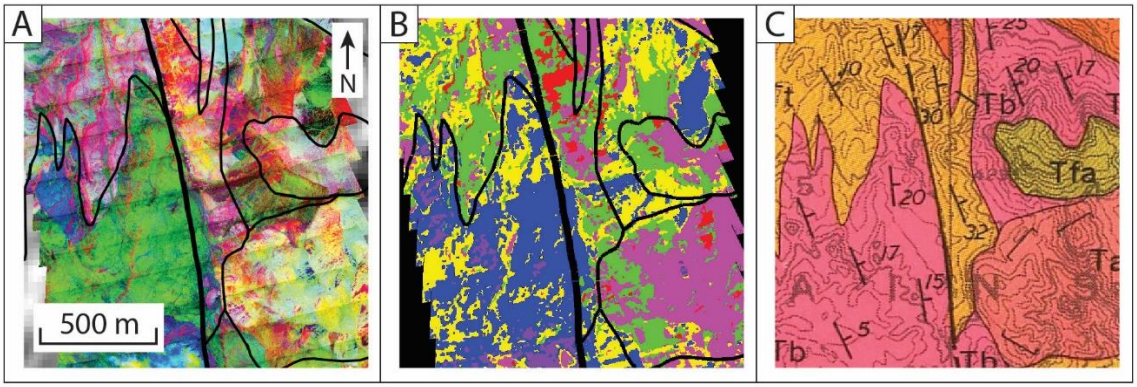

Figure 11

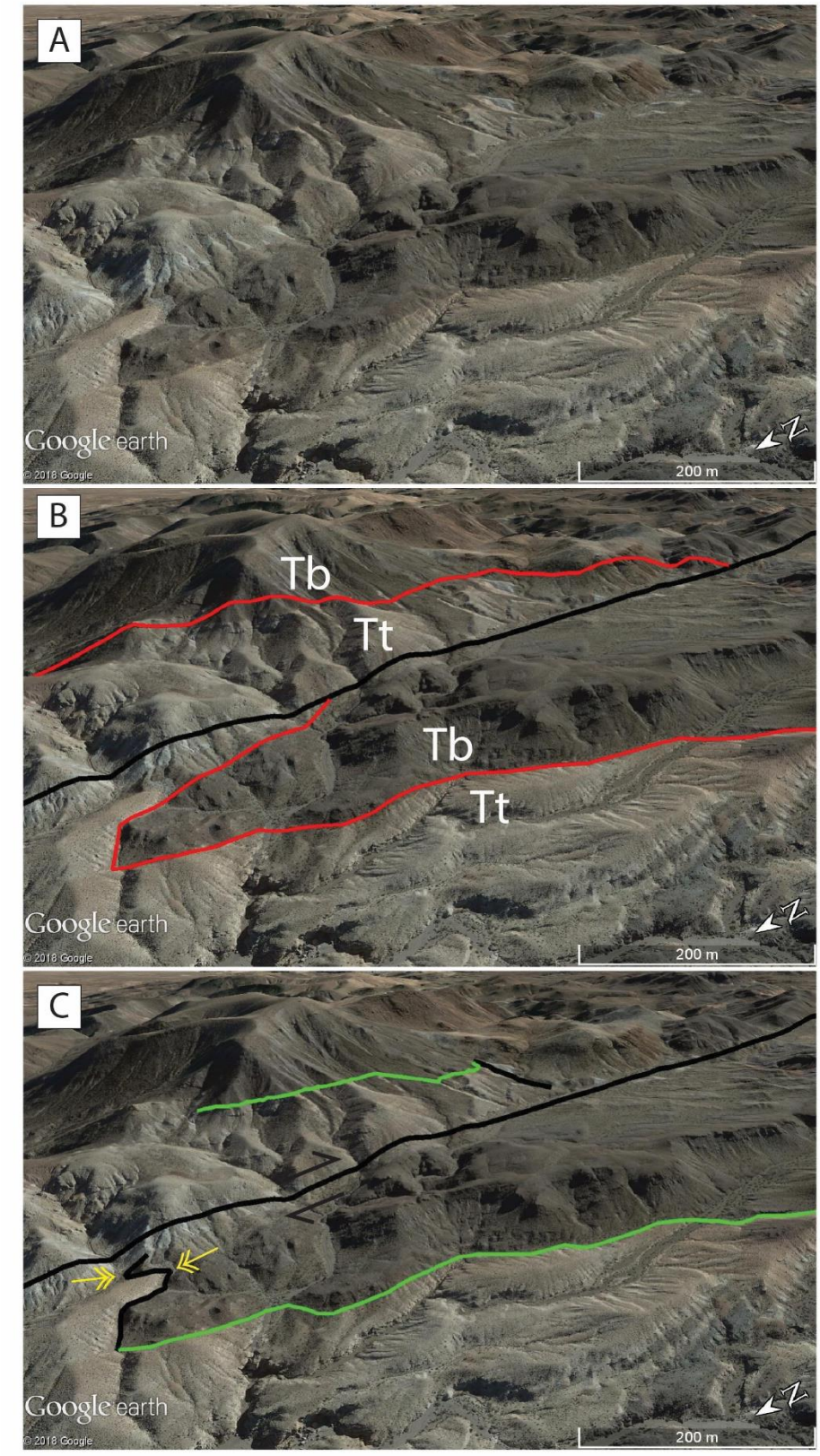
A
Google earth
© 2018 Google
200 m
N
B
Tb
Tt
Tb
Tt
Google earth
© 2018 Google
200 m
N
C
Google earth
© 2018 Google
200 m
N

Figure 12

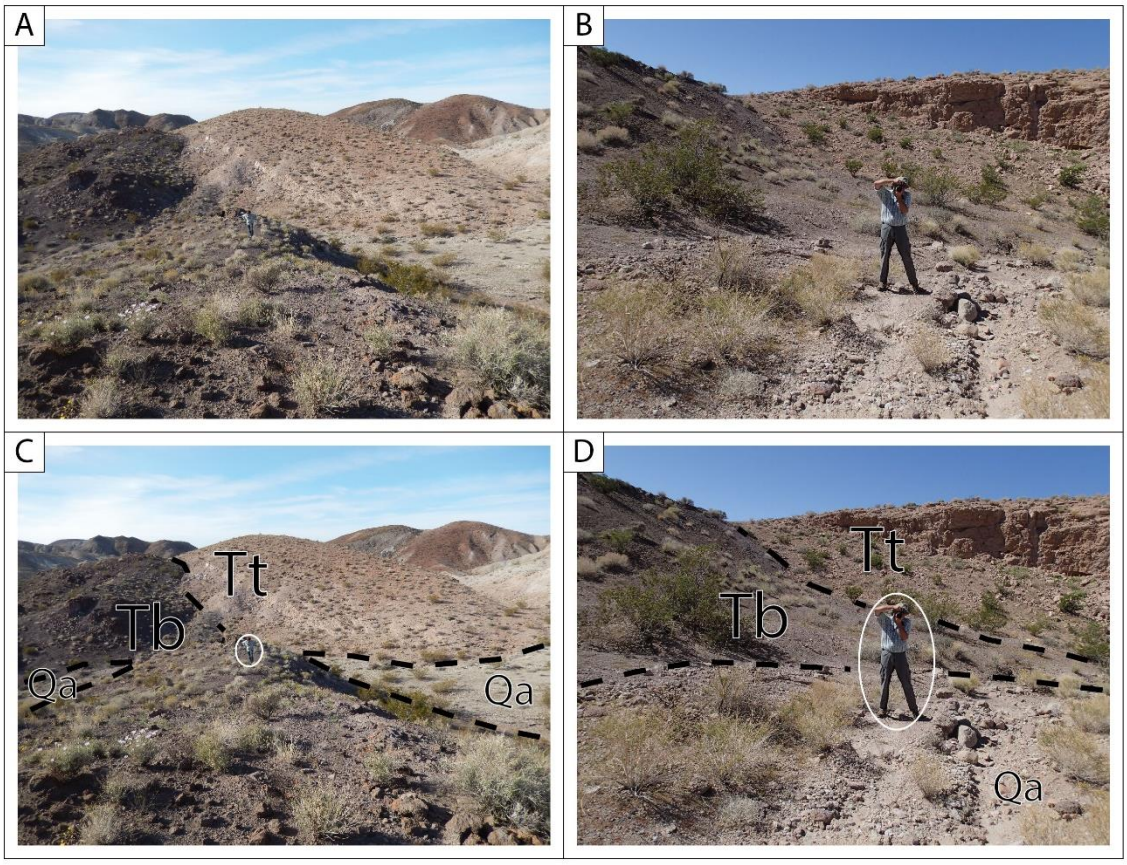

Figure 13

C h a p t e r 4

CHARACTERIZING EMISSIVITY SPECTRA FROM GEOMORPHIC SURFACES ALONG THE SOUTHERN SAN ANDREAS FAULT

Rebecca A. Witkosky[1], Joann Stock[1], David Tratt[2], Kate Scharer[3], Kerry Buckland[2], Paul Adams[2], and Pat Johnson[2]

[1]*California Institute of Technology, Division of Geological and Planetary Sciences, 1200 E. California Blvd., MC 170-25, Pasadena CA 91125*

[2]*The Aerospace Corporation, 2310 E. El Segundo Blvd., El Segundo CA 90245*

[3]*U.S. Geological Survey, 525 S. Wilson Ave., Pasadena, CA 91106-3212*

ABSTRACT

Well-developed varnish and pavement are usually characteristic of relatively older geomorphic surfaces: the environment must be broad, flat, and stable for extended periods of time for these features to reach advanced stages of development. However, varnish and pavement formation rates are not understood well enough for those features alone to be used as a reliable chronometer. In this research, we combine the known ages for a set of terraced geomorphic surfaces along the Mission Creek strand of the southern San Andreas fault in the Coachella Valley, southern California, to explore the use of thermal hyperspectral airborne remote sensing imagery for identifying age-dependent characteristics of spectral emissivity

features. In spectra from an airborne sensor, the band depth of an emissivity minimum at 9.16 μm generally increases with age of geomorphic surface. The spectral position of this feature is within the wavelength range for clay minerals (9.1-9.6 μm), which suggests increasing abundance of clay minerals on older surfaces. Desert varnish is known to contain clay minerals, so it is possible that the increased clay band depth with age manifests from increasing desert varnish development on older surfaces. We collected field data to test for other effects that might contribute to the increased band depth with age. Our field results show that desert varnish and desert pavement scores (higher numerical score assigned to a greater degree of development), and vegetation spacing estimates all display some positive correlation with surface age. Ground-based spectra from hand samples that we collected display a spectral feature at 9.30 μm, which also indicates clay content, but does not occur at the exact same wavelength position as that in the airborne spectra. Most of the airborne and ground-based spectra indicate the presence of clay mineral(s), along with quartz and feldspars. Ground-based vegetation spectra are generally flat and featureless over the wavelengths covered in remote sensing imagery. In summary, it appears that while a clay mineral signal in the airborne spectra is plausible, the overall spectral contrast increases with surface age due to the combination of varnish development, topographic smoothing associated with pavement formation, and increase in vegetation spacing (net decrease in vegetation). This suggests that the positive correlation between spectral contrast in airborne remote sensing spectra and surface age can potentially be used to determine relative ages of Quaternary geomorphic surfaces.

INTRODUCTION

The southern San Andreas fault is a major tectonic plate boundary that is especially hazardous due to its location near many major population centers in southern California. Tectonism in this desert region influences the health and safety of millions of people, so the numerous specific sections and strands of the southern San Andreas fault have been rigorously studied to assess prehistoric and current seismic activity. To assess the risk, we need to know about the slip rates of the faults. To estimate fault slip rates on the basis of tectonic geomorphology, the ages of geomorphic surfaces must be known. Relative ages of surfaces can be assigned using the degree of development of surficial coatings on gravel clasts (desert varnish) and/or surficial smoothing (desert pavement), to characterize and differentiate faulted geomorphic surfaces (alluvial fans or terraces). The degree with which desert varnish and desert pavement has developed over time can indicate the relative or absolute ages of distinct geomorphic units; this type of analysis has been applied to features that have been cut and offset by California's southern San Andreas fault (e.g., Keller et al., 1982; Shifflett et al., 2002; van der Woerd et al., 2006; Behr et al., 2010). In this study, we incorporate both developmental criteria to evaluate relative ages from the perspective of remote sensing imaging spectroscopy.

Desert varnish is a potential chronometer for estimating the ages of geomorphic surfaces, but to accurately employ the chronometer, we need to know how the lithologic coating forms and develops. The formation and development of desert varnish (from herein, sometimes referred to as just "varnish" for brevity) has long attracted interest from geologists, biologists, and others. Varnish can also form in non-arid environments, and is therefore sometimes more generically referred to as "rock varnish." Ideas for the primary

formation mechanism are usually either 1) inorganic chemical alteration of, and addition to, lithologic surfaces, or 2) microbiologic activity (note that (1) and (2) are not mutually exclusive). For both cases, primary formation will also depend on whether the constituent material of the varnish was derived in situ or had been transported to the present site. A combination of these factors likely vary in relative contribution based on the specific regional and local environment. Regardless of the source of origin materials, petrographic observations of varnish usually reveal a microstratigraphy (Perry and Adams, 1978; Reneau et al., 1992), indicating it is an accretionary process, and encouraging attempts to calculate some type of accretion/sedimentation/growth rate (Liu and Broecker, 2000).

In order to use varnish as a chronometer, empirical knowledge about its growth rates is needed. Rates of growth, based on varnish thickness and the age of surfaces determined radiometrically, have been calculated with very broad results. Calculated rates range from <1 to 40 μm/ky (ky = one thousand years), with the caveat that those rates are certainly minima due to an unknown time lag between deposition and inception of growth, and the observation that older samples tend to exhibit slower growth rates (Liu and Broecker, 2000; Spilde et al., 2013). The time lag required for initiating varnish growth has been observed in a number of cases, with estimates of as little as 25 years (Engel and Sharp, 1954), up to about 100 years (Whitley and Dorn, 1987). In specific cases, faster growth rates can be attributed to an environment conducive to accelerated growth (Krinsley et al., 2012), such as more frequent and consistent moisture (Hunt, 1954; Thiagarajan and Lee, 2004). The high variability in growth rates, and the fact that a maximum varnish thickness of c. 200 μm is usually observed (Liu and Broecker, 2000; Spilde et al., 2013), precludes the use of thickness alone as a chronometer.

The idea of using varnish as a chronometer has stimulated various ideas and methods aimed at measuring the formation process. In a given region, a calibrated relationship to geologic time can be established, and then potentially used for future work (e.g., Helms et al., 2003). A rigorous and widely tested application of this method involves establishing a calibrated, standard regional time scale for the Late Pleistocene to which varnish microstratigraphy can be correlated (Liu and Broecker, 2013). This calibrated method has yielded ages that agree with those from independent surface exposure dating methods used on the same lithologic units (Marston, 2003; Phillips, 2003; Liu, 2003). Some other methodologies for using varnish as a chronometer, namely cation ratios, and direct dating using accelerator mass spectrometry, are not yet reliably developed (e.g., see reviews by Beck et al., 1998; Watchman, 2000).

Desert varnish often includes a high relative abundance of clay minerals (Potter and Rossman, 1977), so perhaps geomorphic surfaces with varnished clasts can be spectroscopically distinguished by measuring relative clay content. Due to their predominantly submicroscopic size, clay mineral grains are commonly detected and identified via laboratory methods, including x-ray diffraction (XRD) and spectroscopy. Remote sensing data and methods (i.e., imaging spectroscopy) are an extension of laboratory spectroscopy, and with recent technological development, the limitations of low spectral and spatial resolution have been overcome on many modern platforms.

For this study, we are focusing on distinguishing varnish that has accumulated on a chemically dissimilar (mineralogic/petrologic) substrate material. We can take advantage of previous work that used spectroscopy and remote sensing to determine the mineralogy and petrology of substrate material that lies beneath coatings of desert varnish. Formative

research in lithologic remote sensing has typically involved examining the way varnish represents "noise" that complicates and/or conceals the signal from its mineralogic/petrologic substrate in laboratory and imaging spectroscopy (Kahle and Goetz, 1983; Gillespie et al., 1984; Kahle, 1987; Bartholomew et al., 1989; Rivard et al., 1993; Christensen and Harrison, 1993). In this research, we are focusing on varnish as "signal," exploiting the fact that it is both opaque from manganese and iron oxide content, and contains clay minerals not always present in a substrate material, and so can be detected and identified via remote sensing methods.

Ultimately, we want to relate remote sensing of lithology and active tectonics in a way that benefit society: the age-dependent development of geomorphic surfaces, and the overprinting of continuous tectonic displacement present an opportunity to capture measurements of both time and distance. Desert varnish and related desert pavement surfaces can provide an idea of geologic age (or at least the passage of time into a current state), and tectonics can provide an idea of physical displacement, which together provide the quantities needed for a geologic fault slip rate. Varnish and pavement are often associated with Quaternary unconsolidated lithologic units, and geologic fault slip rates from these relatively young displaced features can have greater relevance for guiding risk and hazard assessment on the current state of a tectonic system.

GEOLOGIC/TECTONIC SETTING

The southern San Andreas fault in the northern Coachella Valley offsets a number of geomorphic surfaces with well-determined exposure ages (Blisniuk and Sharp, 2014). There

is also an abundance of observations of both modern and ancient seismic activity. The prehistoric, historic, and modern seismic activity have been analyzed in three main ways: 1) paleoseismic trenching to establish earthquake recurrence intervals (and in rare cases, calculate fault slip rates); 2) methods in tectonic geomorphology to establish geologic fault slip rates; and 3) Global Positioning System (GPS) and interferometric synthetic aperture radar (InSAR) data and modeling to establish present-day geodetic fault slip rates. All of these types of data can be incorporated into modeling and analyses of seismic hazards along the San Andreas fault (e.g., Jones et al., 2008; Porter et al., 2011; Davis and O'Rourke, 2011). Of these types of seismic hazards analysis mentioned above, our research is most closely related to the tectonic geomorphology approach. An overview of the other two approaches may be found in the Appendix.

Tectonic Geomorphology

The Coachella Valley region contains numerous Late Pleistocene to Holocene recognizable geomorphic features indicating a tectonically active landscape. The Indio Hills (Keller et al., 1982), Mecca Hills, Edom Hill, and Durmid Hill (Bürgmann, 1991) are all archetypal examples of how the Earth's surface responds to active strike-slip fault motion, transpression, and various modes of tectonic buckling. Fluvial channels and alluvial fans are cut and displaced, revealing both historic and prehistoric strike-slip fault motion. Those geomorphic features have been used to estimate geologic slip rates for the southern San Andreas fault, which vary widely, depending on the specific location and/or fault strand(s)

considered. For this research, we chose to analyze the Mission Creek strand of the southern San Andreas fault at Pushawalla Canyon (Figure 1).

Thousand Palms Oasis and Pushawalla Canyon areas in the Indio Hills

The remote sensing data used here includes thermal hyperspectral airborne imagery that covers a set of alluvial/fluvial deposits near the Thousand Palms Oasis and Pushawalla Canyon (Figure 1). These deposits are offset by the Mission Creek strand of the San Andreas fault, and have been dated recently using the ^{10}Be cosmogenic exposure and uranium-series methods (Blisniuk and Sharp, 2014). That study yielded a slip rate of 22-25 mm/yr, somewhat faster than rates from the same fault in nearby areas (e.g., see Behr et al., 2010; Fletcher et al., 2010). By combining our remote sensing data and techniques with their geochronology, we have a prime opportunity to perform mineral spectroscopy on varnished gravels in an area of known geomorphic surface exposure ages. This area is located within the Coachella Valley Preserve in southern California. The Coachella Valley Preserve is a protected, environmentally sensitive area. Thus, an important advantage of using hyperspectral airborne imagery for this type of research is its minimal environmental impact.

CHARACTERIZING ALLUVIAL/FLUVIAL DEPOSITS WITH REMOTE SENSING DATA AND METHODS

The Quaternary alluvial fans and fluvial terraces in this region formed in response to a combination of climatic and tectonic processes. Deposition of the detrital material can

occur under varying climatic influences, including glacial (Owen et al., 2014; Cyr et al., 2016), interglacial (Bull, 1991; Reheis et al., 1996), or transitional glacial-interglacial conditions (e.g., Bull, 1991; Friedrich et al., 2003; Pazzaglia, 2013). When deposition occurs along active faults, the tectonic influence is coupled with the climatic, affecting depositional patterns and the overall structure of the formation. Along the southern San Andreas fault, tectonic activity has contributed to uplifting broad, detrital surface deposits into uplands, forming a series of terraces. After deposition ceased and the geomorphic surfaces stabilized, the influence of the arid desert conditions set in, and the surfaces evolved with age.

The prevailing methods that are currently used for dating Quaternary deposits include analyses of cosmogenic radionuclides, luminescence, and Uranium-Thorium decay series (or "U-series," in this context, usually performed on carbonate formed in soil). All of those methods are rigorous and costly, which has encouraged other researchers to seek new dating methods that consider other physical and chemical aspects of geomorphic surface development. Here, we explore the applicability of using remote sensing data and methods, which have an economic advantage, and also, potential to characterize whole regions, particularly if they are poorly accessible. Remote sensing data and methods can be more accessible because they only require a computer and some software (albeit after significant costs and efforts to launch a platform), instead of a full laboratory setup.

Features of geomorphic surfaces relevant to age that are best characterized via remote sensing include mineralogy/petrology, and topographic surface roughness. Because older fans include a higher fraction of relatively erosion-resistant clasts (Gillespie et al., 1984), multispectral thermal infrared (8-12 μm wavelengths) airborne images produce spectra that are sensitive to compositional changes. Furthermore, as discussed below, the spectral

emissivity minimum moves to a longer wavelength as desert varnish develops on the clasts (Gillespie et al., 1984).

To quantify topographic surface roughness, digital elevation models (DEMs) produced from radar or lidar data are typically employed. With these data, Frankel and Dolan (2007; also see Frankel et al., 2007) found that topographic smoothing at the scale of 5-10 m wavelengths, the typical wavelength of bar and swale structures on alluvial surfaces, appears to occur over a time period of about ≤70 ky, after which roughness can increase if new channels begin to incise the surface as the base level of streams becomes lower. They also noted that a decrease in clast size due to weathering over time might also contribute to the overall smoothing at shorter wavelengths. Data from ground-based lidar, which is sensitive to variation in smaller clast sizes, has also been used to show that Quaternary geomorphic surfaces become topographically smoother over time (Mushkin et al., 2014).

Mushkin et al. (2014) attributed clast size reduction on geomorphic surfaces predominantly to salt weathering and shattering (e.g., Hunt and Mabey, 1966), in addition to the effects of clast exfoliation, and dissolution of carbonate rocks. Their study area was in the Jordan Rift Valley, which also includes the hypersaline Dead Sea. Salt weathering is also a dominant component in alluvial fan surface development at a site in China, where it may have hindered the advanced desert varnish and pavement development that can be comparatively observed in southern California (Farr and Chadwick, 1996). Our study area in the Coachella Valley does not consist primarily of carbonate rocks, and although there is currently a hypersaline water body in the region (the Salton Sea, and also possibly the prehistoric Lake Cahuilla; see the interpretations of Van de Kamp, 1973), salt weathering

does not appear to have played a large role in clast size reduction in the Pushawalla Canyon area.

Many previous studies have combined multiple remote sensing data types to look at the combined effects of compositional varnish and topographic smoothing. Combined approaches can take many forms, one of which used visible wavelength imagery for lithologic character, and a backscatter metric from satellite-borne radar for surface roughness (Farr and Chadwick, 1996). Jayko et al. (2005) used the panchromatic band (0.5-0.9 μm wavelengths) of the Landsat 7 satellite, and surface slope and curvature quantities derived from DEMs. The combined methods of Jayko et al. (2005) worked well in arid regions with minimal vegetation, but faltered in the following areas: 1) where the substrate lithology either quickly develops varnish, or might already resemble the ubiquitous dark color of a substantial varnish (for both cases, mafic volcanic rocks); 2) where varnish-resistant carbonate rocks abound; and 3) where rapidly-eroding fissile shales abound, presumably because higher erosion rates inhibit the stabilization necessary for a substantial coating. It is encouraging for future work that the mapping of geomorphic surfaces, at least to first order, can be fully automated using algorithms for classifying surfaces based on varying roughness and lithologic content (Jayko et al., 2005).

DESERT VARNISH

The primary chemical constituents of desert varnish are typically manganese and iron oxides (Hunt, 1954; Engel and Sharp, 1958; Perry and Adams, 1978), clay minerals (Hunt, 1954; Potter and Rossman, 1977; 1979), and silica (Perry et al., 2006; Aulinas et al., 2015).

Its characteristic black- and red-hued colors result from manganese and iron content (Perry and Adams, 1978). The specific metal oxide minerals can include hematite and birnessite, respectively (Potter and Rossman, 1979). Birnessite ($(Na,Ca,K)Mn_7O_{14}\cdot 3H_2O$) is a manganese oxide mineral that has a layered crystal structure, and is therefore similar to the phyllosilicate clay minerals that can also be present in significant abundance. Clays can compose up to 70% of the varnish (Potter and Rossman, 1977), but samples from some regions do not include a significant clay fraction. Clay-poor samples have been found instead to have main phases that include quartz polymorphs and amorphous silica (Aulinas et al., 2015). Some studies interpreted the silica to have played an important role in overall varnish formation (Perry et al., 2006). Varnishes that are predominantly silica (i.e., resemble more of a silica glaze) have been termed "Si-rich rock varnish" (Aulinas et al., 2015).

The amount of moisture present in the atmosphere, and/or within the microscopic aqueous realm on the lithologic surface, greatly affects the potential development of desert varnish (Hunt, 1954; Thiagarajan and Lee, 2004). Wet zones along river banks are also known to support significant varnish development (Krinsley et al., 2012; references therein). Despite the dependence on regional environmental conditions and ecology, the specifics on the chemical makeup of a given varnish strongly suggest that the varnish material itself does not appear to be derived from its lithologic substrate (Engel and Sharp, 1958; Potter and Rossman, 1977; 1979; Thiagarajan and Lee, 2004; Macholdt et al., 2015). Formation and development thus appears to be independent of the substrate lithology. The metal oxides are likely transported by water (Potter and Rossman, 1979), whereas the provenance of the clay minerals is more likely based on aeolian transport and deposition (Potter and Rossman, 1977; 1979; Perry and Adams, 1978). Some workers support the idea that for long-term stability

and ongoing accretion, the clays and metal oxides must both be present (Potter and Rossman, 1977), while others suggest that the manganese-rich component predates clay deposition (Krinsely et al., 2012).

A microstratigraphy is commonly present in varnish (Perry and Adams, 1978; Reneau et al., 1992; Liu and Broecker, 2000; Liu, 2003; Liu and Broecker, 2013), indicating that formation is primarily depositional or accretionary (however, for a case where microlaminations are absent, see Aulinas et al., 2015). The layered structure can also contain botryoidal or stromatolitic structures (Perry and Adams, 1978), organic compounds (Perry et al., 2006), and/or microbial-sized forms (Krinsely et al., 2012); all of those features suggest that microbiologic activity may be integral to the formation process.

The continuous accretion of varnish into a microstratigraphic structure suggests that increasing thickness might have a systematic dependence on time, but, as in the case of stratigraphy, a number of studies indicate that this is not the case. Difficulties include: 1) some substantial varnish coatings have apparently grown within a few decades to a century (Engel and Sharp, 1958; Krinsley et al., 2012); 2) younger varnishes often appear to have faster accretion rates (Liu and Broecker, 2000; Spilde et al., 2013); 3) those faster accretion rates do not appear to be sustainable for a long time, since varnish thickness >200 μm is rarely observed (Spilde et al., 2013); 4) varnished surfaces at higher elevations might not have survived the effects of glacial erosion during the Late Pleistocene, which means that a maximum age has been imposed for many locations (Quade, 2001); and 5) it might be nearly impossible to account for all of the variation in regional and local environmental factors that control the balance of accretion, erosion, and preservation at any given location.

Microtopography of the lithologic substrate has significant control over varnish accretion rates (Reneau et al., 1992) and resulting thickness (Liu and Broecker, 2000). Both accumulation rates and thickness increase in local topographic troughs and decrease on local peaks (Reneau et al., 1992), analogous to macro- and regional-scale accumulation of sediment in basins. The rapid early accretion model of Reneau et al. (1992), where differential varnish accumulation causes an overall smoothing of the lithologic micro-surface, could explain some instances where higher varnish accumulation rates are found on younger geomorphic surfaces (Liu and Broecker, 2000; Krinsley et al., 2012; Spilde et al., 2013).

THE RELATIONSHIP BETWEEN DESERT VARNISH AND DESERT PAVEMENT

Based on reconnaissance images (field photographs, and visible wavelength satellite imagery), the older geomorphic surfaces in our study area generally have a darker overall color index, which is likely due to a greater degree of desert varnish and desert pavement development. A relatively smooth and well compacted macroscopic desert/stone pavement surface is often associated with moderate to heavy varnish development on coarse gravels. The way that a desert pavement forms has implications for the validity of using varnish as a chronometer. A classical hypothesis regarding desert pavement formation invokes the idea that a geomorphic surface can experience overall deflation, where the coarser interlocking clasts in a pavement have progressively become exposed, agglomerated, and compacted at the surface of the Earth over a long period of time, all while finer sediment is winnowed via

aeolian processes. In this case, a lithologic surface coating of varnish would not be a valid chronometer, since not all of the clasts were exposed at the surface when it first formed. An alternative hypothesis is the "born at the surface" model (Wells et al., 1985; 1995; McFadden et al., 1987), where the coarse, interlocking surficial clasts have been exposed continuously since formation of the geomorphic surface commenced. The "born at the surface" model explains data for pavements with exposure ages similar to those of proximal bedrock source material (Wells et al., 1995). Under this model, any lithologic surface coatings have potentially accumulated continuously over the entire age span of the surface. In that case, the overall varnish development could be a chronometer that records the entire life span of the surface.

Regardless of the pavement formation model, other processes must also be considered. Bioturbation by plants and animals can disrupt the protracted development of substantial desert varnish coatings and associated pavement surfaces. It is also possible that the varnish can undergo diagenesis, including dissolution, and this might always be a state of disequilibrium (Garvie et al., 2008), analogous to erosive forces acting during aggradation in sedimentary basins. While these complications might hinder attempts to see varnish accretion as a chronometer on the microscopic scale, the remote sensing data and methods that we employ here take into account a much broader sample of the overall geomorphic surface. Desert varnish accretion, coupled with desert pavement development, might result in specific characteristics of the geomorphic surface that can be observed and quantified via the synoptic view that airborne hyperspectral imagery provides.

SPECTROSCOPY OF CLAYS AND OTHER RELEVANT MINERALS

The ability to identify submicroscopic clay minerals via spectroscopy is intrinsic to this research. Electromagnetic energy from the Sun interacts with the crystal structure of minerals to produce diagnostic spectral features seen in infrared reflectance and emission spectroscopy. Furthermore, clays are often present in significant abundance on planetary surfaces, yielding strong signals that can be rigorously quantified and interpreted (e.g., Michalski et al., 2006; Ehlmann et al., 2009).

The clay minerals montmorillonite and illite were identified in significant abundance within desert varnish from southern California, using laboratory infrared absorbance spectra (Potter and Rossman, 1977). Montmorillonite is part of the di-octahedral smectite group, which has the general chemical formula: $(½Ca,Na)_{0.7}(Al,Mg,Fe)_4[(Si,Al)_8O_{20}](OH)_4 \cdot nH_2O$ (Deer et al., 1992). The montmorillonite in desert varnish from southern California was c. 50% of a mixed-layer clay component that also included illite (Potter and Rossman, 1979a). Illite has spectral features nearly identical to those of montmorillonite in thermal infrared emissivity spectra (Figure 1a in Michalski et al., 2006), so in this research we are focusing primarily on montmorillonite's spectral features to guide our interpretations of clay mineral content in desert varnish.

Clays and all other silicate minerals display the most prominent spectral feature, the Reststrahlen band, which appears in the thermal wavelength regime (λ = 8-15 μm). The Reststrahlen band occurs as a minimum in emissivity spectra, and is due to Si-O asymmetric stretching vibrations in the crystal lattice (Thomson and Salisbury, 1993). The exact spectral position of the Reststrahlen band is dependent on the degree of silica tetrahedra polymerization in a crystal lattice (Launer, 1952). For the nesosilicate minerals (and the rocks

they form) that have a lower degree of Si-O polymerization (e.g., olivine, garnet, dunite, basalt), the Reststrahlen band generally occurs at longer wavelengths. In contrast, silicates (and rocks) with higher polymerization (e.g., quartz, feldspars, granite, rhyolite) have a Reststrahlen band at shorter wavelengths (see Figure 2 in Hook et al., 2005). The phyllosilicate clay minerals in the smectite group (and kaolinite) have intermediate silica polymerization. These clays have a major spectral feature at a position somewhere in the range 9.1-9.6 μm (Keller and Pickett, 1950; Hunt et al., 1950; Launer, 1952; Farmer, 1974; Bishop et al., 2002a; Frost et al., 2002; Michalski et a., 2006; Bishop et al., 2008). The 9.1-9.6 μm feature is due to Si-O stretching (Bishop et al., 2002a; Frost et al., 2002; Michalski et a., 2006), and therefore represents the Reststrahlen band position for these minerals.

Highly polymerized tectosilicate spectral features are likely to be observed in remote sensing spectra, and they may overlap with features from clay minerals. In general, spectral data must be evaluated on the basis of considering mixtures of minerals that might possibly have spectral features at similar, overlapping, or identical wavelengths. Some of the common tectosilicate minerals were significantly represented in the desert varnish substrate lithology (detrital clasts) from our study area. Figure 2 illustrates that both quartz and montmorillonite clay have a spectral feature near 8.8 μm (also see Figure 5 in Michalski et al., 2006; Bishop et al., 2008). For quartz, this is the primary feature, but for clays, this is a minor, secondary feature. Quartz also has a diagnostic spectral feature, a very distinct doublet (or two Reststrahlen bands, as described by Thomson and Salisbury, 1993) with emissivity minima at 8.4-8.6 μm and 8.8-9.0 μm (Figure 2 in this study; Figure 1 in Conel, 1969; Figure 4 in Christensen et al., 2000; Figure 5 in Michalski et al., 2006). Potassium feldspar has prominent

spectral features at c. 8.7, 9.2, 9.5, and 9.9 μm (Figure 2 in this study; Figure 1b in Thomson and Salisbury, 1993; Figure 5 in Michalski et al., 2006).

The minor spectral features at longer wavelengths are less important to this research. Smectite clays have minor features from 10-13 μm (Keller and Pickett, 1950; Hunt et al., 1950; Launer, 1952), due to aluminum/magnesium/iron hydroxide bending vibrations (Farmer, 1974; Sposito et al., 1983; Bishop et al., 1994; Bishop et al., 2002a; 2002b; Frost et al., 2002; Michalski et al., 2006; Bishop et al., 2008). Other clays (kaolinite and illite) have minor spectral features from 12-13 μm (Keller and Pickett, 1950), as does quartz (Figure 2 in this study; Keller and Pickett, 1949; Hunt et al., 1950; Launer, 1952; Lippincott et al., 1958; Lyon, 1965; Michalski et al., 2006), and feldspars (Thomson and Salisbury, 1993). Tectosilicate spectral features from 12-13.5 μm are due to a symmetric stretching mode in the Si-O molecules, and various Si-O-Al combinations for feldspars (Thomson and Salisbury, 1993). We did not consider minor features from clays at longer wavelengths, partly because some of the other studies were based on transmission spectra, which can sometimes be more revealing than emission spectra (e.g., Michalski et al., 2006).

Furthermore, even though the manganese and iron oxides (birnessite and hematite, respectively) are significant components in desert varnish, we also gave these metal oxides little consideration, because in the wavelengths that our data covered (λ = 7.6-13.2 μm) their infrared absorbance spectra are relatively flat (Figures 3 and 6 in Potter and Rossman, 1979a; Figure 14 in Potter and Rossman, 1979b), and lack any fundamentally diagnostic spectral features.

SPECTRAL MIXTURE MODELS

The combination and mixing of spectral features shows how progressively heavier coats of desert varnish will alter the spectrum of a substrate lithology, including changes in band depth and positions of minima. When a lithologic mixture includes a greater fraction of a certain mineral, the wavelength positions where distinct features occur for that mineral will usually display a greater depth in spectra. When a quartz-rich substrate has a coating of varnish, the minimum in emissivity spectra shifts to a longer wavelength (Gillespie et al., 1984), due to the clay mineral's lower degree of silica polymerization and resultant influence on the Reststrahlen band position. In laboratory and field spectra, spectral features for quartz are progressively modified and obscured by an increasing varnish coating. If the varnish is present in sufficient quantity, its own spectral features, which bear a striking resemblance to those of clay minerals, will completely mask those of the substrate (Figure 13 in Kahle, 1987; Figure 9 in Bartholomew et al., 1989; Rivard et al., 1993).

The results mentioned above from previous research on spectroscopy of desert varnish coatings can be recreated by modeling the spectral effect of mixing clay with tectosilicate minerals. We created linear spectral mixture models using laboratory thermal emission spectra (Christensen et al., 2000), to exemplify the results from previous research (Figure 2). These models also helped guide our own hypotheses on how desert varnish might alter remote sensing spectra from our study area. Linear mixture models of laboratory spectra are accurate in the wavelength range that includes Reststrahlen band positions if surface scattering is prevalent, a condition that is met if the particle sizes of the single mineral components are much larger than the wavelengths in measured spectra (Thomson and Salisbury, 1993). To represent a typical varnish substrate lithology (detrital clasts) from our

study area, we mixed spectra from three common tectosilicates in roughly equal relative abundances: 33% quartz (125-2000 μm), 34% andesine plagioclase feldspar (710-1000 μm), and 33% microcline potassium feldspar (710-1000 μm). Spectral features from each of the three tectosilicates, the deepest of which are in the range 8.5-9.2 μm, are represented in this synthetic "granite" spectrum (Figure 2A). To represent the clay minerals found in desert varnish, we used a spectrum from montmorillonite, which was taken from a pressed pellet (Cooper and Mustard, 1999, noted that clay crystal aggregates behave spectrally like larger particles). As more clay is added to the "granite" substrate, the spectral features of the clay alter and ultimately conceal the granite's spectral features. The clay's major spectral feature at 9.36 um begins to dominate the spectrum at adding as little as 33% to the mixture, and deepens substantially as more is added, representing a heavy coating of desert varnish (Figure 2B).

Based on the results from previous research and from our own spectral mixture modeling, we expect to see in our data a spectral feature in the range 9.1-9.6 μm, due to clay minerals in desert varnish. Different minerals and materials can have spectral features at similar spectral positions (Figure 13 in Launer, 1952), creating some ambiguity when attempting to interpret remote sensing observations. We need to take into account the chemical aspects of other minerals that are known to be present, as well as variation in the physical aspects of lithology (e.g., clast size and topographic surface roughness), and other natural features (e.g., vegetation), that can also contribute to the spectral emission signal. Even if the signal is present and real, we consider various ways for why it changes on the geomorphic surfaces of varying ages and characteristics.

METHODS

Some of the text in the following subsections is copied verbatim from Chapter 2 of this thesis (on remote sensing of the Lavic Lake fault). The wording is identical, or almost identical, because the sensor calibration procedure and the image data processing sequence were the same for the two study areas.

Thermal Hyperspectral Airborne Imagery Acquisition

We collected thermal hyperspectral airborne imagery on 24 September 2015 (at c. 10:45 am to 10:55 am, Pacific daylight savings time) using Mako, a "whiskbroom"-type sensor developed and operated by The Aerospace Corporation. The Mako sensor measures surface radiance in the thermal regime at 128 bands (Hall et al., 2011). For the data used in this study, the wavelength range was 7.6-13.2 μm, with one-meter ground sampling distance (or image pixel resolution), from a flight at 6000 feet above ground level (c. 6800 feet altitude). For the terminology used herein regarding the hyperspectral image data from the Mako whiskbroom sensor, each single "whisk" (or linear track) is a single data cube, so the words "whisk" and "data cube" are used interchangeably. When multiple data cubes (or whisks) are concatenated into a larger image, the set of combined data cubes can be called a "super cube." The full hyperspectral imagery data set presented here consisted of two super cubes (or image swaths) with parallel, adjacent flight lines that were flown in opposing azimuthal directions. The two neighboring super cubes were combined for greater spatial coverage in a single scene. Although a set of combined super cubes can still be called a super

cube, when the two super cubes used here are combined into a single image, we call this the "complete image scene."

The complete image scene covered portions of both the Mission Creek and Banning strands of the southern San Andreas fault. The complete image scene covers a rectangular area, c. 6.1 km along the flight path (roughly parallel to and centered on the Mission Creek strand), and c. 4.7 km wide. The complete image scene consists of 114 whisks total, with 57 whisks in each of the two parallel, adjacent flight swaths. The spatial extent of a single whisk relative to the complete image scene can be seen in Figure 3: in the saw tooth pattern along the sides of the image swath (sides that are parallel to the fault traces), the tip of each tooth is the boundary between two whisks. Two adjacent whisks generally have a small amount of overlap, and for this data, the two parallel, adjacent swaths also have a small amount of overlap.

Mako Sensor Calibration

The Mako airborne hyperspectral infrared sensor underwent radiometric and wavelength calibration. For radiometric calibration, two onboard blackbody sources were observed immediately before and after the scene was acquired. These were stabilized at different temperatures that spanned the expected radiance values of the scene. A linear relation between the known blackbody radiance input and the digital counts output was assumed so that the sensor response could be modeled with multiplicative gain and additive offset terms. The gain and offset terms for the pre- and post-collection calibrations were then time-interpolated to match the actual collection time of the data.

The wavelength calibration was done by observing blackbody sources covered by National Institute of Standards and Technology (NIST) traceable transparent polymer films (with calibrated absorption features), and performing a least-squares fit across the full extent of the focal plane array. For more detailed descriptions of the calibration processes, see Hall et al. (2011) and Buckland et al. (2017).

Hyperspectral Airborne Imagery Data Processing

All of the steps in the following image processing sequence, unless otherwise specified, were completed using the Environment for Visualizing Images Software, version 4.8 (ENVI, Exelis Visual Information Solutions, Boulder, Colorado). We began with data cubes of airborne thermal hyperspectral imagery that had undergone radiometric and wavelength calibration, bad pixel replacement, and spectral smile removal. We first concatenated the 114 data cubes (whisks) that made up the complete image scene into a single "supercube." After that, we could carry out the subsequent processing steps in bulk.

For the hyperspectral image data presented here, we had to remove the first ten bands that covered wavelengths from 7.56-7.96 μm because they were dominated by noise. We proceeded to use bands 11-128 (118 total), with wavelengths from 8.01-13.15 μm. We performed an in-scene atmospheric compensation (ISAC algorithm from Young et al., 2002), setting the regression pixels to maximum hit, the fitting technique to normalized regression, and using for the noise equivalent spectral radiance (NESR), the median value of the super cube. Then, we used a minimum noise fraction (MNF) transformation (Green et al., 1988; note that it is called a "maximum noise fraction" in that paper; also, see Lee et al., 1990) to

identify noise or data artifacts in the imagery. A gradation perpendicular to the flight direction (across track) was present near the edges of each individual data cube, so we discarded this spurious spectral signal in an MNF inverse transformation.

Next, we converted the data from at-sensor radiance to emissivity with the emissivity normalization method (Kealy and Hook, 1993). With the emissivity image, we could extract spectra of the geomorphic surfaces for analyses, since we were characterizing spectra in relation to known surface ages (Table 1).

Before extracting the emissivity spectra, we needed to mask younger, ephemerally active channels that cut into the older surfaces. To achieve this, we used a digital elevation model (DEM) with 1.5 m spatial resolution (created by Ryan Gold) to first calculate from the DEM a slope map, and then use the slope map to mask areas with high slopes (which represent relatively steep walls of the younger channels). The parameters for creating the slope mask were topographic kernel size of 5 to create the slope map (with slope in degrees), and we then masked pixels with a slope value greater than 3 degrees. The slope mask was then intersected with the digitized polygons that represented the mapped geomorphic surfaces with known ages (Figure 4).

To produce a single representative spectrum for each distinct geomorphic surface, we averaged (arithmetic mean) a random sampling for 1% of the total number of pixels within each surface's digitized boundaries. We performed the 1% random spectral sampling a total of five times to capture statistical variability in the spectral data. We also removed the continuum from all of the representative emissivity spectra, so that they could be compared against one another with a normsalized baseline (i.e., with respect to the band depth/strength at wavelength positions for spectral features of interest, see Clark and Roush, 1984). From

herein, we will refer to any hyperspectral airborne imagery emissivity spectra as “airborne remote sensing spectra.” The airborne remote sensing spectra were plotted after being smoothed with a moving average over a three band interval (Figure 5).

We hypothesized that the older surfaces contain a greater fraction of clay minerals (in varnish), and will therefore display a greater band depth somewhere in the wavelength range where the Reststrahlen bands are predicted to occur for clay minerals, which is 9.1-9.6 μm (Bishop et al., 2002a; Frost et al., 2002; Michalski et a., 2006). We chose to focus on the wavelength position at 9.16 μm, because in our airborne remote sensing data, the greatest number of spectra had an emissivity minimum at 9.16 μm. Figure 6 is a plot of airborne spectra band depth at 9.16 μm versus surface age. Whether or not this spectral feature at 9.16 μm corresponds to the fraction of clay minerals present or not will be discussed later, but we analyzed the order of increasing/decreasing relative band depth based on this wavelength position.

If we assume the above hypothesis, then older surfaces will have increased band depth at 9.16 μm. In the following Results section, we will use the phrases “in position” and “out of position” to describe whether the band depth at 9.16 μm for each spectrum is in sequence with the others with respect to the sequence of known surface ages (e.g., a spectrum for the oldest geomorphic surface would be “in position” if it displayed the greatest band depth at 9.16 μm, a spectrum for the second oldest surface would be “in position” if it displayed the second greatest band depth at 9.16 μm, etc.). Interpretations of those results will be discussed in a later section.

Ground Truth Field Work

We also needed field measurements to compare with our airborne remote sensing spectra interpretations. We did field work in the study area from March 2017 through May 2017 to collect ground truth information. We arbitrarily chose from two to four sites located on each geomorphic surface with known age to collect field data. At each site, a square plastic frame, one meter on edge, was placed on the ground to collect data within a confined area that represented the hyperspectral airborne imagery pixel size. First, we took two types of field photographs at each sample site: 1) an overhead (bird's eye) view of the sample square meter (or sample area field photograph); and 2) an overview perspective of the geomorphic surface (or site overview field photograph). To describe the lithologic characteristics of each sample square meter, we collected petrologic data, including primary mineralogy and textures of detrital surface clasts that make up the alluvial fan deposits. We used a combination of field observations and the sample square meter photographs to estimate the dominant (>50% relative abundance) clast size ranges, for sizes down to 1 mm mean diameter (when possible), using percentage diagrams for estimating composition by volume (see Appendix 3 in Compton, 1985). We also collected up to ten lithologic sample chips from most of the field sites.

To assess the degree of desert varnish, and desert pavement development, we established a numerical scale to give each a score, from 1-4, for each sample site (the scores are not single values, but ranges). In the numerical scale, a higher number is a greater degree of development, as follows: 1 = absent/rare, 2 = light/weak, 3 = moderate, and 4 = heavy/strong. Varnish scoring was based mainly on darkening color, and pavement scoring was based mainly on smoothness and compaction (compaction assessed by placing the ball

of a booted foot on the surface and twisting to see how easily clasts broke free from their interlocking arrangement). We acknowledge that these numerical scores are subjective, but our experience in the field allowed us to develop a sense of varnish and pavement development in a relative sense to other sites visited and analyzed.

To quantify the variable presence of vegetation between the surfaces, we estimated the average spacing between desert scrub bushes or other plants, as a proxy for vegetation abundance/density. We also collected several vegetation leaves and branches from a few of the sites.

Rock Area Fraction: Analysis Using Ground-based Field Photographs

We also assessed whether clast size variation existed between surfaces with another independent method. Larger clasts are less susceptible to induced motion, and therefore are more stable and conducive to extended periods of varnish development. Along these lines, we were interested in deriving a quantitative measurement for the fraction of clasts that were above some size threshold. We defined this quantity as the "rock area fraction." Since the terms "rock, sediment, and grains" are undefined with respect to size, we established a definition to quantify our data. To decide which clasts qualify as "rocks," we chose a threshold size of 2.5 cm mean diameter. The edge of the plastic frame that was used to define each sampling area had a thickness of 2.5 cm, so this served as a consistent reference scale in all of the field photographs. With a value defined for size cutoff, we could determine the areal percentage of each sample square meter that was occupied by the larger clasts that were more likely to have a greater degree of varnish development. The remaining lithologic

detrital material, with sizes below 2.5 cm, represented clasts that were generally not large enough (i.e., not kinematically stable) for protracted varnish development.

To complete this analysis, we used the ground-based field photographs of the sample square meter sites. On a printout of each photograph, clasts that were within the sample square meter, and above the size threshold of 2.5 cm, were outlined by hand with vellum tracing paper on a light table (these larger outlined clasts would be included in the "rock" fraction). The tracing paper sheets were scanned to digital image files, and the digital image files were then processed with ImageJ software (Schneider et al., 2012). With ImageJ, we established the scale size in each image, automatically filled all of the clast outlines that were traced, then calculated the fraction of the sample square meter area occupied by the filled clast outlines (i.e., the integrated area occupied by all of the clasts with mean diameter greater than c. 2.5 cm). The remaining fraction of unfilled area was then smaller clast sizes that would not be large and stable enough for protracted varnish development. This analysis allowed us to quantify the fractional area (in percent) of a single airborne remote sensing pixel that was available for varnish development. Note that the total rock area fractions that we calculated are minimum values, because our analysis was inherently subjective, and it is possible that we did not capture every single clast that exceeded the size threshold.

Ground-based Spectra

To observe spectral variation among the geomorphic surfaces on a smaller scale, we used a hand held field spectrometer to directly measure lithologic spectra from the exposed, top (and sometimes varnished) sides of single clast surfaces. In addition to measuring the

single clast lithologic spectra, we also measured spectra from samples of finer, unconsolidated lithologic detrital material (from herein, we will refer to these as "sand" spectra, where "sand" does not imply a technical definition of clast size), and vegetation samples, since these materials were included in noteworthy abundance in our study area. The apparatus we used was an Agilent 4100 ExoScan™ portable Fourier Transform Infrared spectrometer (spot size: 3-5 mm), which measures diffuse reflectance by active source. From herein, we will refer to any spectral measurements that we made with this apparatus as "ground-based spectra." Some of the ground-based spectra were collected in situ, but due to difficulties in the field (e.g., inability to transport all of the equipment to distal field sites, and/or equipment failure), most were collected later, on samples that we brought back. We collected up to ten ground-based spectra from a variety of materials at each site (Table 2).

To compare the general shape and wavelength positions of prominent spectral features between airborne remote sensing and ground-based spectra, the ground-based reflectance spectra were converted to emissivity using Kirchhoff's law. In a general form, Kirchhoff's law states that reflectance and emissivity sum to unity (Robitaille, 2009). The ground-based spectra were diffuse reflectance measurements, which is similar to a conical-hemispherical measurement (see Case 6 from Table 2 in Schaepman-Strub et al., 2006). If seeking quantitative spectral measurements, directional-hemispherical reflectance spectra are usually considered acceptable (assuming isothermal conditions) for converting to emissivity via Kirchhoff's law (Salisbury and Walter, 1989; Salisbury et al., 1994). However, the simple conversion offered by Kirchhoff's law is not generally considered appropriate for converting some other types of reflectance spectra to emissivity (Christensen and Harrison, 1993). Still, other types of spectral reflectance measurements converted to emissivity via

Kirchhoff's law do generally maintain the same general spectral shape as direct spectral emissivity measurements (Figure 3b in Christensen and Harrison, 1993; Figure 4 in Christensen et al., 2000). We did not assume that the ground-based spectra were quantitative to begin with, and since we were mainly concerned with the qualitative aspect of this analysis, we accepted the error involved in converting ground-based diffuse reflectance spectra to emissivity via Kirchhoff's law.

Finally, all of the ground-based spectra were plotted for each site, along with the site average (arithmetic mean), to show how spectra from a mixture of materials within the hyperspectral airborne imagery's pixel size might manifest as a single remote sensing spectrum. From herein, when we refer to any ground-based spectra, we are referring to the single representative site average, unless otherwise specified.

RESULTS

Airborne Remote Sensing Spectra

The results here will be presented according to their respective geomorphic surface names (Table 1). We separated the airborne remote sensing spectra into two groups: from surfaces that are located upstream, and downstream, of the southern San Andreas fault, Mission Creek strand. The spectra were then further subdivided by surface age. The R^2 correlation coefficient between all airborne spectra band depth at 9.16 μm and surface age is 0.59 (Table 3).

For the upstream sets of spectra (Figure 5), the oldest surface, Qt0 (>95 ka), is in position (greatest band depth at 9.16 μm) for four of the five subsets. The two youngest surfaces, Qt3 (13 ka) and Qt4 (<11 ka), are together in position for all five subsets, with the caveat that Qt3, not Qt4, has the least depth for four of the five subsets. In all five of the sampling sets, Qt2 (74 ka) is always out of position, with a greater 9.16 μm band depth than Qt1 (87 ka).

For the downstream sets of spectra (Figure 5), the oldest surface, C0 (>95 ka), is in position (greatest band depth at 9.16 μm) for three of the five subsets, and we note that for the remaining two sets, C2f (26 ka) has the greatest band depth. The youngest surface in the downstream group, C3 (13 ka), is in position (least band depth at 9.16 μm) for all five of the subsets. The downstream group of surfaces are in complete ideal sequence (according to our increasing-band-depth-with-age hypothesis) for two of the five subsets.

Ground Truth Field Work

Primary Mineralogy and Lithologic Textures of Detrital Surface Clasts

Surficial clasts at all of the sample sites had generally similar primary mineralogy and lithologic textures. Quartz/alkali feldspar/plagioclase (QAP) clast compositions of phaneritic (individual crystals generally 1-5 mm) igneous rocks included granite, granodiorite, quartz monzodiorite, and quartz monzonite. Some other types of clasts and/or textures included conglomerate/breccia, gneiss, schist (rich in amphibole and/or biotite mica), pegmatite, porphyry with feldspar megacrysts, and fine-grained mafic (pyroxene-rich)

rocks. At a site on the oldest downstream surface, C0p2 (>95 ka), we noted that the lithologic substrate for some of the most heavily varnished clasts was a mafic schist.

Clast Size Measurements

The results for the dominant (>50% relative abundance, down to 1 mm) clast size ranges are shown in Figure 7. We do not observe any trends, such as a general monotonic increase or decrease, between the dominant clast size ranges and surface age. The R^2 correlation coefficient between mean of dominant (>50%) clast size ranges and surface age is 0.10 (Table 3). The largest range was recorded at a site on the youngest downstream surface, C3p2 (13 ka). In the field, we also observed fewer larger clasts (>30 cm long axis) at a site on one of the older upstream surfaces (Qt1, 87 ka, see site overview field photograph for Qt1p2, Figure S8 in the Supplemental Items).

Desert Varnish and Desert Pavement Development Scores

The scores for degree of desert varnish and desert pavement development are plotted in Figures 8 and 9, respectively. For both sets of scores, we observe a general monotonically increasing trend between score and surface age, with the lowest scores for the youngest surfaces, and the highest for the oldest. The Spearman's rank correlation coefficients (used for categorical variables, see Simspon, 2015) between varnish and pavement scores, and surface age are 0.90 and 0.90, respectively (Table 3). For the downstream surfaces, the general monotonic increase in desert varnish and desert pavement scores is interrupted by a

decline in score for the site C2fp4 on the C2f (26 ka) surface. From our field inspections, we observed that varnish was absent/rare even on larger, more stable boulders, on the younger surfaces on either side of the fault.

Vegetation Abundance

The estimates for average vegetation spacing are shown in Figure 10. There is a generally monotonic increasing trend between average vegetation spacing and surface age. The R^2 correlation coefficient between vegetation spacing and surface age is 0.34 (Table 3).

Additional Field Observations

On the younger upstream surfaces (Qt4, <11 ka, and Qt3, 13 ka), we also observed meter scale bar and swale (hummocky) topography, which was composed of larger clasts (10-20 cm long axes) concentrated on channel bars (see field photographs for Qt4p2 (which was a site directly located on one of the channel bars with larger clasts), Qt3p1, and Qt3p2, Figures S2, S3, and S4 in the Supplemental Items).

At the upstream site Qt1p2 (87 ka), we observed a conspicuous higher relative abundance of red-orange micro- or cryptocrystalline iron-oxide minerals (likely included hematite and goethite; see field photographs for Qt1p2, Figure S8 in the Supplemental Items). It is possible that many of the clasts at the Qt1p2 site were flipped over, because an orange coat on the buried bottom of varnished clasts is often present due to iron oxide formation at soil or sub-soil level (Figures 2 and 3 in Engel and Sharp, 1958; Potter and

Rossman, 1977; 1979a). On the oldest upstream surface Qt0 (>95 ka), we observed the best examples of extremely well-developed, smooth, resistant, heavily varnished desert pavement (see field photographs for Qt0p2, Figure S10 in the Supplemental Items).

At the downstream site C2fp1 (26 ka), we noted a distinct, light pink oxidation on clasts (see sample square meter field photograph for C2fp1, Figure S15 in the Supplemental Items). At the site C0p1 (>95 ka) on the oldest downstream surface, we noted that the dimensions for broader areas with the greatest degree of varnish and pavement development, had their longest dimension parallel to the direction of channel drainage (see site overview field photograph for C0p1, which was taken facing southwest, parallel to the channel drainage direction, Figure S25 in the Supplemental Items). In a view perpendicular to the drainage direction, more vegetated areas were observed in channel rills. The implication of these observations is that channel bars of larger clasts (e.g., gravel/cobbles/boulders) could have ended up being the most heavily varnished and strongly developed pavement surfaces.

Rock Area Fraction

The results for the rock area fraction (minimum, %), calculated for each of the 1-m^2 field sampling sites using image processing software, are shown in Figure 11. There is no general monotonic increase or decrease between the rock area fraction and surface age, and the R^2 correlation coefficient is 0.00 (Table 3). This implies that, for our airborne remote sensing data, the fraction of area for a single pixel that was at least fundamentally available for varnish development did not increase for older surfaces.

However, we noted that for the upstream surfaces (upper panel in Figure 11), the youngest and oldest surfaces had sites with the highest and lowest rock area fractions, respectively: Qt4p2 (<11 ka, a site directly located on one of the channel bars with larger clasts, Figure S2), and Qt0p2 (>95 ka, Figure S10). For the downstream surfaces (lower panel in Figure 11), the sites C2p3 (74 ka, Figure S21) and C2fp4 (26 ka, Figure S18) have the highest and lowest rock area fractions, respectively. Additionally, for the downstream surfaces, the two sites (for which rock area fraction was measured) on the youngest surface (C3, 13 ka, Figures S11 and S12), both have rock area fractions that are greater than any of those from the three sites on the oldest surface (C0, >95 ka, Figures S25-S27). Furthermore, the upstream and downstream surfaces that have the greatest difference for rock area fraction between sites are Qt4 (<11 ka, Figures S1 and S2) and C2 (74 ka, Figures S19-S22), respectively. The upstream and downstream surfaces that have the least difference for rock area fraction between sites are Qt3 (13 ka, Figures S3 and S4) and C3 (13 ka, Figures S11 and S12), respectively. See field photographs for all of the sites referenced above in the Supplemental Items.

Ground-based Spectra

Ground-based spectra for all 27 field sites, along with accompanying sample square meter, and site overview field photographs, are in the Supplemental Items, and a summary of which materials were measured at each site is in Table 2. Figures 12 and 13 are two examples of the ground-based spectra for the sites Qt4p1 (<11 ka) and C0p1 (>95 ka), respectively. Some additional ground-based spectra that are relevant to the discussion of clast

size effects are from the following sites (see Table 2, and the Supplemental Items): Qt4p1 (<11 ka; Figure 12), spectra 1-5; C3p1 (13 ka, Figure S11), spectra 1,8,9; C3sand (13 ka, Figure S13), spectra 1-10; and C2fp4 (26 ka, Figure S18), spectra 4-9. Ground-based spectra of relevance to the consideration of vegetation effects include: Qt4p1 (<11 ka; Figure 12) spectra 6-10; Qt2p2 (74 ka, Figure S6), spectrum 1; and C3veg (13 ka, Figure S14), spectra 1-4. Note that both of these material variation considerations were covered at the upstream site Qt4p1 (<11 ka, Figure 12).

For the ground-based averaged spectra, a first order observation is that measurements from the youngest surfaces (see sites from Qt4 (<11ka) and C3 (13 ka), Figures S1, S2, and S11-S14 in the Supplemental Items) can be relatively flat in the range 9-10 μm, or they can contain a prominent, deeper feature at 9.30 μm. Compare this to ground-based spectra for the oldest surfaces (see site C0p1 (>95 ka) in Figure 13, sites from Qt0 and C0 (both >95 ka), Figures S9, S10, and S25-S27 in the Supplemental Items), which all contain a prominent, deeper feature at 9.30 μm. As stated previously, the ground-based spectral measurements are not quantitative, so we did not expect to see any correlation with surface age for the band depth of any specific features. For completeness, though, the R^2 correlation coefficient between ground-based spectra band depth at 9.30 μm and surface age is 0.04 (Table 3).

The feature at 9.30 μm in ground-based spectra is at odds with the 9.16 μm feature in airborne spectra. Spectra from the oldest surfaces are generally the most representative for maximum band depth at either of the respective wavelength positions, so we plotted a few of the oldest typical airborne and ground-based spectra together on the same axes to illustrate the systematic difference in shape and position of minimum (Figure 14).

DISCUSSION

In our airborne remote sensing spectra, we observed a general increase in band depth (also known as band strength or spectral contrast) of the 9.16 μm feature with age. As reported above in the Results section, some of the remote sensing spectra for geomorphic surfaces display a band depth at 9.16 μm that is in position with respect to the relative band depth for older/younger surfaces. For example, the upstream oldest surface Qt0 (>95 ka) has the greatest band depth at 9.16 μm for four of the five subsets, and the downstream oldest surface C0 (>95 ka) has the greatest band depth for three of the five subsets (Figure 5). The two youngest upstream surfaces, Qt3 (13 ka) and Qt4 (<11 ka), together have the least band depths for all five subsets, and the youngest downstream surface C3 (13 ka) has the least band depth for all five subsets (Figure 5). Furthermore, the downstream surfaces are in complete ideal sequence (band depth at 9.16 μm strictly increases with age) for two of the five subsets (Figure 5). However, there are a number of remote sensing spectra for surfaces that are out of position. Along with airborne spectra band depth at 9.16 μm, the other parameters with correlation coefficients >0.30 include desert varnish and desert pavement scores, and vegetation spacing (Table 3 and Figure 15).

The Effect of Petrology

The likely bedrock sources for alluvial/fluvial deposition in the Indio Hills are in the Little San Bernardino Mountains located immediately to the north east, which generally consist of intrusive crystalline rocks (hornblende diorite-gabbro, and various granitoids), and

metamorphic rocks, various politic and mafic schists (Dibblee, 2008; Lancaster et al., 2012). We expected similarity of clast compositions between surfaces, because they are all alluvial/fluvial deposits (now sets of terraces) along the same source drainage through Pushawalla Canyon. There has only been about 2 km of displacement of the Pushawalla Canyon drainage in the past c. 100 kyr (Blisniuk and Sharp, 2014), so it is unlikely that the eroding bedrock source for the system has shifted to a drastically distant and different source during that time. Therefore, we rule out fundamental petrologic differences in clasts as a reason to explain the spectral variation between surfaces.

The Effect of Other Minerals

We examined the effect of other minerals by comparing the airborne remote sensing (Figure 5), ground-based averaged (Figures 12, 13, 14, Table 2, and Supplemental Items), and the library laboratory spectra (from Christensen et al., 2000; Figure 2 in this study). As discussed previously, the spectral emissivity spectral features that we expected to see were at the following wavelength ranges (in μm, with the attributable mineral(s) in parantheses): 8.2-8.6 (quartz+microcline+andesine), 8.6-9.0 (quartz+microcline+andesine), 9.0-9.4 (microcline); 9.2-9.4 (montmorillonite clay); two separate and distinct features from 9.4-10.0 (microcline+andesine), and two separate and distinct features from 12.4-13.0 (quartz).

Nearly all of the airborne remote sensing and ground-based averages have prominent spectral features at the following wavelengths (μm): 8.2-8.6, 8.6-9.0, two separate and distinct features from 9.4-10.0, and two separate and distinct features from 12.4-13.0 (Figures 5, 12, 13, 14, and Supplemental Items). We correlate these features to the following

corresponding features observed at wavelengths (μm) for specific minerals in the library laboratory spectra, and their synthetic "granite" mixture spectrum (Figure 2): 8.2-8.6 (quartz+microcline+andesine), 8.6-9.0 (quartz+microcline+andesine), two separate and distinct features from 9.4-10.0 (microcline+andesine), and 12.4-13.0 (quartz).

For the Reststrahlen band of clay minerals, the wavelength range of interest is 9.1-9.6 μm (Keller and Pickett, 1950; Hunt et al., 1950; Launer, 1952; Farmer, 1974; Bishop et al., 2002a; Frost et al., 2002; Michalski et a., 2006; Bishop et al., 2008). But we see a particular difference between airborne remote sensing and ground-based average measurements in the range 9.1-9.6 μm. In the majority of the airborne remote sensing spectra (mainly from older surfaces), a distinct spectral feature is present with a minimum at 9.16 μm, and the band depth of that feature generally increases with surface age (Figures 5, 6, 15, and Table 3).

In the majority of the ground-based averaged spectra (Figures 12, 13, 14, and Supplemental Items), a distinct spectral feature is present with a minimum at 9.30 μm. As expected, this 9.30 μm ground-based feature does not generally increase in absolute band depth with surface age in site-averaged spectra, because the ground-based spectrometer is not quantitative (as discussed previously), and furthermore, broad variations exist for the microscopic surface roughness of lithologic sample chips measured, as well as their temperatures at the time of measurement. Yet, it appears that some of the older surfaces might generally exhibit a greater band depth at 9.30, if measured relative to the band depth of the quartz feature from 8.2-8.6 μm.

The library laboratory spectrum for montmorillonite clay (Figure 2B) has its Reststrahlen band at 9.36 μm, and there is another laboratory spectrum from montmorillonite

(Figure 5 in Michalksi et al., 2006) with a Reststrahlen band at 9.33 μm. Considering these observations, the ground-based 9.30 μm feature correlates more closely than the airborne 9.16 μm airborne feature to the 9.36 μm library laboratory montmorillonite Reststrahlen band. The difference in the emissivity minimum at 9.16 μm for airborne spectra and 9.30 μm for ground-based spectra is real and unexplained (Figure 14), so we do not assert that this aspect is unimportant. However, the difference does not completely rule out that the 9.16 μm remote sensing feature could be from clay minerals, so we considered some reasons why the two data sets do not agree.

Our analysis is complicated by the following spectral features from other minerals that overlap with the clay features: the laboratory synthetic "granite" spectrum has a spectral feature centered at about 9.2 μm from microcline and quartz (Figure 2). The synthetic "granite" spectrum has a distinct feature at 8.8 μm that directly overlaps with a feature at the same position from the library laboratory montmorillonite clay spectrum (Figure 2B). Additionally, there is another quartz feature that has been observed at 9.2 μm (Launer et al., 1952). The 9.2 μm feature observed by Launer et al. (1952) was not discussed in detail in that study, so it is possible that they observed a shoulder of one the quartz features, from 9.0-9.4 μm (Figure 2A). It is also possible that smaller particles might shift the minimum of the quartz feature at 8.86, to 9.09 μm (e.g., see models in Figure 6D and 6E in Moersch and Christensen, 1995). The quartz feature from 8.6-9.0 μm (Figure 2A) is clearly present in the majority of our spectra, but it appears to be overprinted by the addition of another spectral feature that extends this limb over into higher wavelengths, up to about 9.30 μm. The addition of this extension into higher wavelengths is probably due to the combined addition of a clay feature from 9.1-9.6 μm, and the microcline feature at 9.2 μm.

If the increased 9.16 μm band depth in airborne remote sensing spectra is only a result of other lithologic factors, such as clast/particle size, surface roughness, degree of clast/particle size sorting, and rock area fraction, then it remains compelling that the spectral signal occurs at the Reststrahlen band for clay minerals. All of our spectra show that minerals with similar and/or overlapping spectral features are present in the overall lithologic mixtures. All in all, both the remote sensing and ground-based spectra represent a similar mixture of minerals, with quartz, feldspars, and clay(s) present, but the problem remains between the 9.16/9.30 μm features, and this will require further investigation. Only the band depth at 9.16 μm in airborne spectra varies systematically with surface age, and the majority of all of the spectra can be explained by similar mineral mixtures, where the mixture does not vary with age. While the increasing band depth (or spectral contrast) with age in airborne remote sensing spectra cannot be explained by varying mineral mixtures alone, the difference between the 9.16/9.30 μm features in airborne/ground-based data sets remains a problem that needs to be addressed.

Definitions of Clast and Particle Size

For the purposes of this discussion and here after, we need to define how we are using terms that refer to the size of lithologic material in loose surficial regolith. The best resolution of our ability in the field to analyze sediment size is limited to ~ ≥1 mm. We use the term "clast(s)" to refer to macroscopic sediment sizes that are ≥1 mm, and "particle(s)" to refer to microscopic sediment sizes that are <1 mm. Following the Wentworth scale for sediment size (e.g., Boggs, 2012), terms for macroscopic clasts ≥1 mm are very coarse sand,

granule(s), pebble(s), cobble(s), and boulder(s), whereas terms for microscopic particles <1 mm are coarse/medium/fine/very fine sand, coarse/medium/fine/very fine silt, and clay. Note that since much of this manuscript involves a detection of clay mineralogy, the reader can assume that when we refer to "clay(s)", we are referencing mineralogy and not particle size. We will avoid using the term "clay(s)" to refer to particle size, but it will be clearly indicated if necessary. Although the majority of the sediment sizes that we were able to analyze were macroscopic clasts ≥1 mm, we acknowledge that our hypothesis is based on a spectral contribution from clay minerals, which are likely present in abundance in smaller size fractions. Thus, there will also be some discussion regarding how microscopic particles <1 mm might also contribute to the remote sensing signals and trends that we observe.

The Effect of Clast and Particle Size

Infrared laboratory spectra show that as microscopic particle size increases, often so does spectral contrast/band depth (Lyon, 1965; Hunt and Vincent, 1968; Conel, 1969; Figure 1 in Salisbury and Walter, 1989; Salisbury and Wald, 1992; Bishop et al., 1994; Cooper and Mustard, 1999; but for examples where this is not always the case, see Hunt and Vincent, 1968; Salisbury et al., 1987). Horgan et al. (2009) acquired similar results in short-wavelength infrared spectra (1.0-2.5 μm), but they also included in their analysis sediment sizes >1 mm to the same effect. The decrease in spectral contrast with decreasing particle size can be partially attributed to volume scattering, where the size of smaller particles causes them to become optically thin and have lower overall opacity (Salisbury and Wald, 1992).

If the effect of spectral contrast and band depth increasing as particle size increases continues to scale up to even larger macroscopic clast sizes, then it is possible that the observed trend in our data is due to variation in dominant clast size on the different geomorphic surfaces. Based on the general pattern of increasing band depth with age in our remote sensing spectra, it follows that this might be due to increasing dominant clast size with age on the Quaternary geomorphic surfaces. Figure 7 shows estimates for dominant (>50%) clast size range for each of the sampling sites on the upstream and downstream sets of surfaces. The correlation coefficient between dominant clast size (mean value of each range) and age is very small, $R^2 = 0.10$ (Figure 15 and Table 3). The dominant clast size varies over the different surfaces, but it fluctuates unpredictably.

Clay minerals could be more abundant in the smaller clast size fraction, below our ability to resolve. Our clast size analysis is limited to fragments that are ≥1 mm, yet we are concerned with looking for evidence that the remote sensing signal is influenced primarily by clay mineralogy. Even though our field data for dominant size of macroscopic individual surficial clasts do not show an increase in size with age, microscopic clay particles can increase in size in a few different ways. Individual clay crystals could grow and increase in size with age as part of their initial formation mechanism via weathering and alteration of existing minerals. Alternatively, individual clay crystals can agglomerate and increase in aggregate size, which is, however, likely for clays that accrete on surfaces to form desert varnish. In addition to increasing band strength with increasing particle size, Cooper and Mustard (1999) also observed that, in coarser samples, the larger clay particles were not individual crystals, but rather amalgamations of smaller particles. As surficial coatings of desert varnish grow, constituent clay particles amalgamating into larger single masses might

result in spectra that are consistent with larger single particles, which is the obvious source of the increasing band depth at 9.16 μm in the airborne spectra.

Most of the ground-based spectra that we collected were from single lithologic sample chips, where clay minerals might be underrepresented. Therefore, spectra of specific relevance to the consideration of clast size effects include "sand" spectra, from finer, unconsolidated lithologic detrital material (see Table 2). In many of the ground-based spectra for single clasts, there is an apparent signal, and remarkable band depth for a feature at 9.30 μm (Figures 13, 14, and Supplemental Items). However, in "sand" spectra, there is also always an apparent signal, but not always remarkable band depth at 9.30 μm (Figures 12, and S11, S13, and S18 in the Supplemental Items).

We wanted to assess whether the smaller clast size fraction had higher clay mineral content. To check this, we observed the spectral behavior at a field site located within an ephemerally active channel (C3sand, 13 ka, Figure S13 in the Supplemental Items). The dominant (>50%) clast size range for C3sand is <1 mm (Figure 7, labeled "(sand sample)"). Interestingly though, for C3sand the ground-based spectra do not have a pronounced band depth at the expected position for clays, from 9.1-9.6 μm (see Figure 1 in Michalski et al., 2006). This supports ruling out a higher relative abundance of any clay minerals in the smaller clast size fractions. Although a noticeable emissivity trough is present in ground-based spectra for C3sand at about 9.30 μm, the feature does not have a significant band depth, especially relative the main quartz doublet located from 8-9 μm. For reference, see a remarkable band depth at about 9.30 μm, relative to the quartz doublet from 8-9 μm, in ground-based spectra for the increasingly older upstream (Qt2, Qt1, Qt0) and downstream (C2, C1, C0) surfaces. Any clay minerals at the site C3sand may have been removed by

fluvial and/or aeolian processes. Or, it is possible that the effects of particle size reduction (reduction in spectral contrast) compete with increasing clay abundance (increasing band depth of features attributable to clay minerals). In any case, a significant band depth is also absent in airborne remote sensing spectra for the C3 surface, which could be why C3 is "in position" for all five sets of spectra (see Results: Airborne Remote Sensing Spectra).

Our data do not show strong correlation between macroscopic clast size and surface age (Figure 15 and Table 3), so we exclude this as a factor that is primarily causing the increasing-band-depth-with-age trend in our remote sensing spectra. However, even though the macroscopic dominant clast size does not generally increase with age, it is likely that the individual microscopic clay crystals are agglomerating with age to manifest as larger particles. These larger particles or coatings could cause the increased band depth for the older surfaces if the agglomeration process occurs via protracted and continuous desert varnish growth. By proxy, this means that the trend in our data could be at least partially dependent on time.

The Effect of Macroscopic Topographic Surface Roughness and Degree of Clast Size Sorting

We did not expect individual clasts to increase in size with age, since rocks at the Earth's surface undergo physical and chemical weathering processes that almost always result in size reduction. Instead, we could hypothesize that clast size would decrease over time, but this by itself would likely decrease spectral contrast and band depth, opposite to the

general trend in airborne remote sensing spectra. Therefore, we must instead consider how clast size and surface morphology are related in a way that could increase band depth.

Figures 8, 9, 15, and Table 3 show that desert varnish and desert pavement scores generally increase with surface age. For surface morphology in general, the term 'desert pavement' is used to describe the primary topographic characteristic of surfaces in warm, arid regions when they become relatively smooth and compacted, which occurs over thousands to tens of thousands of years. McFadden et al. (1987) propose an evolutionary path in which bombardment of larger clasts by eolian dust assists in physical weathering, while the dust also accumulates with other smaller clasts in topographic depressions to form soil that eventually underlies a surficial veneer of stone pavement. The overall effect is a smoothing of the surficial topography, which can increase spectral contrast and band depth. Relatively smooth pahoehoe-style lava flows have been shown to exhibit increased spectral contrast in relation to their rougher, aa-style counterparts of the same composition (Kahle et al., 1988). Similarly, an increase in spectral contrast was also observed for smooth obsidian glass relative to more uneven surfaces on vesiculated pumice (Ramsey and Fink, 1999).

Spectral variation due to surface roughness is known as the cavity effect. With this effect, spectral emissivity increases at all wavelengths, due to energy being reflected multiple times when it encounters internal surfaces of a hollow cavity (Kirkland et al., 2001). The cavity effect on lithology is in play at all scales of physical size, from macroscopic (≥1 mm) hollows due to the random orientations of surficial regolith, down to microscopic (<1 mm) roughness that might be present even on deceptively smooth-appearing lithic fragments (Kirkland et al., 2001). For our purposes, it is possible that for the older surfaces that have smoothed topography coincident with a significant desert pavement formation, the relative

smoothness could be contributing to the increasing 9.16 μm band depth (in airborne spectra) with age.

The evolution towards a smoother surface also involves, to some degree, the effect of clast size sorting. The sorting process likely involves some transport and/or removal of smaller, more labile particles, while larger particles are broken down into smaller fragments by weathering processes. This convergence in clast size for the ultimate surficial material will cause the dominant clast size range to decrease, resulting in a higher degree of sorting. Given the overall character of older, stable terrace surfaces where a moderately- to well-developed desert pavement surface has developed (usually along with substantial coatings of desert varnish on clast surfaces), we could hypothesize a relationship between age and degree of clast size sorting.

The dominant (>50%) clast size range graphs (Figure 7) might show a weak correlation between age and degree of sorting, in the sense that the ranges are generally smaller for sites on older surfaces. If only taking the largest range for each surface, the correlation becomes slightly more compelling. In a youngest/oldest age binary sense for both the upstream and downstream sets of surfaces, the smallest range for the oldest surface is exceeded by the largest range for the youngest surface. Furthermore, the youngest upstream and downstream surfaces (Qt4 and C3 respectively) exhibit both the largest and smallest dominant clast size ranges, which shows a lower overall degree of sorting for the entire surface. This age and sorting relationship is also somewhat qualitatively evident by viewing all of the field site images and noting the relatively chaotic surface morphology of the younger surfaces that results from mixtures of larger clasts, finer particles, and also a greater amount of vegetation (which will be discussed below). On the younger surfaces, our data

show that there can be a greater degree of sorting (smaller range) for individual 1-m^2 pixels (e.g., see C3sand in Figure 7), but the higher variability between sites on single surfaces exhibits greater overall variation (overall lesser degree of sorting).

The youngest upstream and downstream surfaces exhibit the largest difference among dominant (>50%) clast size ranges for multiple sample sites (Figure 7). This implies a lower degree of sorting for younger surfaces, which increases macroscopic roughness and the cavity effect, and ultimately reduces spectral contrast. Although this conclusion implies that the increasing 9.16 μm band depth with age is not necessarily (or entirely) dependent on clay minerals accumulating in desert varnish, the spectral effect is still related to age. It is plausible that a relationship between topographic smoothing and age exists (e.g., see Mushkin et al., 2014), and it is also likely that the relationship is concomitant with desert varnish and pavement development. The topographic smoothing with age can be one of the reasons that there is increased spectral contrast and 9.16 μm band depth with surface age in airborne remote sensing spectra. Topographic smoothing with age is also apparent for the surfaces that we are studying at the meter-scale level: bar and swale hummocky topography was only observed at sites on the younger upstream surfaces (see field photographs for sites Qt4p2 (<11 ka), Qt3p1 and Qt3p2 (13 ka), Figures S2-S4 in the Supplemental Items).

The Effect of Vegetation

It is outside of the scope of this study to consider the identifications, nuances, and associated thermal infrared spectroscopy of specific vegetation types that can be found in the study area. Also, much of the area is usually sparsely vegetated to begin with, given the

regional desert environment. Therefore, we speak with broad generality regarding vegetation species that are present and contributing to remote sensing spectra, and we usually only refer to vegetation in this arid region in the most general sense as "desert scrub." However, we do provide a limited assessment when such data were collected in the field for our purposes. The desert scrub mainly includes an abundance of common, non-deciduous chaparral plants, such as creosote and sage, and other species that are also likely present.

The period that we performed field work in the area (March 2017 through May 2017) followed a very wet winter season; precipitation was the heaviest seen in probably at least a decade in southern California. Thus, many of the field images contain lots of 10 to 50 cm tall plants, including flowers, shrubs, and grasses, in various states of desiccation: these were only present in the spring for a few weeks, following a brief cycle of sprouting, blossoming, and then dying off. This relatively small, flowering vegetation can dominate the scene during spring blooms that follow rainy winter seasons. But due to their ephemeral nature, this vegetation will not play a significant role in contributing to remote sensing spectra, unless the acquisition occurs during a spring bloom. Our airborne remote sensing imagery was collected during the height of summer heat and aridity extremes (the norm for Coachella Valley summers), at 10:45-11:00 am (Pacific daylight savings time), on 24 September 2015.

In the study area, vegetation is generally sparse or absent where desert pavement is well-developed, which coincides with older surfaces (Figures 8, 9, and 10). If present on older surfaces, vegetation is usually localized in/near channels, or flanking areas with pavement (e.g., see field photographs from sites on Qt2 (74 ka) and Qt1 (87 ka), Figures S5-S8 in the Supplemental Items). Vegetation is also absent in the youngest, most active channels on younger surfaces (e.g., see field photographs from C3sand, Figure S13 in the

Supplemental Items). Vegetation found on older surfaces are mostly 1-2 m scrub bushes, but vegetation on younger surfaces is much more abundant and diverse, also including 10-30 cm shrubs, 10-50 cm cacti, and some dead wood.

In our analyses, we included some ground-based spectra of the larger (1-2 m scale), woody, desert scrub bushes that are more drought tolerant and likely to persist year round. At the upstream site Qt4p1 (<11 ka, Figure 12), five ground-based spectra from vegetation were combined with five lithologic spectra into the "Average" mixture spectrum for the 1-m^2 sample area. For Qt4p1, ground-based vegetation spectra samples included: 1) two spectra from some very light green to whitish broad leaves (see sample square meter field photograph in Figure 12A: the small, 10-30 cm light green/white broad-leaved plant included in the upper right corner of the sampling area, possibly *Encelia farinosa*, or white brittlebush?); 2) two spectra of white, leafless (at time of collection), dry, woody, branches from the 30-50 cm white branchy plant (located in the lower right corner of the site overview field photograph in Figure 12B); and 3) one spectrum from a branch of dead wood (located just to the left of the sample square meter in Figure 12B). Also present on the Qt4 surface were 1-2 m green woody scrub, and 10-50 cm cacti. Ground-based spectra for the upstream site Qt2p2 (74 ka) included one vegetation measurement that is averaged with eight other lithologic spectra from within the sample square meter (see Table 2, and Figure S6 in the Supplemental Items). The ground-based vegetation spectrum at Qt2p2 is from a c. 10 cm desiccated ephemeral flowering plant. The downstream site C3veg (13 ka) consists of a single 1-2 m desert scrub bush (see Table 2 and Figure S14 in the Supplemental Items). The bush was light green to yellow, partially desiccated, with woody branches, 1-2 cm thorns, and very narrow (almost needle-like) leaves; this type of plant was commonly encountered,

and it is possibly *Psorothamnus arborescens* (Mojave indigo bush), or *Psorothamnus schottii* (Schott's dalea, personal communication with botanist Jean Pawek).

The ground-based averaged spectra are simplified models that show qualitative effects for how mixtures might manifest in airborne remote sensing spectra that include multiple heterogeneous materials within the 1-m^2 pixel size. We acknowledge that the simplified models presented here are at odds with actual remote sensing spectra (which intrinsically capture greater heterogeneity over a larger sample area), because the latter likely include effects from non-linear mixing of vegetation with a lithologic background (Ray and Murray, 1996). However, these results still give us a broad sense of how the inclusion of vegetation might affect any lithologic signal that is present.

There is a common misconception that vegetation spectra in the thermal infrared wavelength regime (8-14 μm) tend to be flat and featureless (Elvidge, 1988; Ullah et al., 2012). Kahle et al. (1987) did find that desert vegetation had completely flat spectra, but this and other similar observations could be due to the fact that fresh green plant material can contain a significant amount of water weight (40-80%, Elvidge, 1988), and water is flat and featureless in the thermal infrared. We did not make any assumptions about what spectra from vegetation in our study area would look like, but our ground-based measurements for sites Qt4p1 (Figure 12), Qt2p2 and C3veg (Figures S6 and S14 in the Supplemental Items), all show that vegetation spectra are relatively flat and featureless in comparison with the lithologic spectra. Despite the fact that the spectra were collected from distinctly different plants, the five vegetation spectra taken from site Qt4p1 and the single vegetation spectrum taken from site Qt2p2, all are very similar and have very broad emissivity peaks from 8-10 μm wavelengths, which is the specific range where we are looking for distinct emissivity

troughs/minima, and variation in Reststrahlen feature positions (from varying silica-based mineralogy). In our ground-based average spectra that include vegetation, the broad vegetation emissivity peaks from 8-10 μm flatten lithologic Reststrahlen features in the same range, effectively reducing spectral contrast. The similarly flat spectra from C3veg would also produce similar results if incorporated into our models.

The relatively flat ground-based spectra from C3veg (13 ka, Figure S14 in the Supplemental Items), with its needle-like leaves, can be attributed to the cavity effect. In thermal infrared spectroscopy of vegetation, small and/or needle(-like) leaves increase the cavity effect, which, as discussed previously, reduces spectral contrast, especially relative to species with larger and flatter leaves (Ribeiro da Luz and Crowley, 2010; Ullah et al., 2012). Due to higher variability in individual leaf orientations, needle-shaped or needle-like leaves are thought to increase the cavity effect and minimize spectral contrast (Salisbury, 1986; Ribeiro da Luz and Crowley, 2007). Furthermore, there could also be a reduction in spectral contrast due to the cavity effect from microscopic surface roughness on plant surfaces (Ribeiro da Luz and Crowley, 2007).

In considering the effect of vegetation, there also exists the complication that some plant material can be silicified (Ribeiro da Luz and Crowley, 2007; 2010), which could produce the same Reststrahlen features that we are interested in (but from silica-based lithology). Silica present in plants could complicate our spectral analysis, because several specific species (although unlikely to be present in our study area) are known to become silicified and exhibit spectral features in the same 9-10 μm range (Ribeiro da Luz and Crowley, 2010), where we are looking for clay mineral Reststrahlen features.

Because the ground-based vegetation spectra are relatively flat and featureless, we conclude that the effect of vegetation is to reduce the spectral contrast in airborne remote sensing imagery pixels. In the study area, vegetation is more abundant, prominent, and diverse on younger surfaces. Estimates for average spacing of 1-2 m desert scrub bushes generally increase with surface age (Figures 10, 15, and Table 3), so if a silica is present in vegetation and contributing to spectra, we expect a greater contribution to the 9-10 μm feature in younger surfaces. However, we observe that the 9-10 μm spectral feature becomes more prominent in older surfaces with less vegetation. Thus, increased vegetation on younger surfaces is likely responsible for reducing their spectral contrast. It is also plausible that the correlation between increasing band depth at 9.16 μm and surface age can be a manifestation of increased spectral contrast on older surfaces that are more sparsely vegetated. Although this does not directly relate to our hypothesis that clay minerals in desert varnish are mainly responsible for the increase spectral contrast on older surfaces, it still strengthens the positive correlation between increasing spectral contrast and surface age. Therefore, independent of the cause, it is nonetheless still valid that spectral contrast correlates positively with age for geomorphic surfaces in this study area.

The Effect of Rock Area Fraction

Solid and particulate forms of materials exhibit transmission spectra that can vary considerably (Keller and Pickett, 1949), and similarly, when considering the effect of particle size on spectral contrast, the bulk density of the particulate matter must also be taken into account. For example, quartz exhibits greater spectral contrast in Reststrahlen bands not only

when particle size is increased, but also when the particulate is packed as opposed to being left in its loose, unconsolidated form (Salisbury and Eastes, 1985; Salisbury and Wald, 1992). Decrease in either particle size, or in the density of a particulate mass, will result in increased porosity, which can increase the cavity effect (Salisbury and Eastes, 1985) and volume scattering (Salisbury and Wald, 1992), both of which reduce spectral contrast. Therefore, we must also consider the coupled effects that particle size and packing (or density of material) have on our data.

To consider the packing/density effect, we looked at the rock area fraction (minimum, %) at each of our 1-m^2 field sampling sites (Figure 11) (i.e., "solid rock" being larger lithic fragments that represent the material with highest density/lowest porosity, versus smaller, loose sediment grains). On the basis of the arguments stated above and empirical data from previous work, we could hypothesize that the general positive correlation between increasing spectral contrast with surface age in airborne remote sensing spectra might be due to the solid rock (i.e., highest density/lowest porosity) area fraction increasing with surface age. However, we observe no general monotonically increasing trend, or mathematical correlation (Figure 15 and Table 3) for rock area fraction with surface age. Conversely, for the upstream surfaces (upper panel in Figure 11), the highest rock area fraction occurred at a site on the youngest surface (Qt4p2, <11 ka), and the lowest rock area fraction occurred at a site on the oldest surface (Qt0p2, >95 ka). Similarly, for the downstream surfaces, the two sites on the youngest surface (C3, 13 ka) both have rock area fractions that are greater than any of those from the three sites on the oldest surface (C0, >95 ka).

The increased rock area fraction on younger surfaces might be due concentration of larger cobbles and boulders (which quickly add up to a larger fraction), that have not yet been

weathered into smaller clasts. The inherent increase in surface roughness, and subsequent cavity effect, from a greater number of larger clasts, could outweigh the increase in rock area fraction, and ultimately reduce spectral contrast for younger surfaces. In a different way, the older surfaces that have well-developed desert pavement can also have a greater degree of compaction, which also results in higher density/lower porosity. Because increasing spectral contrast can be the effect of increasing density (not necessarily to the point of complete lithification to a solid), it is possible that the increased spectral contrast on older surfaces might be due to the greater degree of compaction found on older surfaces with well-developed desert pavement. Our rock area fraction analysis does not test for this variability, so it is still possible that the greater spectral contrast on older surfaces is caused by decreasing porosity (cavity effect), but not because of a greater rock area fraction.

Other Effects

When analyzed in detail, airborne remote sensing spectra from the downstream C2f (26 ka) surface, were problematic. The C2f surface is located on a steep ridge, directly on the surface trace of the Mission Creek strand (Figures 3 and 4). Not only did we observe the greatest standard deviation in airborne spectra band depth at 9.16 μm (see data point for 26 ka surface age in Figure 6), we also observed great variation when we sampled spectra from the C2f surface by different slope values. With its relatively drastic changes in slope, the C2f surface is dissimilar to any of the other surfaces, with their relatively broad, flat, and stable topography, which is conducive to protracted varnish and pavement development. Recall that in the downstream airborne remote sensing spectra, the oldest C0 (>95 ka) surface is in

position with the greatest band depth at 9.16 μm for three of the five subsets, and for the remaining two sets, C2f (26 ka) has the greatest band depth. This anomaly could be attributed to the spectral variation in C2f caused by increased and variable topographic slope. Thus, we note that the methods used in this research should not be applied to surfaces that lack a relatively broad, flat, and stable topography.

Above, in the Results section (see Ground Truth Field Work: Additional Field Observations), we also noted a distinct, light pink oxidation on clasts at the downstream site C2fp1 (26 ka) site, and a conspicuous higher relative abundance of red-orange oxidation at the upstream site Qt1p2 (87 ka). Oxidization is likely to occur on the buried bottoms of varnished clasts, due to iron oxide formation at soil or sub-soil level (Figures 2 and 3 in Engel and Sharp, 1958; Potter and Rossman, 1977; 1979a). Therefore, it is possible that the greater degree of oxidation observed at these sites represents many of the clasts being flipped over, especially on the steep and topographically unstable downstream C2f (26 ka) surface (see above). Oxides related to desert varnish development likely reduce spectral contrast due to their lack of spectral features in the wavelengths that our data covered (λ = 7.6-13.2 μm, see Figures 3 and 6 in Potter and Rossman, 1979a; Figure 14 in Potter and Rossman, 1979b). This effect could have caused the great spectral variation for the Qt1 and C2f surfaces. In airborne remote sensing spectra, the unexplained variation in the C2f (26 ka) surface was discussed above, and Qt1 (87 ka) was never in position, twice with very shallow band depth at 9.16 μm relative to the other older surfaces. Thus, we note that surfaces with a great degree of iron oxides also might not be suitable for the methods used in this research.

Bishop et al. (1994) observed another factor that could affect spectral contrast for montmorillonite clay: laboratory spectra from montmorillonite clay increased in band depth

with increasing grain size when lab samples were left unpacked, but when packed, the largest size fraction did not display the greatest band depth for a spectral feature at 1.9 μm. Although that wavelength position is outside of the range covered in this research (λ = 7.6-13.2 μm), they mentioned that their packing process resulted in lab samples with a variable degree of alignment and orientation among the particles. Thus, we note that when comparing any spectra to library standards, care should be taken to identify and consider the particle size and degree of packing used for measurements. Namely, when using linear mixture models, particle size should be much larger than the wavelengths in measured spectra (a condition that was met for our models in Figure 2, see caption).

CONCLUSIONS

In airborne remote sensing spectra of geomorphic surfaces along the southern San Andreas fault, we observed positive correlation (R^2 = 0.59) between increasing spectral contrast and band depth at 9.16 μm with surface age (Figures 5, 6, 15, and Table 3). We hypothesized that the increase in band depth at 9.16 μm was related to an increasing relative abundance of clay minerals (clay crystal aggregates) in progressively thicker coatings of desert varnish on older surfaces. To test our hypothesis, we conducted fieldwork to evaluate variation among surfaces in: clast size range, desert varnish and pavement development, vegetation spacing (proxy for abundance or sparsity), and rock area fraction. Of the quantities that we measured, there are no systematic trends related to increasing age for either mean of dominant (>50% relative abundance) clast size range (R^2 = 0.10) or rock area fraction (R^2 = 0.00). The quantities that had a stronger positive correlation with increasing surface age

(Figure 15 and Table 3) were: desert varnish scores (Spearman's rank = 0.90), desert pavement scores (Spearman's rank = 0.90), and vegetation spacing (R^2 = 0.34).

Ground-based field spectra from single lithologic clasts displayed a spectral feature at 9.30 μm that did not generally increase with surface age. While this 9.30 μm ground-based feature is still within the 9.1-9.6 μm range that typifies clay minerals, further analyses will be required to investigate why the main ground-based feature is not at the exact same position as the airborne remote sensing spectral feature at 9.16 μm. Furthermore, ground-based spectra from finer-grained, unconsolidated detrital material did not display increased band depth for the 9.30 μm feature, indicating that clay minerals are not necessarily more prevalent in the smaller clast/particle size fraction. While most of our spectra indicate the presence of some clay mineral(s), the spectra are overprinted with spectral features from common tectosilicate minerals (quartz and feldspars) characteristic of the varnish substrate. Also, ground-based vegetation spectra are very flat and featureless in the thermal wavelengths that correspond to those covered in the airborne remote sensing spectra. Therefore, we conclude that the increasing development of desert varnish and desert pavement, combined with decreasing vegetation, increase spectral contrast in airborne remote sensing spectra. The development of varnish and pavement usually takes a significant amount of time, and often generally decreases vegetation abundance, so an increase in spectral contrast based on these variables is generally related to the passage of time.

While this research does not outline a methodology to derive absolute ages for Quaternary geomorphic surfaces, the ideas presented here might make it possible in the future to determine relative ages, based on relative spectral contrast of geomorphic surfaces. Stricter age constraints could perhaps follow, if an age is known for at least one set of

geomorphic surfaces in a terraced (or otherwise related) series, as a calibration for a larger area or region. The methodology can be expanded to include varying spectral contrast/band depth in spectral features from other minerals (e.g., quartz features at 12.4-13.0 μm), and applied to other known geomorphic surface ages (e.g., see Gray et al., 2014). With the spatial component of tectonic displacement from an overhead perspective (i.e., offset feature identified, then separation distance measured), information derived regarding the time component from relative ages of geomorphic surfaces could potentially be used to estimate a fault slip rate from a single airborne remote sensing image.

ACKNOWLEDGEMENTS

This material is based upon work supported by the National Science Foundation (NSF) Graduate Research Fellowship Program under Grant No. 1144469 awarded to R. Witkosky. Mako airborne hyperspectral imagery was acquired under the auspices of the Aerospace Corporation's Independent Research and Development program. We thank Ginny Short for allowing access to the Thousand Palms Oasis Preserve, Maggie Anderson for processing the ground-based spectral data, and Ryan Gold for creating the DEM of our study area. Reference to any specific commercial products, process, or service by trade name, trademark, manufacturer, or otherwise, does not necessarily constitute or imply its endorsement, recommendation, or favoring by the United States Government. The views and opinions of authors expressed herein do not necessarily state or reflect those of the United States Government, and shall not be used for advertising or product endorsement purposes.

APPENDIX

Literature Review on Seismic Activity along the Southern San Andreas Fault

Paleoseismic Trenching

Paleoseismic trenching along the southern San Andreas fault at sites in the Coachella Valley has yielded recurrence intervals of c. 200 years (Fumal et al., 2002; Philibosian et al., 2011), while a recurrence interval calculated at the Wrightwood site (>100 km to the northwest) is roughly half of that value (Scharer et al., 2007). While it might appear that large, surface-rupturing earthquakes in the Coachella Valley occur less often than on other segments, the paleoseismic data consistently drive the message that the southern San Andreas might be due for a major seismic event soon, since it has been more than 300 years since the most recent large earthquake in the region (Sieh et al., 1989; Sieh and Williams, 1990; Fumal et al., 2002; Philibosian et al., 2011).

Tectonic Geomorphology

Methods in tectonic geomorphology have been used extensively to estimate geologic slip rates for the Coachella Valley segment of the southern San Andreas fault. However, these geologic slip rates can vary widely due to the complexity of the fault zone at some localities. A well-known offset alluvial fan used for fault slip rate analyses is located in the Indio Hills, near Biskra Palms (unfortunately, anthropogenic excavation has now almost

completely obliterated this natural asset). The Biskra Palms site yielded a geologic slip rate of 15.9 ± 3.4 mm/yr (van der Woerd et al., 2006) for the Mission Creek strand of the San Andreas fault. This rate was later updated to about the same central value in a range but with larger uncertainty (12-22 mm/yr), on the basis of greater net slip and more robust age constraints that broadly agreed across multiple independent dating methods (Behr et al., 2010; Fletcher et al., 2010; Benedetti and van der Woerd, 2014). Southeast of Biskra Palms at the Mecca Hills, Shifflett et al. (2002) calculated a significantly slower slip rate of 5-8 mm/yr. To the immediate northwest of Biskra Palms, the overall San Andreas fault structure becomes complex as the parallel Banning strand (located southwest of the Mission Creek strand) comes into play. The slip rate for the Mission Creek strand increases to 22-25 mm/yr at Pushawalla Canyon (Blisniuk and Sharp, 2014), then remarkably decreases to 4 ± 2 mm/yr at Thousand Palms Oasis (Fumal et al., 2002); all of this variation occurs within a distance of <10 km from the Biskra Palms site (Figure 1). Farther to the northwest, the Banning strand has a Holocene slip rate of 4-5 mm/yr (Gold et al., 2015), and the fault structure becomes more complex with the parallel Garnet Hill strand somewhat enigmatically coming into play to the southwest of the Banning strand (e.g., Cardona et al., 2015; Cardona, 2016). At the northwest terminus of the Coachella Valley, the San Andreas fault zone's structure becomes very complex, as multiple strands with opposing left lateral (Kendrick et al., 2015) and oblique right lateral with reverse/thrust (Huerta, 2015; 2017) relative fault motion interact through the San Gorgonio Pass (Yule, 2009).

Tectonic Geodesy

While geologic fault slip rates are averaged over centuries to millennia (or even greater time periods), geodetic fault slip rates are averaged over years to decades. Also, geologic fault slip rates are usually strict minima when based on reconstructing piercing points, such as an offset lithologic contact or stream channel. These fundamental data type differences could perhaps explain why geodetic slip rates for the southern San Andreas fault are generally faster than the geologic rates. A current geodetic slip rate for the southern San Andreas fault from combined InSAR and GPS was 25 ± 3 mm/yr (Fialko, 2006). With that rate significantly higher than those found from the geology, a revised fault geometry in the structural model used slowed the geodetic rate to 18 ± 1 mm/yr (Lindsey and Fialko, 2013), putting it closer to the geologic rates mentioned above (usually <20 mm/yr). Slip rates for the southern San Andreas fault from GPS data agree to some extent with geologic rates because they generally decrease to the northwest from a maximum of c. 23 mm/yr in the southeast (Spinler et al., 2010). Note that this observation only holds if the aforementioned result of Shifflett et al. (2002) is ignored.

REFERENCES CITED

Aulinas, M., Garcia-Valles, M., Fernandez-Turiel, J.L., Gimeno, D., Saavedra, J., and Gisbert, G., 2015, Insights into the formation of rock varnish in prevailing dusty regions: Earth Surface Process and Landforms, v. 40, p. 447-458, doi: 10.1002/esp.3644.

Bartholomew, M.J., Kahle, A.B., and Hoover, G., 1989, Infrared spectroscopy (2.3-20 μm) for the geological interpretation of remotely-sensed multispectral thermal infrared data: International Journal of Remote Sensing, v. 10, n. 3, p. 529-544.

Beck, W., Donahue, D.J., Jull, A.J.T., Burr, G., Broecker, W.S., Bonani, G., Hajdas, I., and Malotki, E., 1998, Ambiguities in direct dating of rock surfaces using radiocarbon measurements: Science, v. 280, 2132-2139, doi: 10.1126/science.280.5372.2132.

Behr, W.M., Rood, D.H., Fletcher, K.E., Guzman, N., Finkel, R., Hanks, T.C., Hudnut, K.W., Kendrick, K.J., Platt, J.P., Sharp, W.D., Weldon, R.J., and Yule, J.D., 2010, Uncertainties in slip-rate estimates for the Mission Creek strand of the southern San Andreas fault at Biskra Palms Oasis, southern California: Geological Society of America Bulletin, v. 122, n. 9/10, p. 1360-1377, doi: 10.1130/B30020.1.

Benedetti, L.C., and van der Woerd, J., 2014, Cosmogenic nuclide dating of earthquakes, faults, and toppled blocks: Elements, v. 10, n. 5, p. 357-361, doi: 10.2113/gselements.10.5.357.

Bishop, J.L, Pieters, C.M., and Edwards, J.O., 1994, Infrared spectroscopic analyses on the nature of water in montmorillonite: Clays and Clay Minerals, v. 42, n. 6, p. 702-716.

Bishop, J., Madejová, J., Komadel, P., and Fröschl, H., 2002a, The influence of structural Fe, Al, and Mg on the infrared OH bands in spectra of dioctahedral smectites: Clay Minerals, v. 37, p. 607-616.

Bishop, J., Murad, E., and Dyar, M.D., 2002b, The influence of octahedral and tetrahedral cation substitution on the structure of smectites and serpentines as observed through infrared spectroscopy: Clay Minerals, v. 37, p. 617-628.

Bishop, J.L., Lane, M.D., Dyar, M.D., and Brown, A.J., 2008, Reflectance and emission spectroscopy study of four groups of phyllosilicates: smectites, kaolinite-serpentines, chlorites and micas: Clay Minerals, v. 43, p. 35-54, doi: 10.1180/claymin.20080.43.1.03.

Blisniuk, K., and Sharp, W.D., 2014, Estimating geologic slip rates on the southern San Andreas Fault, California: U-series and ^{10}Be dating: U.S. Geological Survey Final Technical Report for USGS Award No. G13AP00031, 9 p.

Boggs, S., Jr., 2012, Principles of sedimentology and stratigraphy, fifth edition: New Jersey, Pearson Education Inc., 585 p.

Buckland, K.N., Young, S.J., Keim, E.R., Johnson, B.R., Johnson, P.D., and Tratt, D.M, 2017, Tracking and quantification of gaseous chemical plumes from anthropogenic emission sources within the Los Angeles Basin: Remote Sensing of Environment, v. 201, p. 275- 296, doi: 10.1016/j.rse.2017.09.012.

Bull, W.B., 1991, Geomorphic responses to climate change: New York, Oxford University Press, 326 p.

Bürgmann, R., 1991, Transpression along the southern San Andreas fault, Durmid Hill, California: Tectonics, v. 10, n. 6, p. 1152-1163.

Cardona, J.E., Yule, D., Scharer, K., and Huerta, B., Constraining the most recent surface rupture on the Garnet Hill fault, Coachella Valley, CA, *in* Proceedings, Southern California Earthquake Center Annual Meeting, Palm Springs: California, Volume XXV, p 138-139.

Cardona, J.E., 2016, Constraining the most recent surface rupture on the Garnet Hill strand, San Andreas fault, Coachella Valley, California [M.S. thesis]: Northridge, California State University, 67 p.

Christensen, P.R., and Harrison, S.T., 1993, Thermal infrared emission spectroscopy of natural surfaces: application to desert varnish coatings on rocks: Journal of Geophysical Research, v. 98, n. B11, p. 19819-19834.

Christensen, P.R., Bandfield, J.L., Hamilton, V.E., Howard, D.A., Lane, M.D., Piatek, J.L., Ruff, S.W., and Stefanov, W.L., 2000, A thermal emission spectral library of rock-forming minerals: Journal of Geophysical Research, v. 105, n. E4, p. 9735-9739.

Clark, R.N., and Roush, T.L., 1984, Reflectance spectroscopy: Quantitative analysis techniques for remote sensing applications: Journal of Geophysical Research, v. 89, n. B7, p. 6329-6340.

Compton, R.R., 1985, Geology in the Field: New York, John Wiley and Sons, Inc., 398 p.

Conel, J.E., 1969, Infrared emissivities of silicates: experimental results and a cloudy atmosphere model of spectral emission from condensed particulate mediums: Journal of Geophysical Research, v. 74, n. 6, p. 1614-1634.

Cooper, C.D., and Mustard, J.F., 1999, Effects of very fine particle size on reflectance spectra of smectite and palagonitic soil: Icarus, v. 142, p. 557-570, doi: 10.1006/icar.1999.6221.

Cyr, A.J., Miller, D.M., Menges, C., Schmidt, K.M., Mahan, S.A., Maher, K., and Liu, T., 2016, Paleoclimatic controls on Pleistocene alluvial fan deposition in the Mojave and Colorado deserts and southern Great Basin, southwestern USA: Geological Society of America Abstracts with Programs, v. 48, n. 7, doi: 10.1130/abs/2016AM-285938.

Davis, C., and O'Rourke, T., 2011, 2011, Shakeout Scenario: water system impacts from a M_w 7.8 San Andreas earthquake: Earthquake Spectra, v. 27, n. 2, p. 459-476.

Deer, W.A., Howie, R.A., and Zussman, J., 1992, An introduction to the rock-forming minerals, second edition: England, Pearson Education Limited, 696 p.

Dibblee, T.W., Jr., 2008, Geologic map of the Thousand Palms and Lost Horse Mountain 15 minute quadrangles, Riverside County, California (edited by John A. Minch): Santa Barbara Museum of Natural History, Dibblee Geology Center Map #DF-372, scale 1:62500, 1 sheet.

Ehlmann, B.L., et al., 2009, Identification of hydrated silicate minerals on Mars using MRO-CRISM: Geologic context near Nili Fossae and implications for aqueous alteration: Journal of Geophysical Research, v. 114, n. E00D08, doi:10.1029/2009JE003339.

Elvidge, C.D., 1988, Thermal infrared reflectance of dry plant materials: 2.5-20.0 μm: Remote Sensing of Environment, v. 26, p. 265-285.

Engel, C.G., and Sharp, R.P, 1958, Chemical data in desert varnish: Bulletin of the Geological Society of America, v. 69, p. 487-518.

Farmer, V.C., 1974, Chapter 15, The layer silicates, *in* Farmer, V.C., ed., The infra-red spectra of minerals: London, Mineralogical Society Monograph 4, p. 331-363.

Farr, T.G., and Chadwick, O.A., 1996, Geomorphic processes and remote sensing signatures of alluvial fans in the Kun Lun Mountains, China: Journal of Geophysical Research, v. 101, n. E10, p. 23091-23100.

Fialko, Y., 2006, Interseismic strain accumulation and the earthquake potential on the southern San Andreas fault system: Nature, v. 44, p. 968-971, doi:10.1038/nature04797.

Fletcher, K.E.K., Sharp, W.D., Kendrick, K.J., Behr, W.M., Hudnut, K.W., and Hanks, T.C., 2010, ^{230}Th/U dating of a late Pleistocene alluvial fan along the southern San Andreas fault: Geological Society of America Bulletin, v. 122, n. 9/10, p. 1347-1359, doi: 10.1130/B30018.1.

Frankel, K.L., and Dolan, J.F., 2007, Characterizing arid region alluvial fan surface roughness with airborne laser swath mapping digital topographic data: Journal of Geophysical Research, v. 112, n. F02025, doi:10.1029/2006JF000644.

Frankel, K.L., et al., 2007, Cosmogenic 10Be and 36Cl geochronology of offset alluvial fans along the northern Death Valley fault zone: Implications for transient strain in the eastern California shear zone: Journal of Geophysical Research, v. 112, n. B06407, doi: 10.1029/2006JB004350.

Friedrich, A.M., Wernicke, B.P., Niemi, N.A., Bennett, R.A., and Davis, J.L., 2003, Comparison of geodetic and geologic data from the Wasatch region, Utah, and implications for the spectral character of Earth deformation at periods of 10 to 10 million years: Journal of Geophysical Research, v. 118, n. B4, 2199, doi:10.1029/2001JB000682.

Frost, R.L., Kloprogge, J.T., and Ding, Z., 2002, Near-infrared spectroscopic study of nontronites and ferruginous smectite: Spectrochimica Acta Part A: Molecular and Biomolecular Spectroscopy, v. 58, n. 8, p. 1657-1668, doi: 10.1016/S1386- 1425(01)00637-0.

Fumal, T.E., Rymer, M.J., and Seitz, G.G., 2002, Timing of large earthquakes since A.D. 800 on the Mission Creek strand of the San Andreas fault zone at Thousand Palms Oasis, near Palm Springs, California: Bulletin of the Seismological Society of America, v. 92, n. 7, p. 2841-2860.

Garvie, L.A.J., Burt, D.M., and Buseck, P.R., 2008, Nanometer-scale complexity, growth, and diagenesis in desert varnish: Geology, v. 36, n. 3, p. 215-218, doi: 10.1130/G24409A.1.

Gillespie, A.R., Kahle, A.B., and Palluconi, F.D., 1984, Mapping alluvial fans in Death Valley, California, using multichannel thermal infrared images: Geophysical Research Letters, v. 11, n. 11, p. 1153-1156.

Gillespie, A.R, Kahle, A.B., and Walker, R.E., 1987, Color enhancement of highly correlated images. II. Channel ratio and “chromaticity” transformation techniques: Remote Sensing of Environment, v. 22, p. 343-365.

Gold, P.O., Behr, W.M., Rood, D., Sharp, W.D., Rockwell, T.K., Kendrick, K., and Salin, A., 2015, Holocene geologic slip rate for the Banning strand of the southern San Andreas

fault, southern California: Journal of Geophysical Research: Solid Earth, v. 120, doi: 10.1002/2015JB012004.

Green, A.A., Berman, M., Switzer, P., and Craig, M.D., 1988, A transformation for ordering multispectral data in terms of image quality with implications for noise removal: IEEE Transactions on Geoscience and Remote Sensing, v. 26, no. 1, p. 65-74.

Hall, J.L., Boucher, R.H., Gutierrez, D.J., Hansel, S.J., Kasper, B.P., Keim, E.R., Moreno, N.M., Polak, M.L., Sivjee, M.G., Tratt, D.M., and Warren, D.W., 2011, First flights of a new airborne thermal infrared imaging spectrometer with high area coverage, *in* Andresen, B.F., Fulop, G.F., and Norton, P.R., eds., Infrared Technology and Applications XXXVII, Proceedings of SPIE, v. 8012, p. 8012031- 8012037.

Helms, J.G., McGill, S.F., and Rockwell, T.K., 2003, Calibrated, late Quaternary age indices using clast rubification and soil development on alluvial surfaces in Pilot Knob Valley, Mojave Desert, southeastern California: Quaternary Research, v. 60, p. 377-393, doi:10.1016/j.yqres.2003.08.002.

Hook, S.J., Dmochowski, J.E., Howard, K.A., Rowan, L.C., Karlstrom, K.E., and Stock, J.M., 2005, Mapping variations in weight percent silica measured from multispectral thermal infrared imagery—Examples from the Hiller Mountains, Nevada, USA, and Tres Virgenes-La Reforma, Baja California Sur, Mexico: Remote Sensing of Environment v. 95, p. 273-289.

Horgan, B.H., Bell, J.F. III, Noe Dobrea, E.Z., Cloutis, E.A., Bailey, D.T., Craig, M.A., Roach, L.H., and Mustard, J.F., 2009, Distribution of hydrated minerals in the north polar region of Mars: Journal of Geophysical Research, v. 114, n. E01005, doi: 10.1029/2008JE003187.

Huerta, B., Yule, D., and Heermance, R., 2015, Structure and geomorphology of Whitewater Hill and slip transfer from the Banning and Garnet Hill strands of the San Andreas fault, *in* Proceedings, Southern California Earthquake Center Annual Meeting, Palm Springs: California, Volume XXV, p 156.

Huerta, B.E., 2017, Structure and geomorphology of west Whitewater Hill, a compressive stepover between the Banning and Garnet Hill strands of the San Andreas fault, Whitewater, CA [M.S. thesis]: Northridge, California State University, 64 p.

Hunt, J.M., Wisherd, M.P., Bonham, L.C., 1950, Infrared absorption spectra of minerals and other inorganic compounds: Analytical Chemistry, v. 22, n. 12, p. 1478-1497, doi: 10.1021/ac60048a006.

Hunt, C.B., 1954, Desert varnish: Science, v. 120, n. 3109, p. 183-184.

Hunt, C.B., and Mabey, D.R., 1966, Stratigraphy and structure, Death Valley, California: United States Geological Survey Professional Paper 494-A, 162 p.

Hunt, G.R., and Vincent, R.K., 1968, The behavior of spectral features in the infrared emission from particulate surfaces of various grain sizes: Journal of Geophysical Research, v. 73, n. 18, p. 6039-6046.

Jayko, A.S., Menges, C.M., and Thompson, R.A., 2005, Digital method for regional mapping of surficial basin deposits in arid regions, example from central Death Valley, Inyo County, California: United States Geological Survey Open-File Report 2005-1445, 31 p.

Jones, L.M., et al., 2008, The ShakeOut Scenario: United States Geological Survey Open-File Report 2008-1150, 308 p.

Kahle, A.B., 1987, Surface emittance, temperature, and thermal inertia derived from Thermal Infrared Multispectral Scanner (TIMS) data for Death Valley, California: Geophysics, v. 52, n. 7, p. 858-874.

Kahle, A.B., Madura, D.P., and Soha, J.M., 1980, Middle infrared multispectral aircraft scanner data: analysis for geological applications: Applied Optics, v. 19, n. 14, p. 2279-2290.

Kahle, A.B., and Goetz, A.F.H., 1983, Mineralogic information from a new airborne thermal infrared multispectral scanner: Science, v. 222, n. 4619, p. 24-27.

Kahle, A.B., Gillespie, A.R., Abbott, E.A., Abrams, M.J., Walker, R.E., and Hoover, G., 1988, Relative dating of Hawaiian lava flows using multispectral thermal infrared images: A new tool for geologic mapping of young volcanic terranes: Journal of Geophysical Research, v. 93, n. B12, p. 15239-15251.

Kealy, P.S., and Hook, S.J., 1993, Separating temperature and emissivity in thermal infrared multispectral scanner data: implications for recovery of land surface temperatures: IEEE Transactions on Geoscience and Remote Sensing, v. 31, n. 6, p. 1155-1164.

Keller, W.D., and Pickett, E.E., 1949, Absorption of infrared radiation by powdered silica minerals: American Mineralogist, v. 34, n. 11-1, p. 855-868.

Keller, W.D., and Pickett, E.E., 1950, The absorption of infrared radiation by clay minerals: American Journal of Science, v. 248, n. 4, p. 264-273.

Keller, E.A., Bonkowski, M.S., Korsch, R.J., and Shlemon, R.J., 1982, Tectonic geomorphology of the San Andreas fault zone in the southern Indio Hills, Coachella Valley, California: Geological Society of America Bulletin, v. 93, p. 46-56.

Kendrick, K.J., Matti, J.C., and Mahan, S.A., 2015, Late Quaternary slip history of the Mill Creek strand of the San Andreas fault in San Gorgonio Pass, southern California: The role of a subsidiary left-lateral fault in strand switching: Geological Society of America Bulletin, v. 127, n. 5/6, p. 825-849, doi:10.1130/B31101.1.

Kirkland, L., Herr, K., Keim, E., Adams, P., Salisbury, J., Hackwell, J., and Treiman, A., 2001, First use of an airborne infrared hyperspectral scanner for compositional mapping: Remote Sensing of Environment, v. 80, p. 447-459.

Krinsley, D.H., Dorn, R.I., DiGregorio, B.E., Langworthy, K.A., and Ditto, J, 2012, Rock varnish in New York: An accelerated snapshot of accretionary processes: Geomorphology, v. 138, p. 339-351, doi:10.1016/j.geomorph.2011.09.022.

Lancaster, J.T., Hayhurst, C.A., and Bedrossian, T.L., 2012, Preliminary geologic map of Quaternary surficial deposits in southern California, Palm Springs 30’ X 60’ quadrangle: Geologic compilation of Quaternary surficial deposits in southern California, California Geological Survey Special Report 217, Plate 24, scale 1:100,000.

Launer, P.J., 1952, Regularities in the infrared absorption spectra of the silicate minerals: American Mineralogist, v. 37, n. 9-10, p. 764-784.

Lee, J.B., Woodyatt, S., and Berman, M., 1990, Enhancement of high spectral resolution remote- sensing data by a noise-adjusted principal components transform: IEEE Transactions on Geoscience and Remote Sensing, v. 28, n. 3, p. 295-304.

Lindsey, E.O., and Fialko, Y., 2013, Geodetic slip rates in the southern San Andreas Fault system: effects of elastic heterogeneity and fault geometry: Journal of Geophysical Research: Solid Earth, v. 118, p. 689-697, doi:10.1029/2012JB009358.

Lippincott, E.R., Valkenburg, A.V., Weir, C.E., and Bunting, E.N., 1958, Infrared studies on polymorphs of silicon dioxide and germanium oxide: Journal of Research of the National Bureau of Standards, v. 61, n. 1, p. 61-70.

Liu, T., 2003, Blind testing of rock varnish microstratigraphy as a chronometric indicator: results on late Quaternary lava flows in the Mojave Desert, California: Geomorphology, v. 53, p. 209-234, doi:10.1016/S0169-555X(02)00331-8.

Liu, T., and Broecker, W.S., 2000, How fast does rock varnish grow?: Geology, v. 28, n. 2, p. 183-186.

Liu, T., and Broecker, W.S., 2013, Millennial-scale varnish microlamination dating of late Pleistocene geomorphic features in the drylands of western USA: Geomorphology, v. 187, p. 38-60, doi: 10.1016/j.geomorph.2012.12.034.

Lyon, R.J.P., 1965, Analysis of rocks by spectral infrared emission (8 to 25 microns): Economic Geology, v. 60, p. 715-736.

Macholdt, D.S., et al., 2015, Microanalytical methods for in-situ high-resolution analysis of rock varnish at the micrometer to nanometer scale: Chemical Geology, v. 411, p. 57-68, doi: 10.1016/j.chemgeo.2015.06.023.

Marston, R.A., 2003, Editorial note: Geomorphology, v. 53, p. 197, doi: 10.1016/S0169-555X(02)00329-X.

McFadden, L.D., Wells, S.G., and Jercinovich, M.J., 1987, Influences of eolian and pedogenic processes on the origin and evolution of desert pavements: Geology, v. 15, p. 504-508.

Michalski, J.R., Kraft, M.D., Sharp, T.G., Williams, L.B., and Christensen, P.R., 2006, Emission spectroscopy of clay minerals and evidence for poorly crystalline aluminosilicates on Mars from Thermal Emission Spectrometer data: Journal of Geophysical Research, v. 111, n. E03004, doi: 10.1029/2005JE002438.

Moersch, J.E., and Christensen, P.R., 1995, Thermal emission from particulate surfaces: A comparison of scattering models with measured spectra: Journal of Geophysical Research, v. 100, n. E4, p. 7465-7477.

Mushkin, A., Sagy, A., Trabelci, E., Amit, R., and Porat, N., 2014, Measuring the time and scale- dependency of subaerial rock weathering rates over geologic time scales with ground-based lidar: Geology, v. 42, n. 12, p. 1063-1066, doi:10.1130/G35866.1.

Owen, L.A., Clemmens, S.J., Finkel, R.C., and Gray, H., 2014, Late Quaternary alluvial fans at the eastern end of the San Bernardino Mountains, southern California: Quaternary Science Reviews, v. 87, p. 114-134, doi: 10.1016/j.quascirev.2014.01.003.

Pazzaglia, F.J., 2013, Fluvial terraces, *in* Schroder, J., and Wohl, E., eds., Treatise on Geomorphology: Academic Press, San Diego, California, v. 9, Fluvial Geomorphology, p. 379-412, http://dx.doi.org/10.1016/B978-0-12-374739-6.00248-7.

Perry, R.S., and Adams, J.B., 1978, Desert varnish: evidence for cyclic deposition of manganese: Nature, v. 276, p. 489-491.

Perry, R.S., Lynne, B.Y., Sephton, M.A., Kolb, V.M., Perry, C.C., and Staley, J.T., 2006, Baking black opal in the desert sun: the importance of silica in desert varnish: Geology, v. 34, n. 7, p. 537-540, doi: 10.1130/G22352.1.

Philibosian, B., Fumal, T., and Weldon, R., 2011, San Andreas fault earthquake chronology and Lake Cahuilla history at Coachella, California: Bulletin of the Seismological Society of America, v. 101, n. 1, p. 13-38, doi: 10.1785/0120100050.

Porter, et al., 2011, The ShakeOut Scenario: a hypothetical M_W 7.8 earthquake of the southern San Andreas fault: Earthquake Spectra, v. 27, n. 2, p. 239-261.

Potter, R.M., and Rossman, G.R., 1977, Desert varnish: the importance of clay minerals: Science, v. 196, n. 4297, p. 1446-1448, doi: 10.1126/science.196.4297.1446.

Potter, R.M., and Rossman, G.R., 1979a, The manganese- and iron-oxide mineralogy of desert varnish: Chemical Geology, v. 25, p. 79-94.

Potter, R.M., and Rossman, G.R., 1979b, The tetravalent manganese oxides: identification, hydration, and structural relationships by infrared spectroscopy: American Mineralogist, v. 64, p. 119-1218.

Phillips, F.M., 2003, Cosmogenic ^{36}Cl ages of Quaternary basalt flows in the Mojave Desert, California, USA: Geomorphology, v. 53, p. 199-208, doi: 10.1016/S0169-555X(02)00328-8.

QGIS Development Team, 2018, QGIS Geographic Information System, Open Source Geospatial Foundation Project: https://qgis.org/en/site/ (accessed September 2017).

Quade, J., 2001, Desert pavements and associated rock varnish in the Mojave Desert: how old can they be?: Geology, v. 29, n. 9, p. 855-858.

Ramsey, M.S., and Fink, J.H., 1999, Estimating silicic lava vesicularity with thermal remote sensing: a new technique for volcanic mapping and monitoring: Bulletin of Volcanology, v. 61, p. 32-39.

Ray, T.W., and Murray, B.C., 1996, Nonlinear spectral mixing in desert vegetation: Remote Sensing of Environment, v. 55, p. 59-64.

Reheis, M.C., Slate, J.L., Throckmorton, C.K., McGeehin, J.P., Sarna-Wojcicki, A.M., and Dengler, L., 1996, Late Quaternary sedimentation on the Leidy Creek fan, Nevada-California: geomorphic responses to climate change: Basin Research, v. 12, p. 279-299.

Reneau, S.L., Raymond, R., Jr., and Harrington, C.D., 1992, Elemental relationships in rock varnish stratigraphic layers, Cima volcanic field, California: implications for varnish development and the interpretation of varnish chemistry: American Journal of Science, v. 292, p. 684-723.

Ribeiro da Luz, B., and Crowley, J.K., 2007, Spectral reflectance and emissivity features of broad leaf plants: Prospects for remote sensing in the thermal infrared (8.0-14.0 μm): Remote Sensing of Environment, v. 109, p. 393-405, doi:10.1016/j.rse.2007.01.008.

Ribeiro da Luz, B., and Crowley, J.K., 2010, Identification of plant species by using high spatial and spectral resolution thermal infrared (8.0-13.5 μm) imagery: Remote Sensing of Environment, v. 114, p. 404-413, doi:10.1016/j.rse.2009.09.019.

Rivard, B., Petroy, S.B., and Miller, J.R., 1993, Measured effects of desert varnish on the mid- infrared spectra of weathered rocks as an aid to TIMS imagery interpretation: IEEE transactions on Geoscience and Remote Sensing, v. 31, n. 1, p. 284-291.

Robitaille, P. -M., 2009, Kirchhoff's law of thermal emission: 150 years: Progress in Physics, v. 4, p. 3-13.

Salisbury, J.W., and Eastes, J.W., 1985, The effect of particle size and porosity on spectral contrast in the mid-infrared: Icarus, v. 64, p. 586-588.

Salisbury, J.W., 1986, Preliminary measurements of leaf spectral reflectance in the 8-14 μm region: International Journal of Remote Sensing, v. 7, n. 12, p. 1879-1886.

Salisbury, J.W., Walter, L.S., and Vergo, N., 1987, Mid-infrared (2.1-25 μm) spectra of minerals: First edition: United States Geological Survey Open-File Report 87-263, 389 p., https://pubs.er.usgs.gov/publication/ofr87263 (accessed April 2018).

Salisbury, J.W., and Walter, L.S., 1989, Thermal infrared (2.5-13.5 μm) spectroscopic remote sensing of igneous rock types on particulate planetary surfaces: Journal of Geophysical Research, v. 94, n. B7, p. 9192-9202.

Salisbury, J.W., Wald, A., and D'Aria, D.M., 1994, Thermal-infrared remote sensing and Kirchhoff's law 1. Laboratory measurements: Journal of Geophysical Research, v. 99, n. B6, p. 11897-11911.

Salisbury, J.W., and Wald, A., 1992, The role of volume scattering in reducing spectral contrast of Reststrahlen bands in spectra of powdered minerals: Icarus, v. 96, p. 121-128.

Schaepman-Strub, G., Schaepman, M.E., Painter, T.H., Dangel, S., and Martonchik, J.V., 2006, Reflectance quantities in optical remote sensing-definitions and case studies: Remote Sensing of Environment, v. 103, p. 27-42, doi:10.1016/j.rse.2006.03.002.

Scharer, K.M., Weldon, R.J., Fumal, T.E., and Biasi, G.P., 2007, Paleoearthquakes on the southern San Andreas fault, Wrightwood, California, 3000 to 1500 B.C.: a new method for evaluating paleoseismic evidence and earthquake horizons: Bulletin of the Seismological Society of America, v. 97, n. 4, p. 1054-1093, doi: 10.1785/0120060137.

Schneider, C.A., Rasband, W.S., and Eliceiri, K.W., 2012, NIH Image to ImageJ: 25 years of image analysis: Nature Methods, v. 9, n. 7, p. 671-675.

Shifflett, H.S., Gray, M.G., Grannell, R., and Ingram, B. L., 2002, New evidence on the slip rate, renewal time, and late Holocene surface displacement, southernmost San Andreas fault, Mecca Hills, California: Bulletin of the Seismological Society of America, v. 92, n. 7, p. 2861-2877.

Sieh, K., Stuiver, M., and Brillinger, D., 1989, A more precise chronology of earthquakes produced by the San Andreas fault in southern California: Journal of Geophysical Research, v. 94, n. B1, p. 603-623.

Sieh, K.E., and Williams, P.L., ,1990, Behavior on the southernmost San Andreas fault during the past 300 years: Journal of Geophysical Research, v. 95, n. B5, p. 6629-6645.

Simpson, S.H., 2015, Creating a data analysis plan: what to consider when choosing statistics for a study: Canadian Journal of Hospital Pharmacy, v. 68, n. 4, p. 311-317.

Spilde, M.N., Melim, L.A., Northup, D.E., and Boston, P.J., 2013, Anthropogenic lead as a tracer of rock varnish growth: Implications for rates of formation: Geology, v. 41, n. 2, p. 263-266, doi:10.1130/G33514.1.

Spinler, J.C., Bennett, R.A., Anderson, M.L., McGill, S.F., Hreinsdóttir, S., and McCallister, A., 2010, Present-day strain accumulation and slip rates associated with southern San Andreas and eastern California shear zone faults: Journal of Geophysical Research, v. 115, B11407, doi:10.1029/2010JB007424.

Sposito, G., Prost, R., and Gaultier, J.-P., 1983, Infrared spectroscopic study of adsorbed water on reduced-charge Na/Li-montmorillonites: Clays and Clay minerals, v. 31, n. 1, p. 9-16.

Thiagarajan, N., and Lee, C.-T.A., 2004, Trace-element evidence for the origin of desert varnish by direct aqueous atmospheric deposition: Earth and Planetary Science Letters, v. 224, p. 131-141, doi:10.1016/j.epsl.2004.04.038.

Thomson, J.L., and Salisbury, J.W., 1993, The mid-infrared reflectance of mineral mixtures (7-14 μm): Remote Sensing of Environment, v. 45, p. 1-13.

Ullah, S., Schlerf, M., Skidmore, A.K., and Hecker, C., 2012, Identifying plant species using mid-wave infrared (2.5-6 μm) and thermal infrared (8-14 μm) emissivity spectra: Remote Sensing of Environment, v. 118, p. 95-102, doi:10.1016/j.rse.2011.11.008.

Van de Kamp, P.C., 1973, Holocene continental sedimentation in the Salton basin, California: a reconnaissance: Geological Society of America Bulletin, v. 84, p. 827-848.

van der Woerd, J., Klinger, Y., Sieh, K., Tapponnier, P., Ryerson, F.J., and Mériaux, A.-S., 2006, Long-term slip rate of the southern San Andreas Fault from ^{10}Be-^{26}Al surface exposure dating of an offset alluvial fan: Journal of Geophysical Research, v. 111, n. B04407, doi:10.1029/2004JB003559.

Watchman, A., 2000, A review of the history of dating rock varnishes: Earth-Science Reviews, v. 49, p. 261-277.

Wells, S.G., Dohrenwend, J.C., McFadden, L.D., Turrin, B.D., and Mahrer, K.D., 1985, Late Cenozoic landscape evolution on lava flow surfaces of the Cima volcanic field, Mojave Desert, California: Geological Society of America Bulletin, v. 96, p. 1518-1529.

Wells, S.G., McFadden, L.D., Poths, J., and Olinger, C.T., 1995, Cosmogenic ^{3}He surface-exposure dating of stone pavements: Implications for landscape evolution in deserts: Geology, v. 23, n. 7, p. 613-616.

Whitley, D.S., and Dorn, R.I., 1987, Rock art chronology in eastern California: World Archaeology, v. 19, n. 2, p. 150-164, doi: 10.1080/00438243.1987.9980031.

Young, S.J., Johnson, B.R., and Hackwell, J.A., 2002, An in-scene method for atmospheric compensation of thermal hyperspectral data: Journal of Geophysical Research, v. 107, no. D24, p. 4774-4793.

Yule, D., 2009, The enigmatic San Gorgonio Pass: Geology, v. 37, n. 2, p. 191-192, doi: 10.1130/focus022009.1

FIGURE CAPTIONS

Figure 1 (p. 349): Overview map of the study area, which is located in the Coachella Valley of southern California. Base map is Google Earth satellite imagery in true color (imagery date: 14 July 2016). Image was annotated to show the main strands of the southern San

Andreas fault (arrows represent relative fault motion), which is the main boundary between the Pacific and North American tectonic plates at this location. The rectangle is the footprint of the thermal hyperspectral airborne imagery used for this research. Interstate 10, and the Palm Springs International Airport are shown for geographic markers. BP: Biskra Palms; IH: Indio Hills; PC: Pushawalla Canyon; SAF-B: San Andreas fault, Banning strand; SAF-MC: San Andreas fault, Mission Creek strand; THAIF: thermal hyperspectral airborne imagery footprint; TPO: Thousand Palms Oasis.

Figure 2 (p. 350): Examples of laboratory thermal infrared emission spectra, and linear spectral mixture models for minerals relevant to this research. Spectra used here are from the library of Christensen et al. (2000), and mineral names are accompanied by the sample numbers (in parentheses) from that library. We used the linear "checkerboard" model (Christensen and Harrison, 1993) to calculate spectra for the mixtures shown. (A) Single tectosilicate mineral components combined to make a synthetic "granite," which represents a typical desert varnish coating substrate lithology found in the study area. Ratio of quartz/andesine/microcline is 33/34/33, and particle size ranges are: quartz = 125-2000 μm; andesine = 710-1000 μm; microcline = 710-1000 μm. (B) Montmorillonite clay (proxy for desert varnish coating) combined with the "granite" substrate to model the anticipated effect of a progressively heavier desert varnish coating ("granite/mont" is the mixing ratio for the two endmember components). The clay's major absorption feature at 9.36 um begins to dominate the spectrum as more is added to the mixture. The montmorillonite sample was a pressed pellet (Cooper and Mustard, 1999, noted that clay crystal aggregates behave spectrally like larger particles). (C) Field photograph (for scale, hammer is 33 cm long) that

exemplifies the variable degree of varnish development observed on clasts. Some of the clasts are circled and labeled to relate physical specimens to the spectral models shown in (A) and (B): the synthetic "granite" spectrum could represent the clast labeled "'granite' endmember" (which is not varnished); the granite/mont = 67/33 (or 33/67) spectra could represent the clasts labeled "intermediate mixtures" (which have light/moderate varnish); and the montmorillonite spectrum could represent the clast labeled "montmorillonite endmember" (i.e., with its heavy varnish coating, a spectrum of this clast might resemble the spectrum for montmorillonite clay, which can be a significant component in a typical varnish, see text for further explanation and references). As heavier varnish coatings tend to have greater physical thickness, a roughly linear relationship between increasing spectral band depth and varnish thickness has been observed in laboratory spectra of varnish-coated samples (Christensen and Harrison, 1993), which supports the linear spectral mixture models in (A) and (B).

Figure 3 (p. 351): Thermal hyperspectral airborne imagery of the Thousand Palms Oasis area, Coachella Valley, southern California (for larger spatial context, imagery footprint can be seen in Figure 1). The complete image scene is shown here, and displayed in false colors assigned to band ratios, which remove the effects of varying illumination due to topography (Kahle et al., 1980; Gillespie et al., 1987). Band ratio assignments are: red, 11.1/9.5; green, 11.5/9.1; blue, 12.4/8.6 (all values are wavelengths in microns). The false color assignments highlight geological features (such as the varnish we are studying), and other forms of land surface cover. General false color interpretation is as follows: red represents younger sediments, green represents older varnished surfaces, and blue represents vegetation. Thick

black lines are faults: only the main splays are shown here, so the imagery is not overly obscured. Arrows indicate relative fault motion. PC: Pushawalla Canyon; SAFMCS: San Andreas fault, Mission Creek strand; SAFBS: San Andreas fault, Banning strand; TPO: Thousand Palms Oasis. Lower left photograph is of Mako, the Aerospace Corporation's thermal hyperspectral sensor, mounted in the belly of an airplane and ready to fly (photo taken by David Tratt). Mako is essentially a large camera that takes aerial images of thermal radiation emitted by land surfaces. Lower left illustration shows the Mako sensor's viewing geometry. Base map is an SRTM 1 arc-second DEM hillshade (from the USGS Earth Resources Observation and Science website, https://eros.usgs.gov/, accessed on 09/02/2017). Map was produced using QGIS software (QGIS, 2018).

Figure 4 (p. 352): Same as Figure 3, but with color-coded digitized polygons for the mapped and dated geomorphic surfaces (Kate Scharer, personal communication; Blisniuk and Sharp, 2014) that we used for this research. The surface ages were derived with a combination of methods: cosmogenic exposure (beryllium-10) dating, and also uranium-series dating (ages shown in lower left key; ka: kiloannum). To the north east, upstream from where the San Andreas fault, Mission Creek strand, intersects Pushawalla Canyon, we grouped the cluster of surfaces for analyses, and we referred to this group as the "upstream" set of surfaces (or surface deposits). Similarly, to the south west, downstream from the San Andreas fault, Mission Creek strand, we grouped all of these other surfaces, and referred to this group as the "downstream" set of surfaces (or surface deposits).

Figure 5 (p. 353): Airborne remote sensing emissivity spectra of the geomorphic surfaces (for surface names and ages, see Table 1, for locations, see Figure 4). To display spectral variability, there are five subsets of randomly generated spectra for each of the upstream and downstream sets of surfaces (single spectra shown here are the average of multiples, see text). The continuum has been removed from all spectra, and they were also smoothed over a three band interval.

Figure 6 (p. 354): Airborne spectra band depth at 9.16 μm versus surface age. Error bars in surface age are from values in Table 1. Error bars in band depth are from the standard deviation of values calculated from all of the spectra in Figure 5.

Figure 7 (p. 355): Dominant (>50% relative abundance) clast size range plots for field sites on the upstream (upper panel) and downstream (lower panel) sets of surfaces. Clast sizes were not measured at the downstream sites C3sand and C3veg.

Figure 8 (p. 356): Desert varnish scores for field sites on the upstream (upper panel) and downstream (lower panel) sets of surfaces. A higher number is a greater degree of development, as follows: 1 = absent/rare, 2 = light/weak, 3 = moderate, and 4 = heavy/strong.

Figure 9 (p. 357): Desert pavement scores for field sites on the upstream (upper panel) and downstream (lower panel) sets of surfaces. A higher number is a greater degree of development, as follows: 1 = absent/rare, 2 = light/weak, 3 = moderate, and 4 = heavy/strong.

Figure 10 (p. 358): Vegetation spacing estimates for field sites on the upstream (upper panel) and downstream (lower panel) sets of surfaces. The values for upstream sites Qt0p1 and Qt0p2 are off the chart, and noted numerically (30 and 50 m, respectively). The higher spacing means that older surfaces are less vegetated.

Figure 11 (p. 359): "Rock" area fraction values for field sites on the upstream (upper panel) and downstream (lower panel) sets of surfaces. Values are minimums, in percent.

Figure 12 (p. 360): Upstream field site Qt4p1 (<11.3 ka). (A) sample square meter field photograph (frame is 1 meter on edge, with a thickness of 2.5 cm). Site name/age seen on clipboard (lower right) is obsolete. Gray card (upper right) is present for a potential color analysis that was not completed for this study. Clasts on clipboard and gray card are not representative, but were placed to secure items from heavy wind. (B) Site overview field photograph (sample frame is 1 meter on edge). (C) Ground-based spectra are from sand and vegetation samples. Site name and age are in the upper right corner. The final, thicker spectrum is the site average (arithmetic mean) for all spectra.

Figure 13 (p. 361): Downstream field site C0p1 (>94.5 ka). (A) sample square meter field photograph (frame is 1 meter on edge, with a thickness of 2.5 cm). Site name/age seen on clipboard (lower right) is obsolete. Gray card (upper right) is present for a potential color analysis that was not completed for this study. Clasts on clipboard and gray card are not representative, but were placed to secure items from heavy wind. (B) Site overview field photograph (sample frame is 1 meter on edge). (C) Ground-based spectra are from arbitrarily

chosen lithologic clast samples that were distributed across the sampling area. Site name and age are in the upper right corner. The final, thicker spectrum is the site average (arithmetic mean) for all spectra.

Figure 14 (p. 362): Airborne (blue) and ground-based (red) spectra plotted on the same axes to show the systematic difference in shape and position of the emissivity minimum for each of the data sets. The emissivity minimum is at 9.16 μm in airborne spectra, and 9.30 μm in ground-based spectra. Airborne spectra are from Figure 5: "Airborne 1" is Qt0 (>95 ka), from the second of the five (counting down from the top) upstream sets, and "Airborne 2" is C0 (>95 ka), from the first of the five downstream sets. "Ground 1" is the field site Qt0p2 (>95 ka, Figure S10) average spectrum, and "Ground 2" is the field site C0p1 (>95 ka, Figure 13) average. For the most direct comparison, we performed the exact same processing steps on the ground-based spectra as we did on the airborne spectra (ground-based spectra resampled to the airborne wavelengths, continuum removal performed, then smoothed). We also vertically scaled (stretched) all of the spectra shown here to the one that had the greatest emissivity range (which was Qt0p2).

Figure 15 (p. 363): Summary of correlation coefficients between each parameter and surface age. All values are R^2, except for those for desert varnish and desert pavement scores, which are Spearman's rank correlation coefficient (used for categorical variables, see Simpson, 2015). Exact numerical values are in Table 3.

TABLES

Table 1: Geomorphic surface names and ages[1]			
Surface names			
Upstream[2]	Downstream[2]	Age (ka)	Age (ka) used in text[3]
Qt4	-	<11.3	<11
Qt3	C3	12.7 ± 1.4	13
-	C2f	26.00 ± 7.55	26
Qt2	C2	74.40 ± 5.15	74
Qt1	C1	87.3 ± 7.2	87
Qt0	C0	>94.5	>95

[1]Names and ages are from Blisniuk and Sharp (2014), and Kate Scharer, personal communication. See Table 4 in Owen et al. (2014) for a detailed comparison of the nomenclature of geomorphic surfaces and their ages, and how they compare from area to area in the desert southwest.
[2]Upstream and downstream are relative to the Mission Creek strand of the southern San Andreas fault, see Figures 3 and 4.
[3]In most cases where the name of a surface is cited in the text, the age is also included for reference, with the age rounded to the nearest whole number, in ka units, and the uncertainty discarded, for brevity.

Table 2: Summary of ground-based spectra							
Field site	Age (ka) used in text[1]	GPS easting[2]	GPS northing[2]	Single clast spectra #'s	"Sand"[3] spectra #'s	Vegetation spectra #'s	Total usable spectra (not including site average)
Qt4p1[4]	<11	0566905	3743636	-	1-5	6-10	10
Qt4p2	<11	0566647	3743466	1-10	-	-	10
Qt3p1	13	0566949	3743509	1-10	-	-	10
Qt3p2	13	0566794	3743443	1-9	-	-	9
Qt2p1	74	0567024	3743301	1-10	-	-	10
Qt2p2	74	0567019	3743375	2-9	-	1	9
Qt1p1	87	0567179	3743334	1-10	-	-	10
Qt1p2	87	0567122	3743351	1-9	-	-	9
Qt0p1	>95	0567424	3743166	1-10	-	-	10
Qt0p2	>95	0567455	3742949	1-10	-	-	10
C3p1	13	0564570	3741612	2-7	1,8,9	-	9
C3p2	13	0565467	3742974	1-9	-	-	9
C3sand	13	0564681	3741973	-	1-10	-	10
C3veg	13	0565037	3742861	-	-	1-4	4
C2fp1	26	0565089	3743300	1-10	-	-	10
C2fp2	26	0564947	3743239	1-8	-	-	8
C2fp3	26	0564803	3743250	1-10	-	-	10
C2fp4	26	0564885	3743129	1-3	4-9	-	9
C2p1	74	0564630	3742626	1-10	-	-	10
C2p2	74	0564533	3742720	1-9	-	-	9
C2p3	74	0564731	3743148	1-9	-	-	9
C2p4	74	0564482	3743238	1-10	-	-	10
C1p1	87	0564226	3743652	1-9	-	-	9
C1p2	87	0564299	3743682	1-10	-	-	10
C0p1[5]	>95	0564320	3743216	1-10	-	-	10
C0p2	>95	0564223	3743046	1-10	-	-	10
C0p3	>95	0564039	3743231	1-10	-	-	10

[1]See Table 1.
[2]All GPS locations are given in UTM coordinates, zone 11S.
[3]"Sand" refers to spectra measured from samples of finer, unconsolidated lithologic detrital material, and does not imply a technical definition of grain size.
[4]Figure 12.
[5]Figure 13.

Table 3: Summary of correlation coefficients[1] between each parameter and surface age	
Parameter (units)	Correlation coefficient
Mean of dominant (>50%) clast size ranges (cm)	0.10
Varnish score (dimensionless)[2]	0.90
Pavement score (dimensionless)[2]	0.90
Vegetation spacing (m)	0.34
“Rock” area fraction (percent)	0.00
Airborne spectra band depth at 9.16 μm (emissivity, dimensionless)	0.59
Ground-based spectra band depth at 9.30 μm (emissivity, dimensionless)	0.04

[1]All values are R^2, unless otherwise specified.
[2]Spearman’s rank correlation coefficient.

FIGURES

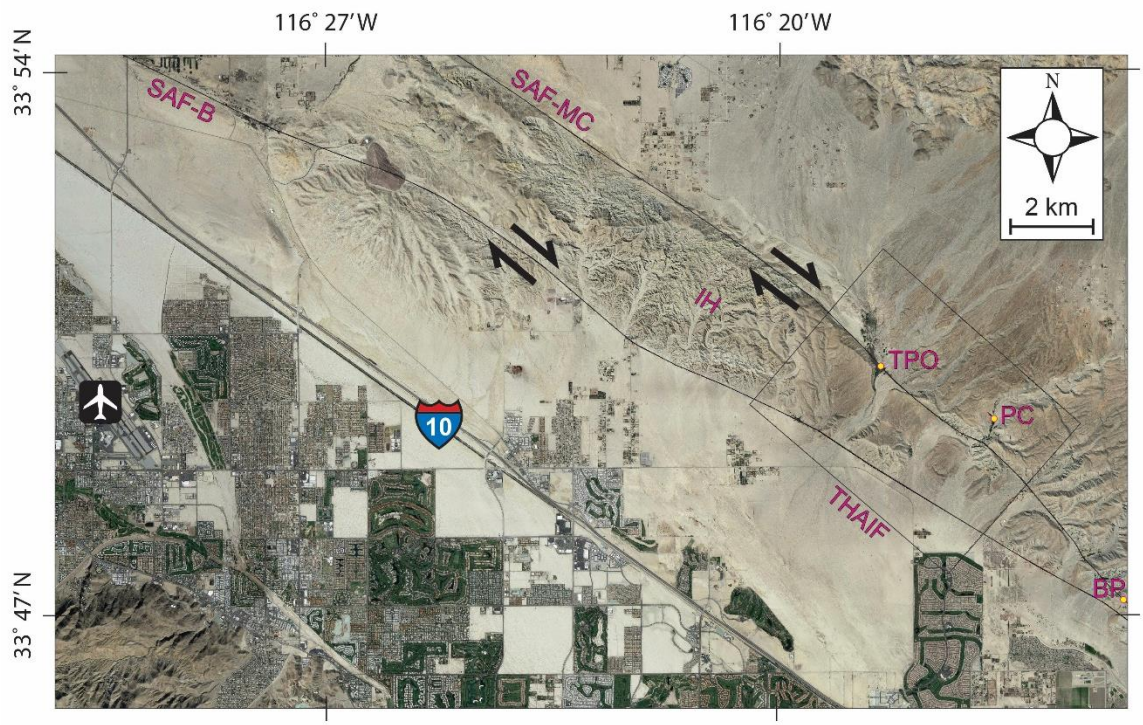

Figure 1

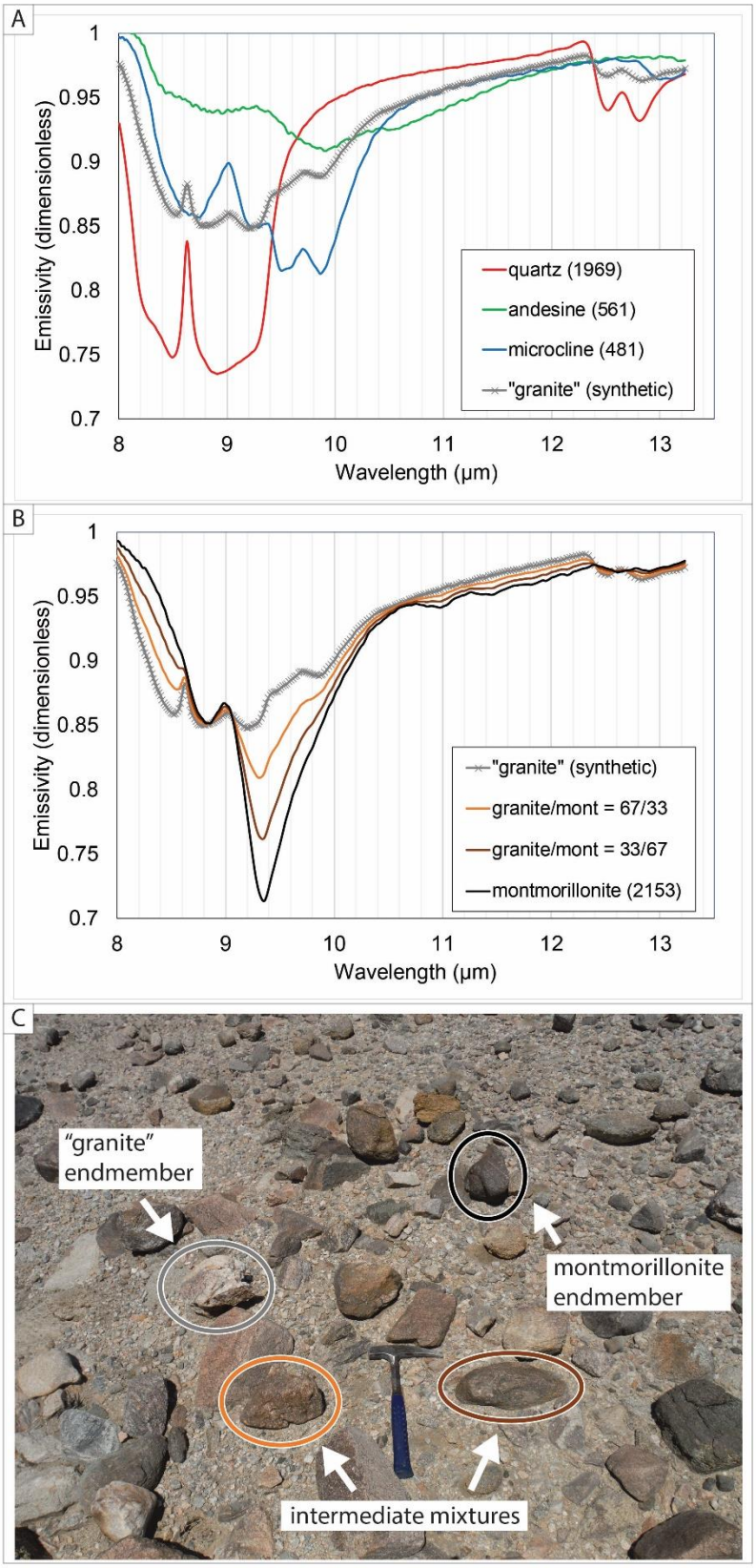
A
Emissivity (dimensionless)
1
0.95
0.9
0.85
0.8
0.75
0.7
8
9
10
11
12
13
Wavelength (μm)
quartz (1969)
andesine (561)
microcline (481)
"granite" (synthetic)
B
Emissivity (dimensionless)
Wavelength (μm)
"granite" (synthetic)
granite/mont = 67/33
granite/mont = 33/67
montmorillonite (2153)
C
"granite" endmember
montmorillonite endmember
intermediate mixtures

Figure 2

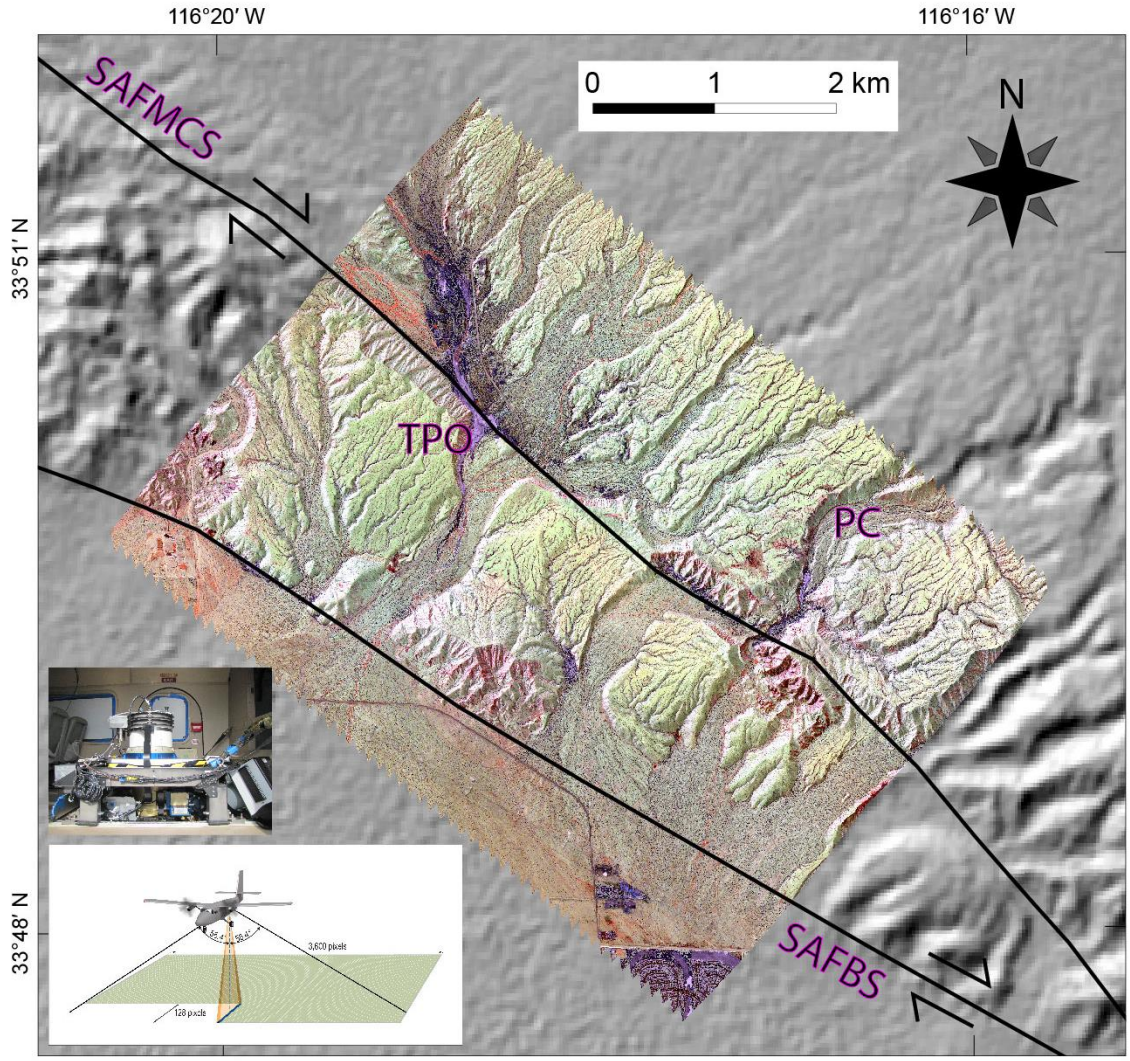
116°20′ W
116°16′ W
33°51′ N
33°48′ N
SAFMCS
TPO
PC
SAFBS
0
1
2 km
N
3,600 pixels
128 pixels

Figure 3

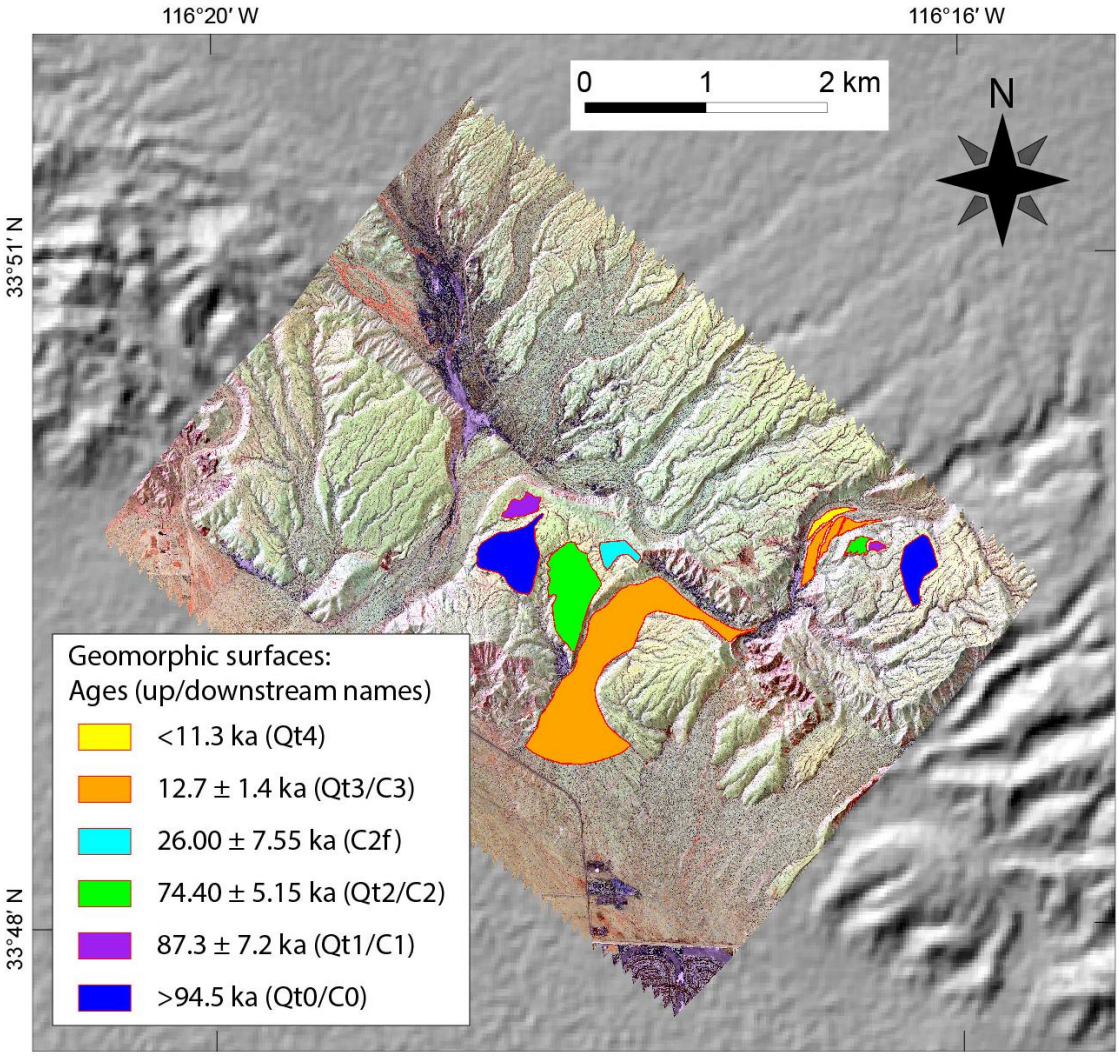
116°20′ W
116°16′ W
33°51′ N
33°48′ N
0
1
2 km
N
Geomorphic surfaces:
Ages (up/downstream names)
<11.3 ka (Qt4)
12.7 ± 1.4 ka (Qt3/C3)
26.00 ± 7.55 ka (C2f)
74.40 ± 5.15 ka (Qt2/C2)
87.3 ± 7.2 ka (Qt1/C1)
>94.5 ka (Qt0/C0)

Figure 4

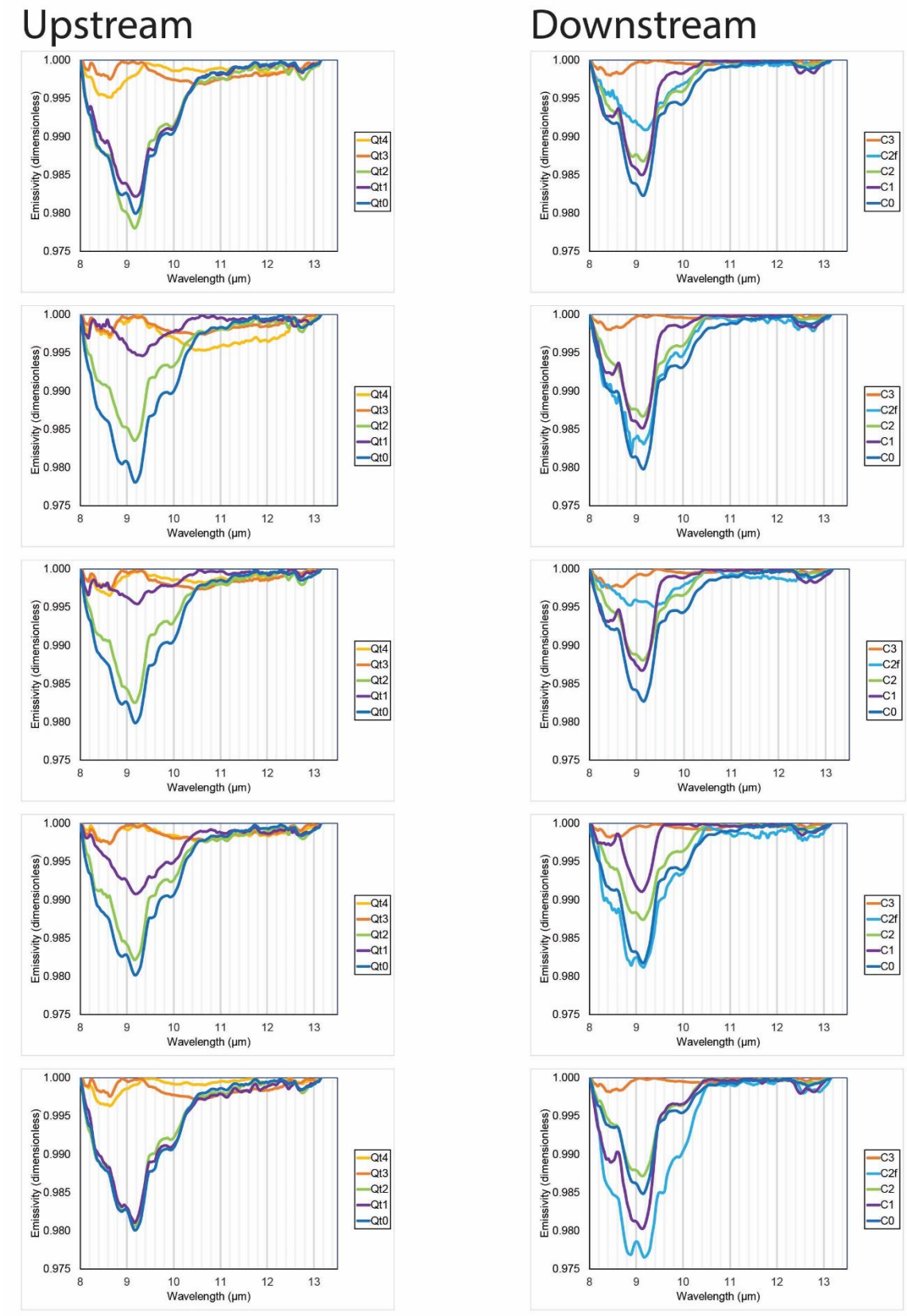
Upstream
Downstream
Emissivity (dimensionless)
Wavelength (μm)
1.000
0.995
0.990
0.985
0.980
0.975
8
9
10
11
12
13
Qt4
Qt3
Qt2
Qt1
Qt0
C3
C2f
C2
C1
C0

Figure 5

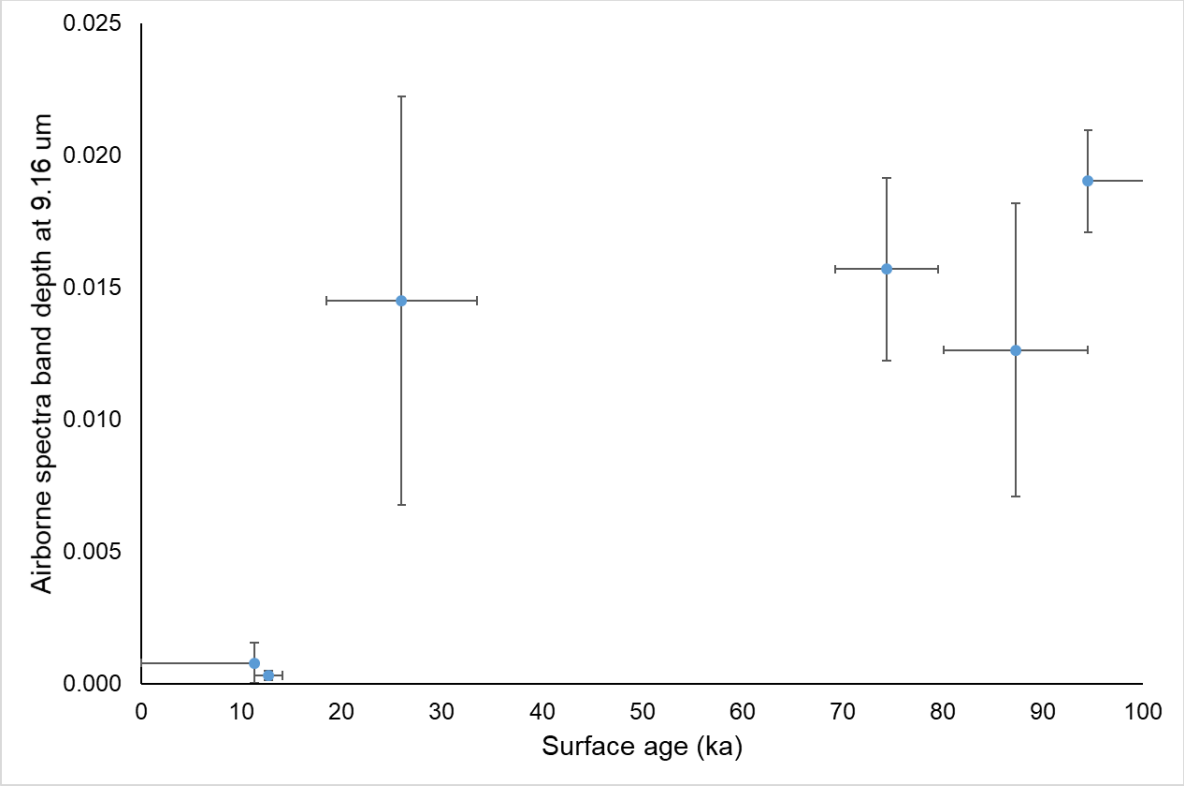
0.025
0.020
0.015
0.010
0.005
0.000
Airborne spectra band depth at 9.16 um
0
10
20
30
40
50
60
70
80
90
100
Surface age (ka)

Figure 6

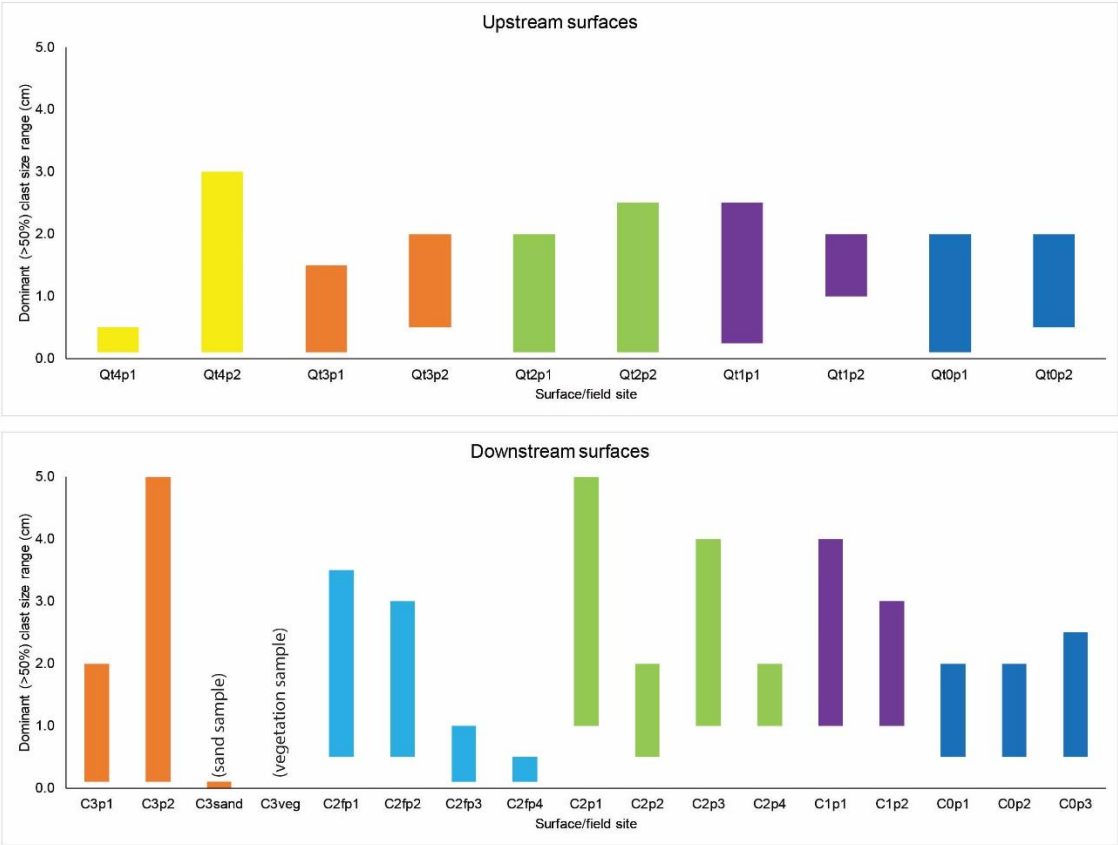
Upstream surfaces
Dominant (>50%) clast size range (cm)
5.0
4.0
3.0
2.0
1.0
0.0
Qt4p1
Qt4p2
Qt3p1
Qt3p2
Qt2p1
Qt2p2
Qt1p1
Qt1p2
Qt0p1
Qt0p2
Surface/field site
Downstream surfaces
Dominant (>50%) clast size range (cm)
5.0
4.0
3.0
2.0
1.0
0.0
C3p1
C3p2
C3sand
(sand sample)
C3veg
(vegetation sample)
C2fp1
C2fp2
C2fp3
C2fp4
C2p1
C2p2
C2p3
C2p4
C1p1
C1p2
C0p1
C0p2
C0p3
Surface/field site

Figure 7

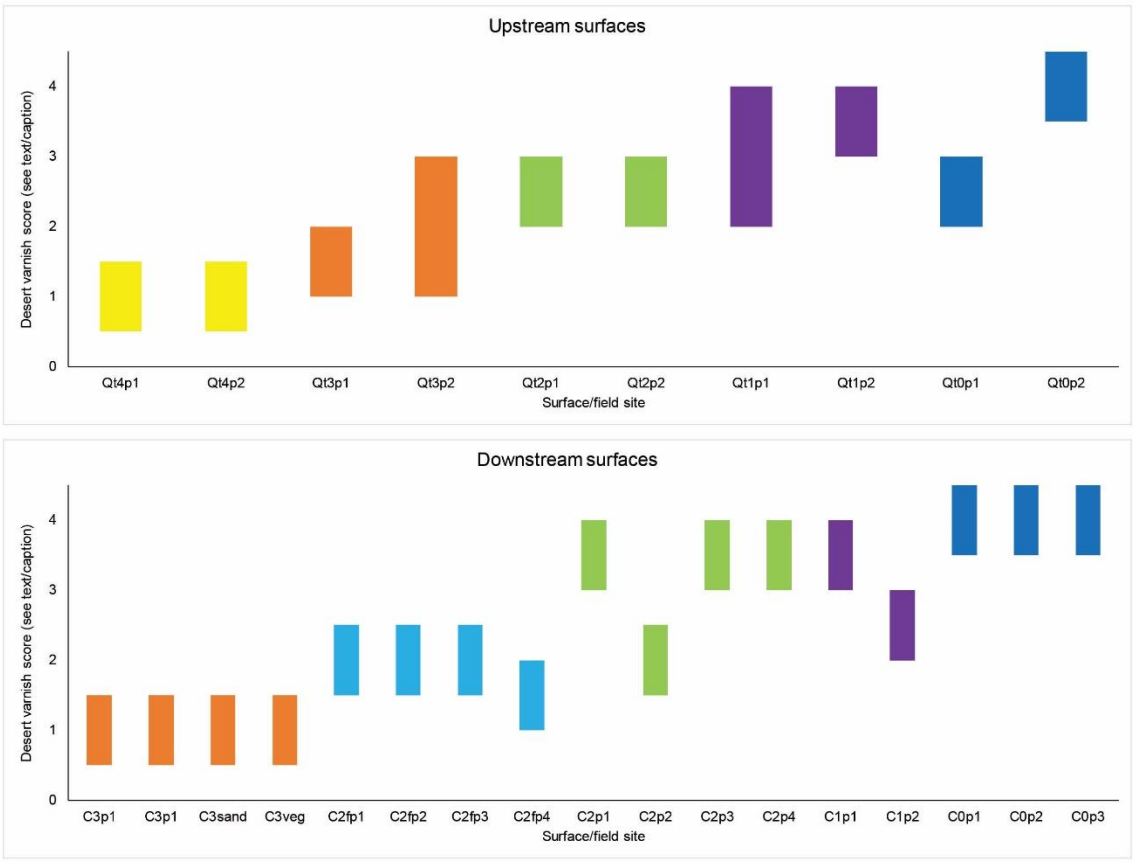
Upstream surfaces
Desert varnish score (see text/caption)
0
1
2
3
4
Qt4p1
Qt4p2
Qt3p1
Qt3p2
Qt2p1
Qt2p2
Qt1p1
Qt1p2
Qt0p1
Qt0p2
Surface/field site
Downstream surfaces
Desert varnish score (see text/caption)
0
1
2
3
4
C3p1
C3p1
C3sand
C3veg
C2fp1
C2fp2
C2fp3
C2fp4
C2p1
C2p2
C2p3
C2p4
C1p1
C1p2
C0p1
C0p2
C0p3
Surface/field site

Figure 8

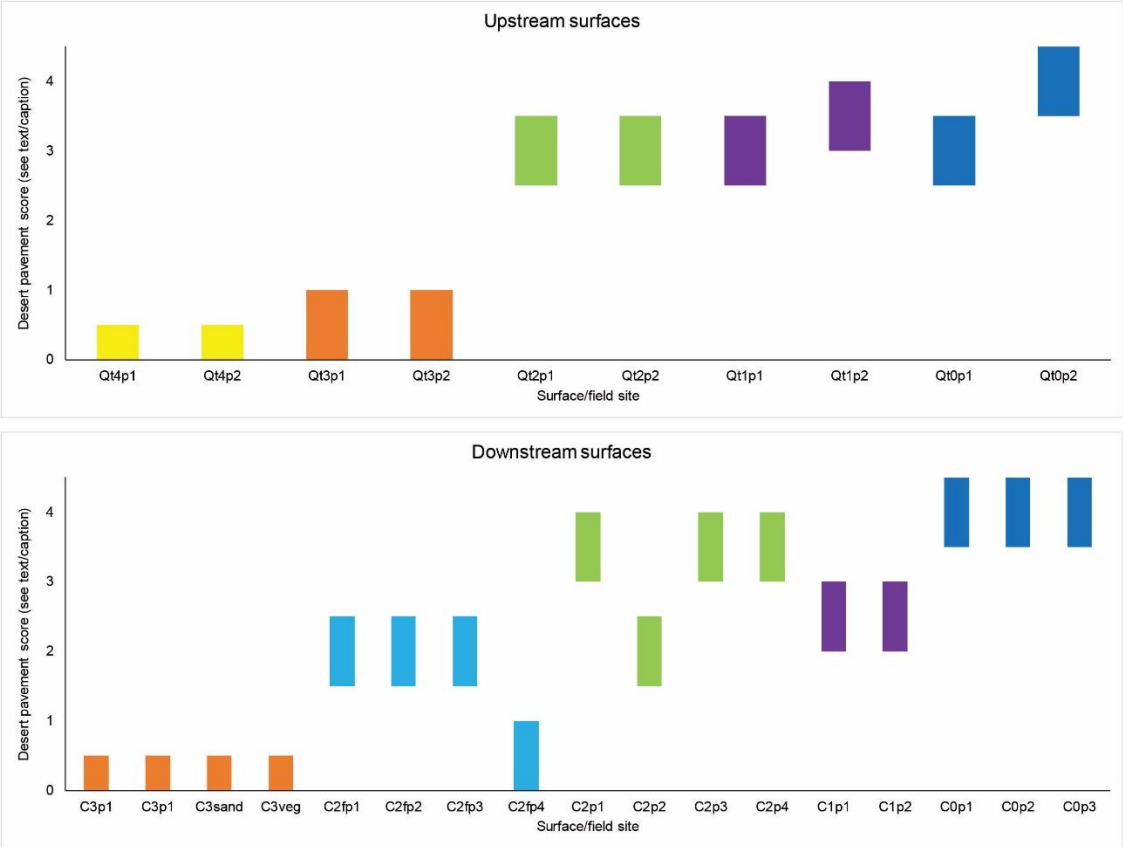
Upstream surfaces
Desert pavement score (see text/caption)
0
1
2
3
4
Qt4p1
Qt4p2
Qt3p1
Qt3p2
Qt2p1
Qt2p2
Qt1p1
Qt1p2
Qt0p1
Qt0p2
Surface/field site
Downstream surfaces
Desert pavement score (see text/caption)
0
1
2
3
4
C3p1
C3p1
C3sand
C3veg
C2fp1
C2fp2
C2fp3
C2fp4
C2p1
C2p2
C2p3
C2p4
C1p1
C1p2
C0p1
C0p2
C0p3
Surface/field site

Figure 9

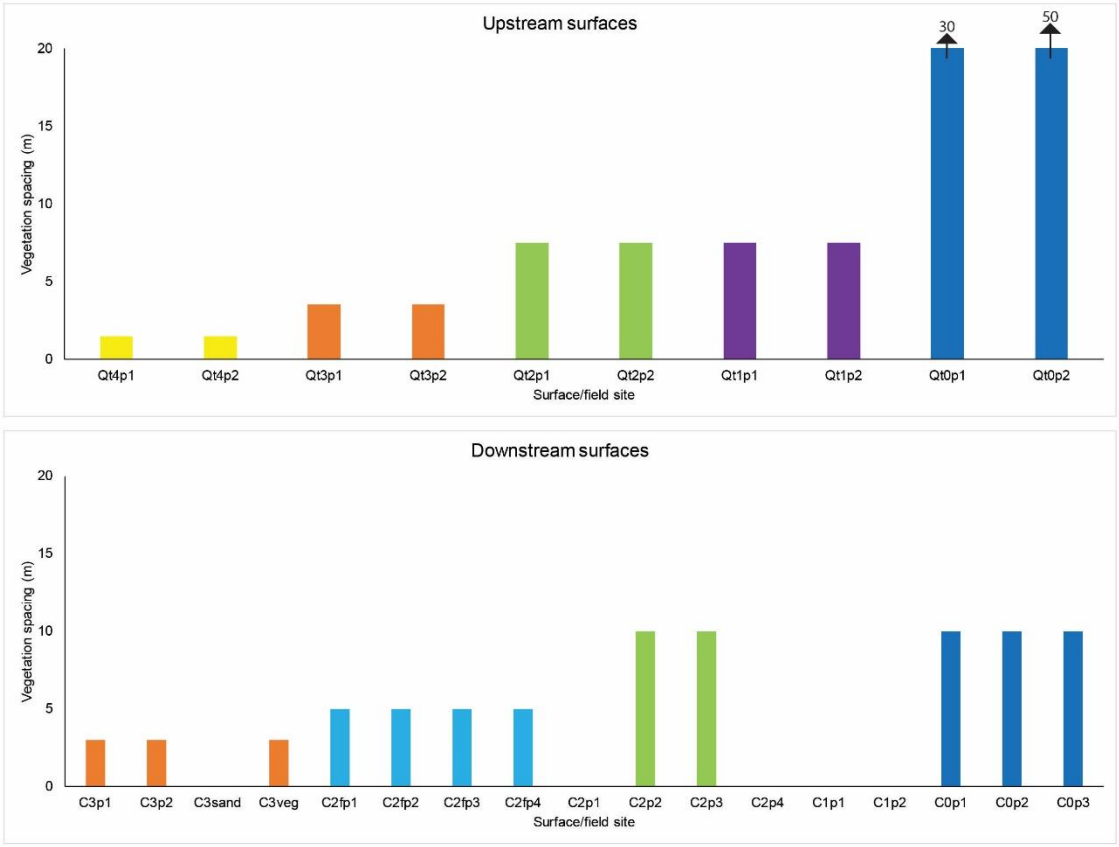
Upstream surfaces
Vegetation spacing (m)
20
15
10
5
0
30
50
Qt4p1
Qt4p2
Qt3p1
Qt3p2
Qt2p1
Qt2p2
Qt1p1
Qt1p2
Qt0p1
Qt0p2
Surface/field site
Downstream surfaces
Vegetation spacing (m)
20
15
10
5
0
C3p1
C3p2
C3sand
C3veg
C2fp1
C2fp2
C2fp3
C2fp4
C2p1
C2p2
C2p3
C2p4
C1p1
C1p2
C0p1
C0p2
C0p3
Surface/field site

Figure 10

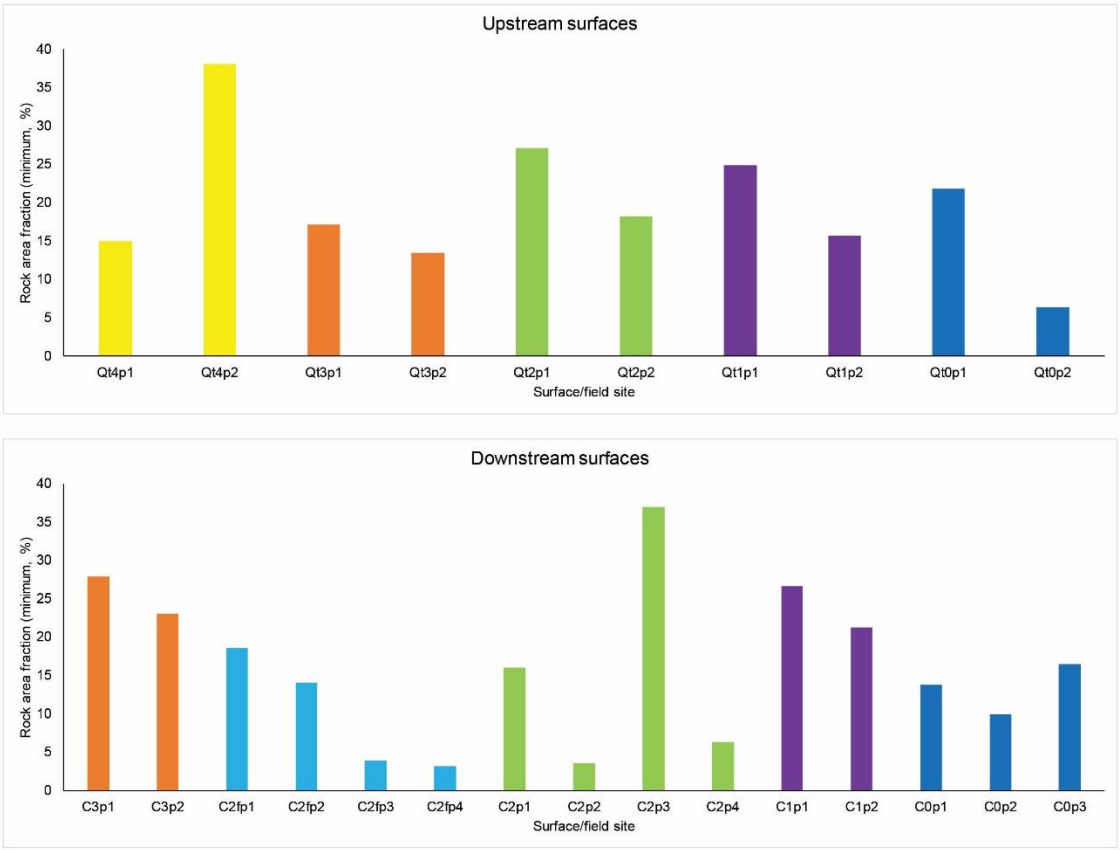
Upstream surfaces
Rock area fraction (minimum, %)
0
5
10
15
20
25
30
35
40
Qt4p1
Qt4p2
Qt3p1
Qt3p2
Qt2p1
Qt2p2
Qt1p1
Qt1p2
Qt0p1
Qt0p2
Surface/field site
Downstream surfaces
Rock area fraction (minimum, %)
0
5
10
15
20
25
30
35
40
C3p1
C3p2
C2fp1
C2fp2
C2fp3
C2fp4
C2p1
C2p2
C2p3
C2p4
C1p1
C1p2
C0p1
C0p2
C0p3
Surface/field site

Figure 11

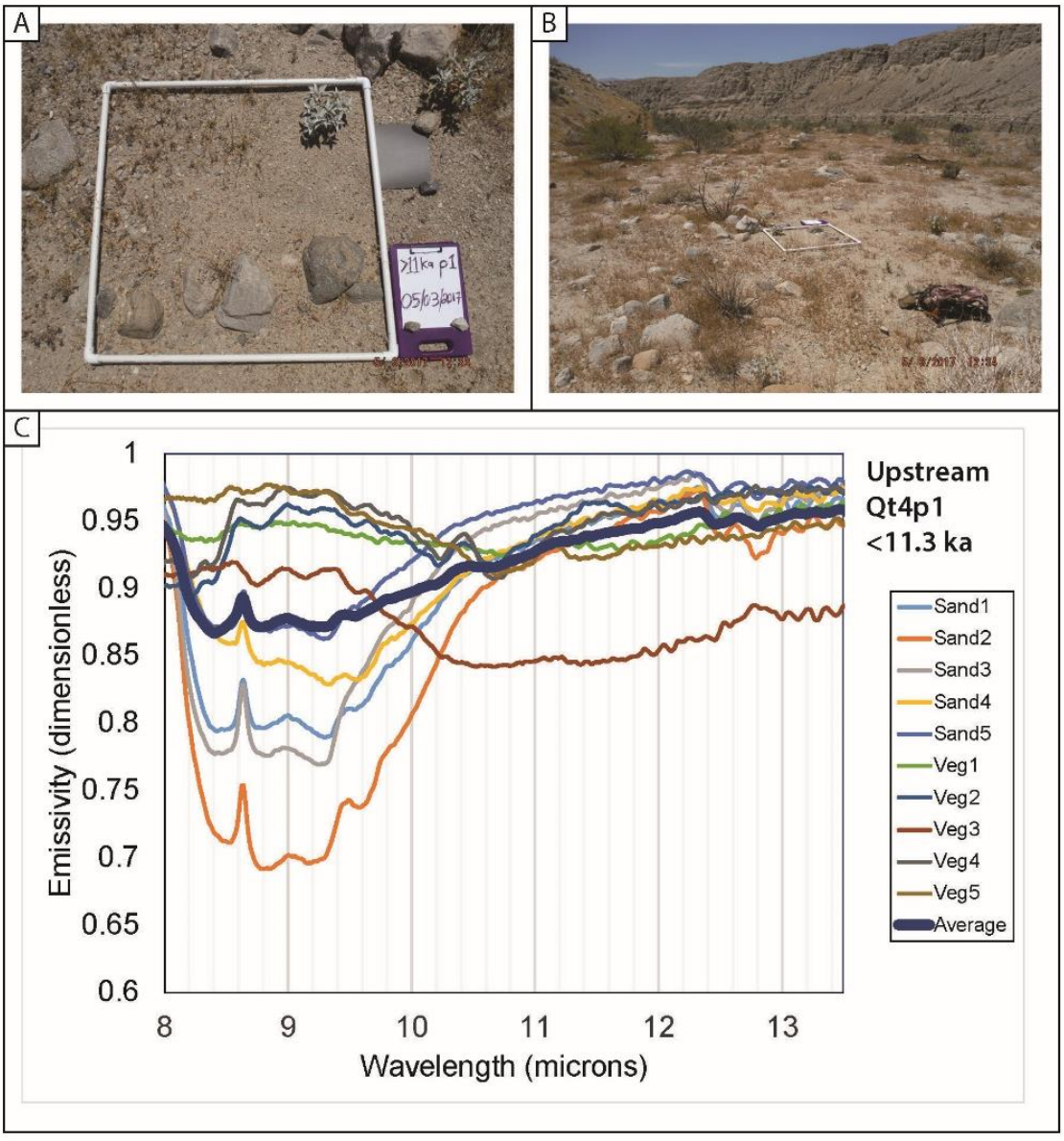
A
B
C
Emissivity (dimensionless)
1
0.95
0.9
0.85
0.8
0.75
0.7
0.65
0.6
8
9
10
11
12
13
Wavelength (microns)
Upstream
Qt4p1
<11.3 ka
Sand1
Sand2
Sand3
Sand4
Sand5
Veg1
Veg2
Veg3
Veg4
Veg5
Average

Figure 12

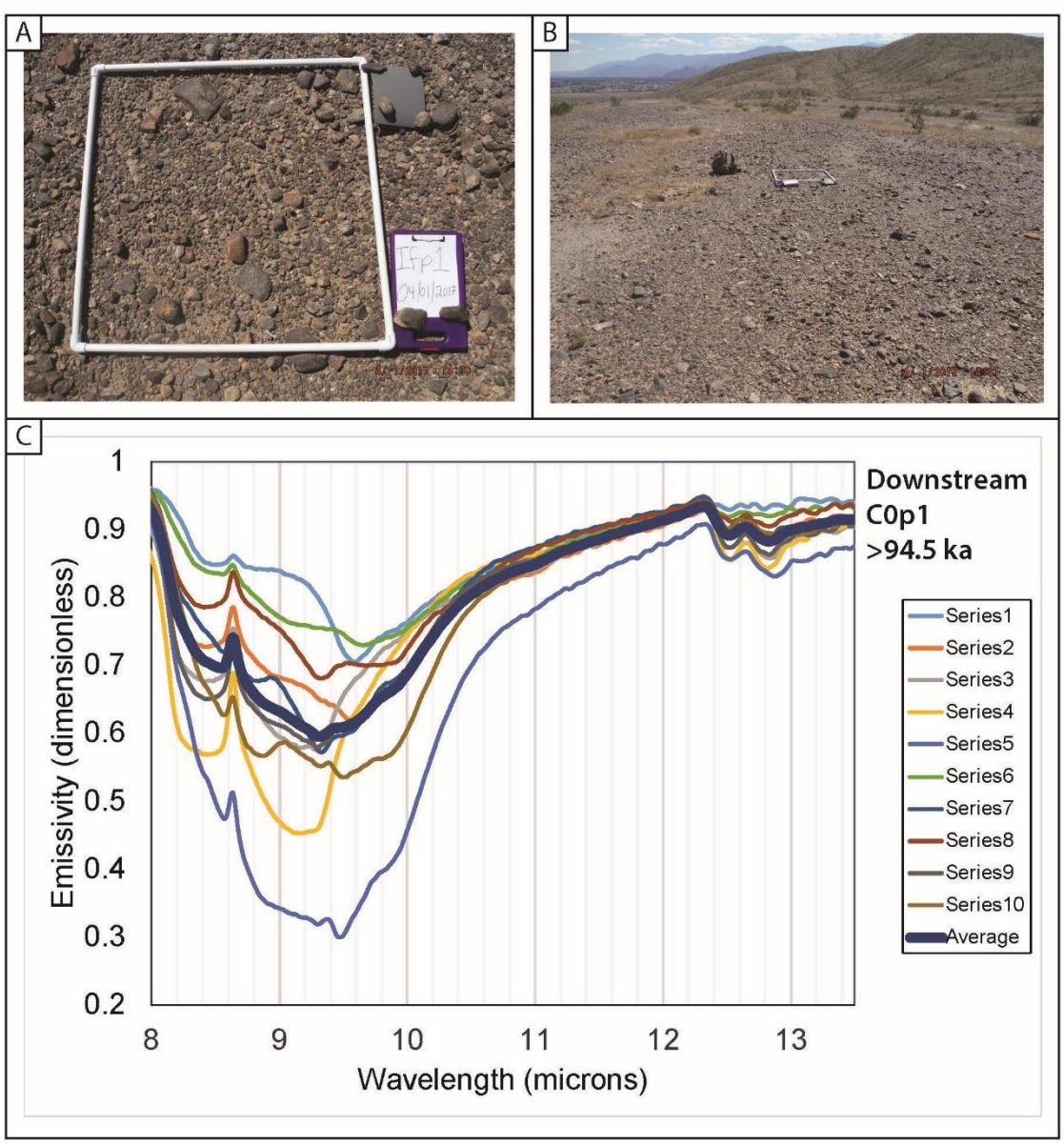
A
B
C
Downstream
C0p1
>94.5 ka
Emissivity (dimensionless)
Wavelength (microns)
1
0.9
0.8
0.7
0.6
0.5
0.4
0.3
0.2
8
9
10
11
12
13
Series1
Series2
Series3
Series4
Series5
Series6
Series7
Series8
Series9
Series10
Average

Figure 13

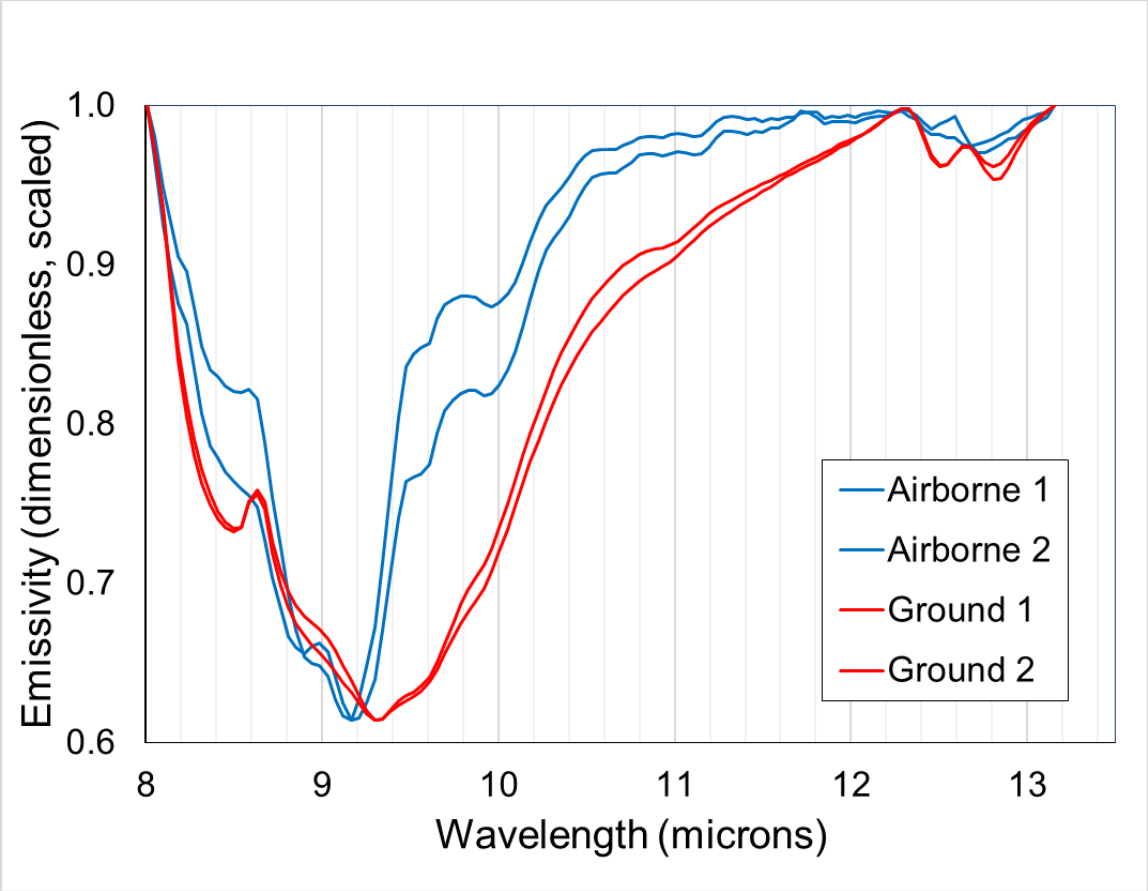
1.0
0.9
0.8
0.7
0.6
Emissivity (dimensionless, scaled)
8
9
10
11
12
13
Wavelength (microns)
Airborne 1
Airborne 2
Ground 1
Ground 2

Figure 14

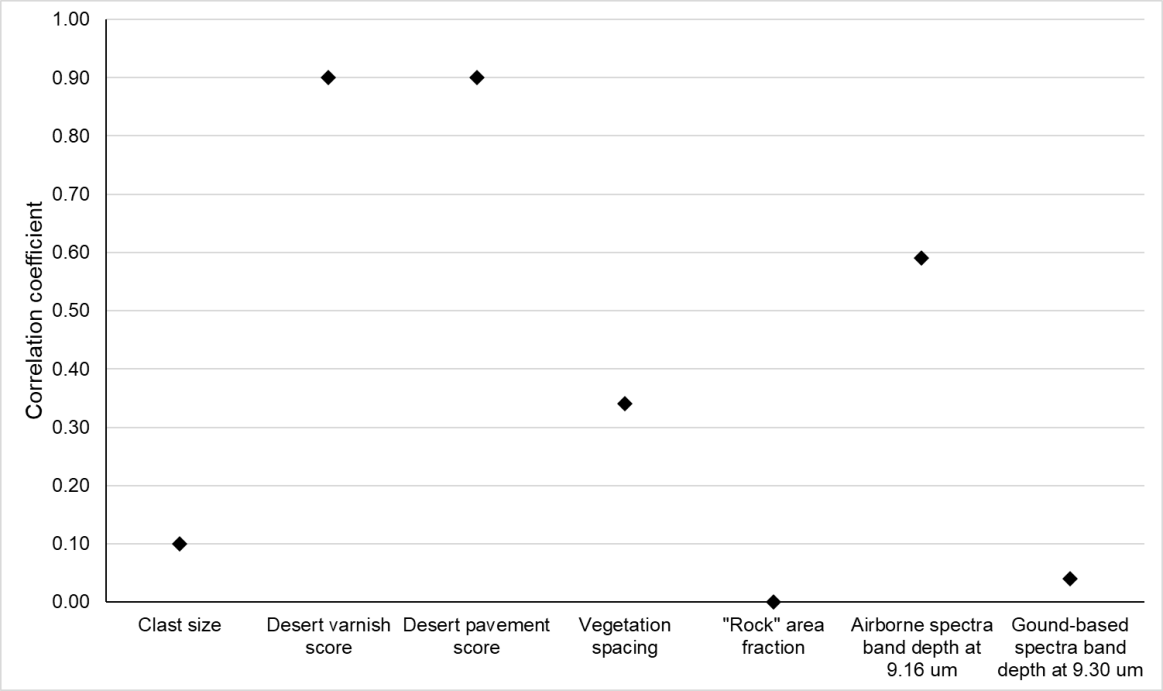
1.00
0.90
0.80
0.70
0.60
0.50
0.40
0.30
0.20
0.10
0.00
Correlation coefficient
Clast size
Desert varnish score
Desert pavement score
Vegetation spacing
"Rock" area fraction
Airborne spectra band depth at 9.16 um
Gound-based spectra band depth at 9.30 um

Figure 15

SUPPLEMENTAL ITEMS

Figure Captions

Figures S1-S27 (pp. 365-391): Field photographs and ground-based spectra for all 27 field sites (see Tables 1 and 2 in main text, site locations included in Table 2). (S1)-(S10), upstream field sites, in chronological order from youngest to oldest. (S11)-(S27), downstream field sites ordered from youngest to oldest. For each supplementary figure: (A) sample square meter field photograph (frame is 1 meter on edge, with a thickness of 2.5 cm). Site name/age seen on clipboard (lower right) is obsolete. Gray card (upper right) is present for a potential color analysis that was not completed for this study. Clasts on clipboard and gray card are not representative, but were placed to secure items from heavy wind. (B) Site overview field photograph (sample frame is 1 meter on edge). (C) Ground-based spectra. The accurate site name and age are in the upper right corner. The final, thicker spectrum is the site average (arithmetic mean) for all spectra.

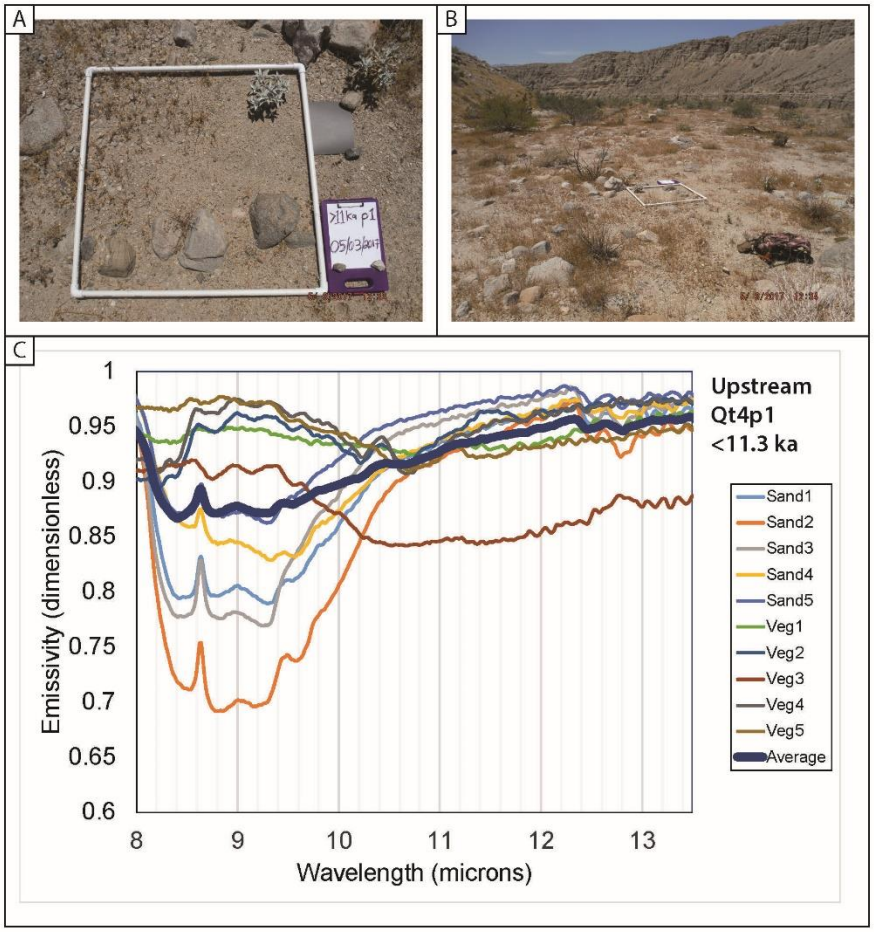
A
B
C
Emissivity (dimensionless)
1
0.95
0.9
0.85
0.8
0.75
0.7
0.65
0.6
8
9
10
11
12
13
Wavelength (microns)
Upstream
Qt4p1
<11.3 ka
Sand1
Sand2
Sand3
Sand4
Sand5
Veg1
Veg2
Veg3
Veg4
Veg5
Average

Figure S1

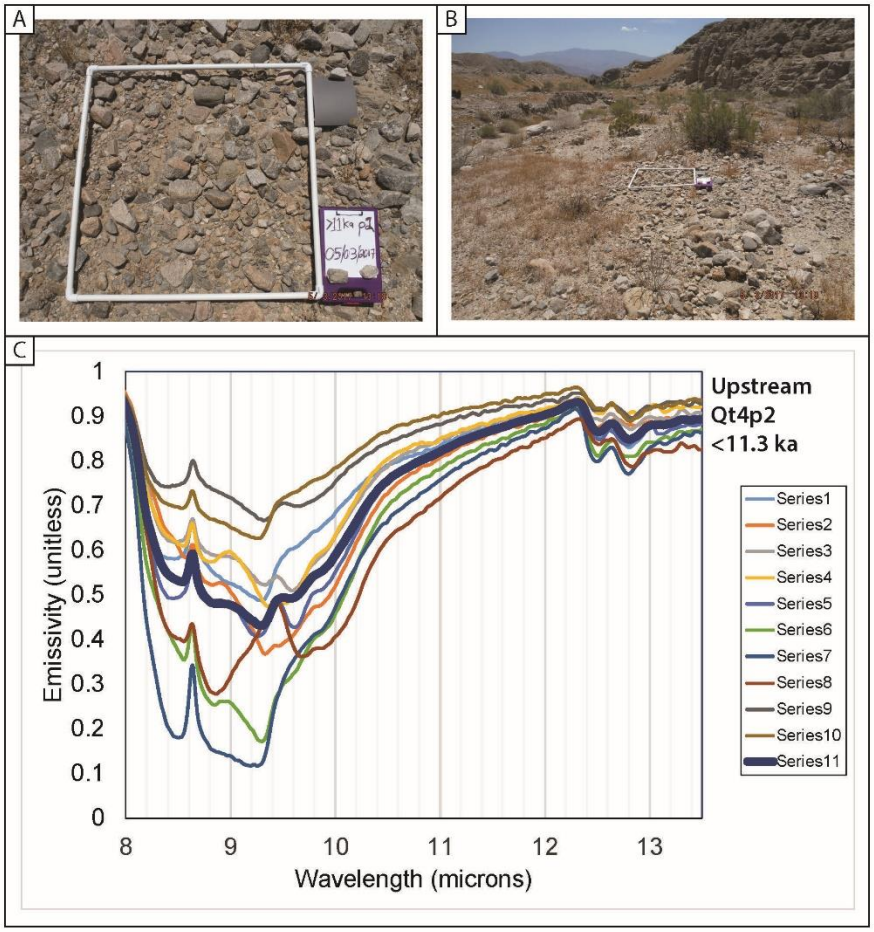
A
B
C
Upstream
Qt4p2
<11.3 ka
Emissivity (unitless)
Wavelength (microns)
Series1
Series2
Series3
Series4
Series5
Series6
Series7
Series8
Series9
Series10
Series11

Figure S2

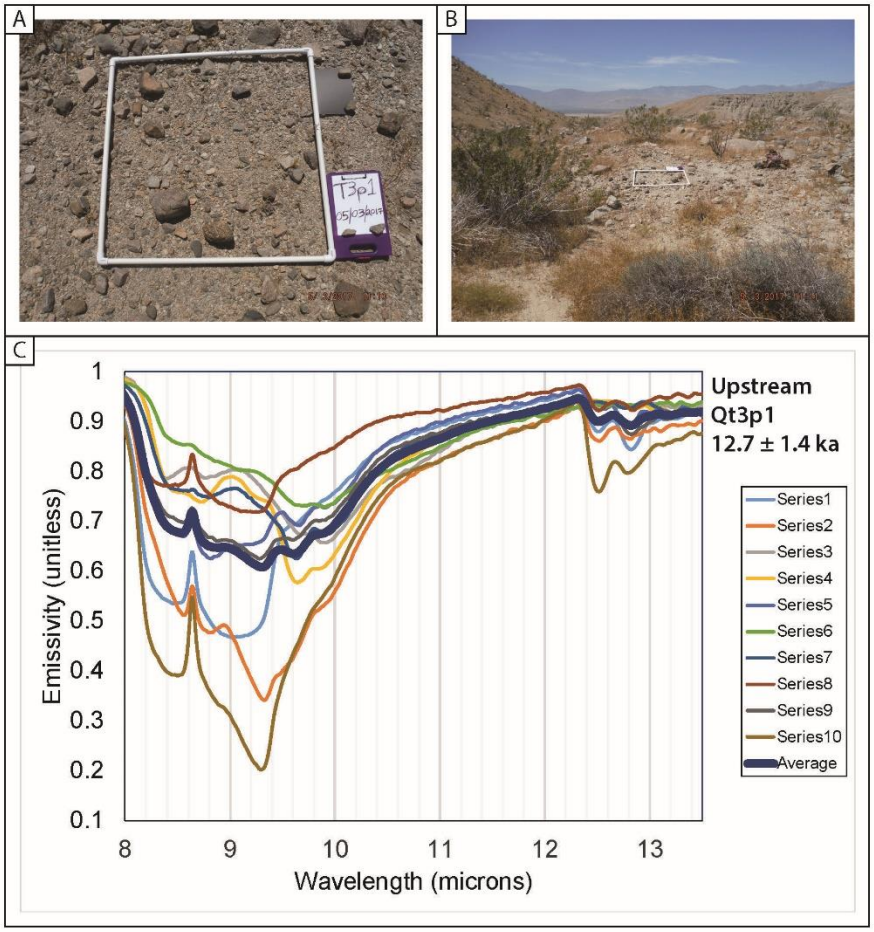
A
B
C
Upstream
Qt3p1
12.7 ± 1.4 ka
Emissivity (unitless)
Wavelength (microns)
1
0.9
0.8
0.7
0.6
0.5
0.4
0.3
0.2
0.1
8
9
10
11
12
13
Series1
Series2
Series3
Series4
Series5
Series6
Series7
Series8
Series9
Series10
Average

Figure S3

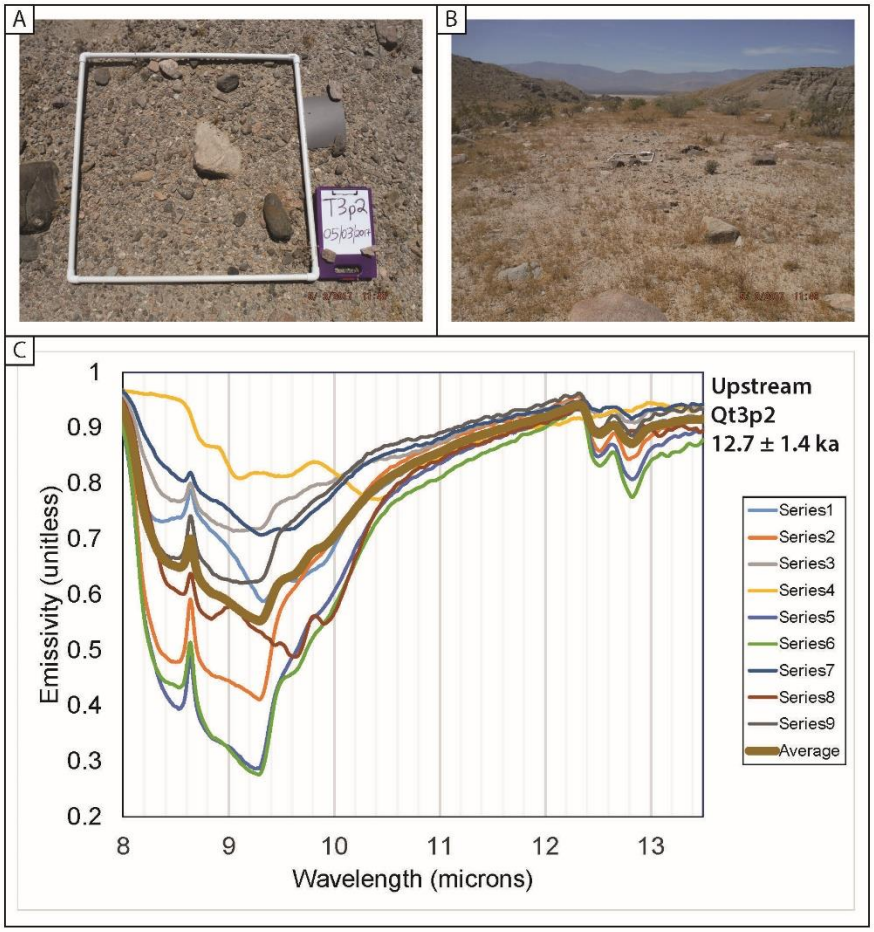
A
B
C
T3p2
05/03/2011
Upstream
Qt3p2
12.7 ± 1.4 ka
Emissivity (unitless)
1
0.9
0.8
0.7
0.6
0.5
0.4
0.3
0.2
8
9
10
11
12
13
Wavelength (microns)
Series1
Series2
Series3
Series4
Series5
Series6
Series7
Series8
Series9
Average

Figure S4

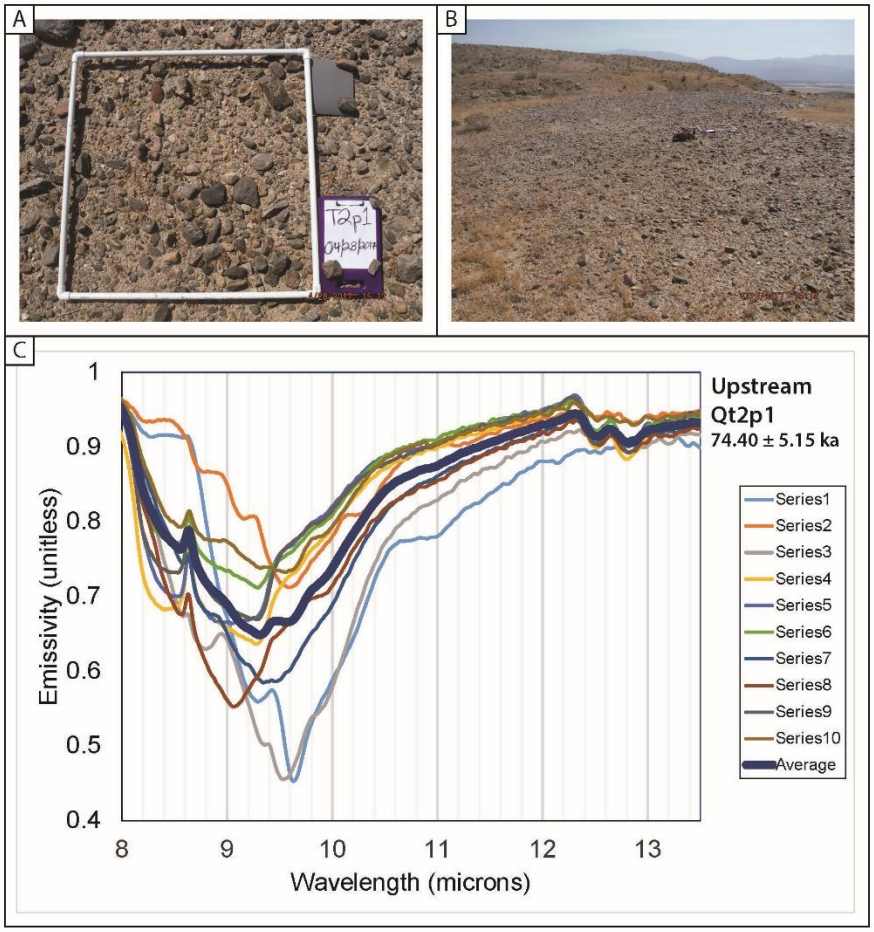
A
B
C
Upstream
Qt2p1
74.40 ± 5.15 ka
Emissivity (unitless)
Wavelength (microns)
1
0.9
0.8
0.7
0.6
0.5
0.4
8
9
10
11
12
13
Series1
Series2
Series3
Series4
Series5
Series6
Series7
Series8
Series9
Series10
Average

Figure S5

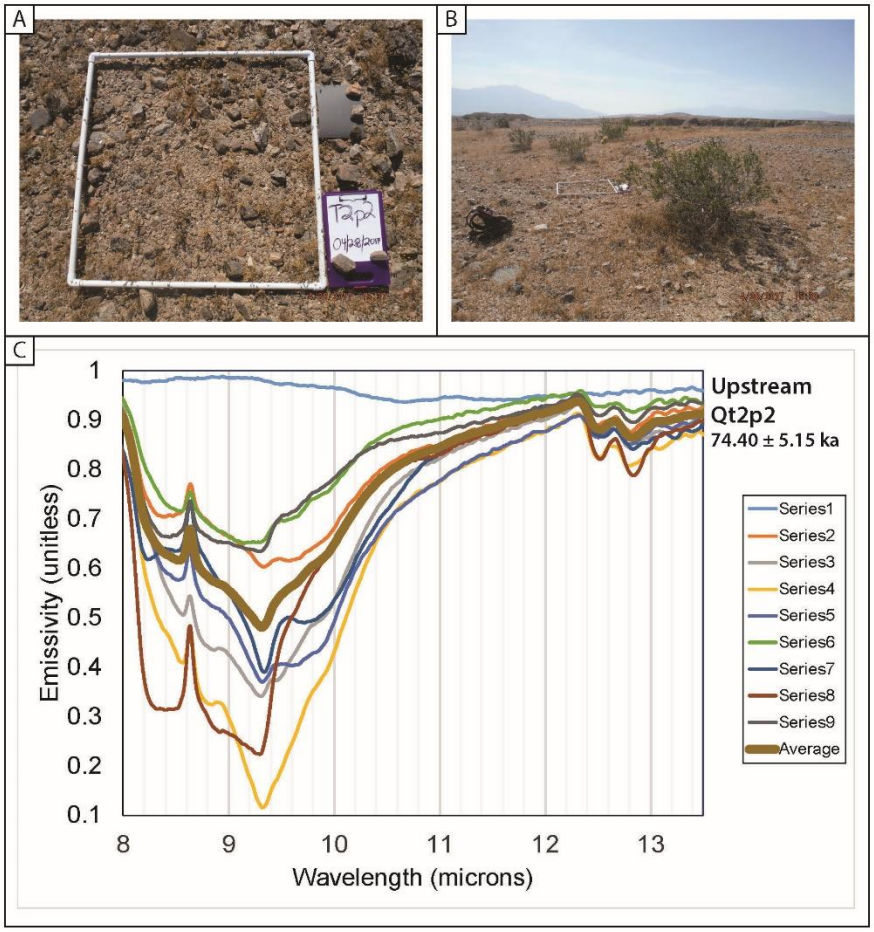
A
B
C
Upstream
Qt2p2
74.40 ± 5.15 ka
Emissivity (unitless)
Wavelength (microns)
Series1
Series2
Series3
Series4
Series5
Series6
Series7
Series8
Series9
Average

Figure S6

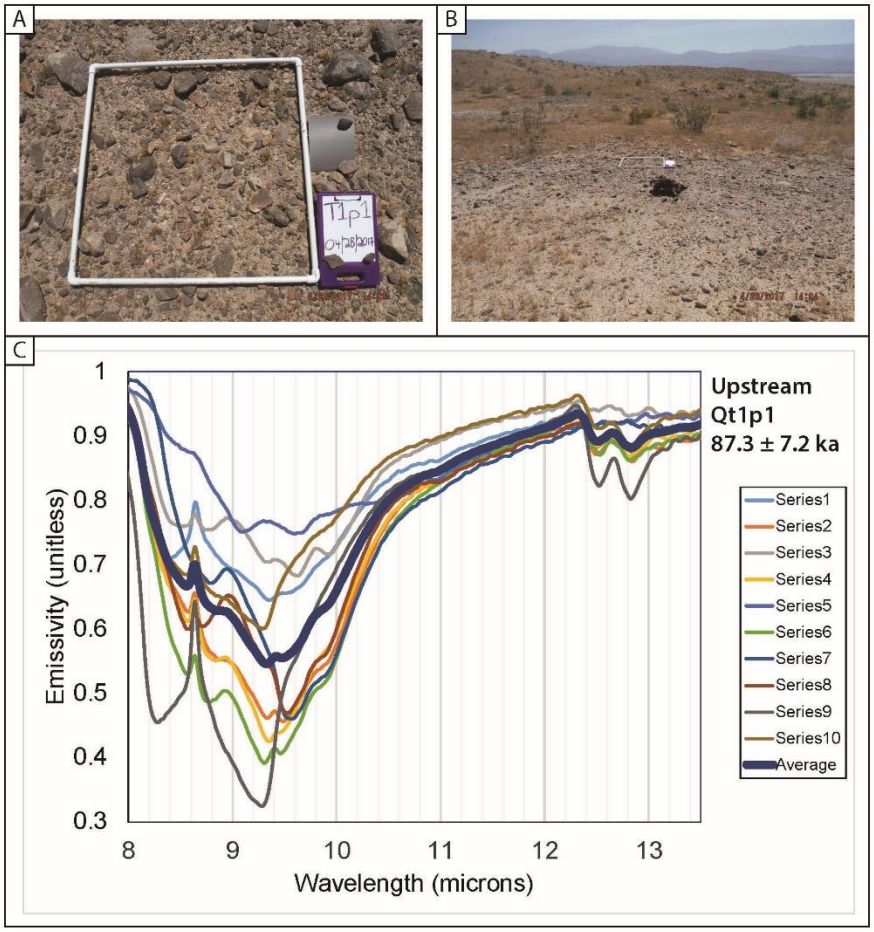
A
B
C
T1p1
Upstream
Qt1p1
87.3 ± 7.2 ka
Emissivity (unitless)
Wavelength (microns)
1
0.9
0.8
0.7
0.6
0.5
0.4
0.3
8
9
10
11
12
13
Series1
Series2
Series3
Series4
Series5
Series6
Series7
Series8
Series9
Series10
Average

Figure S7

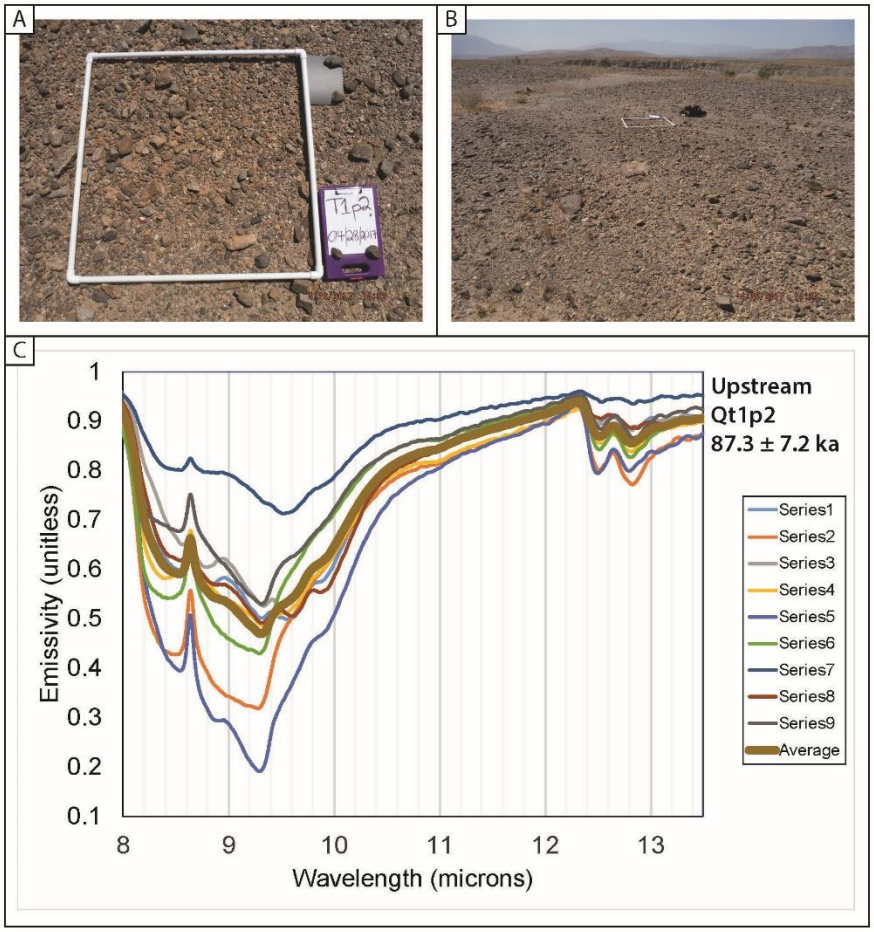
A
B
C
T1p2
Upstream
Qt1p2
87.3 ± 7.2 ka
Emissivity (unitless)
Wavelength (microns)
1
0.9
0.8
0.7
0.6
0.5
0.4
0.3
0.2
0.1
8
9
10
11
12
13
Series1
Series2
Series3
Series4
Series5
Series6
Series7
Series8
Series9
Average

Figure S8

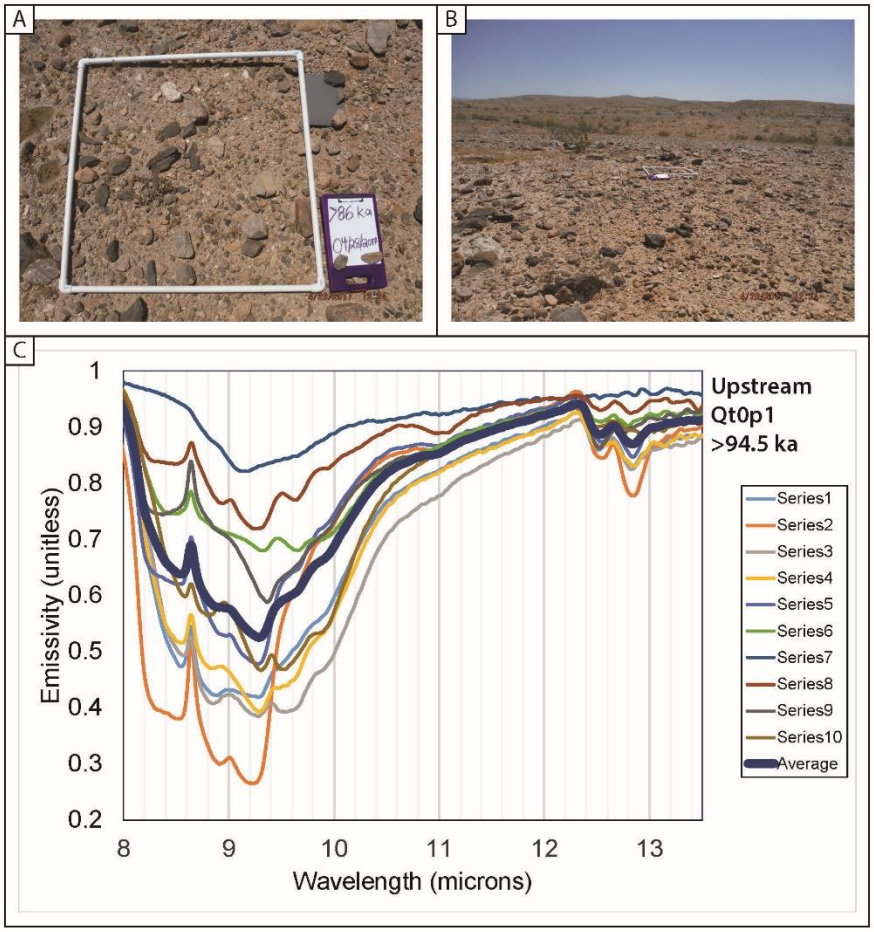
A
B
C
>86 ka
Upstream
Qt0p1
>94.5 ka
Emissivity (unitless)
Wavelength (microns)
1
0.9
0.8
0.7
0.6
0.5
0.4
0.3
0.2
8
9
10
11
12
13
Series1
Series2
Series3
Series4
Series5
Series6
Series7
Series8
Series9
Series10
Average

Figure S9

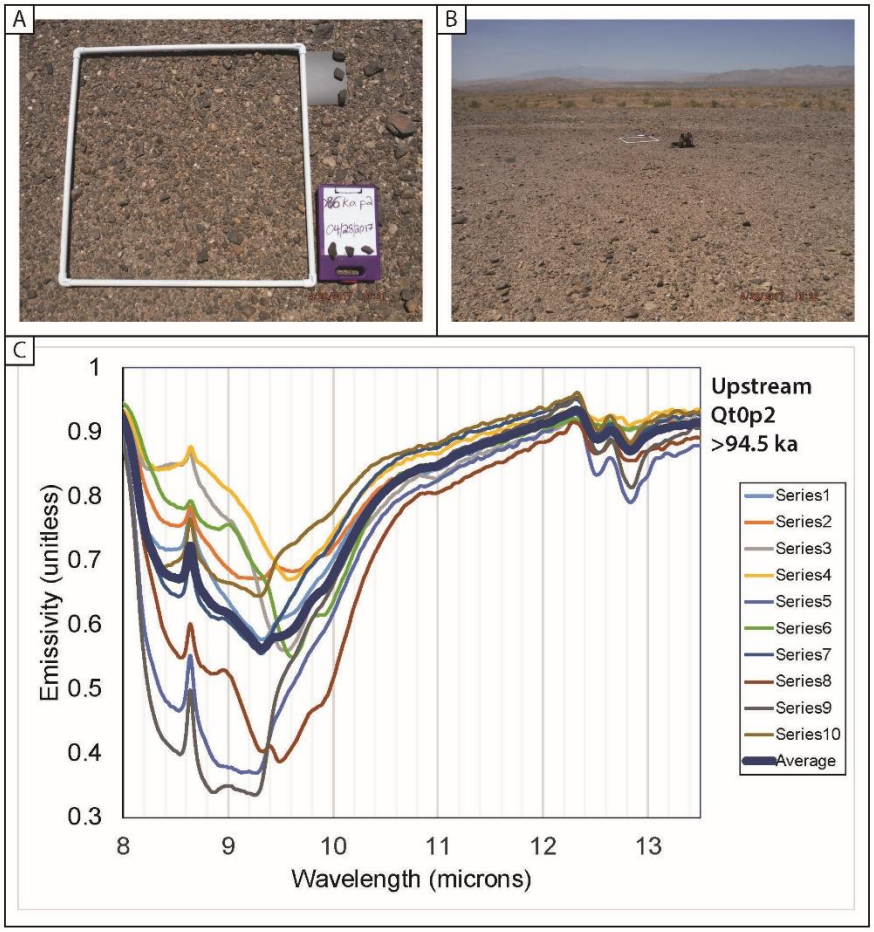
A
B
C
Upstream
Qt0p2
>94.5 ka
Emissivity (unitless)
Wavelength (microns)
1
0.9
0.8
0.7
0.6
0.5
0.4
0.3
8
9
10
11
12
13
Series1
Series2
Series3
Series4
Series5
Series6
Series7
Series8
Series9
Series10
Average

Figure S10

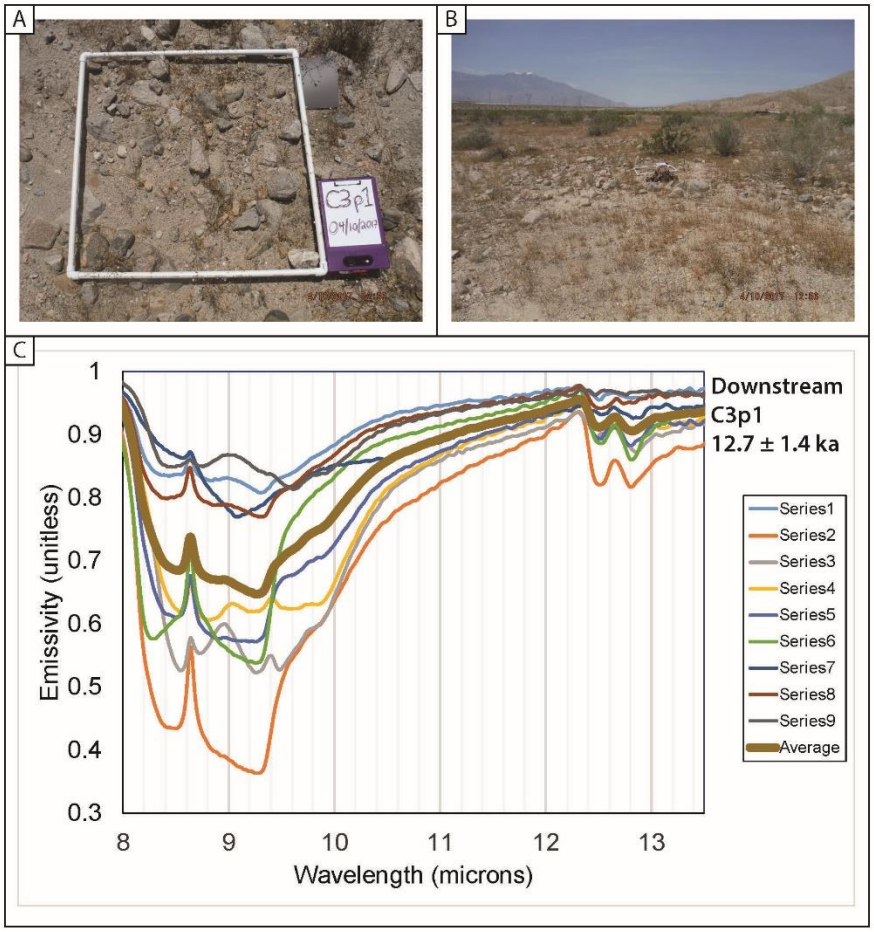
A
B
C3p1
C
Downstream
C3p1
12.7 ± 1.4 ka
Emissivity (unitless)
1
0.9
0.8
0.7
0.6
0.5
0.4
0.3
8
9
10
11
12
13
Wavelength (microns)
Series1
Series2
Series3
Series4
Series5
Series6
Series7
Series8
Series9
Average

Figure S11

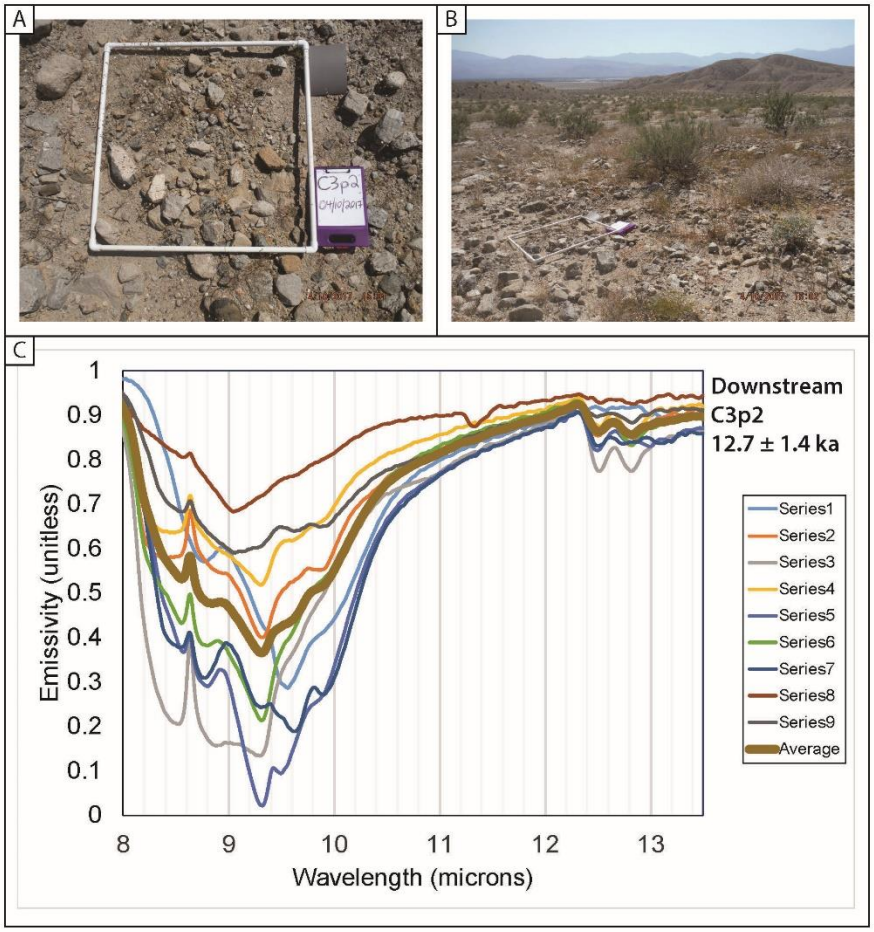
A
B
C
C3p2
Downstream
C3p2
12.7 ± 1.4 ka
Emissivity (unitless)
Wavelength (microns)
Series1
Series2
Series3
Series4
Series5
Series6
Series7
Series8
Series9
Average

Figure S12

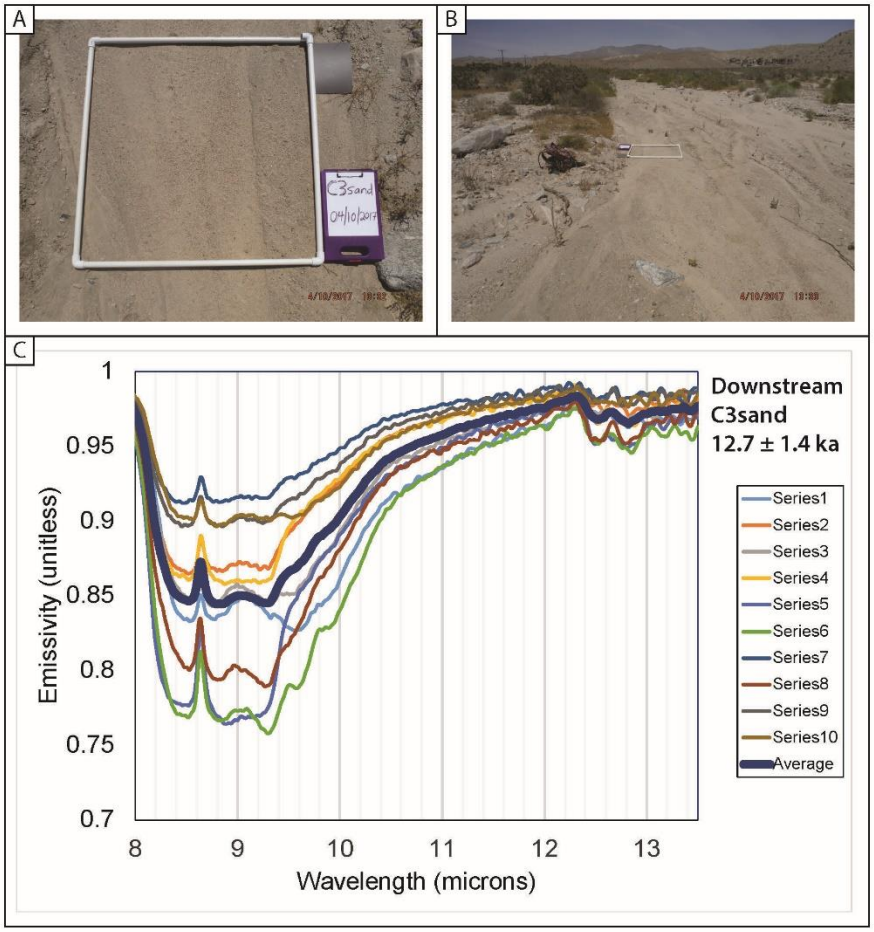
A
B
C3sand
04/10/2017
C
Emissivity (unitless)
1
0.95
0.9
0.85
0.8
0.75
0.7
8
9
10
11
12
13
Wavelength (microns)
Downstream
C3sand
12.7 ± 1.4 ka
Series1
Series2
Series3
Series4
Series5
Series6
Series7
Series8
Series9
Series10
Average

Figure S13

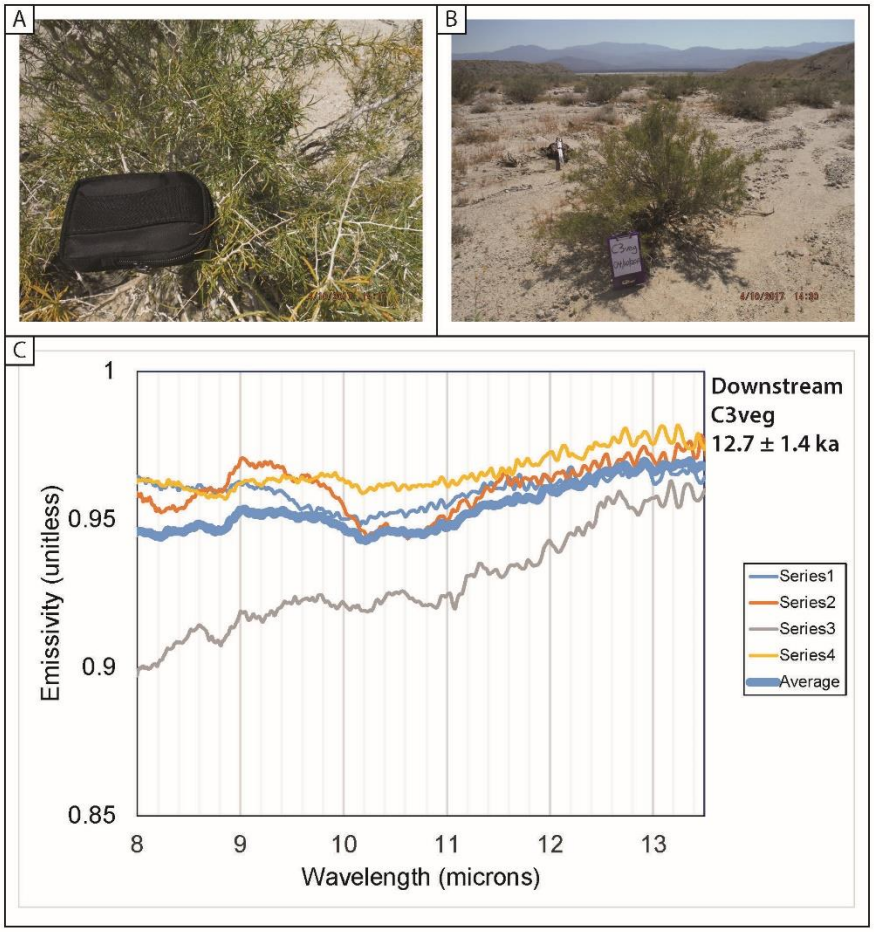
A
B
C
1
0.95
0.9
0.85
Emissivity (unitless)
8
9
10
11
12
13
Wavelength (microns)
Downstream
C3veg
12.7 ± 1.4 ka
Series1
Series2
Series3
Series4
Average

Figure S14

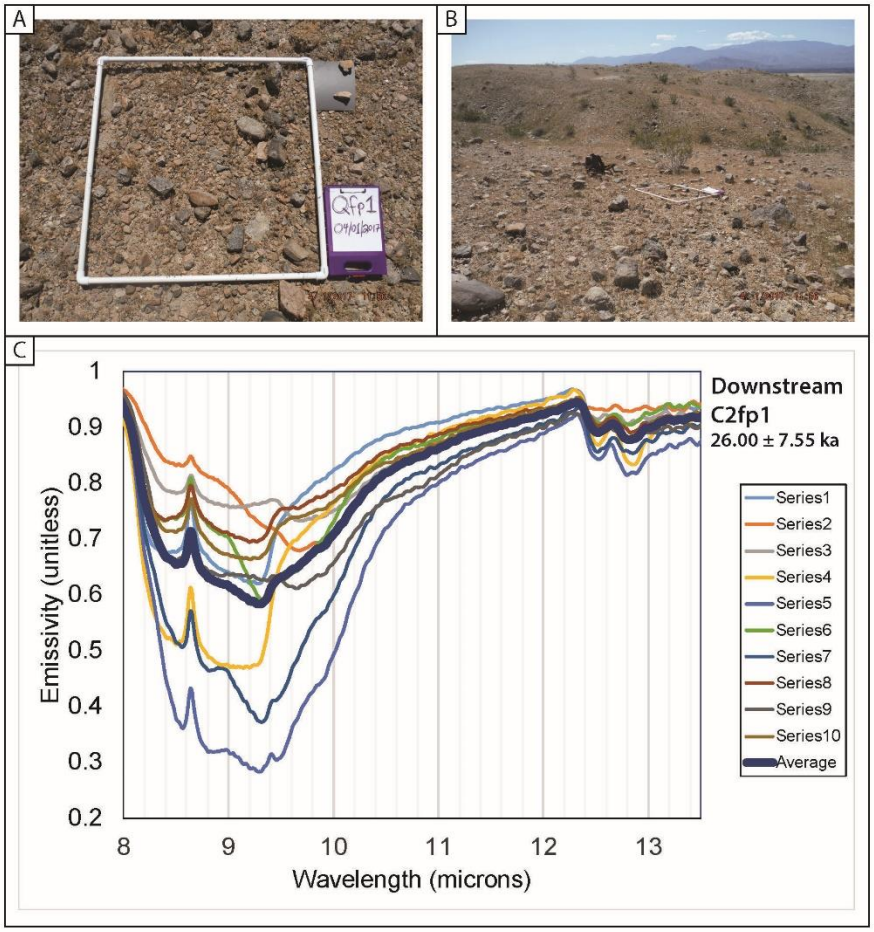
A
B
C
Qfp1
Downstream
C2fp1
26.00 ± 7.55 ka
Emissivity (unitless)
Wavelength (microns)
1
0.9
0.8
0.7
0.6
0.5
0.4
0.3
0.2
8
9
10
11
12
13
Series1
Series2
Series3
Series4
Series5
Series6
Series7
Series8
Series9
Series10
Average

Figure S15

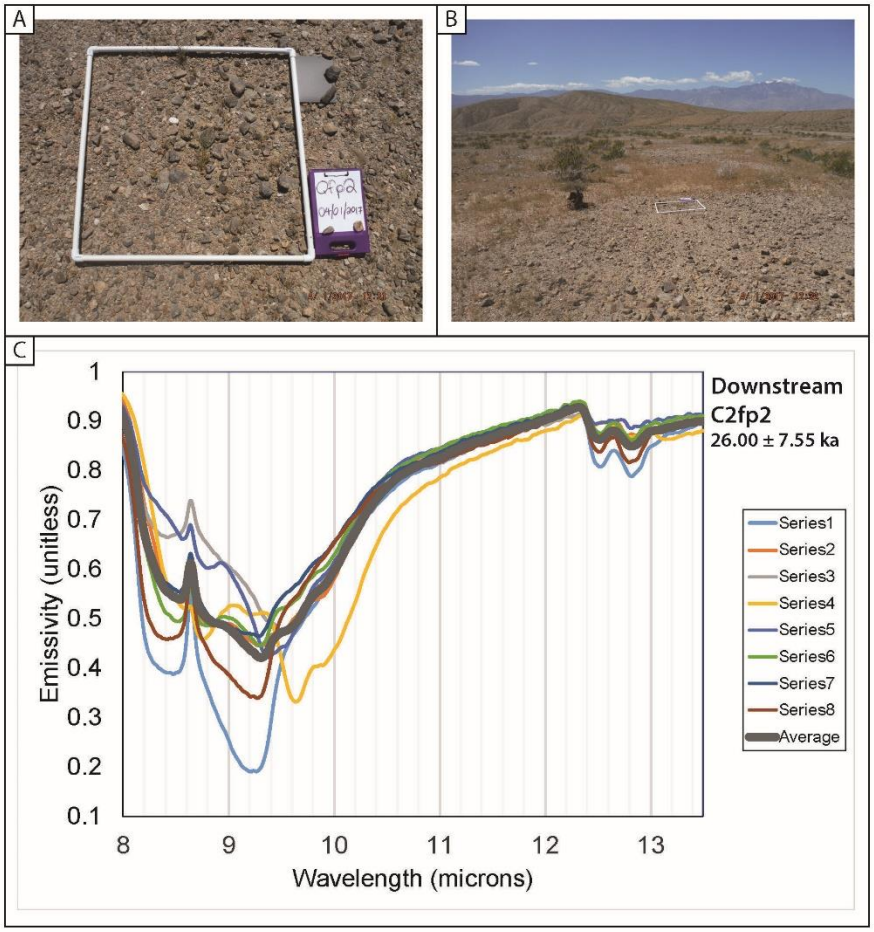
A
B
C
Downstream
C2fp2
26.00 ± 7.55 ka
Emissivity (unitless)
Wavelength (microns)
1
0.9
0.8
0.7
0.6
0.5
0.4
0.3
0.2
0.1
8
9
10
11
12
13
Series1
Series2
Series3
Series4
Series5
Series6
Series7
Series8
Average

Figure S16

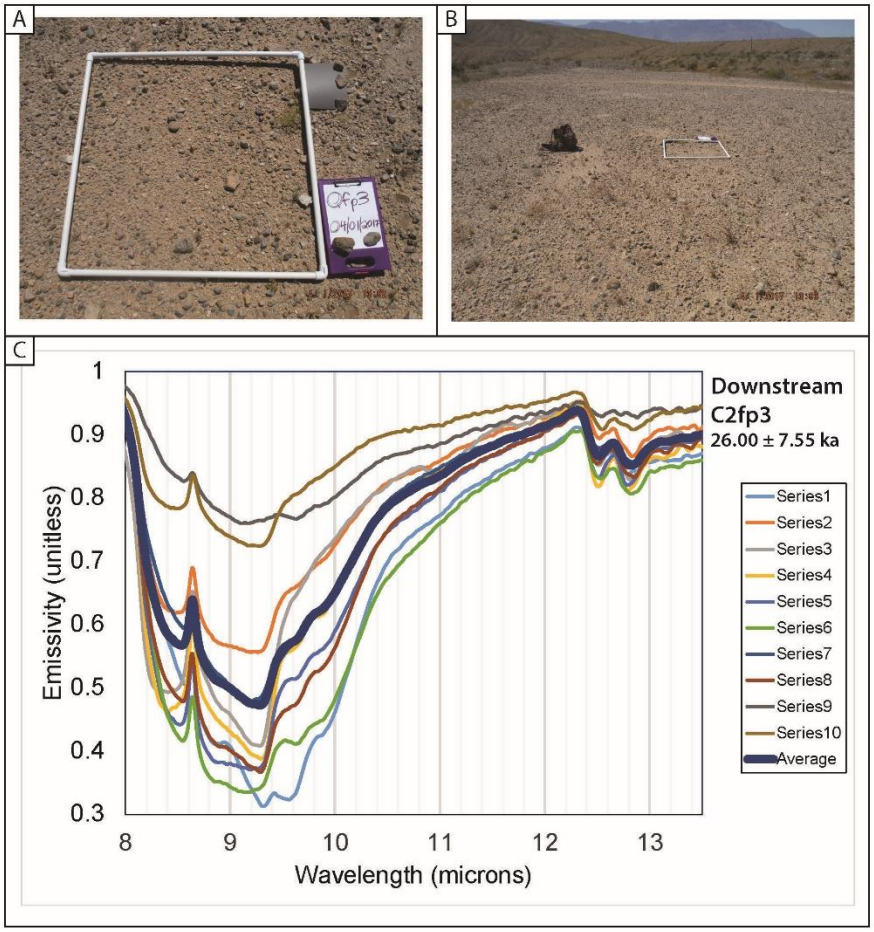
A
B
C
Qfp3
Downstream
C2fp3
26.00 ± 7.55 ka
Emissivity (unitless)
Wavelength (microns)
1
0.9
0.8
0.7
0.6
0.5
0.4
0.3
8
9
10
11
12
13
Series1
Series2
Series3
Series4
Series5
Series6
Series7
Series8
Series9
Series10
Average

Figure S17

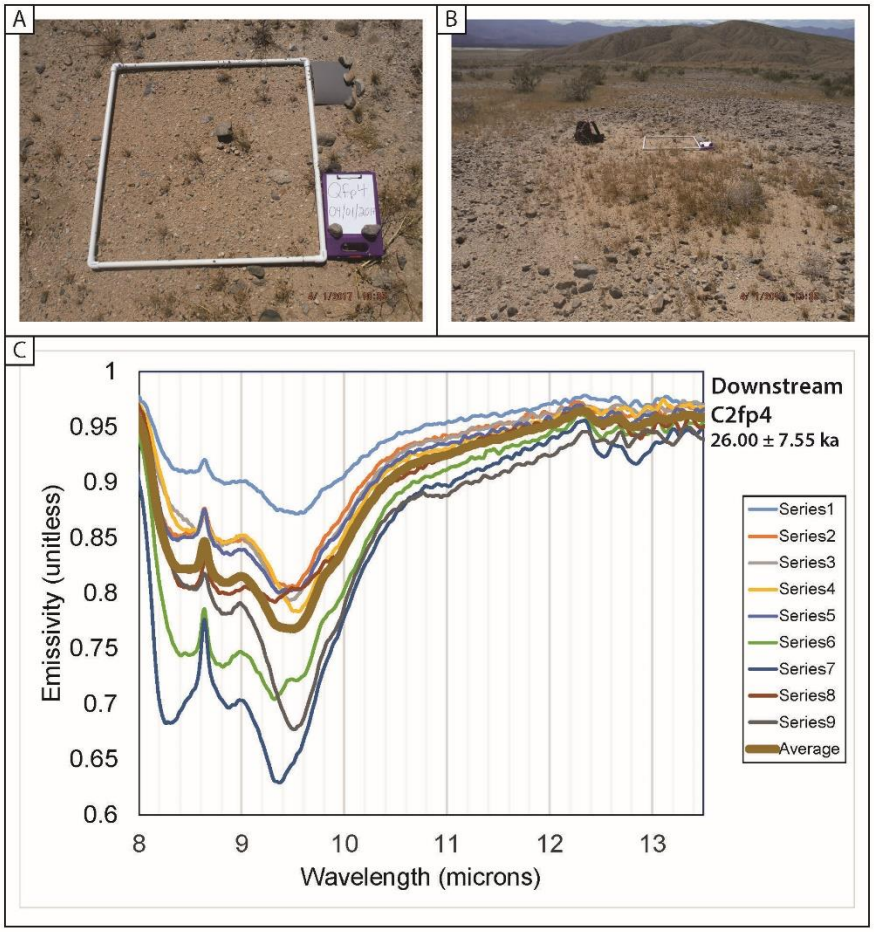
A
B
C
Downstream
C2fp4
26.00 ± 7.55 ka
Emissivity (unitless)
Wavelength (microns)
1
0.95
0.9
0.85
0.8
0.75
0.7
0.65
0.6
8
9
10
11
12
13
Series1
Series2
Series3
Series4
Series5
Series6
Series7
Series8
Series9
Average

Figure S18

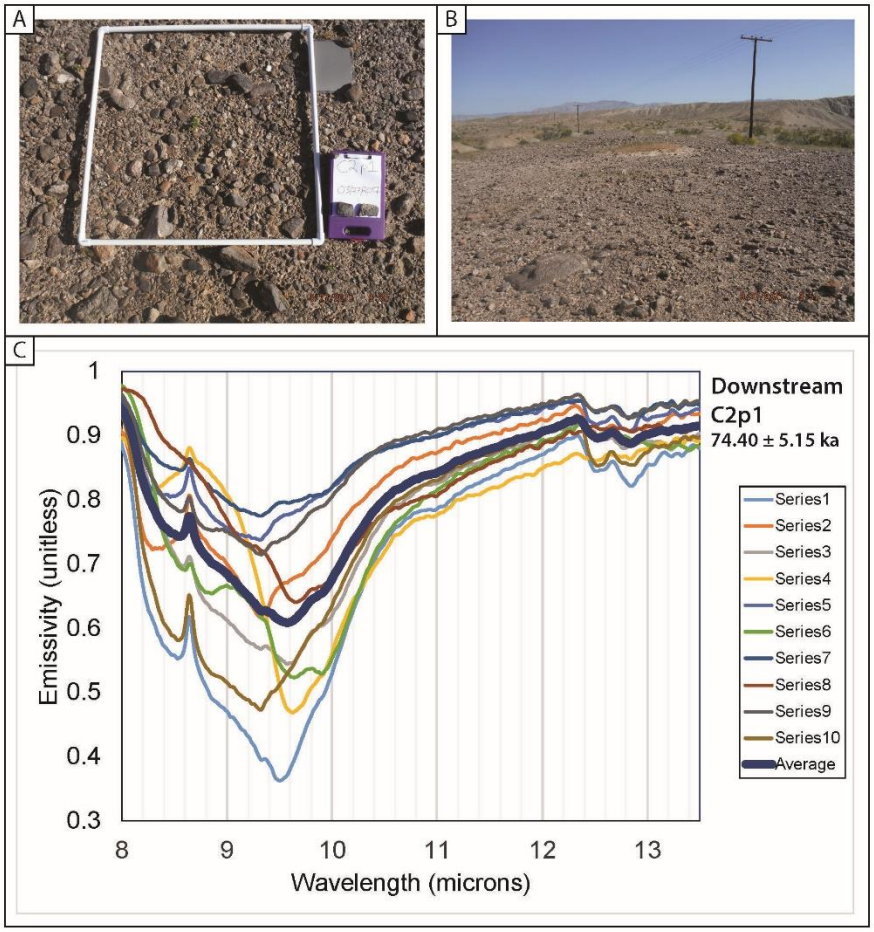
A
B
C
Downstream
C2p1
74.40 ± 5.15 ka
Emissivity (unitless)
1
0.9
0.8
0.7
0.6
0.5
0.4
0.3
8
9
10
11
12
13
Wavelength (microns)
Series1
Series2
Series3
Series4
Series5
Series6
Series7
Series8
Series9
Series10
Average

Figure S19

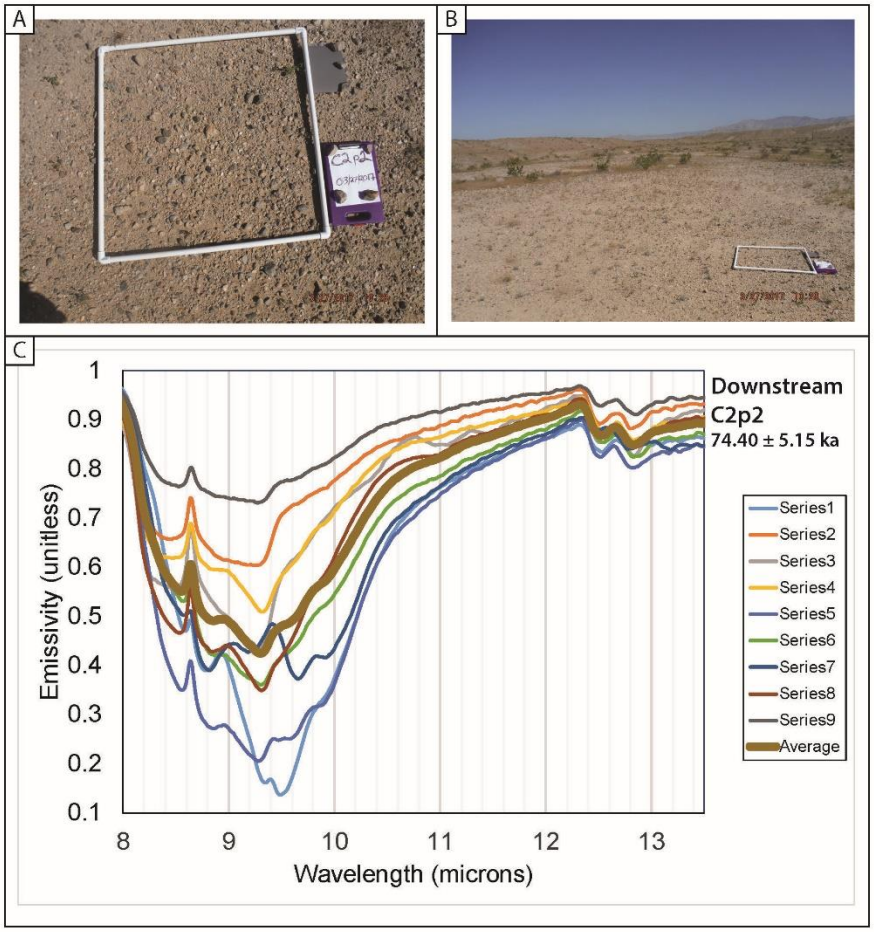
A
B
C
Downstream
C2p2
74.40 ± 5.15 ka
Emissivity (unitless)
Wavelength (microns)
1
0.9
0.8
0.7
0.6
0.5
0.4
0.3
0.2
0.1
8
9
10
11
12
13
Series1
Series2
Series3
Series4
Series5
Series6
Series7
Series8
Series9
Average

Figure S20

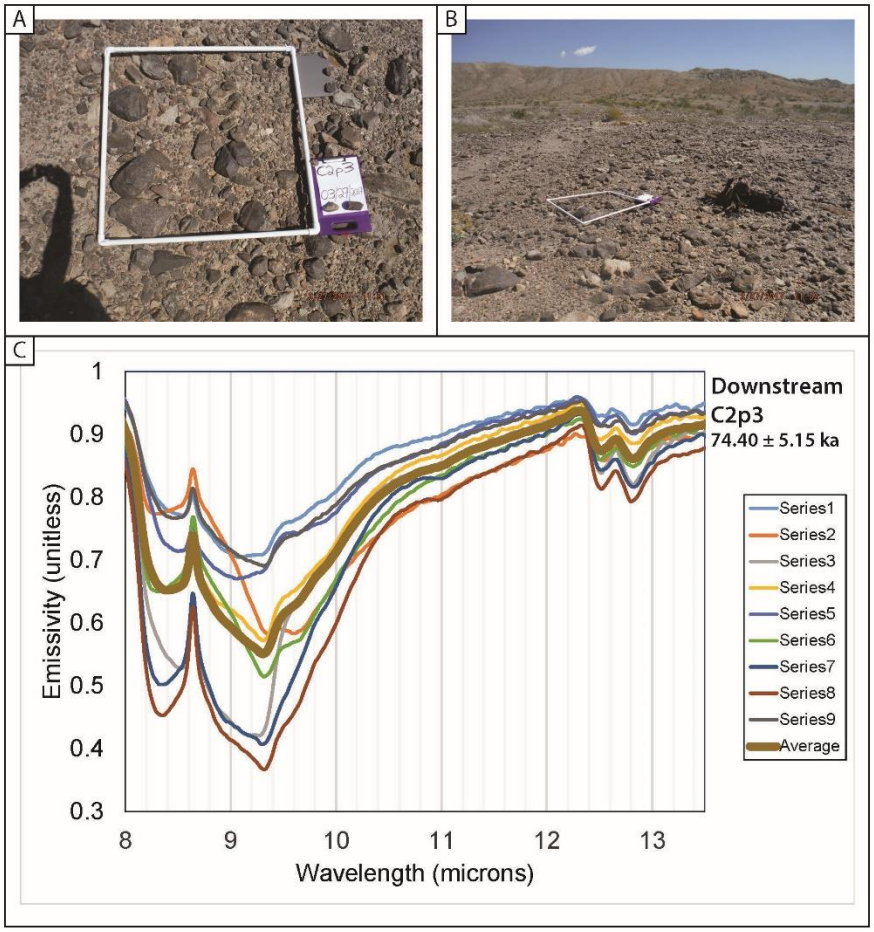
A
B
C
Downstream
C2p3
74.40 ± 5.15 ka
Emissivity (unitless)
Wavelength (microns)
1
0.9
0.8
0.7
0.6
0.5
0.4
0.3
8
9
10
11
12
13
Series1
Series2
Series3
Series4
Series5
Series6
Series7
Series8
Series9
Average

Figure S21

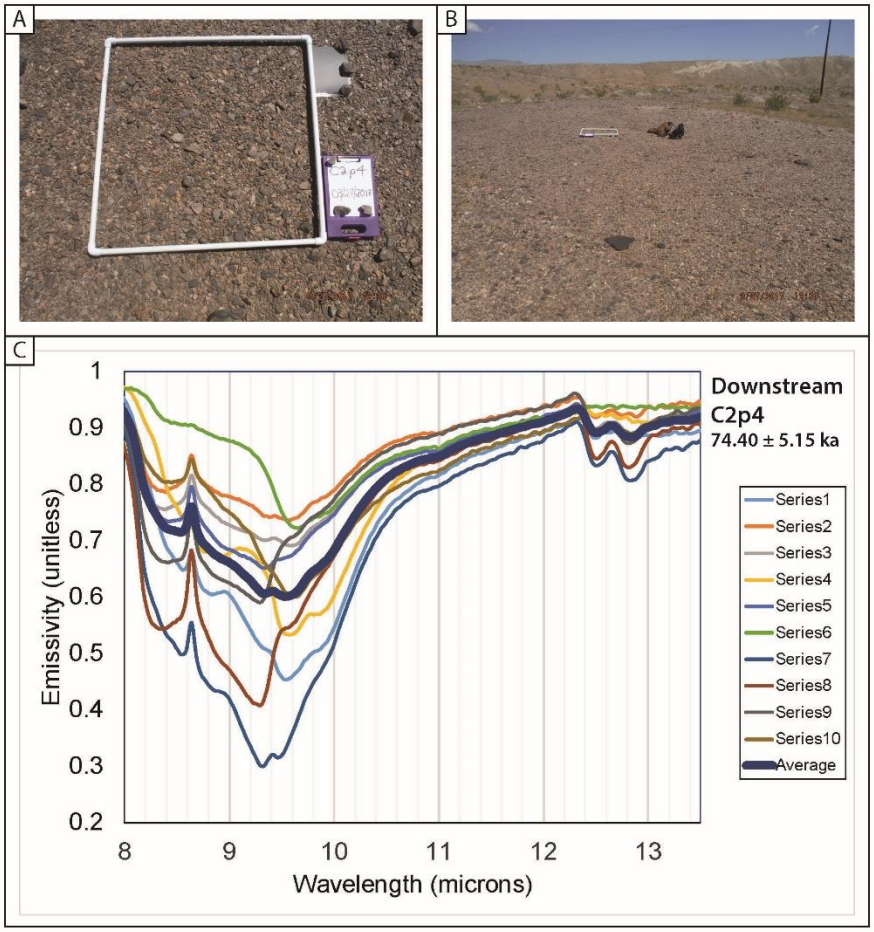
A
B
C
Downstream
C2p4
74.40 ± 5.15 ka
Emissivity (unitless)
Wavelength (microns)
1
0.9
0.8
0.7
0.6
0.5
0.4
0.3
0.2
8
9
10
11
12
13
Series1
Series2
Series3
Series4
Series5
Series6
Series7
Series8
Series9
Series10
Average

Figure S22

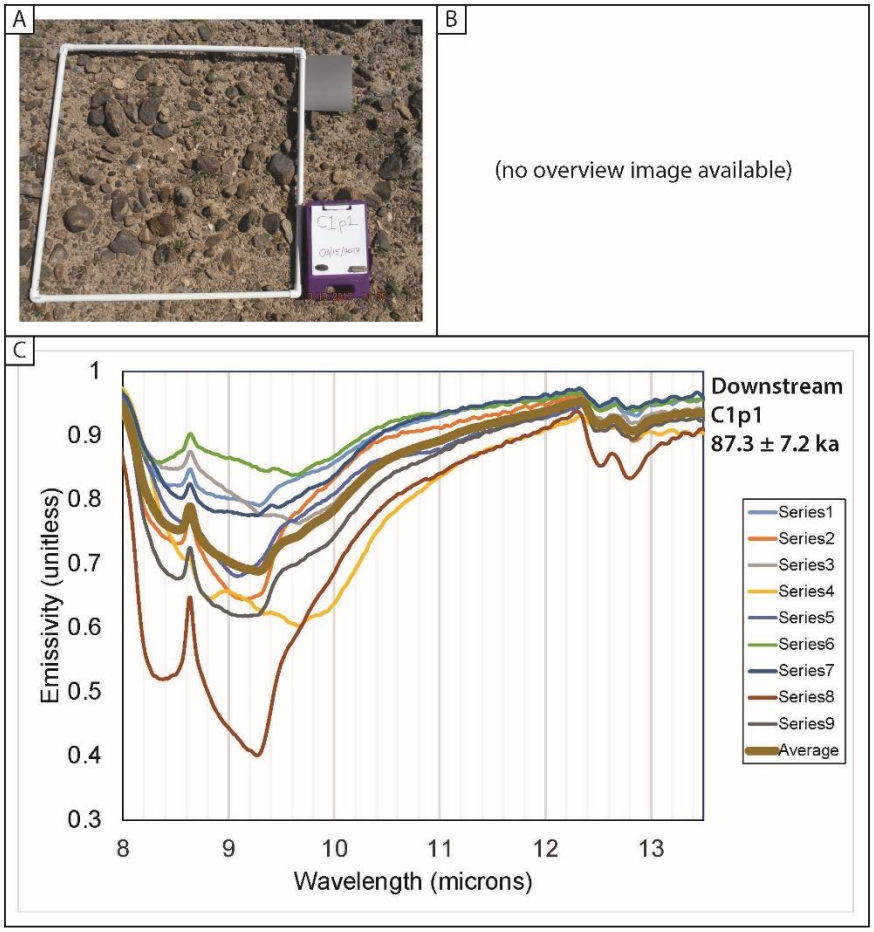
A
B
(no overview image available)
C
Downstream
C1p1
87.3 ± 7.2 ka
Emissivity (unitless)
Wavelength (microns)
Series1
Series2
Series3
Series4
Series5
Series6
Series7
Series8
Series9
Average

Figure S23

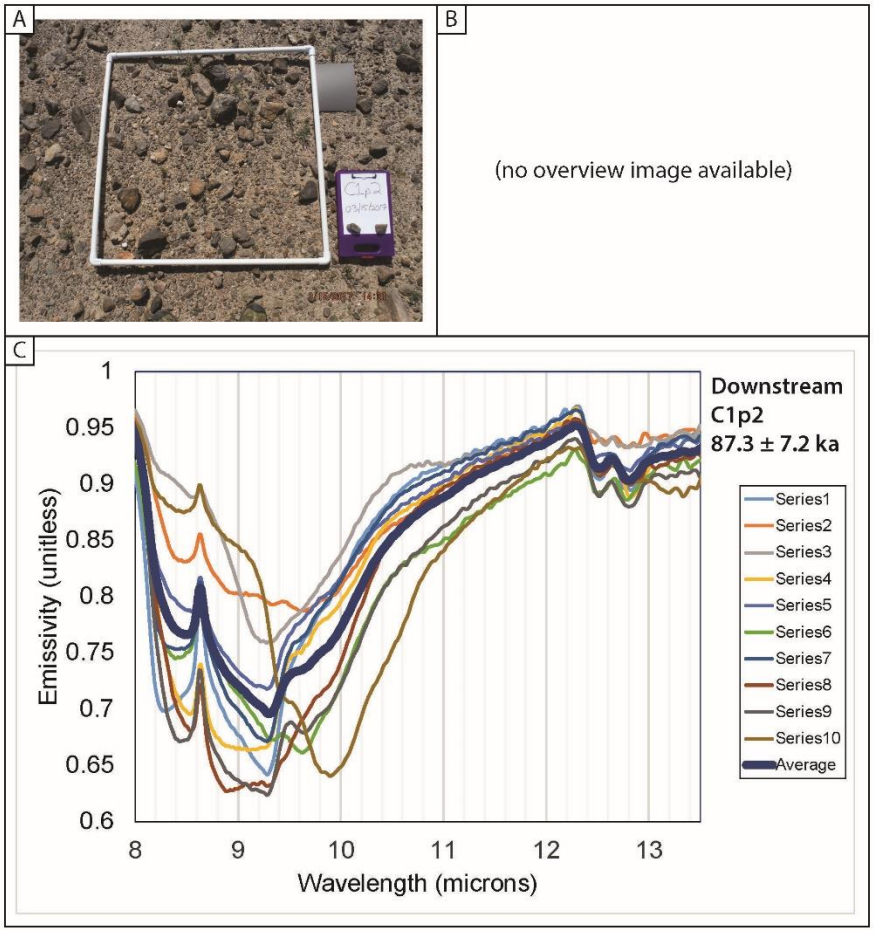
A
B
(no overview image available)
C
Downstream
C1p2
87.3 ± 7.2 ka
Emissivity (unitless)
Wavelength (microns)
1
0.95
0.9
0.85
0.8
0.75
0.7
0.65
0.6
8
9
10
11
12
13
Series1
Series2
Series3
Series4
Series5
Series6
Series7
Series8
Series9
Series10
Average

Figure S24

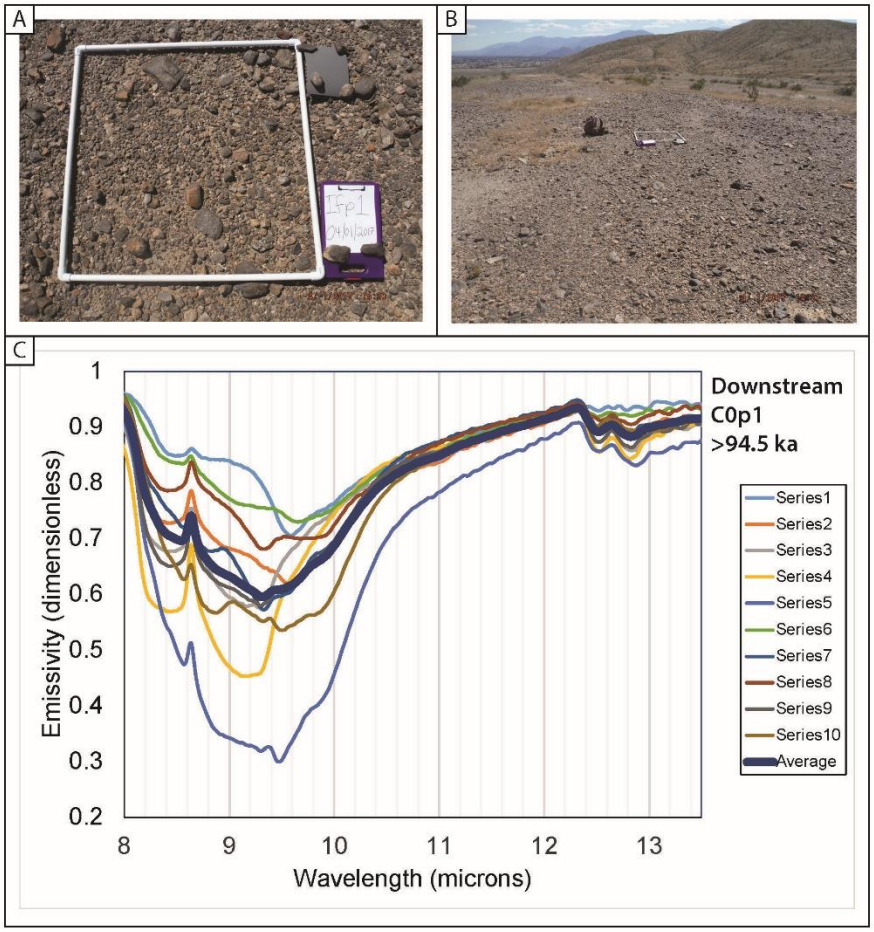
A
B
C
Downstream
C0p1
>94.5 ka
Emissivity (dimensionless)
Wavelength (microns)
1
0.9
0.8
0.7
0.6
0.5
0.4
0.3
0.2
8
9
10
11
12
13
Series1
Series2
Series3
Series4
Series5
Series6
Series7
Series8
Series9
Series10
Average

Figure S25

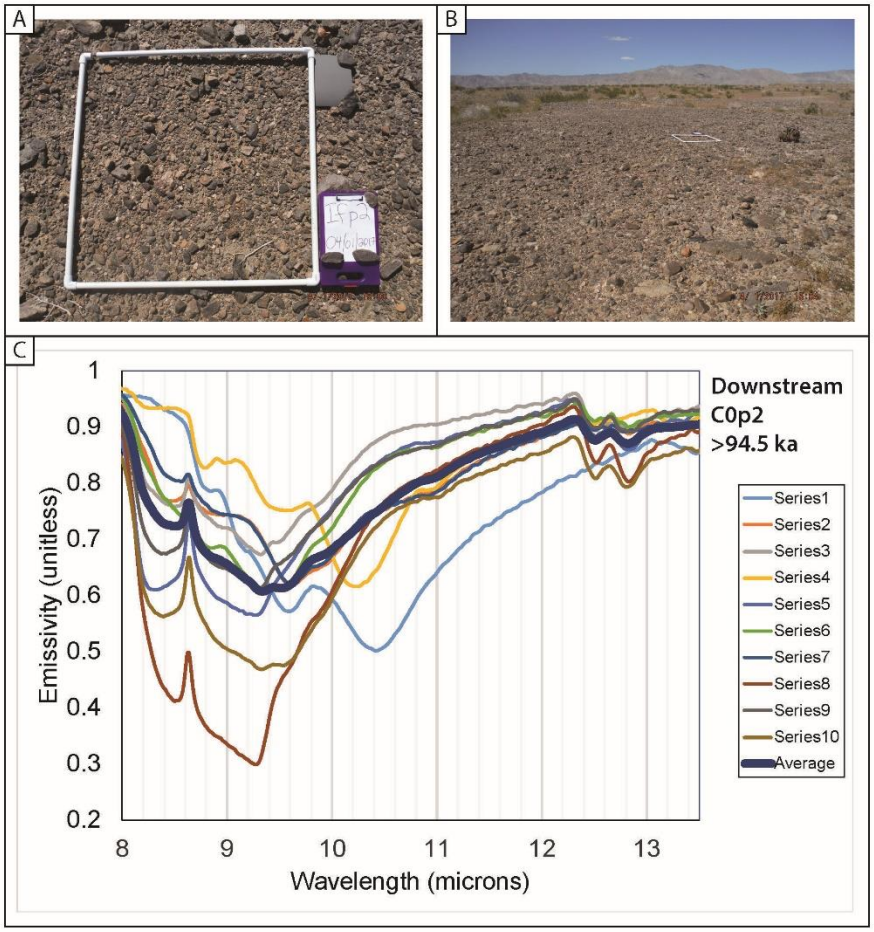
A
B
C
Downstream
C0p2
>94.5 ka
Emissivity (unitless)
Wavelength (microns)
1
0.9
0.8
0.7
0.6
0.5
0.4
0.3
0.2
8
9
10
11
12
13
Series1
Series2
Series3
Series4
Series5
Series6
Series7
Series8
Series9
Series10
Average

Figure S26

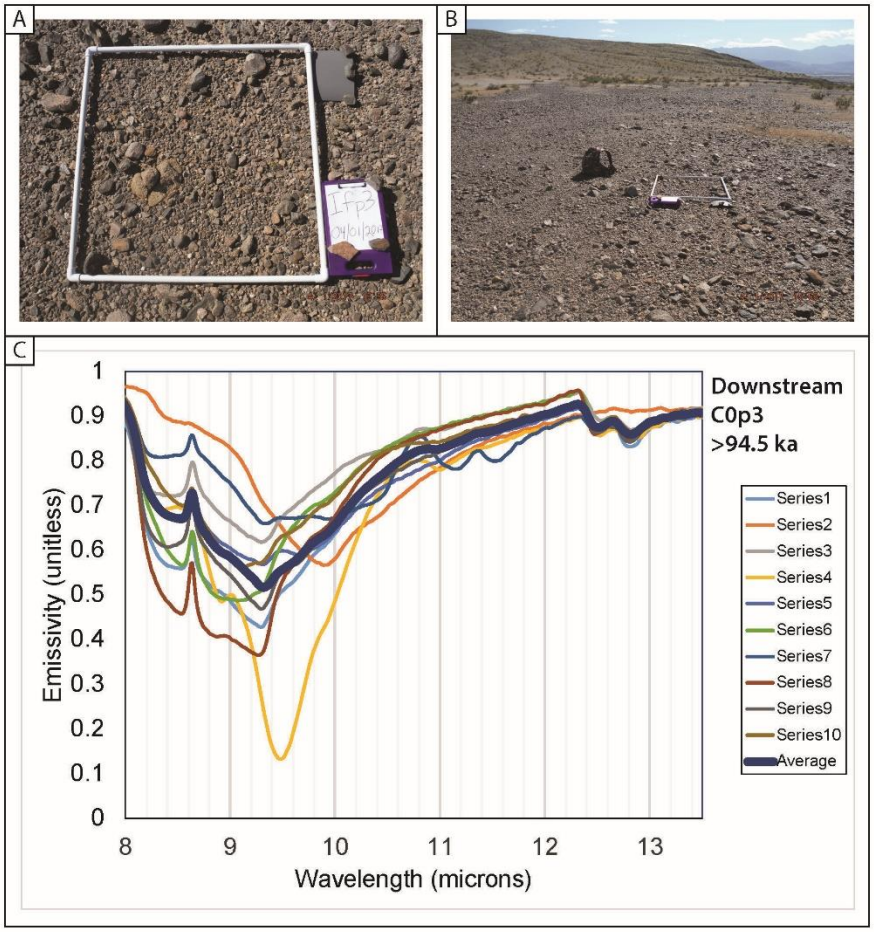
A
B
C
Downstream
C0p3
>94.5 ka
Emissivity (unitless)
Wavelength (microns)
1
0.9
0.8
0.7
0.6
0.5
0.4
0.3
0.2
0.1
0
8
9
10
11
12
13
Series1
Series2
Series3
Series4
Series5
Series6
Series7
Series8
Series9
Series10
Average

Figure S27